# Air-gun signal post-processing and sound transmission modelling in shallow water

## Noise impact of marine seismic exploration on great whales

BENJAMIN TRIMOREAU

Department of Civil and Environmental Engineering
*Division of Applied Acoustics*
*Vibroacoustics Group*
CHALMERS UNIVERSITY OF TECHNOLOGY
Göteborg, Sweden 2011
Master's Thesis 2011:135

Air-gun signal post-processing and sound transmission modelling
in shallow water
Noise impact of marine seismic exploration on great whales

Master's Thesis 2011:135

Department of Civil and Environmental Engineering
Division of Applied Acoustics
Vibroacoustics Group
Chalmers University of Technology
SE-41296 Göteborg
Sweden

Tel. +46-(0)31 772 1000

Cover:
BRAHSS project logo (Behavioural Response of Australian Humpback whales to Seismic Surveys). This paper is part of BRAHSS.

Reproservice / Department of Civil and Environmental Engineering
Göteborg, Sweden 2011

Air-gun signal post-processing and sound transmission modelling in shallow water
Noise impact of marine seismic exploration on great whales
BENJAMIN TRIMOREAU
Department of Civil and Environmental Engineering
Division of Applied Acoustics
Vibroacoustics Group
Chalmers University of Technology

# Abstract

Marine seismic surveys using a collection of air-guns are commonly used to map sea bottom structures. The noise impact of horizontal air-gun sound transmission in shallow water on marine megafauna as humpback whales is a substantial concern. This paper is part of the 4-year national project BRAHSS (Behavioural Response of Australian Humpback whales to Seismic Surveys). The work aims at studying the sound propagation of air-gun sound impulses through an empirical and a numerical method. The data sets are from the 2010 trials and are used to provide inputs of the numerical model as the geoacoustic properties of the sea bottom. The final outcome is the calculation of the sound exposure levels with range at experimentally followed whales. The bioacoustic tasks aiming at assessing the level of disturbance on the whales will be carry out by bioacousticians from universities of Sydney, Queensland and Curtin.

**Key words: underwater acoustics, marine seismic survey, air-gun noise, horizontal sound propagation, shallow water, sound transmission modelling, wavenumber integration technique, humpback whale.**

To my mum

# Acknowledgements

I would like to thank my colleagues of the CMST who were complementary and friendly. A special thank to Rob McCauley, Alec Duncan, Sasha Gavrilov and Iain Parnum. I am grateful to Ann and Kim who made easy all my administrative requests. A general thanks to the CMST to allow me to work in such a nice subfield of acoustics. Thank you to the UTC and Chalmers, my two universities which gave me the freedom to study and work abroad. I dedicate this thesis to my mum, Françoise, who is still sharing with us her joy of living.

# Contents

# 1 Introduction

This thesis deals with underwater acoustics, in a context of man-made noise impact studies on marine megafauna. Much of the man-made noise in the sea is at low-frequencies which overlaps hearing sensitivity of great whales below 1000 Hz creating the concern of impacts of the noise on whales [1].

Among the sources of noise, seismic exploration sounds have been a major concern for several decades. In these surveys, petroleum companies or geophysical institutes measure the earth's geo-properties in the ocean using powerful explosive or nonexplosive sound sources.

## 1.1 Noise pollution from seismic surveys

The impact of seismic surveys on surrounding animals is a concern due to significant propagation of lateral sound. The known good match between the frequency distribution of seismic exploration sounds and the hearing sensitivity of great whales increases the need to study their impacts. The fact that marine mammals rely on acoustics as a survival tool - for orientation, food foraging, communication, etc. - justify the importance of such studies.

Those sounds are short pulses separated by quiet periods. Nonexplosive sources as air-gun arrays are dominantly used nowadays. These arrays comprise a collection of air-guns distributed over a chosen geometry and towed behind a seismic vessel (see Fig. 1).

**Figure 1:** *Seismic vessel towing an air-gun array and hydrophone arrays (marineinsight.com).*

An air-gun allows the sudden release of air into the water which creates a sound pulse. The air-guns within the array are fired synchronously to produce a powerful highly directional bottom-directed pulse. The reflected or refracted waves are then recorded and processed to image acoustically the sub-bottom structures. Typically, an air-gun array produces waterborne sounds with broadband source levels of 220-

225 dB re 1μPa-m (1 metre away from the source) [1]. Most of the pulse energy is in low frequencies (< 50 Hz) with significant energy up to 1000 Hz. Note that, in this paper, low frequencies will typically refer to frequencies below around 100Hz and high frequencies typically to frequencies of a few hundred Hz and above.

The surveys are usually made in shallow water areas where multipath sound propagation and leakage occur. Such an environment is called ocean waveguide, where high-frequency acoustic energy can propagate with quite small attenuation.

The probability that a whale will be exposed to the near vertical downward propagating direct pulse is fairly small [2]. This is not true with the surrounding environment and strong sound pulses are projected horizontally into the water in certain directions, and these can be detected many kilometres away [1]. The propagation of this waterborne wave is the central theme of this paper. Fig. 2 illustrates this issue. The bottom-directed waves - of much higher energy - are represented by the black arrows and penetrate effectively through the sea bottom layers.

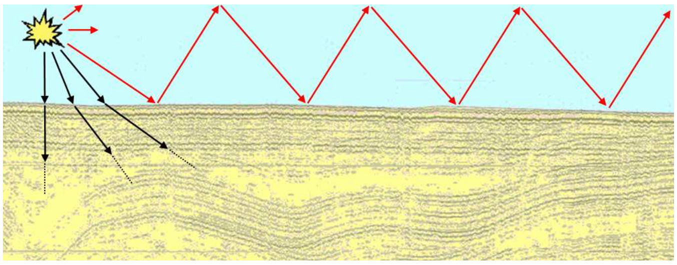

**Figure 2:** *Illustration of lateral sound propagation in shallow water from a seismic source (yellow explosion). Black arrows indicate the desired propagation for geophysical purpose.*

Thus, the broadband acoustic energy distribution of the waterborne wave in the ocean waveguide has to be predicted using either empirical or numerical methods. The tasks undertaken during this thesis are dedicated to this issue as well as a description of all the parameters involved.

## 1.2 Context of work: the JIP project

In 2010, the Joint Industry Program (JIP) - a group of petroleum companies and contractors - funded a consortium of Australian universities to study the impact of marine petroleum exploration on great whales, and more specifically in this project, humpback whales. The project is called BRAHSS (Behavioural Response of Australian Humpback whales to Seismic Surveys) and implies two years of trials on the east coast of Australia and two years on the west coast.

In September and October 2010, the first series of trials were made off Peregian Beach, Queensland in Australia. The Centre for Marine Science and Technology (CMST) was in charge of air-gun operations and whale observations from the source vessel. A single seismic source - an air-gun - was operated near to humpback whales in coastal waters up to 40 m deep. A series of hydrophones were deployed on the seabed to measure the air-gun signals with range (i.e. distance source - receiver). Other sensors were used as well to measure important parameters as water temperatures or air-gun parameters.

In parallel of the trials, meticulous whale observations were undertaken from the seismic vessel and the shore as seen in Fig. 3 below.

**Figure 3:** *Humpback whale observations from the seismic vessel during the JIP 2010 experiments.*

The idea was to use afterwards the different measured data sets of air-gun signals for two purposes: the first one is to give information about the area - in order to define the parameters which are significant in sound propagation; and the other one is to follow an empirical approach to define received levels at experimentally followed whales.

After the initial data post-processing step, a numerical approach was undertaken in order to predict the received level at any depth and any range in the experimental area. This method uses the measured data sets - which give inputs regarding the acoustic environment and verification. The choice of the technique describing sound propagation in shallow water has to be relevant to find a compromise between accurate results and simplification of the real environment. Some simplification is required given the complexity of an ocean waveguide environment, especially in terms of geoacoustic parameters of the sea bottom.

The GPS positions of the source and its source level are known inputs from measurements. The position of the receivers - i.e. the followed whales - is a reasonably known input given that the whale tracks were recorded during the air-gun operations.

The final outcome of this research is to quantify the received air-gun levels at whales over the experimental area and compare the results from measurements and simulation.

The assessment of the actual degree of disturbance on whales is not a demanding task in this thesis and will be investigated by bioacousticians from Universities of Queensland, Sydney and Curtin.

## 1.3 Basics of underwater acoustics

A brief introduction on underwater acoustics seems necessary for readers who are not familiar with this field. Underwater sound propagates much faster than airborne sound with a typical sound speed of 1500 m/s. The water column is described as a conceptual column of water from sea surface to bottom. The sound speed depends on the water depth, temperature and salinity. Thus, a sound speed profile can be defined within the water column as the example in Fig. 4.

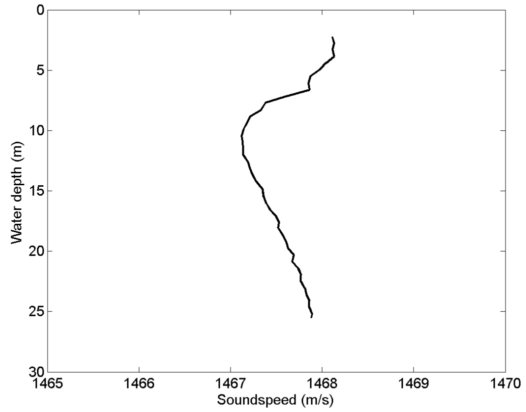

**Figure 4:** *Example of a measured sound speed profile within the water column.*

As in airborne acoustics, a reference sound pressure is used in underwater acoustics to calculate levels in dB. It has been adopted that this reference pressure $P_0$ is 1 µPa. The reference intensity $I_0$ is 1 pW/m$^2$.
The intensity level and sound pressure level are described as in airborne acoustics:

$$I_{dB} = 10\log(\frac{I}{I_0}) \quad (1)$$

$$SPL_{dB} = 20\log(\frac{P}{P_0}) \quad (2)$$

A common variable used in underwater acoustics is the sound pressure density spectrum level - also written as sound spectrum levels. Its unit is dB re 1µPa$^2$/Hz and it gives the distribution of sound versus frequency, i.e. the sound pressure per unit frequency.
Sound propagation in water is described with the transmission loss (TL) as in airborne acoustics. In dB, the transmission loss can be expressed as the difference between the levels at two distances. The closest distance is usually a reference distance, e.g. 1 m. Strictly speaking, TL is a positive quantity but it is plotted downward to visualize the way in which a sound diminishes with increasing distance.

A major component of transmission loss is spreading loss. From a point source in a uniform water medium, sound spreads outward as spherical waves [1]. Spherical spreading is generally appropriate in the near-field, e.g. for range R < D in an ocean waveguide of water depth D. The mean square pressure varies inversely with the square of the distance from the source. The transmission loss at range R is given as:

$$TL = 20 \log R \tag{3}$$

Cylindrical spreading occurs in the ocean waveguide when the water medium is bounded by perfect reflectors. It is only appropriate at long ranges (R >> D). The various reflected waves combine and form a cylindrical wave. The mean square pressure varies inversely with distance from the source and the transmission loss if given as:

$$TL = 10 \log R \tag{4}$$

Fig. 5 gives the transmission loss in dB for pure spherical and cylindrical spreading against range. The transition range is defined as the distance at which spherical spreading stops and cylindrical spreading begins. They only give an idea of the evolution of the sound field in a real environment where various environmental loss mechanisms occur. These factors are discussed in section 2.3. As an example, Fig. 5(b) includes linear absorption (from the water medium) and scattering losses (from different physical mechanisms), i.e. a loss of 0.5 dB per km.

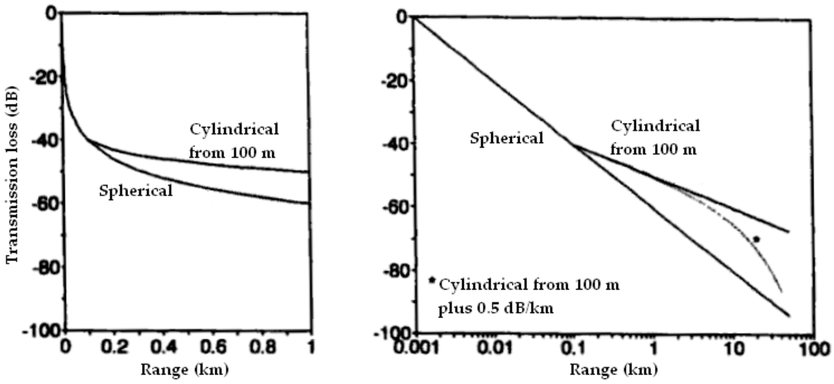

**Figure 5:** *Sound transmission loss versus distance with pure spherical, combined spherical and cylindrical spreading with transition range 100 m, and (in right only) the latter plus linear absorption and scattering losses of 0.5 dB/km. Linear distance scale (left). Logarithmic distance scale (right) (Richardson, 1995).*

Other specific acoustic descriptors are used for animal effect studies of impulsive underwater noise. They are described in section 3.1.2.

# 2 Theoretical aspects

This chapter provides the relevant theoretical material to describe the propagation of lateral sounds from seismic surveys in a shallow water environment.

The first step is to define the source of underwater noise, i.e. an air-gun in the case of the JIP project.

As an introduction of sound propagation in an ocean waveguide, the second section deals with the normal mode theory in an ideal waveguide where no environmental factor is taken into account.

Then, the subsequent section describes how the natural variables of a real ocean waveguide environment affects sound propagation; and what environmental factors are likely to have a dominant impact and change from different geographical regions.

The final section deals with theoretical material on air-gun signals transmission in shallow water and the parameters involved.

## 2.1 Noise generated from seismic surveys using air-guns

The aim here is to identify the interesting part for the geophysicists of the signal produced by air-guns. In parallel, the part of the signal studied in a context of animal effect studies is identified, i.e. the acoustic energy propagating efficiently within the ocean waveguide in the lateral direction.

Seismic surveys typically use reflection seismic technique which requires air-gun arrays and that is discussed in the second section.

The standard parameters regarding the seismic source are discussed in these sections.

### 2.1.1 Single air-gun

A single air-gun is considered for the moment. The use of an air-gun array - i.e. a collection of air-guns - and its implications are discussed in 2.1.2.

A seismic source aims to produce a powerful bottom-directed sound pulse, centred in low-frequencies to allow a strong bottom penetration. The sea bottom is made of different geological layers and each layer has its own density. At the interface between two layers, the density contrast causes the incident wave to be reflected or refracted, according to Snell's law. The record and the analysis of either the reflected or refracted data give information on the geoacoustic properties of each detected layer.

The frequency distribution of the emitted signal is carefully controlled to find a compromise between very low frequencies (< 50 Hz) which allow deep penetration into the earth and higher frequencies (a few hundred Hz) which give better data resolution.

Basically, an air-gun produces a sudden release of compressed air into the water. Air-guns can be of different sizes, which modify the frequency range and the level of the emitted acoustic energy. As an example, Fig. 6 shows a picture of the air-gun used for the JIP project, when it was not operated.

**Figure 6:** *Bolt 600B air-gun with a 20 in$^3$ firing chamber and bolted into a yellow towfish (JIP).*

The air-gun is towed behind the seismic vessel and immersed at a stable depth and horizontal position. Its depth is a key feature for the properties of the emitted signal. During operations, it takes alternatively a charged and a fired state. Fig. 7 shows the main elements composing an air-gun and its position at each state.

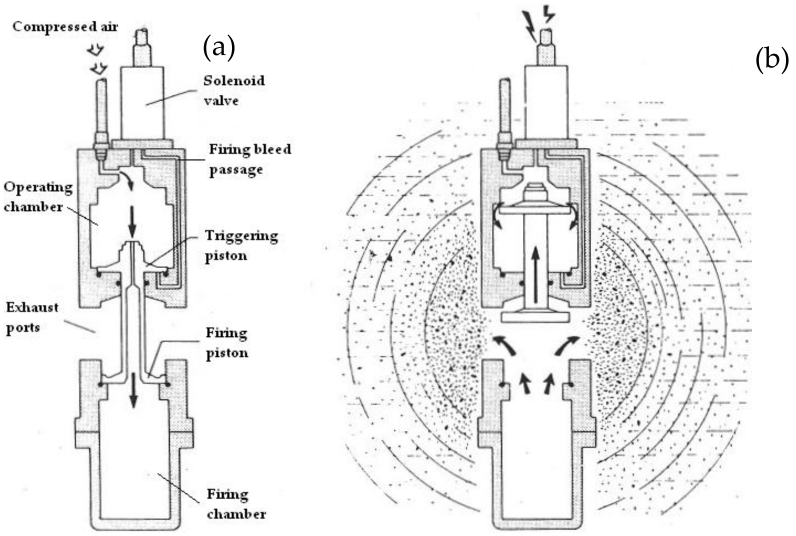

**Figure 7:** *Charged state (a) and fired state (b) of an air-gun (Hutchinson and Detrick, 1984).*

In the charged state, the idea is to fill the operating chamber with compressed air, as well as the firing chamber through the piston orifice. The firing bleed passage on Fig. 7(a) is shut off by the solenoid valve at this moment. The piston is forced hard up against the two chambers seals by the air pressure. The air-gun firing is triggered by an electric signal, opening the firing bleed passage via the solenoid valve. The air pressure is then equalized on both sides of the piston in the operating chamber and the gas of the firing chamber is suddenly released into the water, through the exhaust ports as shown in Fig. 7(b).

The air release generates an acoustic signal which is a sound pulse. A single air-gun is not specifically designed to emit a downward pulse but air-guns arrays focus sound propagation towards the sea bottom. However, there is inevitably sound propagation in all directions either with one or several air-guns. Fig. 8 below shows two images from a video sequence showing the firing of a horizontal 2-airgun array.

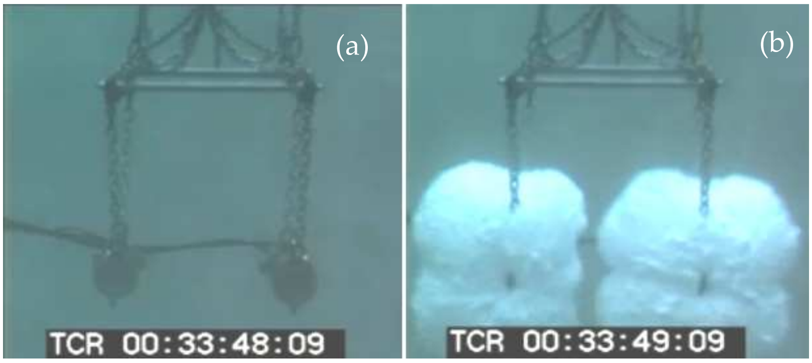

**Figure 8:** *Pictures from 2 air-guns mounted together. (a) Before being fired. (b) Just after being fired.*

The downward propagation is characterized at the source by the air-gun pressure signature measured at 1 m with a hydrophone. Fig. 9(a) gives a typical air-gun near-field signature versus time. The first peak is the desired peak for seismic survey purposes - and it corresponds to the initial air release shown in Fig. 8(b). It is the primary pulse and it has a wide frequency band of energy. The next peaks are the bubble pulses which come from the expansion-collapse cycle of a bubble. This cycle occurs just after the initial air release and causes interferences with the primary pulse. Thus, air-guns do not provide ideal sound pulses - i.e. a single spike - as explosives can do.

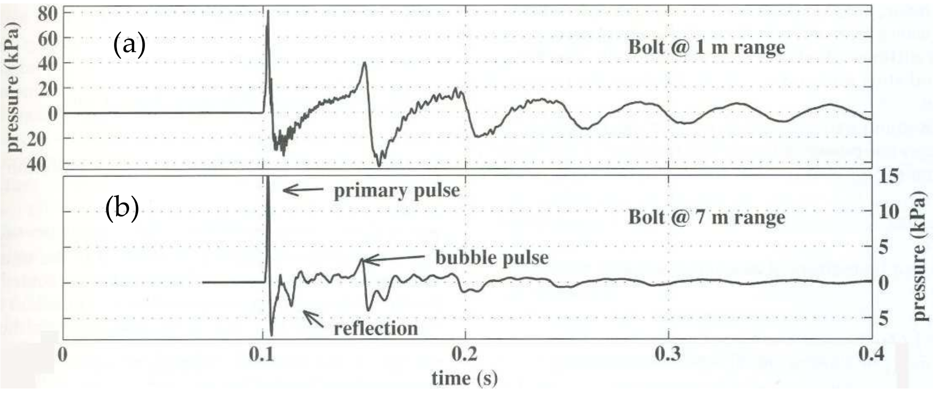

**Figure 9:** *Examples of air-gun signals from a Bolt 600B at 1 m (a) and 7 m (b). The air-gun depth was 5 m and the water depth 10 m. The air-gun pressure was 10 MPa ( McCauley, 2000).*

Fig. 9(a) shows the surface ghost effect. It is represented by the negative and dephased peaks. This comes from the reflection of the acoustic wave at the sea surface. Although the hydrophone was mounted close to the air-gun, the amplitudes of the surface ghost are noticeable.

The signal in Fig. 9(b) - recorded 7 m away from the source - has a gun-surface reflection at 1.4 ms and a gun-bottom reflection at 5.6 ms after primary pulse.

The signals shown in Fig. 9 highlight some of the problems inherent in describing air-gun signals. Particularly, what are the measures most relevant to horizontal sound propagation? The different descriptors used in animal effect studies from an impulsive sound source are detailed in 3.1.2.

The surface ghost is a substantial limitation for seismic survey purposes as it narrows the useful frequency band for seismic data. Thus, the choice of air-gun depth comes to find the compromise - mentioned earlier - between low and high frequencies. The sea surface reflected energy appears clearly in the sound spectrum levels - as seen below - at a given higher frequency. The low-frequency band below this particular frequency is the useful band for seismic data.

Deeper air-gun - with frequencies below 50 Hz - allows deeper bottom penetration but provides a poor data resolution. In reality, air-guns are operated at depths from around 5 to 9 meters. It is a convenient choice as there are practical difficulties of providing a continuous gas supply to a deep air-gun. This choice of deployment depth has direct consequences in terms of lateral sound propagation; with much lower transmission loss levels at great distance for deeper air-guns (see section 2.4).

The frequency band of main energy of the emitted sound pulse depends directly on the firing chamber size and operating pressure of the air-gun. A small firing chamber air-gun, i.e. around 10 or 20in$^3$, produces a broadband pulse as shown in Fig. 10 (measured data).

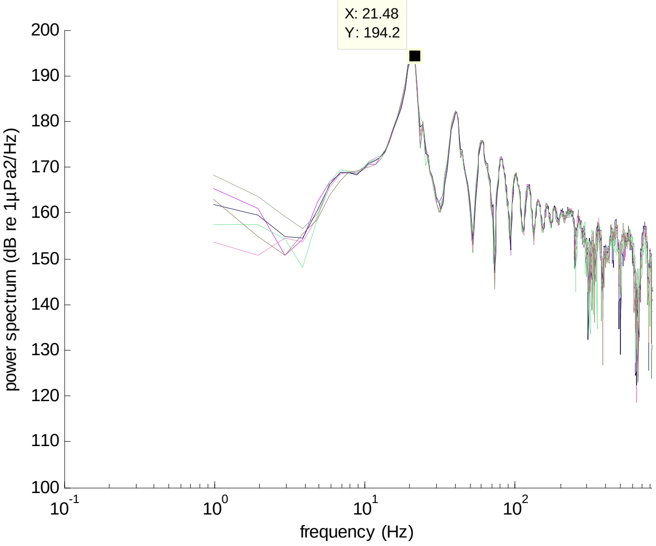

**Figure 10:** *Recorded density power spectrum levels (up to 800 Hz) of 5 consecutive shots from a 20 in$^3$ firing chamber air-gun. Near-field hydrophone at 0.85m and data calculated at 1 m (JIP data).*

Fig. 10 shows a primary pulse energy at 21.5 Hz (194.2 dB re 1μPa$^2$/Hz) with significant energy up to 1000 Hz (140 dB re 1μPa$^2$/Hz).

The use of larger guns arranged in an array flattens the bubble pulses and move the spectrum to lower frequencies.

It is interesting to notice on the spectra in Fig. 10 that the primary pulse at 21.5 Hz is followed by peaks up to 200 Hz which correspond to the bubble oscillations. The region from around 200 Hz denote the sea surface reflected energy with levels up to 155 dB re 1μPa$^2$/Hz and is the notch of the useful frequency band of seismic data.

The data above 1 kHz is mainly noise, which may be due to vibrations of the towfish around the gun. The near-field data of the JIP experiments are processed in detail in section 3.2.1.

Generally, the geophysicists require a seismic source producing the highest acoustic energy possible from very low frequencies (a few Hz) to a few hundred Hz. That is why they use a collection of air-guns. The energy at higher frequencies -with significant near-field levels - is therefore not of an interest to image the sea bottom structures but is likely to propagate horizontally due to less bottom penetration and modal propagation.

The operational setup of an air-gun (compressor, trigger generator, etc.) is illustrated later. The air-guns are typically configured to fire at a specific rate (e.g. 10 s) during the surveys, in order to provide usable data by the geophysicists.

### 2.1.2 Reflection seismic technique - Use of air-gun arrays

Reflection seismic technique is most commonly used for marine geophysical surveys. The other and older technique - refraction seismic - was used in this paper. As said earlier, air-gun arrays are the most common seismic sources.

Reflection seismic aims at measuring the reflected energy from subsurface density contrasts. For that, it is required to place the receivers nearby the source, along vertical ray paths. Typically, a long cable containing many hydrophones - called streamer - is towed behind the air-gun array as seen in Fig. 11.

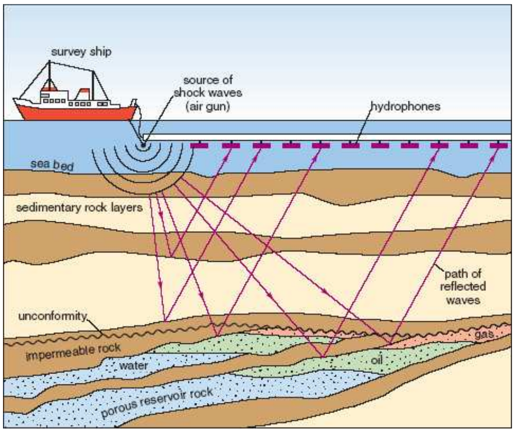

**Figure 11:** *Illustration of a reflection seismic technique deployment.*

A large number of receivers and source locations allow imaging sea bottom structures in 3D.

The use of the high-energy reflected waves permits to detect and map layers with different sound speeds and provides good data resolution - in opposition to refraction seismic. It is important here to state that each layer - in addition of its density - is characterized with its compressional sound speed. Generally, the deeper the layer, the greater the compressional sound speed. Fig. 12 gives an idea of standard layer distributions. The real environment is often much more complex and velocity inversion does occur as well as having non-homogeneous thin layers of different materials. Reflection seismic provides correct mappings in regions where velocity inversions occur. However the analysis of the recorded signals is tricky in this technique as the reflected signals from beneath the seafloor overlap with the waterborne arrivals.

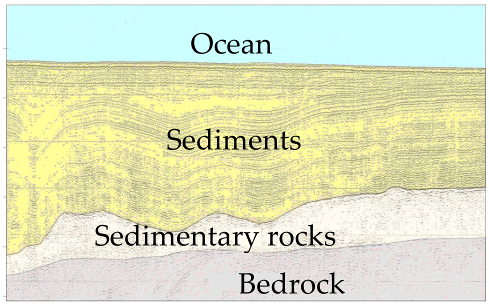

**Figure 12:** *Idea of a typical subsurface layers distribution.*

Fig. 13 below gives an example of seismogram. The theory behind, in order to obtain mappings of the geological layers - and spot hydrocarbon traps as visible in Fig. 11 - is not developed here.

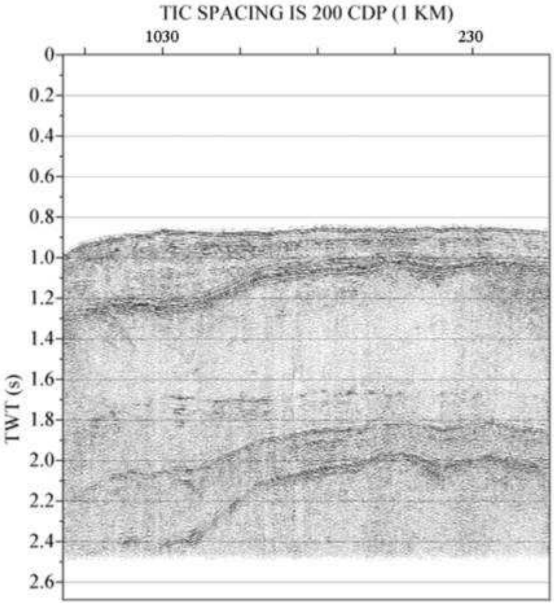

**Figure 12:** *Seismogram from a marine survey using reflection seismic. It plots the received signals vs. range and time (data collected by USGS in the Gulf of Mexico, 1999).*

An air-gun array fire synchronously a collection of guns with a mixture of firing chamber sizes (e.g. from 10 to 2000 in$^3$) allowing the generation of a stronger pulse with a broad frequency spectrum and centred in very low frequencies. The most powerful arrays have source levels as high as 259 dB re 1μPa-m and total gun volumes as large as 130 L (Parrot, 1991). The array can be considered as a single stronger powerful source. The bubble responses of each air-gun are more or less cancelled due to the mixture of gun sizes as seen in Fig. 14.

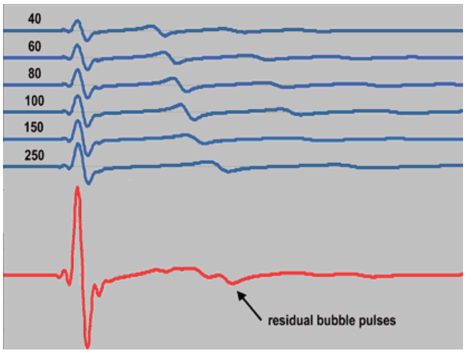

**Figure 14:** *Far-field signature of 6 air-guns vs. time, with firing chamber sizes from 40 to 250 in$^3$ and far-field signature of the 6-air-gun array in red (tle.geoscienceworld.org).*

The directivity of the source is improved too as each array has its own specific radiation pattern - which is always concentrated downwards. The control of the array directivity does not avoid lateral energy propagation. A pulse generated from a typical array has largest amplitude in the 10-120 Hz interval with strong energy up to 500-1000 Hz. As said before, the geophysical response is primarily analysed in the low frequency band up to 300 Hz [2]. The high-frequency components are weak compared to the low-frequency components but strong compared to standard ambient noise levels [1].

Arrays are usually deployed horizontally, mainly due to practical reasons. A vertical array is less likely to be stationary. Having a horizontal collection of air-guns affects dramatically lateral sound propagation in addition of choosing great gun depths. The pulse transmitted depends therefore on the gun sizes, number, spacing and operating pressure. Fig. 15 illustrates a typical horizontal air-gun array design.

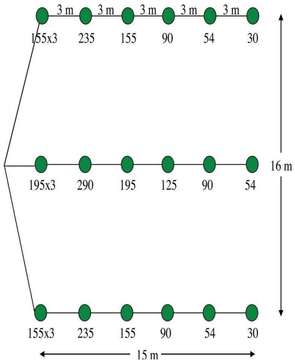

**Figure 15:** *Example of horizontal air-gun array geometry. The numbers below the gun stations are gun volumes in in3 (geoexpro.com).*

## 2.2 Normal mode theory - Ideal waveguide case

This section is relevant to understand that the acoustic energy trapped in a waveguide propagate as discrete modes. And understand the implication of having modal propagations - especially on received signals at long distances.

"Shallow" means a water depth in which sound is propagated to a distance by repeated reflections from both surface and bottom [3]. It enables then the propagation of sound over long distances. In the context of the thesis, the acoustic environment refers to coastal waters with water depths from 20 to 40 m.

As said earlier, the acoustic propagation depends upon many natural variables which are not taken into account here. These environmental factors introduce various loss mechanisms and that is discussed in 2.3.

The normal-mode method, developed by Pekeris (1948), is a useful tool to model this propagation of discrete frequency-dependent modes. The method is valid only for ranges much greater than the water depth (R >> D). As in airborne acoustics within a duct, the normal modes are complicated functions, each representing a wave travelling outward from the source. Their amplitudes are a function of the source, receiver and water depths. Each function can be defined by both a distinct shape function $\psi_m(z)$ and a distinct horizontal wavenumber $k_{rm}$.

The model of waveguide which is considered in this section is idealized, assuming a constant water depth, a homogeneous and uniform water medium, a pressure-release boundary condition at the sea surface and a perfect rigid bottom. Fig. 16 illustrates the problem - called the isovelocity problem in the literature. The water depth is D, the sound speed and the wavenumber in the water column are c and k.

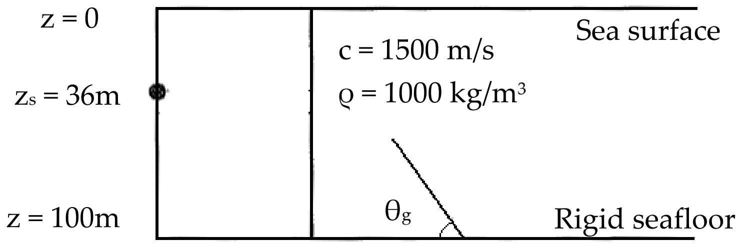

**Figure 16:** *Isovelocity problem model. The grazing angle for the acoustic waves is indicated by $\theta_g$. The water depth D is 100m and the source depth is 36m.*

Thus, the only loss mechanism introduced here is that, at a given frequency, a mode requires at least one-quarter wavelength within the water depth ($D > \lambda/4$) to propagate without attenuation. That can be explained in considering the seabed grazing angle of an incident wave, noted $\theta_g$ and taken relative to the horizontal as shown in Fig. 16.

For a given mode, the higher the frequency, the smaller the grazing angle. And, at a given frequency, the higher the order of the mode, the larger the grazing angle. This is true for any waveguide and that is related to the frequency dependence of the so-called group velocity for each mode. This is explained in detail at the end of the section.

The combinations of wavelength and grazing angle that match the boundary conditions determine the most efficient modes of propagations. Fig. 17 gives the shapes of the first and the second modes of the isovelocity problem, at two different frequencies.

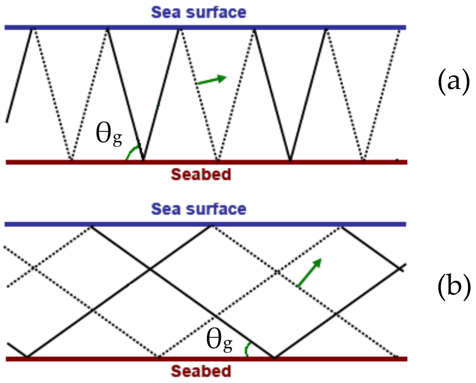

**Figure 17:** *First (a) and second (b) modes of the isovelocity problem. Solid line represents a wave crest (pressure maximum) and dotted line is a trough (pressure minimum). Green arrows show direction of propagation of wavefronts.*

It shows that the surface and the bottom boundary conditions are being simultaneously met, i.e. a zero pressure at the surface and a maximum pressure at the bottom.

Each mode has a well-defined low-frequency cutoff. Below this particular frequency, the mode propagates only with attenuation and is not effectively trapped in the waveguide [3]. This is due to a sudden high value of the propagating speed below cutoff (see Fig. 19) which increases significantly the mode wavelength.

Hence, the higher the frequency, the more modes are present. The presence of many modes creates complicated interference patterns in the sound field which decrease dramatically the transmission loss.

Fig. 18 gives the transmission loss (dB) versus range and frequency for a so-called Pekeris waveguide, i.e. the isovelocity problem with a fluid seabed. The influence of having a fluid seabed is discussed in section 2.3.4. However, the figure below illustrates well the evolution of the sound field, related to the notion of interference pattern.

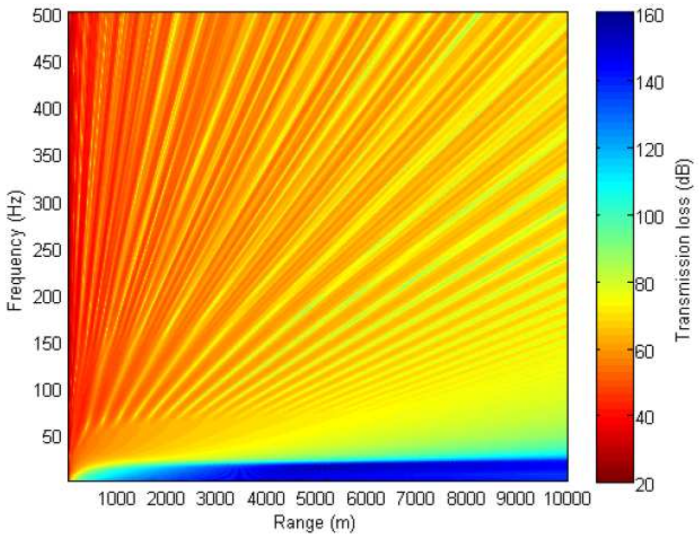

**Figure 18:** *Modelled transmission loss vs. range and frequency (SCOOTER program) for a 40-meter deep Pekeris waveguide. The source depth is 5 m and the receiver depth 15 m (Duncan, 2009).*

Thus, as the frequency is reduced, the interference pattern becomes less and less complicated as the higher order modes progressively cut off. Finally, below the so-called waveguide cutoff frequency ($f_0$ = c/4D for the isovelocity problem and around 20Hz in Fig. 18), all modes are cut off and the transmission loss increases markedly [4].

To conclude, horizontal waterborne sound propagation is dominated by lossless modal propagations - with more energy in high frequencies. This is an intrinsic feature of any ocean waveguide.

Analytically, the shape functions $\psi_m(z)$ of each mode are the eigenfunctions, solutions of the Helmholtz equation. As in airborne acoustics, the Helmholtz equation is the time-independent form of the wave equation which uses the technique of separation of variables.

Jensen [5] gives the modal form of the Helmoltz equation (5) and the boundary conditions for $\psi_m(z)$ at the sea surface and the bottom (6).

$$\rho(z)\frac{d}{dz}\left[\frac{1}{\rho(z)}\frac{d\psi_m(z)}{dz}\right]+\left[\frac{\omega^2}{c^2(z)}-k_{rm}^2\right]_m\psi(z)=0 \tag{5}$$

$$\begin{cases}\psi(0)=0\\ \dfrac{d\psi}{dz}(z=D)=0\end{cases} \tag{6}$$

Where z is the position in the water column, $\rho$ the water density, $\psi_m$ the mode shape, $\omega$ the angular frequency, c the water sound speed, $k_{rm}$ the horizontal wavenumber and D the waveguide depth.

The general solution and the final solution of equation (5) are respectively given by (7) and (8):

$$\psi_m(z) = A \cdot \sin(k_z z) + B \cdot \cos(k_z z) \tag{7}$$

$$\psi_m(z) = \sqrt{\frac{2\rho}{D}} \sin(k_{zm} z) \tag{8}$$

The vertical wavenumber $k_{zm}$ is defined as:

$$k_{zm} = \sqrt{k^2 - k_{rm}^2} = \left(m - \frac{1}{2}\right)\frac{\pi}{D} \tag{9}$$

The dispersion relation which relates the horizontal wavenumber $k_{rm}$ and the frequency is defined as:

$$k_{rm} = \sqrt{\left(\frac{\omega}{c}\right)^2 - \left[\left(m - \frac{1}{2}\right)\frac{\pi}{D}\right]^2} \tag{10}$$

The dispersion relation indicates that $k_{rm}$ is frequency-dependent. Each mode has then a different phase velocity and the phase velocity for a given mode varies with frequency. The latter effect is called geometrical dispersion [5]. The phase velocity $v_m$ is the speed at which a constant phase front propagates horizontally through the waveguide and is defined as:

$$v_m = \frac{\omega}{k_{rm}} \tag{11}$$

The more important quantity for describing pulse propagation in a waveguide is the group velocity $u_m$ [5]:

$$u_m = \frac{d\omega}{dk_{rm}} \tag{12}$$

The group velocity is the horizontal velocity at which energy travels in the waveguide. This concept can be best illustrated through an example, i.e. the Pekeris waveguide already cited before. Fig. 19 gives the computed dispersion curves for the first 4 modes.

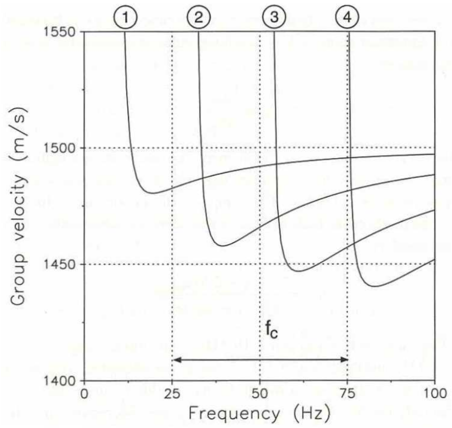

**Figure 19:** *Dispersion curves for the 4 modes of the Pekeris waveguide (Jensen, 1993).*

First, it can be stated that each curve shows a defined cutoff frequency for the considered mode, e.g. the first mode exists only above 10.8 Hz. The part of the group velocity curve that is most important extends to the right of the local minimum where $u_m$ asymptotically approaches the sound speed in the water column (c = 1500 m/s). Thus, the propagating modes are slower than the sound in water with a minimum propagating speed at low frequencies - the so-called Airy phase. At high frequencies, they propagate faster and at smaller grazing angles. The grazing angle $\theta_g$ can thus be expressed as:

$$\theta_g = \arcsin(\frac{k_{rm}}{k_1}) \qquad (13)$$

Where $k_{rm}$ is increasing with decreasing frequency according to Fig. 19 and relation (12). The expression (13) for $\theta_g$ demonstrates clearly that low-frequency energy correspond to high-angle energy.

At cutoff, the group velocity reaches rapidly the bottom sound speed (1600 m/s in Fig. 19) and the mode is attenuated rapidly.

Geometrical dispersion has a strong physical meaning. Thus, a received sound pulse at a great distance is elongated and consists in various waterborne waves arriving at different times. The first arrivals are the high-frequency parts of the modes and the later arrivals are the low-frequency parts (Airy phase) of the higher modes.

As an example, the propagation of a pulse centered at 50Hz with a 50-Hz bandwidth is considered. According to Fig. 19, only the first three modes will be excited. However, the mode 3 will only be weakly excited as the peak energy (50 Hz) is below cutoff. At a great distance, the first arrival will be the high-frequency part of mode 1 (1495.5 m/s) and the trailing edge will be the Airy phase of mode 3 (1446.5 m/s). Fig. 20 shows a computed version of the received pulse at a distance of 30 km from the source.

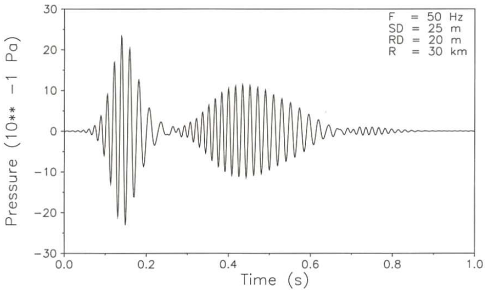

**Figure 20:** *Modelled received pulse at 30 km from the source within the Pekeris waveguide. The source depth is 25 m and the received depth is 20 m. The total signal dispersion is 0.7 s (Jensen, 1993).*

## 2.3 Real ocean waveguide environment

The previous model of ocean waveguide is an over-simplified model of the real ocean. Sound propagation depends on many natural variables of the sea bottom, water medium and sea surface. Thus, various loss mechanisms can be introduced by absorption, scattering, refraction or transmission. It is crucial here to describe the environmental factors which are significant in sound propagation and which can vary dramatically in space or time.

Moreover, the ambient noise in the sea is inevitably an important parameter when studying the noise impact of man-made noise on marine mammals. The first section deals with this issue.

### 2.3.1 Shallow water ambient noise

In a context of animal effect studies, the ambient noise in the sea is an important parameter which requires to be watched closely. Thus, the assessment of a certain received level of man-made noise and its possible effect is accurately defined if the background noise is taken into account. This point is discussed further in section 3.1.2. Fig. 21 illustrates the theoretical interrelationships of the source level of a man-made noise, range from the source, ambient noise level and response threshold in determining detection and response distances of a marine mammal [1].

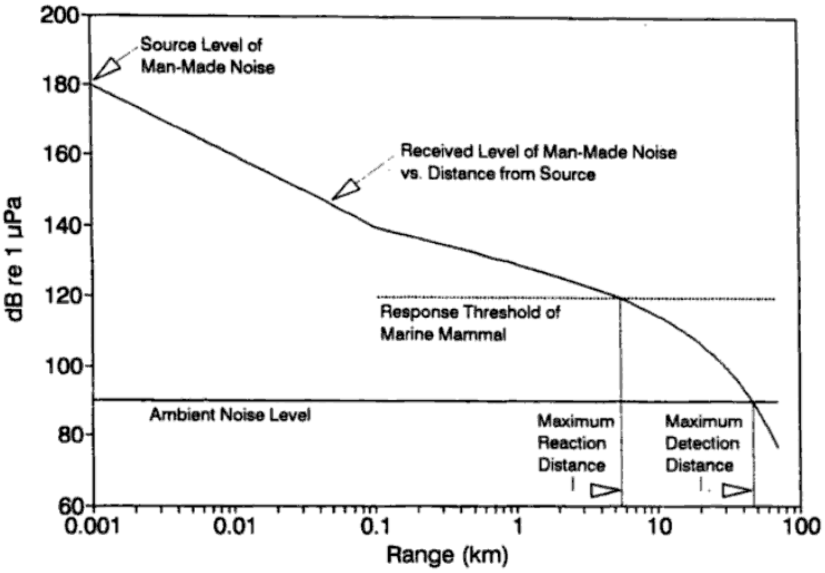

**Figure 21:** *Received level vs. range from a source level of man-made noise (Richardson, 1995).*

In reality, the background noise level – subjects to significant variations in space and time – is only likely to change the maximum detection distance of the marine mammal for great ranges. In the absence of a second source of man-made noise, the response threshold is often much greater than the ambient level.

In shallow water, there are three primary sources of ambient noise, i.e. distant shipping, industrial, or seismic-survey noise; wind and wave noise; and biological noise. Typical levels are hard to predict given that there is a wide range of ambient noise levels for different shallow water acoustic environment. It is closely linked to the sensitivity of the natural variables – discussed in the subsequent sections – likely to affect sound propagation. Ambient noise in shallow water is better predicted by wind speed than wave height in many conditions. The seabed type – reflective or absorptive – is also a substantial factor and levels are likely to be significantly higher over a reflective seabed.

Above 500 Hz, levels are often 5-10 dB higher in coastal than in deep water with corresponding wind speeds (Urick, 1983). Below 300 Hz, levels tend to be lower in shallow water in the absence of man-made noise. The latter statement adds concerns regarding received energy of lateral sounds from seismic surveys in shallow water.

Last but not least, abnormal background noise represents a limitation for underwater sound measurements. Setting a high gain within the recording system is a solution to avoid outputs with low signal-to-noise ratios. As seen later in the JIP data post-processing, biological noise - i.e. humpback whale vocalisations - can significantly lower the quality of recorded air-gun signals with range.

### 2.3.2 Variations at the sea surface

The sea surface in many conditions can be approximated as a quasi-perfect reflector. Thus, the strong impedance contrast at the interface water-air ($Z_{air}/Z_{water} \approx 3.10^{-4}$) involves a reflection coefficient R which tends to -1, whatever the incident angle. The reflected waves are then out-of-phase, as seen in Fig. 9.

The simplification made in section 2.2 - assuming a pressure-release boundary condition at the sea surface - is therefore reasonable.

However a rough sea state creates scattering effects. Scattering is a mechanism for loss, interference and fluctuation [5]. In the case of a rough sea, it causes attenuation of the mean acoustic field propagating in the ocean waveguide. Recall that the scattered energy propagates in all directions. The attenuation from scattering effect increases with increasing frequency, as many loss mechanisms. Note that because the ocean surface moves, it will also generate acoustic fluctuations [5].

These environmental factors are often not dominant in shallow water acoustic propagation, especially in the presence of a smooth ocean - which is directly related to wind speeds.

### 2.3.3 Water column variables

The water medium can affect shallow water sound propagation due to two main effects, i.e. seawater absorption and refraction from sound speed gradients. Both mechanisms increase with increasing frequency.

Absorption by seawater is not a dominant aspect of sound transmission in the ocean. However, an accurate analytical model should include this parameter. As the attenuation increases linearly with frequency, the wave attenuations $\alpha$ are generally given in units of dB per wavelength. The absorption inside the sea bottom is much higher than in water. For example, at 100 Hz the attenuation in seawater is around 0.004 dB/km, whereas the compressional wave attenuation in bottom materials varies from between 2 dB/km in basalt to around 63 dB/km for silt [5].

The variation of sound speed within the water column is likely to noticeably modify the acoustic paths by refraction. Thus, refraction causes rays to be bent toward the direction of slower sound speed, since the portion of the wavefront travelling in the region of higher sound speed advances faster than the remaining portion [1]. This feature is often not dominant in shallow water. Nevertheless, a large sound speed structure may lead to significant refractions at high frequencies, which result in convergence and shadow zones. A given received level may be therefore enhanced or lowered by refraction.

This mechanism is intrinsically related to three natural variables - upon which the water sound speed depends - i.e. the salinity, the water temperature and the water depth. The sound speed increases with increasing salinity, temperature and pressure. In a limited region of coastal waters, water temperature is likely to be the dominant factor for sound speed variations within the water column. Investigations regarding the effect of a small sound speed structure on horizontal sound propagation with range in a waveguide are presented in the last chapter of this paper. Note that, for low frequencies where the air-gun energy mostly is, there is likely to be no significant effect on sound transmission for small variations around 1 m/s.

When recording underwater sound for a given period, it is important to measure in parallel the water temperature within the water column in order to detect any sudden variation.

### 2.3.4 Contribution of the sea bottom

This section deals with the consequences for the waterborne acoustic waves to interact with a real model of sea bottom. This is a structure which can vary either in composition, slope or roughness. These factors are likely to be highly variable in space.

#### 2.3.4.1 Acoustic conversion within the bottom

Depending on the grazing angle and the geoacoustic properties of the seabed, a certain part of the incident acoustic energy is transmitted into the bottom. This mechanism is called bottom loss and has a dominant effect on shallow water sound propagation - especially at low frequencies. A general mechanism is that, in any type of seabed, high-angle energy is rapidly attenuated due to bottom penetration.

Recall that, depending on the material rigidity, the transmission can result in an acoustic conversion either in compressional or shear waves. The particle motions of these body waves are well-known and are recalled in Fig. 22. Note that the compressional waves are noted P-waves and the shear waves S-waves in this paper.

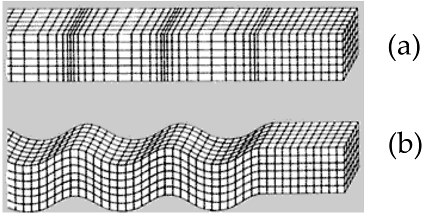

**Figure 22:** *P-wave particle motion (a) made of compressions and expansions and S-wave particle motion (b).*

Basically, a slow-speed formation as sediments - with a rigidity which is considerably less than of a solid - supports only one type of body wave, i.e. a compressional wave. Such materials can be modelled as fluid and their compressional wave speeds $c_P$ are usually slightly higher than the water sound speed.

The influence on sound propagation of the other bottoms types with higher rigidity and propagation speeds - where both body wave types can propagate - depends noticeably on their geoacoustic parameters - especially their shear wave speeds $c_S$.

The ocean bottom - as seen briefly in section 2.1.2 - is made of several geological layers. Each of those layers has its own geoacoustic parameters which are mainly the compressional wave speed $c_p$, the shear wave speed $c_s$, the compressional wave attenuation $\alpha_p$, the shear wave attenuation $\alpha_s$ and the density $\varrho$. In addition to those, the reflection coefficient versus the grazing angle is a key feature for a given seabed. Recall that, typically, the deeper the layer, the greater the compressional wave speed.

In this section, a stress is made on two types of formations, usually found in the upper layers - i.e. sand and soft rock. Upper layers are more likely to contribute to the in-water sound field than deep layers. An effective acoustic penetration depth can be defined to assess this contribution.

An example of soft rock is a low density limestone which has a shear speeds slightly smaller than the water sound speed. Many underwater rock outcrops are made of such a soft rock. Hard materials such as volcanic rocks - with high shear speeds up to 2500 m/s - are usually found in the deep ocean basement are likely to play a role only for low-frequency acoustic energy.

Note that the geological layers of the sea bottom in a real environment are often not homogenous and do not have a constant depth with range.

In order to describe the impact of bottom loss with frequency, recall that, as frequency is increased, the seabed grazing angle for a given mode reduces. Thus, the mode can be thought of as traversing the reflection coefficient vs. grazing angle curve from 90° to 0° [6]. Fig. 23(a) gives the geoacoustic parameters of calcarenite - a type of limestone - and sand seabeds. Their reflection coefficient curves vs. grazing angle are given in Fig. 23(b). Calcarenite is a highly variable material but the geoacoustic properties chosen appear to be typical, with a shear speed of 1400 m/s. The shear speed in sand is considered very low - around 300 m/s - and can be then roughly modelled as a fluid (i.e. no shear wave propagation).

(a)

| Material | Calcarenite | Sand |
|---|---|---|
| Density (kg.m$^{-3}$) | 2400 | 1800 |
| Compressional wave speed (m.s$^{-1}$) | 2800 | 1700 |
| Compressional wave attenuation (dB/wavelength) | 0.1 | 0.8 |
| Shear wave speed (m.s$^{-1}$) | 1400 | - |
| Shear wave attenuation (dB/wavelength) | 0.2 | - |

(b)

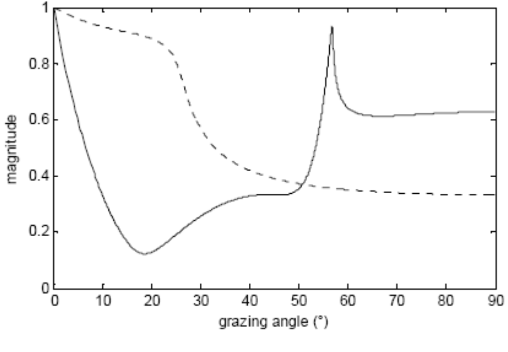

**Figure 23:** *Geoacoustic parameters for calcarenite and sand (a). Magnitude of the plane-wave pressure reflection coefficient vs. grazing angle (b) for a sand (dotted curve) and a calcarenite seabed (solid curve) (Duncan, 2009).*

Each reflection coefficient curve can be divided into three domains of sound propagation and, consequently, three frequency domains. The compressional wave critical angle $\theta_c$ for which total internal reflections occurs - equals to 28° for sand and

58° for calcarenite in Fig. 23(b) - represents a natural demarcation. For grazing angles above critical, there is acoustic conversion in compressional waves into the bottom. For both seabeds considered, the shear speed is smaller than the water sound speed which means that there is not shear wave critical angle. The shear waves are therefore leaking into the bottom, whatever the grazing angle.

Each domain depends on the value taken by the horizontal wavenumber $k_{rm}$ of each mode. Consider the wavenumber for horizontally propagating plane waves in the water $k_1$ and the in the bottom $k_2$. For increasing frequency, $k_{rm}$ for a given mode approaches naturally the wavenumber $k_1$, i.e. the group velocity of the mode tends to the water sound speed - as seen in Fig. 19.

The three spectral domains are:

- $0 < k_{rm} < k_2$: the continuous spectrum where waves are radiating into the bottom, thus leaking energy away from the waveguide. Consequently no lossless modes can exist in this spectral domain. On the other hand this part of the spectrum reflects the presence of leaky modes which are decaying in amplitude with range [5]. That corresponds to low frequencies and large grazing angles above the critical angle for P-waves.
- $k_2 < k_{rm} < k_1$: the discrete spectrum where the field is propagating vertically in the water and is exponentially decaying in the bottom. This part of the spectrum contains the discrete poles corresponding to lossless modes. This corresponds to higher frequencies and small grazing angles below critical.
- $k_{rm} > k_1$: the evanescent spectrum where wave components in both water and bottom are exponentially decaying in the vertical. This corresponds to high frequencies and very small grazing angles.

The reflection coefficient curve for sand seabed in Fig. 23(b) shows a classic contribution to the sound field for a fluid ocean bottom, i.e. strong bottom loss in low frequencies - for grazing angles above critical for P-waves. It results in higher transmission loss in the low frequencies compared to a rigid-bottom waveguide. That adds a second loss mechanism in this frequency region, in addition of having a few propagating modes. Thus, in Fig. 18 - presenting the transmission loss vs. range and frequency for a sand seabed in a 40-m waveguide - the high transmission loss region below 100 Hz is partly due to bottom loss. Weak shear leakage occurs for small grazing angles - i.e. R is slightly less than 1 - but this acoustic conversion in shear waves in fluid bottoms has not a significant impact on in-water sound field.

Regarding the calcarenite seabed, of particular note is the very rapid reduction in reflection coefficient in Fig. 23(b) with increasing angle that occurs for small grazing angles [6]. This is related to the strong coupling between the water sound speed and the shear speed in calcarenite. Thus, at low frequencies all the modes have substantial grazing angles and - because of the sharp dip down to 10° in Fig. 23(b) - are strongly attenuated. Fig. 24 gives the modelled transmission loss vs. range and frequency for an infinite calcarenite seabed in the same conditions as Fig. 18. It shows a wedge shaped high transmission loss region corresponding to the sharp dip in the reflection coefficient - from 30 to 150 Hz. Then, at a certain higher frequency, the grazing angle of the lowest order mode is reduced to the point where its reflection coefficient is high enough to allow it to make a noticeable contribution to the received field [6]. As the frequency is increased further, the mode 1 reflection coefficient continues to increase, as do the reflection coefficients of the higher order modes, giving rise to the modal interference pattern in the high frequency region.

Another particular feature of the plot in Fig. 24 is the thin horizontal bands of low transmission loss in the low frequencies. They represent effective in-water sound propagations which occur at specific frequencies at which one of the normal modes has a grazing angle corresponding to the seabed P-wave critical angle. These low attenuation lines - which are not discernible for sand in Fig. 18 - are due to the sharp peak in the reflection coefficient curve of a calcarenite seabed in Fig. 23(b) for the P-wave critical angle.

Finally, the reduction of transmission loss at very low frequencies in Fig. 24 is discussed below and is related to the propagation of the so-called Scholte wave.

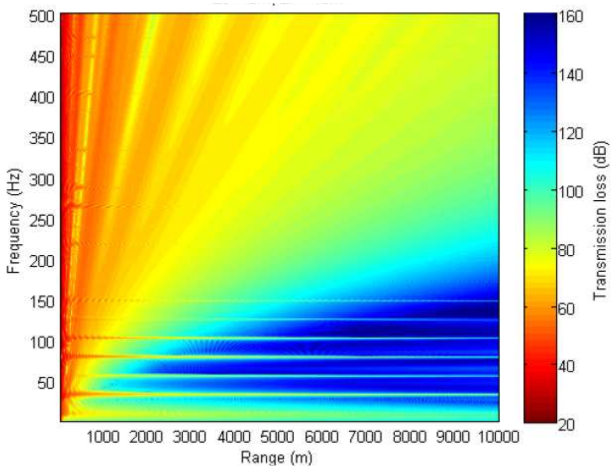

**Figure 24:** *Modelled transmission loss vs. range and frequency for a 40-meter waveguide with a calcarenite seabed. The source depth is 5 m and the receiver depth 15 m (from [4]).*

This comparison demonstrates that an outcrop made of a soft rock is much more absorptive than a sand seabed, especially at low frequencies. That results in a sharp drop off in the received levels at a given position over a soft rock outcrop. Thus, the excitation of shear waves in the bottom often becomes the dominant loss mechanism for waterborne sound in low-frequency shallow-water acoustics [5].

When a rock layer is overlain by a sand layer, it is said to be partly acoustically isolated. The sand thickness in acoustic wavelengths determines its effect on the propagation [4]. Thus, the effective acoustic penetration depth mentioned before is frequency-dependent and, at high frequencies, details of the bottom composition are required only in the upper few meters of the seafloor. As an example, acoustic energy around 10 Hz can propagate into the bottom at depths up to 150-180 m and therefore will interact with the deep ocean basement.

It should also be emphasized that - as within the water column - the body wave sound speeds in the bottom have a gradient with depth. Typical sediments have positive gradients of around 1 m/s.

Note that the contribution to the sound field for a hard rock seabed ($c_s > 1500$ m/s) is less significant than for soft rocks as no shear leakage occurs for low grazing angles - increasing therefore the seabed reflectivity.

In addition of reflecting or converting the in-water acoustic energy, the ocean bottom medium allows the propagation of specific waves at the different geological interfaces. Generally, low acoustic frequencies can propagate with reasonable levels in any type of seabed, but the attenuation is naturally higher in slow-speed formations as sand. They are three kinds of interface waves relevant to the context of this paper, i.e. the compressional headwave, the shear headwave and the Scholte wave.

The compressional headwave - simply called headwave - occurs at grazing angles fractionally less than the P-wave critical angle of the lower medium. It results from refraction and propagates along the interface at the P-wave speed of the lower medium and is re-radiated back into the water at a further range. Its contribution to the in-water sound field is weak and in very low frequencies. It may have some biological implications - which this paper is not focused on. However, it is useful to study the geoacoustic parameters of the layers - which is done using refraction seismic. They are therefore discussed in detail in section 3.3.3. Note that at the frequencies corresponding to the thin bands in Fig. 24, there is reinforcement between the in-water modes and the headwaves, and strong headwaves arrivals are observed [6]. There is not such a reinforcement in a fluid medium as sand but headwaves do propagate in sand but are strongly attenuated with range.

In the same way, shear headwaves occur at the S-wave critical angle of a layer. They are therefore relevant only for deep high-speed materials with a shear speed much higher than the water sound speed. They are usually not well-discerned and not of a substantial interest.

Scholte wave is a so-called seismic wave which propagates along the interface between two media with different shear speeds. The lower medium requires being elastic, i.e. having a substantial shear speed. Scholte waves occur in the evanescent spectrum ($k_{rm} > k_1$) for very small grazing angles and their amplitudes are exponentially decaying away from the guiding interface. Their propagation speeds - usually slightly slower than the S-wave speed of the lower media - and attenuations are closely related to the shear properties of the formations. Besides, there is no low-frequency cutoff for Scholte waves. Reasonably strong arrivals can be then recorded if the receiver is close to the considered interface. In the modelled plot of transmission loss for calcarenite seabed in Fig. 24, the S-wave attenuation $\alpha_s$ was chosen low enough to show consistent Scholte wave arrivals at all ranges, from 0 to 20 Hz. They usually attenuate much faster in a real elastic medium.

#### 2.3.4.2 Scattering loss from a rough seabed

As from a rough sea surface, acoustic scattering occurs for a rough seabed. Recall that scattering loss increases with frequency.

The roughness of a seabed depends mainly on its type. Sand seabeds are likely to be plane surfaces whereas several types of rocky seabeds present a high roughness. The surface roughness is defined as the ratio between the characteristic amplitude of the relief and the wavelength of the acoustic signal [7]. When interacting with a rough surface, part of the incident wave is reflected with no deformation other than an amplitude loss in the specular direction (coherent part of the signal). The remainder of the energy is scattered in the entire space, included back towards the source (backscattered signal). Lurton (2002) explains that low interface roughness induces naturally a much lower scattering distributed around the specular direction. That is illustrated in Fig. 25 below. The figures do not include transmission into the bottom.

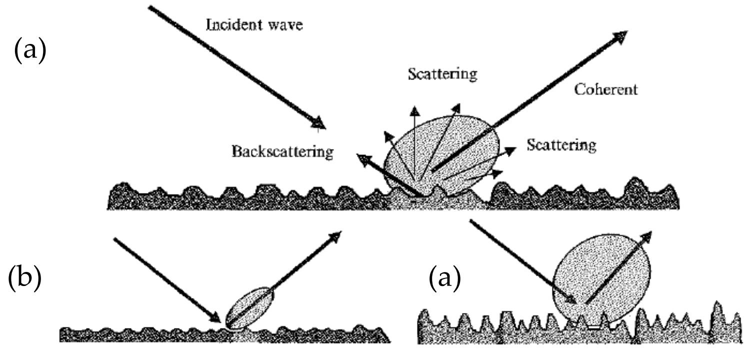

**Figure 25:** *Coherent reflection and scattering of incident wave (a). Comparison of the scattered field between low interface roughness (b) and high interface roughness (c) (Lurton, 2002).*

The impact of scattering loss from a rough seabed on the sound field is often noticeable but is, for instance, usually less than bottom loss in an ocean waveguide.

#### 2.3.4.3 Bottom slope effects

The slope of the bottom may have a significant influence on sound transmission in shallow water [1]. They are two distinct interesting changes in terms of acoustic radiation along with a change in bottom slope, i.e. a change in volume of available water and a change in the grazing angles of sound rays with the bottom and surface.

Thus, a downward slope permits sound energy to spread out in a larger volume and this tends to result in a reduced sound level. However, the grazing angles become smaller and there are less bottom and surface reflections per kilometre, i.e. less energy loss. The latter has a stronger influence in many bottom conditions and, thus, a downward slope tends to increase the received levels compared to a constant-depth waveguide.

Conversely, an upward slope results in a net increase in sound transmission loss due to greater reflections. In addition, depth can be reduced to the point where modal transmission is not supported ($D < \lambda \backslash 4$) and the remaining sound energy is attenuated very rapidly [1].

## 2.4 Sound transmission of air-gun signals in shallow water

As a conclusion of these theoretical aspects regarding lateral sound propagation within an ocean waveguide of seismic exploration sounds, this section exposes some of the known features on air-gun transmission.

The variations in air-gun array designs and their implication on horizontal sound propagation will not be dwelled upon here. However it is worth emphasizing that with elongated array whose long axis is in line with the tow direction, sound levels directly ahead of and behind the seismic ship may be at least 10 dB less than levels directly downward or to the side [1]. Consequently, received air-gun levels at long range can vary dramatically with horizontal aspect with the strongest lateral radiation abeam the long axis of the array.

As seen with normal mode theory and bottom loss effect, as sound pulses propagate horizontally in shallow water, low frequencies attenuate rapidly, leaving only the higher-frequency energy. The received signals at great distances are elongated due to geometrical dispersion and the main first waterborne arrival is in high-frequencies, followed by a low-frequency trailing edge. That is well illustrated in Fig. 26 presenting the pressure waveforms and the waterfall spectrograms of received pulses at three different ranges - 5, 1.9 and 11.1 km.

Fig. 26(c) points up the downward "chirp", from 200-400 Hz to 100-200Hz in the waterfall spectrogram. The waveform in Fig. 26(c) is smeared in time due to the superposition of several signals, i.e. the propagating modes undergoing a multitude of bottom and sea surface reflections.

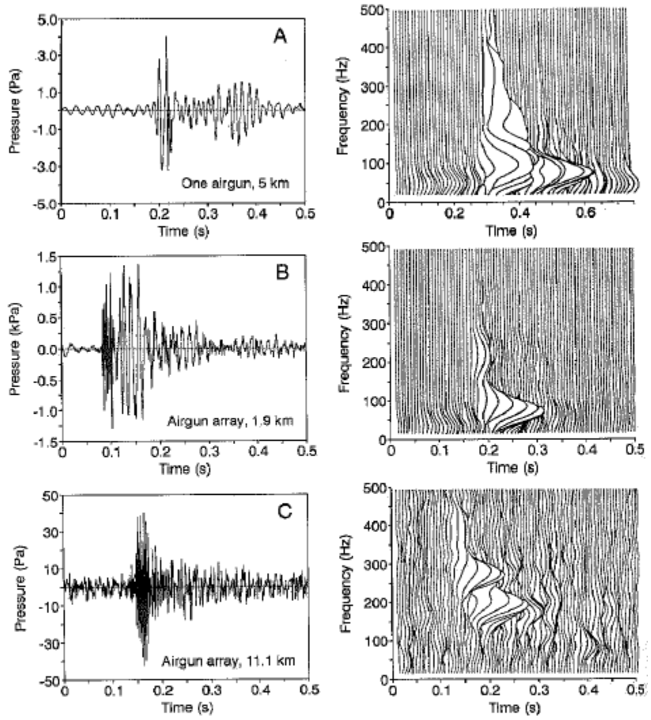

**Figure 26:** *Pressure waveforms and waterfall spectrograms of air-gun pulses at various ranges. Pulse from a single air-gun (0.66 L) at 5 km (a). Pulse from a 28-L array at 1.9 km (b) and 11.1 km (c).*

Strong headwave arrivals are often discerned on distant air-gun shot waveforms. There can be distinct headwave arrivals showing the presence of several geological layers and they are often a first arrival - as the compressional sound speed in the bottom is usually much greater than the water sound speed. As said earlier, the re-radiated sound from such bottom-travelling energy is of an interest here only to define the geoacoustic parameters of the detected layers. Its contribution to the sound field and its biological implication are not studied.

Fig. 27 gives examples of received levels vs. range curves for different types of seismic surveys and their best-fit regression curves. The range considered in this graph are up to 80 km. Note that detection ranges can exceed 100 km during quiet times with efficient propagation or in deep water but a single air-gun in shallow water is likely to be detected only up to 10 km. The acoustic environment and the deployment depths of the surveys in Fig. 27 correspond to standard cases.

The decreases in those examples can be described by spherical or cylindrical spreading loss (i.e. 20 or 10 log range) plus a linear function of range for losses due to absorption and scattering. This is not the case at all with more complex conditions as deploying the source at a shallow depth or being in the presence of an absorptive seabed or a change in the seabed type. Indeed, the geometrical spreading are only based on a conservation of energy argument and is often only useful for putting an upper bound on levels.

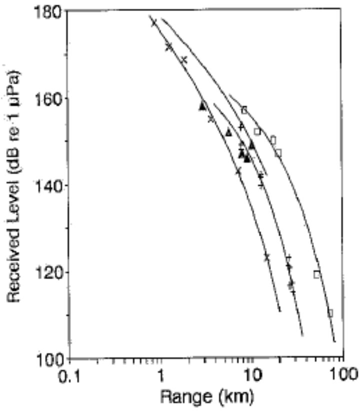

**Figure 27:** *Examples of seismic survey noise vs. range, in continental shelf waters (adapted from Greene and Richardson, 1988).*

The surface reflections – involving a 180° phase change - are a key feature regarding air-gun transmission and this aspect is increased with very shallow air-guns and/or shallow receivers. This phenomenon – called Lloyd mirror effect – is strongest with low-frequency tones and in calm sea conditions [1]. Thus, placing a shallow air-gun at depth below 10 m may lead to an interference zone for small ranges and, beyond this zone, propagation loss is often higher than normal. The boundaries of the interference region are determined by:

$$2(d_1 d_2)^{0.5} < R < \frac{4 d_1 d_2}{\lambda} \tag{14}$$

Thus, if a tone of 40 Hz is considered, the interference region applies for ranges below 16 m for a source depth $d_1$ of 5 m and receiver depth $d_2$ of 30 m.

The shallower the source and the closer to the horizontal the propagation path, the nearer the direct and surface reflected path lengths are to being the same and the more the combined signal is reduced. A sharp drop off in the received levels vs. range curves is often observed at sufficiently long ranges, either in empirical or numerical results. In deep water, this drop off can be as strong as 40log(R). However, the geophysicists require placing the seismic source at a substantial depth (above 5 m) to avoid the strong elimination of acoustic energy and allow a reasonable penetration into the earth.

According to the same effect, received levels of air-gun pulses are lower just below the surface than at deeper depths [1]. As an example, received levels at ranges 9-17 km were 1-4 dB less at 9 m than at 18 m (Greene, 1985).

Seismic pulses travelling upslope are attenuated much faster due to strong bottom loss and, conversely, greater levels are expected in the presence of a downward slope - as explained previously. However, slight slopes might not have substantial effect on air-gun sound transmission.

In some conditions, the received levels from an air-gun array may attenuate more rapidly than a single air-gun. This difference may be due to surface reflections that depend on array aspects. However, the much stronger source signature of an array results naturally in higher received levels than for a single air-gun.

In summary, air-gun arrays or single air-guns produce noise pulses with very high peak levels. However, the short duration of each shot limits the total energy. With increased distance from the source, received pulses generally decrease in level but increase in duration. Beyond a few kilometres, higher frequencies tend to arrive first in an ocean waveguide. Sound transmission and received levels may vary upon many variables as the sea bottom structure and slope, array designs, source and receiver depths. Other factors – mentioned in section 2.3 – might affect more lightly air-gun transmission as sound speed variations within the water column.

# 3 Empirical approach - JIP 2010 trials

## 3.1 Method of the experiments

### 3.1.1 Map of the area and equipment deployed

As mentioned in the introduction, the JIP 2010 trials aimed at simulating a series of seismic surveys, using a single air-gun. The covered experimental area was in coastal waters, from around 25 to 40 m deep.

More precisely, the zone is a known migratory route for humpback whales when they head south to Antarctica every year in September/October. They were therefore humpback whale pods and single whales in the surroundings during the surveys. Appendix 1 provides a map of Australia showing the migration legs of Humpback whales along western and eastern Australian coasts and the location of the experiments. The presence of the animals was crucial for the project in order to analyse their behaviours through meticulous observations from the seismic vessel and an inland point. However, any recorded whale vocalizations with the deployed receivers were not of interest in this paper and represents a source of substantial background noise in terms of data post-processing. The analysis of whale observations - added up with the outcomes from this thesis - will be carried out by the bioacousticians at the CMST. Note that the extended experimental area has been already used in the past for similar studies.

The actual measurements were made during 1 month, from 26th September till 24th October 2010. There were two main types of operations, i.e. deploying the acoustic receivers at fixed locations for short periods and conducting 1-hour seismic surveys with the single air-gun.

The surveys were conducted each day on task and were following two recurring tracks. The first track goes along the coast, follows roughly the 30-m bathymetry line and heads north (slightly east). The second track starts nearby the starting point of the first track, goes away from the shore - i.e. heads east - and covers waters roughly from 25 to 40-m deep. Both tracks are approximately 7-km long.

Typically - each day on task - the air-gun was operated for one hour either upon the north or east track. Each survey is called air-gun run (AG) in this paper. Controls runs (CT) were conducted as well on the same days for statistical purposes, with the air-gun deployed but not operated. They are not of a use in the present study.

The acoustic receivers used are called noise loggers. The CMST used four of them during the 1-month experiments. They were typically deployed on the seabed at a fixed position for a few days in order to record and cover a few air-gun surveys. They can be thought of as experimental humpback whale positions.

Thus, in this paper, a pair of one receiver (i.e. a set of noise logger) and one survey (air-gun run) is always considered when presenting the results.

As an example of day on task, Fig. 28 gives the vessel track on the 16th October (in pink).

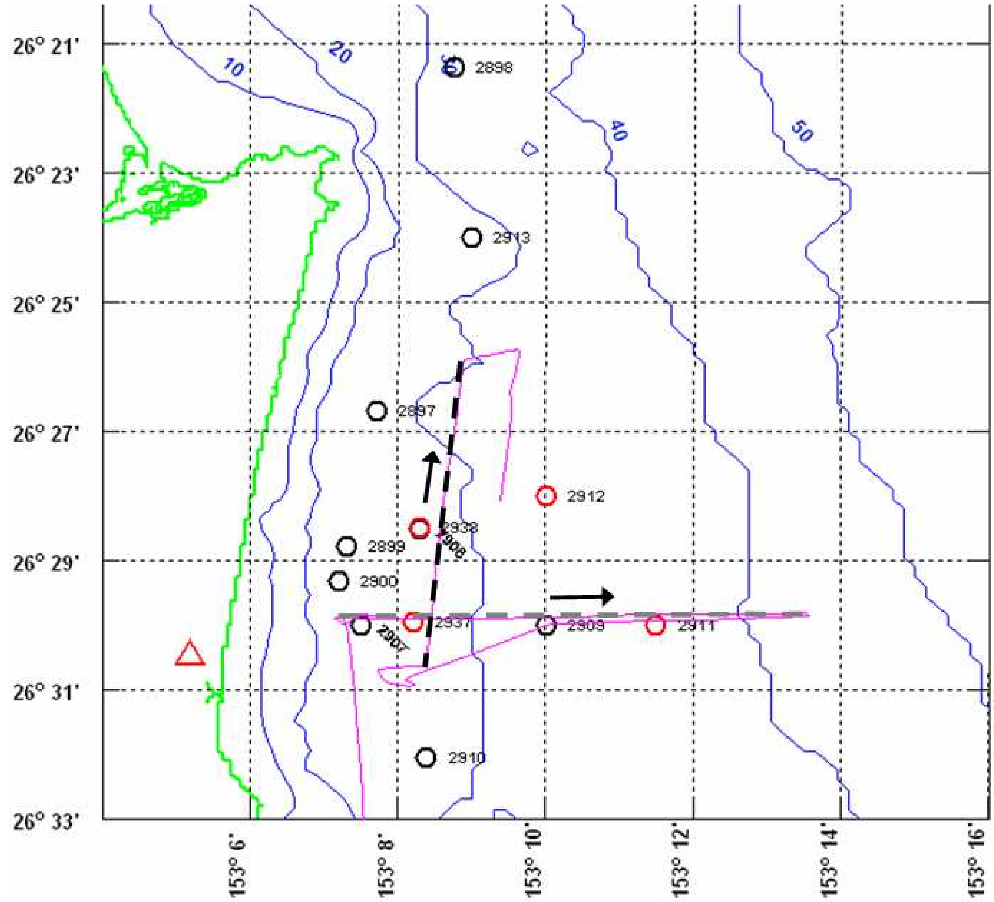

**Figure 28:** *Vessel track on the 16th October (pink lines). The green contour denotes the coast line. The black dotted line represents a 1-hour air-gun survey following the north track (AG11). The grey dotted line is a control run upon the east track. Noise logger sets in red circles were present on this day. Noise loggers deployed at other times are in black circles. The red triangle locates the inland whale observation point.*

An air-gun run (AG11) was conducted upon the north track this day - see the black dotted line - and a control run (CT08) upon the east track - see the grey dotted line. These two lines are representative of the two recurring tracks. The red circles indicate the positions of the four deployed noise loggers on this day (sets 2911, 2912, 2937 and 2938). The black circles show the positions of the noise loggers at other times during the 1-month trials. Each noise logger position is called set and is recognized with a specific number 29XX. They were 13 sets in total. Notice that sets 2908 and 2938 were located very close to each other and that sets 2913 and 2898 were deployed quite far up north. Of a particular note is the inaccuracy of the blue bathymetry lines in Fig. 28 which come from a national atlas. They just give an idea of the global topography in the area.

Such recurring tracks (north and east) were used for the surveys in order to compare properly the received air-gun noise levels at the different receiver positions. The received levels may vary significantly - as seen in the theoretical aspects - in space, especially with sea bottom variations in structure and slope.

Naturally, the air-gun runs following the same pattern differed slightly as Appendix 2 shows it. However, all surveys of the same pattern are quite similar to each other and their received air-gun level data can be compared.

For exact information, Appendix 3 gives the tables of the vessel activities each day on task. For each day, it gives the run type (either air-gun run AG or control run CT), the approximate run heading (east E or north N) and the time and location of run start and end points. There were 17 air-gun runs in total (AG01 to AG17). Note that some air-gun runs were not useful to process, i.e. AG01, AG03, AG10 and AG17. AG01 had wrong parameters (i.e. air-gun depth and vessel track) and the others had too small number of emitted shots. Therefore, only the 13 remained surveys were studied in this paper - as highlighted in Appendix 3.

Sea noise loggers are sound recording devices which are used to deploy underwater acoustic observatories. The main element of a noise logger is a hydrophone. The latter is plugged into a sound recorder and a preamplifier. The instrumentation is provided with a large battery pack. Hydrophone data is stored temporarily on a memory flash card which transfers data regularly to a hard disk. Fig. 29 below shows two of the used noise loggers.

**Figure 29:** *Two noise loggers from the JIP experiments. The body contains mainly a battery pack and electronics. The external wire is connected to the hydrophone.*

For the JIP 2010 trials, in most cases, the noise loggers were sampling 12 minutes of every 15 minutes at 8 kHz sample rate. The 3-minute breaks were meant to store data. A gain of 17 dB was set on each set of noise logger. For some sets, multiple gains were used (-3 and 17 dB) to avoid saturation of short range air-gun signals.

Four noise loggers designed by the CMST and placed on the seabed were then provided. Three different hydrophone models were used, either a HiTec HTIU90, a Massa TR1026C or a Reson TC4034. Only the systems with HiTec hydrophones were set at 4 kHz sample rate.

In addition of the acoustic sensor, each noise logger was equipped with a temperature logger. Another temperature logger was placed 11 meters above each noise logger. The temperature data was entirely stored for both temperature loggers during the time of the noise logger deployments.

For exact information, the table in Appendix 4 gives the detail of the noise logger deployments during the 1-month trials. Of particular interest is the last column providing the overlapping air-gun runs with each noise logger records. Their different locations can be seen on a high quality map in Appendix 5.

The calibration of each hydrophone was made before its deployment and using a white noise calibrator. The calibration data was simply inputted in the post-processing codes in Matlab, taking into account the gains of the different devices in the noise logger (sound recorder, hydrophone, etc.).

A frequency response curve of CMST-design noise logger is given in Appendix 6, for a Massa TR1026C hydrophone. The frequency responses curves for the other loggers slightly differ but Appendix 6 gives a general idea of their shapes. The frequency band of interest for the JIP data is approximately below 800 Hz down to a few Hz. The frequency response is not flat, especially in low frequencies. A low-frequency roll-off was deliberately applied to the sea noise to "flatten" the naturally high levels of low frequency sea noise and so increase the system dynamic range. The response of each noise logger in low frequencies depends on its capacitance and more particularly on the capacitance of its preamplifier. Thus, the noise logger outputs required to be compensated to provide correct data. This step was not a demanding task during this thesis. It requires calculating the Fast Fourier Transform of the waveforms to obtain amplitude and phase information. The amplitudes were then multiplied at each frequency by the correct amplitude correction from the frequency response of the considered noise logger.

Note that the recovery of the deployed gear required the use of acoustic releases. Such a device permits the release of a buoy when triggered remotely by an acoustic command signal.

The single air-gun used for the trials was a Bolt 600B with a 20 in$^3$ (~ 0.33 L) firing chamber - seen previously in Fig. 6. It was set on a theoretical 10 s repetition rate. The gas was supplied with a 9 cuft/min Bauer electric three stage scuba compressor using 2 high pressure, G sized gas cylinders as reservoirs. The air-gun was towed 18 m astern the source vessel and was kept at a theoretical depth of 5.6 m. The air-gun was bolted into a towfish to make easier the towing. The towfish was connected to two tow lines and floats (see Fig. 30). Note that the first survey (AG01) used only one tow line causing an incorrect air-gun depth.

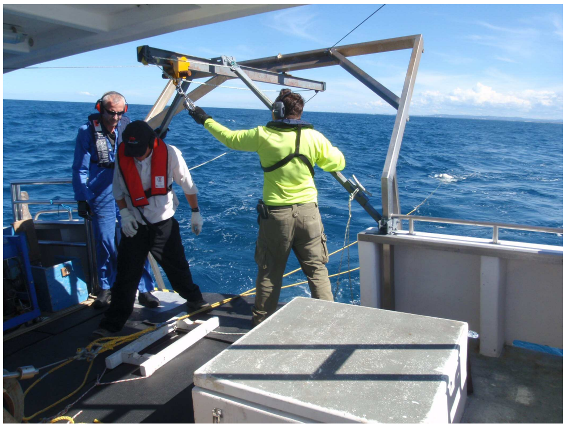

**Figure 30:** *Deployed air-gun and the deployment gantry showing the two tow lines.*

A typical air-gun operational setup is given in Appendix 7. Two cables are plugged into the air-gun, i.e. the air and the solenoid cable. The air cable is naturally connected to the compressor and other elements in order to feed the gun with a constant pressure of 2000 psi. The solenoid cable is linked to a trigger generator previously set at the desired repetition rate. A picture showing the compressor, the gas bottles, the air-gun (not deployed) and deployment gantry can be found in Appendix 8.

For statistical purposes during each survey, three sensors were placed into the towfish, in the near-field of the air-gun, i.e. a near-field hydrophone, a temperature logger and a pressure logger. The near-field hydrophone was placed 0.85 m away from the source. A simple calculation can lead to the level at 1 meter, giving then the so-called air-gun signature in the near-field (waveform and sound pressure density spectrum levels). The pressure sensor measured the air-gun depth - substantial parameter in terms of air-gun lateral sound radiation.

All the temperature or pressure loggers used in the project were Aquatech 520PT (at the air-gun) or Aquatech 520T devices (at the noise loggers).

In addition, a GPS Genius was connected to the air-gun fire control system to log time and location of each triggered shot.

Before describing the data post-processing step - carried out in Matlab - the main descriptors of impulsive signals used in a context of animal effect studies are presented in the next section.

### 3.1.2 Descriptors of impulsive air-gun signals

When studying the noise from a source producing pulses at regular rate, it is best to consider each pulse waveform at a time. The extraction of the air-gun shots from the noise logger JIP data is described next, when presenting the results. An example of a distant shot waveform is given in Fig. 30 (set of noise logger 2908, air-gun run AG08 made on 6th October). The amplitude is given in Pa, after converting it from mV using the recorded calibration values. For this example, the waveform was arbitrary chosen as 1.6-s long. The pulse length is a key issue for describing distant air-gun energy. Indeed, the time boundaries of such a signal may depend on variable levels of background noise and propagation phenomena as headwaves - bottom-travelling wave, already discussed in 2.3.4. An early headwave arrival may be discerned in the waveform in Fig. 31, before the main waterborne arrival. The pulse length is usually defined from the cumulative squared pressure curve which usually overestimates the actual air-gun shot length.

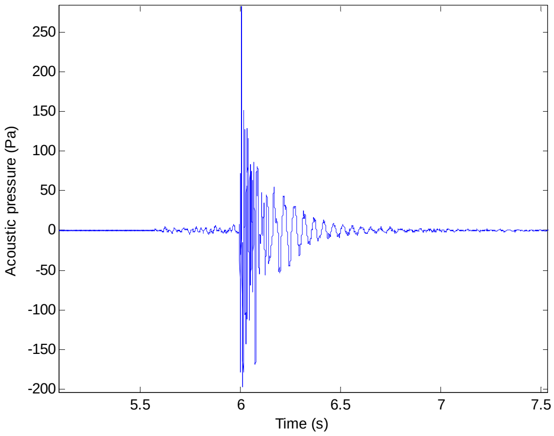

**Figure 31:** *Received waveform of an air-gun shot at 1.2 km. Set 2908, air-gun run AG08. The peak maximum is centred at 0.6 s.*

Here is a list - non-exhaustive - of descriptors which can be calculated from a sound pulse signal: peak maximum and minimum pressure levels (dB re 1μPa), peak-to-peak pressure level (dB re 1μPa), cumulative energy ($Pa^2$.s), pulse length (s), mean squared pressure levels (dB re 1μPa), ambient noise level used in analysis (dB re 1μPa), equivalent energy level/sound exposure level (dB re $1\mu Pa^2$.s) or sound pressure density spectrum level (dB re 1. $\mu Pa^2/Hz$).

Some of these factors are known, e.g. the signal peak values which are easily obtained. They are not used in this paper but are usually relevant to animal hearing systems as they may determine the maximum displacements which occur in the mechanical transduction process of sound reception. However since hearing in most vertebrates requires temporal summation of nerve firings, peak levels may not reflect maximum perceived sound levels [8]. The peak values are particularly dependent on the sampling rate set within the noise logger. The sampling rate must be appropriate to include more than 95% or the air-gun signal energy. Peak-to-peak pressure ($p_{PP}$) were calculated from the pressure waveform p(t) as:

$$p_{pp} = \max(p(t)) + \left|\min(p(t))\right| \tag{15}$$

And the peak-to-peak pressure level as:

$$L_{pp} = 10\log_{10}\left(\frac{p_{pp}^2}{10^{-6}}\right) \tag{16}$$

The cumulative energy in $Pa^2.s$ is an important parameter to describe the quantity of acoustic energy vs. time. It is calculated as:

$$E_{cum} = T_s \cdot \sum_i p_i^2 \tag{17}$$

Where $T_s$ is the sampling increment ($1/f_s$) and the squared pressure of each element i are summed in a cumulative fashion.

The pulse length T is taken from the cumulative squared pressure curve. Thus, the 5% and 95% points along this curve are used in calculations to standardise the air-gun signal start and end times. The signal length is relevant to point up geometrical dispersion within the ocean waveguide of the received shots at different ranges.

Assuming the signal start and end points ($T_0$ and $T_E$) are the same, the mean squared pressure and mean intensity values are equal and calculated as:

$$p_{ms} = \frac{1}{T}\int_{T0}^{TE} p^2(t)dt \tag{18}$$

And the corresponding mean squared pressure level as:

$$L_{pms} = 10\log_{10}\left(\frac{p_{ms}}{10^{-12}}\right) \tag{19}$$

From (18), it can be seen that the mean squared depend on the pulse length T, often ambiguously defined due to the possible presence of headwaves or significant ambient noise. Note that the problem related to headwave arrivals may be avoided in applying a high pass filter from a given low frequency. It was not done in this paper as the mean squared pressure levels were not used.

The ambient noise $p_n$ can be easily defined in the analysis by measuring the mean squared pressure values between air-gun shots. The ambient noise level is calculated as:

$$L_n = 20\log_{10}\left(\frac{p_n}{10^{-6}}\right) \tag{20}$$

Thus, the sound pressure within the air-gun signal p(t) is now written $p_{s+n}(t)$ to indicate that it includes the ambient noise.

The so-called equivalent energy function is defined as:

$$E_s(t) = T_s \cdot \sum_i p^2_{(s+n)i} - \overline{p^2_n} \tag{21}$$

Where $\overline{p^2_n}$ is the mean squared ambient noise and every element i of the pressure waveform are summed in a cumulative fashion. The equivalent energy level - also called sound exposure level (SEL) - is a single value in dB re 1µPa².s and is the average of the last fraction of the curve $E_s(t)$:

$$SEL = 10\log_{10}(\frac{\overline{E_s(t)}}{10^{-12}}) \tag{22}$$

The fraction has to be defined, e.g. the last 20th part of $E_s(t)$.

Because of the problems inherent in using the peak signals or the mean squared pressure, sound exposure levels (SEL) delivered by each air-gun shot were used to describe received air-gun levels throughout this paper.

Finally, the sound pressure density spectrum level - in dB re 1. µPa²/Hz - is also calculated for each pulse, describing the distribution of sound versus frequency. The choice of the frequency resolution has to be chosen carefully when calculating this spectrum.

Fig. 32 summarizes how an air-gun shot can be acoustically described. It gives the example of a shot waveform with its corresponding cumulative squared pressure curve and pressure density spectrum level. The SEL value for this shot was 148.08 dB re 1µPa².s.

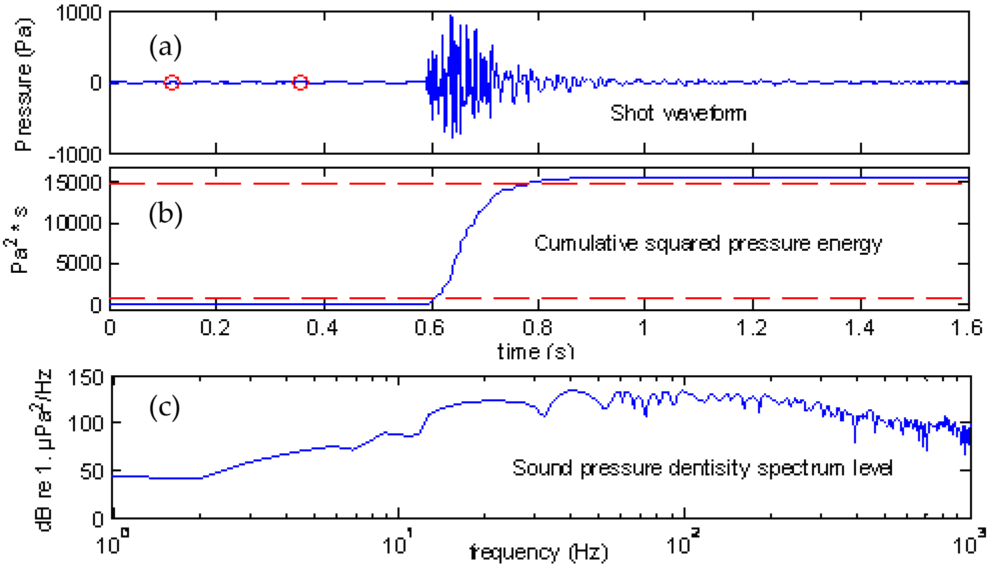

**Figure 32:** *Waveform of a received shot at 2.2 km (a), the cumulative squared pressure curve (including ambient noise) showing air-gun energy vs. time (b) and the density spectrum (frequency resolution of 1.95 Hz) (c). The two red dots on the waveform denote the portion used to define the ambient noise in the analysis. The two threshold lines in (b) show respectively the 5% and 95% points along the cumulative energy curve.*

The time-dependent variables (e.g. the SEL) can be plotted over range given that the distance air-gun - noise logger was logged and calculated for each shot. As an indication how each measure tracks signal energy, Appendix 9 gives - for a given air-gun survey - received peak-to-peak, mean squared pressure and sound exposure levels with range. Note that the SEL values are the lowest and that variations occur for mean squared pressure level at great distances.

All these descriptor calculations from noise logger data are processed using Matlab codes. This is detailed in section 3.3.

## 3.2 Follow-up data and water sound speed calculations

The measured follow-up data are meant to keep track in time of parameters which are important in sound propagation, i.e. the air-gun characteristics and the water temperature. The air-gun features are mainly its strength (the so-called air-gun signature) and its depth, measured respectively with the near-field hydrophone and the pressure sensor. The water temperature may be an important parameter on sound propagation if strong variations occur in time and space - which is directly related to the wind conditions. Note already that the seismic vessel used in the JIP trials was on task only in calm sea conditions and the results of received air-gun levels at different locations and time are likely to be almost weather-independent.

Thus, the actual definition of the acoustic environment is therefore likely to be mainly related to the sea bottom properties throughout the covered area – given the conditions of the experiments. This is discussed in section 3.3.

Last but not least, water temperature measurements permit to calculate sound speed profiles within the water column at different locations of the covered area and times of the trials. These measured outcomes were used in the coming analysis, either in the refraction seismic technique or in the numerical model.

### 3.2.1 Air-gun characteristics

A near-field hydrophone (HiTec HTIU90 model) was bolted into the towfish 0.8521 m away from the air-gun and connected to a - 20 dB attenuator. The near-field signals were continuously logged during air-gun operations to a Sound Devices SD744T digital recorder sampling at 32 kHz and 10 dB gain to *.wav files. Fig. 33 shows the air-gun and the yellow towfish, when not operated on the vessel deck. The tow lines can also be discerned on the picture.

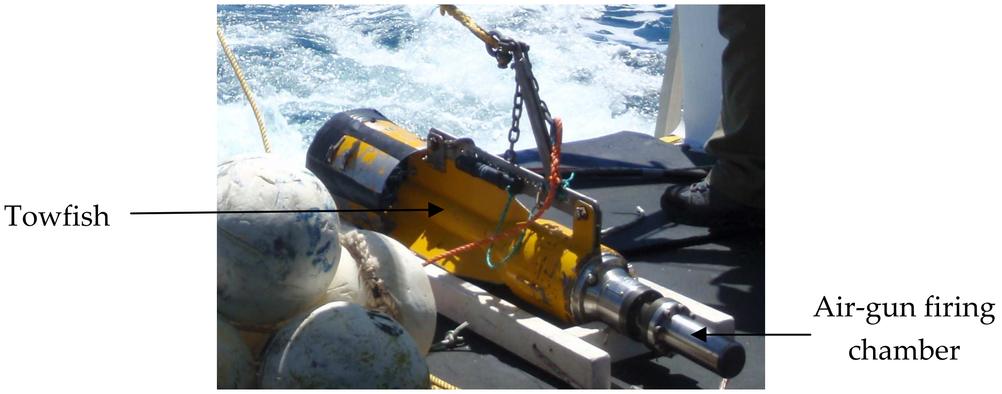

**Figure 33:** *Bolt 600B air-gun bolted into the towfish (yellow body). All the equipment measuring data in the air-gun near-field were bolted into the towfish.*

The idea was to keep track of the air-gun signature during the time of each survey and check the consistency of the shot waveforms as well as their sound pressure density spectrum levels over frequency. The near-field data is subject to sensitive variations related to many factors as the gun pressure, the seabed reflections, the reverberation from the gun itself or bubble oscillations. They are substantial to look at as they represent the amount of acoustic energy radiated in the ocean waveguide.

Mention that the hydrophone was wired up backwards during the project so the inverse of its data was taken into account. This common error has no consequence on the results.

As an example, Fig. 34 gives the recorded waveforms (voltage vs. time) for a typical conducted survey (AG07). The values in V are not of importance here and are just meant to compare the data between the surveys. The results are presented in Pa when considering a single air-gun shot (see Fig. 35).

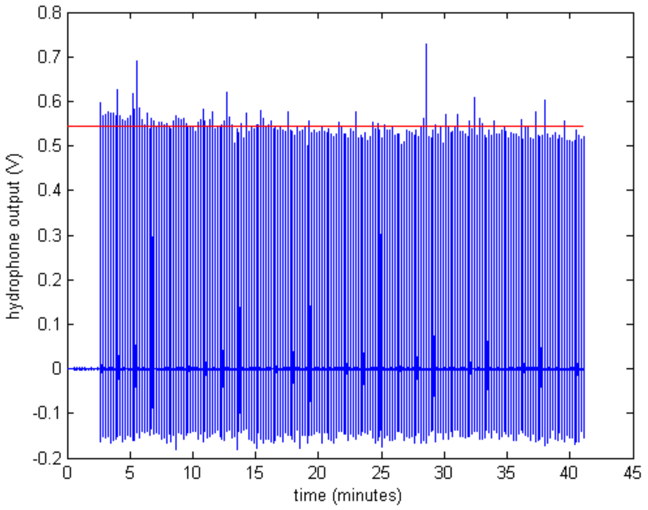

**Figure 34:** *Near-field hydrophone output during the first 41 minutes of survey AG07, in V vs. time (minutes). This block contains 197 shot waveforms. The red line denotes the mean primary pulse amplitude in the block.*

The block provides approximately the first 40 minutes of the survey - over 62 minutes - as the complete data were too heavy to process. The gaps between the shots are not well discerned in the plot as the scale is too large. The actual repetition rate was quite consistent between the surveys and around 11.5 s, instead of the desired 10 s. Note that one survey (AG14) was set with a different rate, around 17.5 s which has no major influence for the technical analysis.

The red line in Fig. 34 denotes the mean primary pulse amplitude (around 0.54 V) for the block and points up slight variations. Note that there was a slight decrease of amplitudes with time in this survey which may be related to a decrease in gun pressure. Some shots also appear to have abnormal greater energies (up to 0.68 V).

Considering blocks of the same size (about 41 minutes), the outputs of the near-field hydrophone for other noteworthy surveys (AG02, AG06, AG11 and AG14) can be found in Appendix 10. Besides, Appendix 11 is a table comparing the mean primary pulse amplitudes between the surveys, still considering 41-minute blocks. This table points out substantial variations, especially AG11 and AG12 which had abnormal weak shot amplitudes. These results are either related to a low gun pressure (known to be reasonably consistent during the 1-month trials) or a problem with the air-gun sealing. For instance, the presence of seaweed around the air-gun sealing can affect directly the source level.

The difference in source levels between the surveys is theoretically not a major issue as they can all reflect the effect of the acoustic field. Thus, runs AG11 and AG12 provide high values of SEL and their data can still be compared with other surveys.

The global mean value of primary pulse amplitude (around 0.54 V) was used to pick a typical shot waveform. This waveform will be used afterwards in the numerical model in order to input a sound source as close as possible to the reality. Using such a standard source in the model generates obviously disparities with the measurements as no variation of amplitudes at the source is taken into account. The chosen shot came from survey AG16.

In order to measure the actual air-gun signature, the near-field data was converted to sound pressure (Pa). The conversion used the calibration factor including the hydrophone sensitivity, its gain and the gain of the sound recorder. The sound pressure values were then calculated at 1 m using a spherical spreading loss. Using such a geometrical spreading in the near-field is quite accurate. Sea water absorption was not taken into account in the calculations which is a fair simplification. Spherical spreading implies sound intensity varies inversely with the square of the distance from the source.

The pressure values at 1m were then calculated using the following formula.

$$p(t,1m) = p(t,0.8521) * \frac{0.8521}{1^2} \tag{23}$$

Fig. 35 is a plot of the chosen waveform which can be considered as typical, with a primary pulse amplitude of around 0.145 MPa-m.

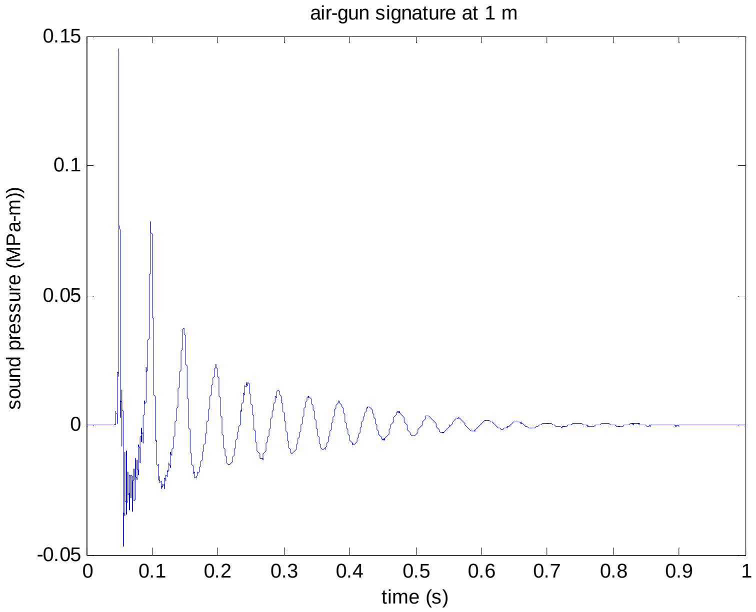

**Figure 35:** *43th emitted shot waveform from survey AG16. Chosen as a typical source level of the JIP trials.*

As explained in the theoretical aspects, Fig. 35 shows the desired primary pulse - where air-gun energy is concentrated - followed with the bubble pulses. It also shows the surface ghost effect, i.e. dephased and negative reflected energy. The waveform shapes were quite consistent between the surveys, except for AG11 and AG12 which presented much weaker peaks. As mentioned earlier, this result is probably related to an air-gun sealing issue during these two surveys.

From this air-gun signature, a typical sound exposure level at the source can be calculated, using the cumulative energy curve in $Pa^2$.s (see equation 17). The portion of this curve used to calculate the SEL was the last 1/20th as illustrated in Fig. 36. The portion of noise used in the analysis was taken between two points at the beginning of the waveform. This value of 200.5 dB re 1$\mu Pa^2$.s-m can be used to calculate theoretical received levels with range using geometrical spreading (spherical or cylindrical).

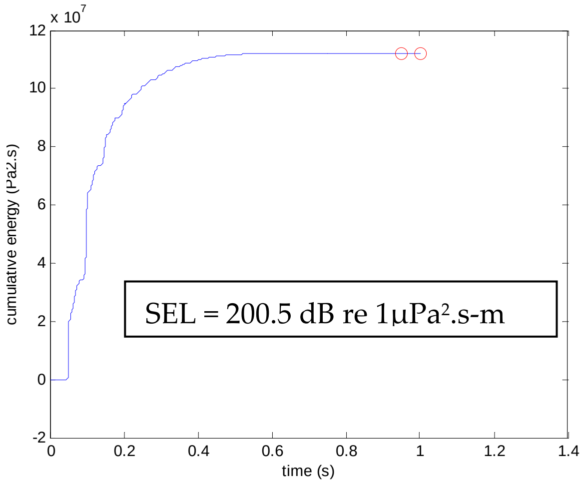

**Figure 36:** *Cumulative energy (Pa$^2$.s) vs. time (s) for the chosen typical shot waveform. The two red circles denote the points considered to calculate the sound exposure level.*

The sound pressure density spectrum levels were calculated for every shot waveform. The values were calculated 1 m away from the source, using equation (24) below, assuming the usual spherical spreading loss.

$$L_{dB}(1m) = L_{dB}(0.8521m) - 20\log_{10}(\frac{1}{0.8521}) \qquad (24)$$

These values are very important as they denote the frequency range of main energy for each survey. Their mean levels were calculated and plotted on the same figure - as shown in Fig. 37. Note that the curve for AG02 is missing and that all other relevant surveys are considered.

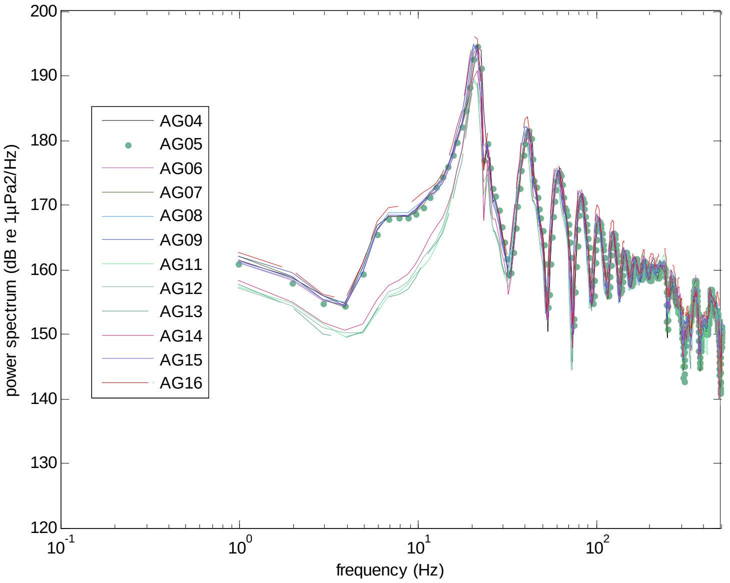

**Figure 37:** *Sound pressure density spectrum levels (dB re 1. μPa$^2$/Hz) vs. frequency (Hz) curves for the studied air-gun surveys. Each curve is the mean density spectrum levels in each survey considering its N total emitted shots. Only the results up to 500Hz are shown.*

Fig. 37 represents a good result as it shows a fair consistency between the surveys regarding the frequency distribution of the produced air-gun energy. Thus, the primary pulse was between 20.5 and 21.5 Hz with levels around 194 dB re 1µPa²/Hz-m. The next main bubble pulses were at 41 Hz, 61 Hz, 81Hz, 101 Hz, etc.

Note the important gaps in the results for low frequencies below 18 Hz. These differences do not matter for sound transmission and are likely to result from towfish vibrations or limitations of the recording devices in low frequencies (near-field hydrophone and sound recorder). However, these limitations were analytically compensated in Matlab codes.

From around 250Hz - as illustrated in Fig. 38 - the spectrum levels points out the source ghost effect, i.e. the sea surface reflected energy. As discussed in the theoretical aspects, the frequency region of this energy is directly related to the air-gun depth and defines the useful frequency band for seismic data. Thus, the air-gun depth for the JIP trials - around 5.4 m as seen below - is quite shallow moving the notch of reflected energy in Fig. 37 to higher frequencies. It results in higher transmission loss levels at a given received range compared to a deeper deployment depth, due to interference between the direct and reflected field.

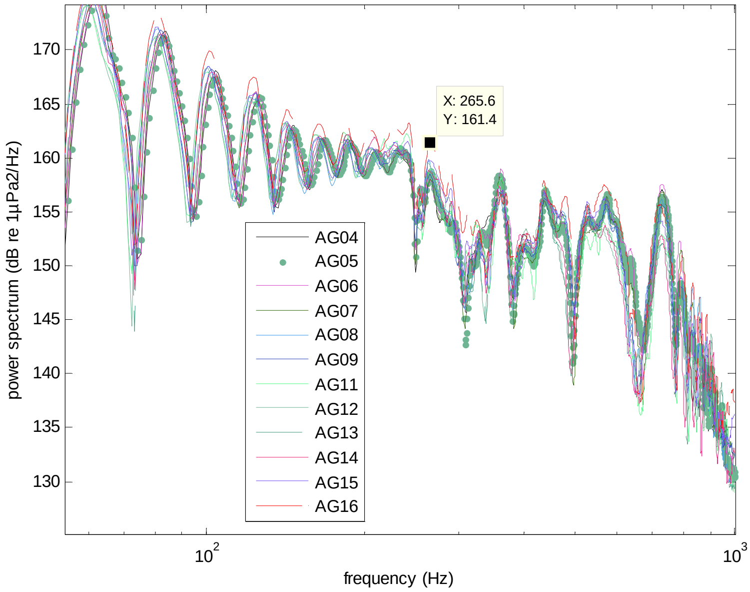

**Figure 38:** *Zoom in higher frequencies up to 1000 Hz of the curves from Fig. 36, showing frequency components resulting from the sea surface reflection of the air-gun acoustic energy.*

The near-field data above 800Hz is only noise and that is plausibly related to vibrations of the towfish surrounding the air-gun - as it has been previously pointed out in CMST studies.

Another particular consistent feature in the spectrum level curves was an additional peak around 24 Hz following the primary pulse peak – as shown in Fig. 39.

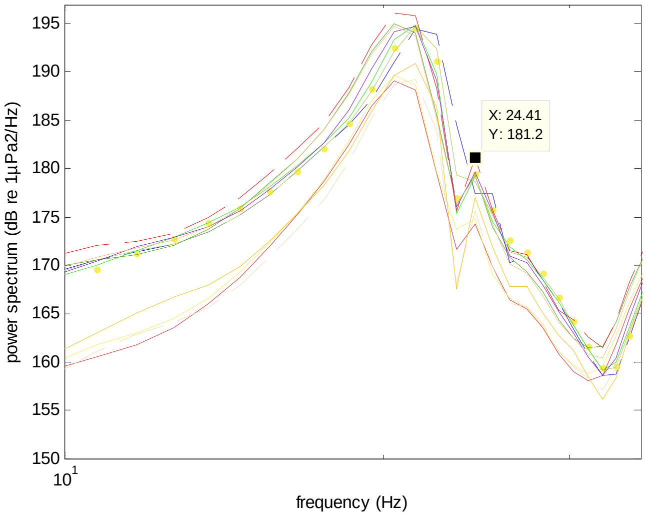

**Figure 39:** *Zoom at the primary pulse of Fig. 37, showing an additional peak around 24 Hz.*

The result showed in the figure above results certainly from a particular reflection of the primary pulse energy. There are many possible reflectors as the seabed of the vessel. Another explanation could be a flexural wave propagating down the towfish slower than the in-water signal. It may correspond to the bottom bounced energy of the primary pulse.

In addition of the near-field hydrophone, a pressure sensor was mounted in the towfish to measure the air-gun depth (Aquatech 520PT logger). The use of two tow lines from the seismic vessel was meant to keep an approximate desired air-gun depth of around 5.6 m. The results were processed in Matlab - particularly to convert the data into water depth (m). They show a reasonable consistency for a given survey as well as between the different surveys. However, the importance of this parameter and its implication in terms of lateral sound radiation of the air-gun energy makes it relevant to look at in detail. It is then crucial to have similar air-gun depths in order to compare properly the results between the surveys.

The mean air-gun depth between the 13 relevant surveys was around 5.43 m. Fig. 40 displays typical results of air-gun depths (run AG13). The standard variation of air-gun depth values within each survey was not substantial. Note that the scattered data points were consistent and are related to data points during shot firings.

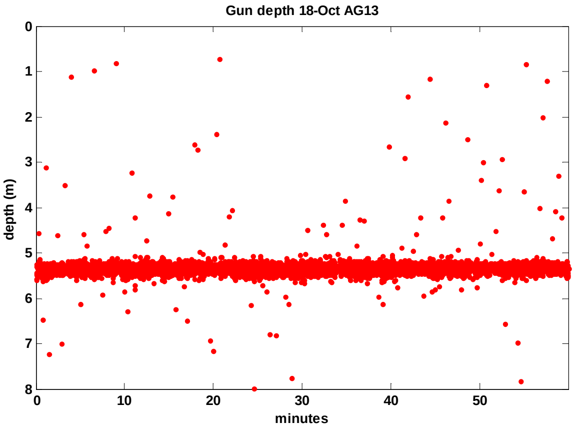

**Figure 40:** *Air-gun depth in water depth (m) vs. time (minutes) for survey AG11 (16th October). 0 m represents the sea surface level.*

Some surveys presented particular results as AG11 and AG12 having the shallowest air-guns (respectively around 5.04 and 5.07 m) and with higher depths only during the first minutes of operations. Anyway, this difference in deployment depth of around 40 cm is likely to be not substantial for sound transmission.

For extended information, Appendix 12 and Appendix 13 provide examples of air-gun depth vs. time for other surveys (notably AG11 and AG12) and a table gathering air-gun depth data for each run (starting depth, ending depth and average depth). Note that the variations in air-gun depths are closely related to the seismic vessel speed during operations.

### 3.2.2 Water temperature measurements

The last sensor mounted at the air-gun was a temperature logger (Aquatech 520PT logger). It kept track of the water temperature around the air-gun during operations.

Combined with the other temperature data of the project - measured at the noise logger locations -, it was used to define sound speed profile within the water column at different spots. Thus, abnormal temperature variations were analysed with care as sound propagation may be affected by refraction within the water column, especially in high frequencies. However - except in a case of major variations of a few °C - the water temperature and sound speeds are not dominant parameters for sound propagation in shallow water as discussed in the theoretical aspects. Anyway, a typical measured sound speed profile is required, especially for accurate numerical modelling.

The biggest variations of water temperature at the air-gun occurred for surveys AG04, AG14 and AG16. For these surveys, a significant increase of temperature is visible during the air-gun operations, with the most sudden change for AG14 - i.e. about 0.35 °C around 30 minutes. Generally, the data showed reasonable low variations, either within each run or between the runs. Fig. 41 provides an example of curve temperature at the air-gun with time. The considered survey is AG12 and it shows a typical result.

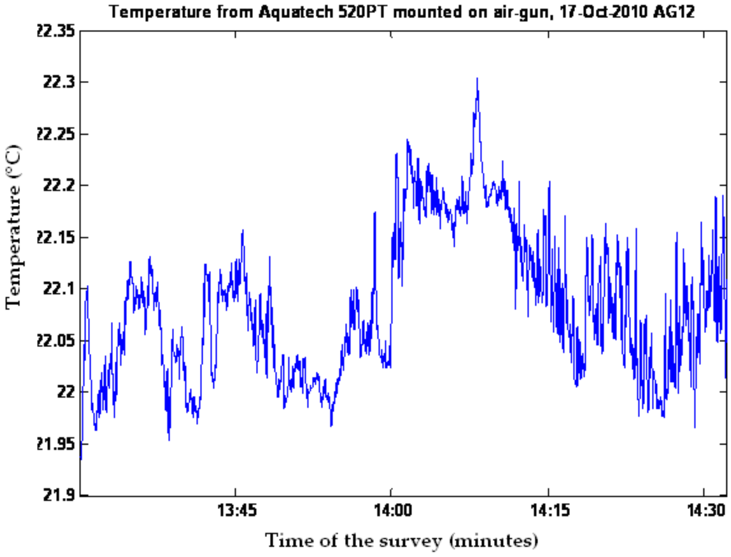

**Figure 41:** *Water temperature (°C) at the air-gun for survey AG12 over time (min). The survey length was around 63 minutes. The mean temperature was 22.08 °C with a standard variation of 0.07 °C.*

Appendix 14 and 15 provide extended information on these data, i.e. temperature curves for other surveys and a table gathering statistics. The mean value of water temperature at the air-gun for the project was about 22.18 °C.

At last, temperature sensors at the noise loggers and 11 m above them were measuring the water temperature for the time of their deployments. Fig. 42 illustrates the position of these sensors for a deployed noise logger on the seabed.

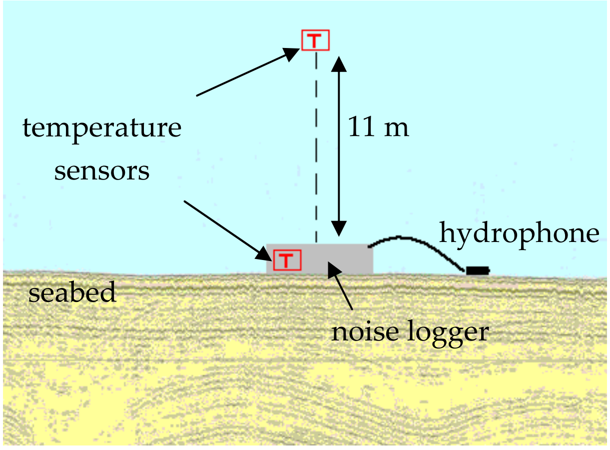

**Figure 42:** *Illustration of the positions of the two temperature sensors at each set of noise logger.*

These data were interesting to look at to check the variations of the water temperature within a few days - at different seabed positions within the area and over the experiments term. These variations are related to the weather conditions, especially wind speeds. Fig. 43 displays such data - water temperature in °C at the seabed and 11 m above seabed vs. time in days. It gives the data from the sets of noise logger 2937 and 2938, deployed at the same periods. Note that set 2938 was pulled out around 5 days before set 2937.

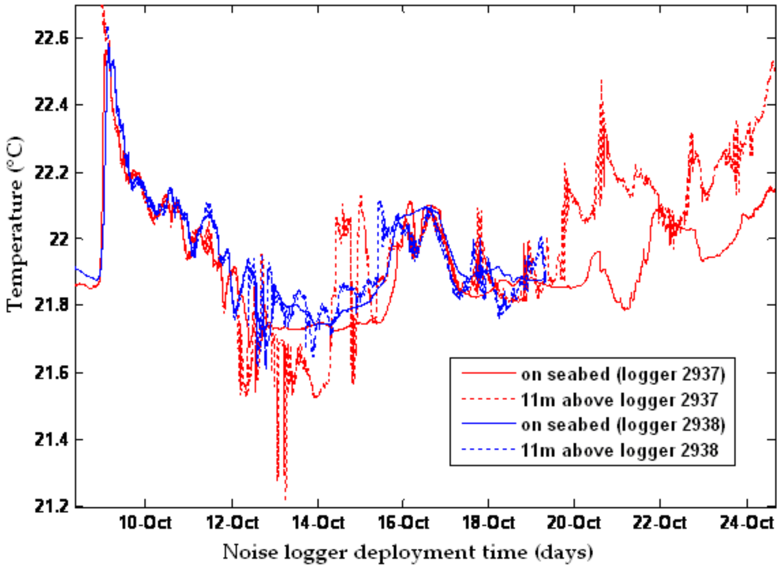

**Figure 43:** *Water temperature (°C) vs. time (days) for set 2937 and 2938 from the temperature loggers at the seabed and 11 m above seabed deployed at the noise logger locations.*

As for the water temperature data at the air-gun, these data do not show enough high variations to consider them as significant factors in sound propagation. However, slight variations did occur and it may affect directly the measured sound speed profiles in the water column, depending the time at which the water temperature is taken. For instance, a sudden change in temperature is pointed out 11 m above the seabed around the 6 and 7th October for the noise loggers deployed at this time (sets 2907, 2908, 2909 and 2910). For illustration, Appendix 16 gives examples of temperature curves for other sets of noise loggers. Appendix 17 and 18 provide two tables gathering - for each set of noise logger- mean and standard variation values respectively for the sensor at the seabed and 11 m above seabed.

### 3.2.3 Sound speed profiles calculations

The temperature data at different locations and times were used to define empirical sound speed profiles within the water column. Although water temperature vary mainly in time, it also vary in space and more particularly in the water column - even for an area as shallow as 30-m deep. The sound speed values fluctuate then in the same manner than the temperature in the water column.

The idea was to pick a time at which the temperature sensor mounted on the air-gun was almost aligned with a position of a noise logger - i.e. with the other sensors, at the seabed and 11 m above the seabed. Note that the depth values of the noise loggers were interpolated using a national atlas (bathymetry grid) and are not that precise.

Three sound speed profiles were calculated from measured data for three different times: the 5th October around 15:17, the 17th October around 13:40 and the 18th October around 10:42. For these defined times, the air-gun was operated nearby a set of noise logger and the time of the closest range was picked up. The mean temperature was calculated for each sensor over a 6-minute period (3 minutes before and after the defined time).

Appendix 19 illustrates the three considered cases of air-gun passing nearby a set of noise logger. The closest distance air-gun - noise logger occurred for set 2909 and survey AG07 (5th October), i.e. 71 m. This approach is obviously not perfectly accurate as the 3 sensors were never perfectly aligned and it requires assuming that the water temperature does not vary significantly in a given horizontal area up to 300x300 m. This assumption is reasonable according to the previous water temperature results.

Fig. 44 gives the results of mean temperature within the water column for the three considered cases. The depth of the temperature sensor at the air-gun was taken from the air-gun depth data.

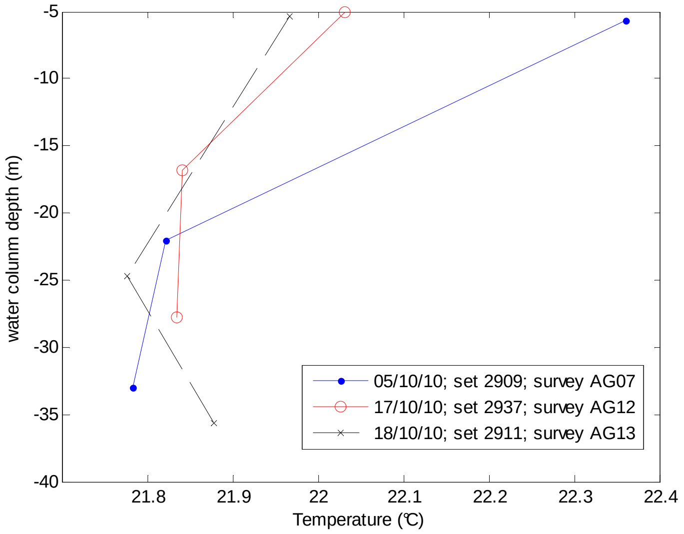

**Figure 44:** *Mean water temperature within the water column for the three considered cases, i.e. 5th October (set 2909, survey AG07), 17th October (set 2937, survey AG12) and 18th October (set 2911, survey AG13).*

As discussed earlier, the water sound speed depends on three factors: water temperature, water depth (pressure) and water salinity. The salinity values were interpolated from an atlas. These values were then not accurate but that is reasonable given that salinity is not a dominant parameter in the determination of water sound speed. The sound speed profiles were calculated using Medwin's formula which can be applied for water temperatures below 35 °C, salinities below 45 psu and water depth below 1000 m.

$$
\begin{aligned}
c_w &= 1449.2 + 4.6 \cdot T(°C) - 0.055 \cdot T(°C)^2 + 0.00029 \cdot T(°C)^3 \\
&+ (1.34 - 0.010 \cdot T(°C)) \cdot (S(psu) - 35) + 0.016 \cdot D(m)
\end{aligned}
\tag{25}
$$

The formula (25) gives the water sound speed $c_w$ in m/s with inputs as salinity S in psu, temperature T in °C and water depth D in m.
Fig. 45 shows therefore the results of sound speed profiles at the different times and locations considered.

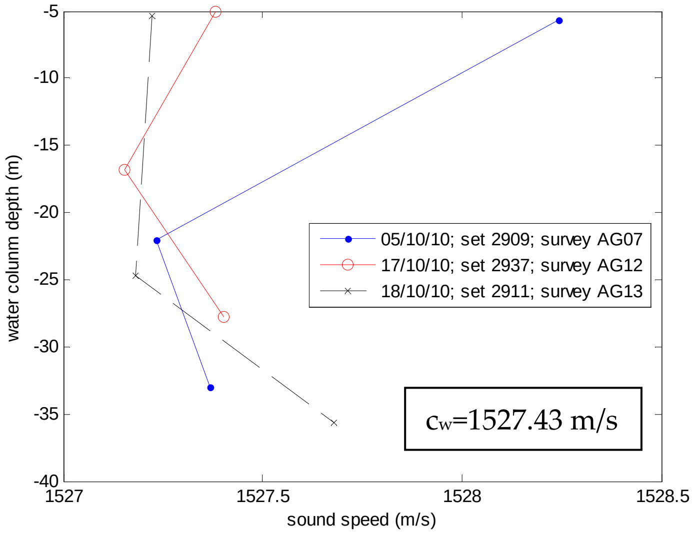

**Figure 45:** *Calculated sound speed profiles within the water column for the three considered cases.*

Notice first that the sound speed profiles are naturally directly related to the water temperature profiles in Fig. 44. From the calculated data in Fig. 45 - corresponding at different times and locations of the JIP experiments - a global mean water sound speed value in the water column can be calculated and was found as 1527.43 m/s. It is a substantial empirical result - in addition of the sound speed profiles - as it will be used in the refraction seismic technique to describe the speed of a hypothetical direct wave propagating in the ocean waveguide.
The results given in Fig. 45 show a small vertical sound speed structure, even for the blue curve which has the highest standard variation (0.55 m/s). Their impacts on sound propagation are then likely to be insignificant, except maybe at the higher frequencies of the radiated air-gun energy (> 200-300 Hz). In section 4 dealing with the numerical approach, the effect on sound propagation of such small vertical sound speed structures in a 30-m water depth waveguide was investigated.

## 3.3 Noise logger data analysis

### 3.3.1 Steps followed in Matlab

Before presenting the results, all the steps followed to extract the air-gun shots within the noise logger data sets are detailed in this section. Each set of noise logger listed in Appendix 4 recorded the ocean background noise for the time of their deployment. As an indication, the longest record was set 2937 deployed for 16 days and covered 8 air-gun surveys (from AG10 to AG17). The ambient noise records outside the surveys are not of interest. Therefore, the relevant data required first to be isolated. This was the first step and it was carried out in defining the time overlap between the noise logger records and the triggered air-guns shots. Recall that the noise loggers were storing sound pressure data every 12 minutes when the sample rate was set at 8 kHz. Thus, the measured data corresponding to a 1-hour air-gun survey was typically stored in from 4 to 6 blocks of 12 minutes. For the only two sets (2911 and 2912) configured with a sample rate at 4 kHz, the blocks were 26-minute long. Note that there was no measurement during the 3-minute breaks which generate gaps within the plots of the results.

The recording time in the noise logger and the times of the triggered air-gun shots are known inputs, thus a Matlab code can simply isolate the desired blocks. As an illustration, Fig. 46 provides the waveform of the first block of data (over 5 blocks) from the set of noise logger 2937 which measured the received air-gun levels from survey AG11 on the 16th October. The amplitude represents the output of the noise logger, in mV.

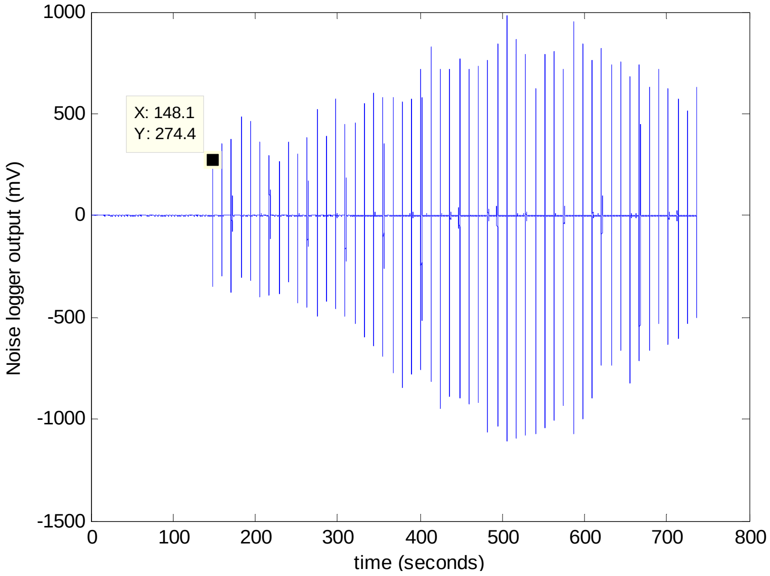

**Figure 46:** *First block from set of noise logger 2937 covering run AG11. Waveform in voltage (mV) vs. time (s). The block length is 12 minutes and 16 s. The first detected shot was at 148.1 s and the block contains the first 52 shot of the run.*

The first part of the signal in Fig. 46 is background noise up to 148.1 s, time of the first emitted shot in run AG11. Recall that the repetition rate between the shots was in reality around 11.5-11.6 s, instead of the desired 10 s. It can be seen from the waveform that the seismic vessel approached the receiver up to the closest range (value around 1.1 V at 520 s in Fig. 46). Thus, most of the results of received signals are split into two parts: approach and departure.

Note that most of the sets of noise logger were configured with a positive gain of +17 dB. For set 2900, an additional channel was added with a negative gain of -3 dB to avoid signal saturation at close range. Sets 2911 and 2912 - set at a 8 kHz sample rate - used two channels with different gains as well, i.e. +20 and +40 dB. Only one case of signal saturation occurred for set 2911 and run AG14, which required using the channel with a smaller gain.

The next step was meant to extract the shots from all the isolated relevant blocks. In a case of high signal-to-noise ratio data (as in Fig. 46), the peaks were indexed using a Matlab function of peak detection. This task required setting a given threshold - based on the amplitude of the weaker shot in the block - and a given time distance between the peaks - set at 9 s during the analysis.

If the data was noisy but with air-gun energy still sufficiently high compared to the ambient noise, then the shots were picked up visually. This task was carried out in plotting the waveforms and the power density spectrum levels for each block of considered data. The shots already extracted before using a threshold were denoted. The low signal-to-noise ratio shots were selected by the user at his discretion, considering that there was no point analysing shots with too little air-gun acoustic energy. Appendix 20 illustrates this task with an extract of noise logger output including consistent whale vocalisations as strong ambient noise which occur on the 27th September (set 2900, survey AG02). The appendix permits also to point up the broadband feature of distant air-gun energy and its overlapping with acoustic energy from humpback whale songs.

The length of the pulse signals used in analysis were arbitrary chosen as 12 s with the peak centred in the middle at 6 s. This length is not of importance as only the defined time boundaries of the pulse are taken into account. As discussed in 3.1.2, the definition of these boundaries is an ambiguous task which is only avoided by describing the air-gun signals with the sound exposure levels (SEL).

As mentioned earlier, the mean source of noise for the data sets from the JIP trials was humpback whale vocalisations which implied low-energy data. It is the case for sets from 2897 to 2900 which covered the survey AG02. The sets 2898 and 2913 which were deployed up north the area (see map in Appendix 5) provided only low-energy air-gun signals and unusable data. Notice also that set 2912 provided mostly weak data due to a configuration problem in this noise logger.

Recall that only surveys AG02, AG04, AG05, AG06, AG07, AG08, AG09, AG11, AG12, AG13, AG14, AG15 and AG16 were interesting to process.

Besides, the task illustrated in Appendix 20 was useful as well to detect sources of false shot detection, as shrimp noise. Fig. 47 shows a recorded waveform of an impulsive signal resulting from a shrimp signal. The non-repetitive pattern of such external pulses often made easy their separation with air-gun pulses. It was particularly useful for the data from set 2911 and run AG13.

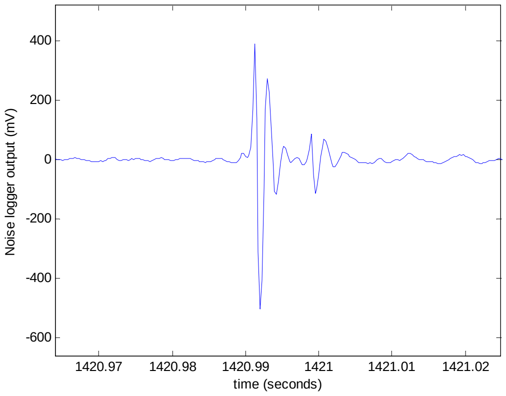

**Figure 47:** *Recorded waveform of a "shrimp noise" which can be confused with an air-gun pulse if not analysed carefully.*

In addition of whale songs, abnormal powerful external source of background noise occurred for some surveys as discussed in the next section.

Before calculating the descriptors for impulsive signals, the calibration data were inputted into the Matlab post-processing codes in order to convert noise logger outputs in sound pressure (Pa). The calibration was performed in the field and the calibration data was stored at this moment.

An intermediate step was to assemble all the stored shots within each block to obtain all the received air-gun signals for a given survey. Thus a Matlab file was created for each survey, containing a given number of shots with sufficient air-gun energy. Fig. 48 gives an example of a stored shot (12-s sample). The maximum peak pressure in this example is around 76 Pa for a range at 3.17 km. This value is typical as it will be seen later from transmitted energy from a single air-gun. Note that an air-gun array can generate received waveform with maximum peak pressure around 0.8 kPa at 1.5 km.

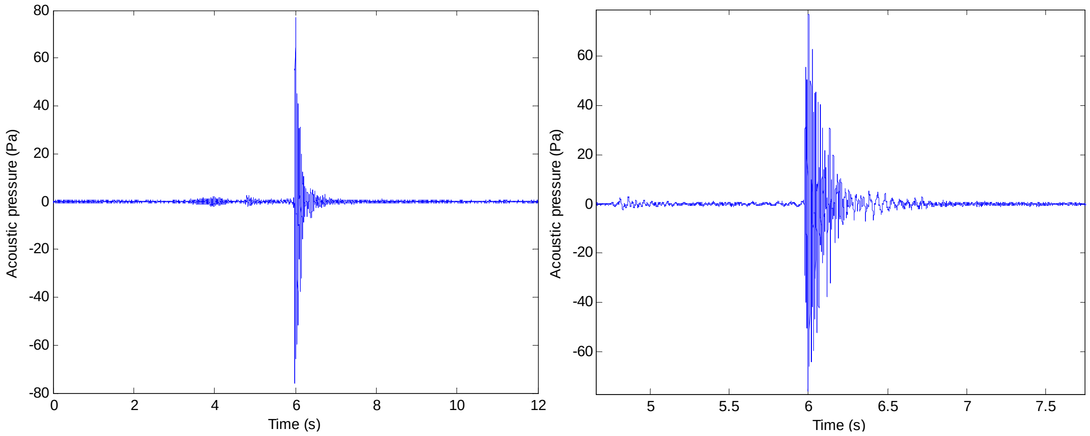

**Figure 48:** *Typical high-energy air-gun shot waveform, resulting from the data post-processing steps applied on each survey and set of noise logger. 12-s sample (left) and zoom on the pulse (right). The range was 3.17 km for this shot.*

Each shot was then analysed to calculate the desired descriptors cited in 3.1.2. This process was already explained and well illustrated with Fig. 32. The ambient noise used in analysis - especially to obtain the sound exposure levels (SEL) - was taken by measuring the mean squared pressure values for a given part of the waveform, either before or after the pulse. This technique biases the results when strong and non-consistent background noise occur but often describe the actual level of received background noise at the time the air-energy is received at the considered target.

The main descriptors of interest in this paper for a given survey will be the sound exposure levels in dB re 1µPa$^2$.s and the sound pressure density spectrum levels, which are respectively range-dependent; and range and frequency-dependent.

The calculation of the range R "received shot - air-gun position" from the measured data is substantial and has to be quite accurate. It was simply calculated using the easting and northing coordinates of each fixed noise logger and each emitted air-gun shot positions. The latter are known from the GPS logger connected to the air-gun triggering system.

## 3.3.2 Analysis of the results

### 3.3.2.1 Ambient noise levels

First, it was interesting to look at the ambient noise levels throughout the data sets. They should be unrelated to any received air-gun energy and strong variations were noticed between surveys, especially due to whale vocalizations and other sources of man-made noise. The noise levels were as high as 120 dB re 1µPa for some surveys. As an example, Fig. 49 shows the ambient noise for survey AG08 recorded with set 2908. The source was approaching the noise logger at the end of the survey and was identified as an engine noise (likely airborne noise from a helicopter).

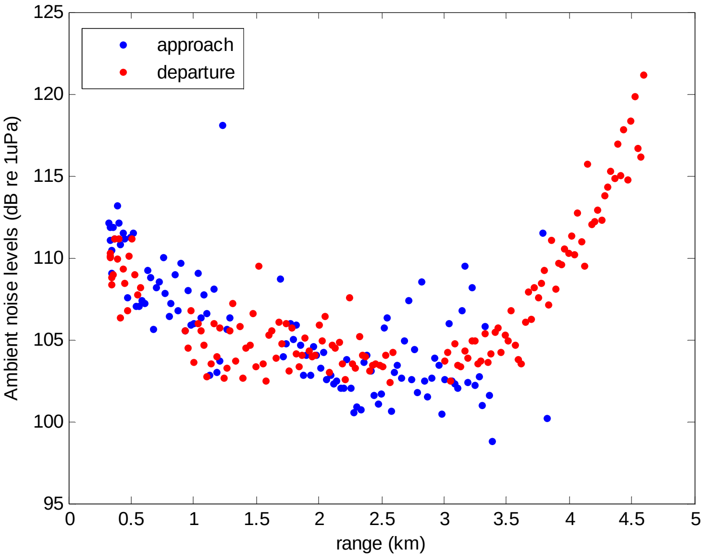

**Figure 49:** *Ambient noise levels vs. range for survey AG08 recorded with set 2908. The data is split into the air-gun approach and departure. Each data point corresponds to an air-gun shot.*

Another specific event of sudden external noise occurred on the 18th October and is illustrated in Appendix 21.

Apart from these cases, the ambient noise levels were quite consistent with typical values around 100-105 dB re 1µPa. The general results of background noise are then not substantial for the analysis of the received SEL at any given position.

### 3.3.2.2 Introduction to SEL and sound spectrum levels analysis

As mentioned earlier, the variations in space - i.e. the changes in seabed and sub-surface structure - are likely to be the dominant impact on sound propagation in the conditions of the JIP trials. Moreover, the previous section showed that the follow-up data in time do not vary significantly.

Before analysing properly the sea bottom structures - i.e. using the refraction seismic technique -, it is interesting first to look at the sound exposure levels vs. range as well as the sound pressure density spectrum levels vs. range and frequency. The evolution of these data with range may point up changes in sea bottom properties. The SEL vs. range curves for each survey are analysed first.

As discussed in the theoretical aspects, the received air-gun levels in shallow water can be sometimes predicted with spherical and cylindrical spreading. In the present case, fitting the air-gun received levels with these spreading is likely not to be successful, mainly due to the Lloyd mirror effect - i.e. having a shallow source - as well as sudden changes of seabed properties. As discussed earlier, the direct sound propagation path undergoes a 180° phase change from sea surface reflection which causes a destructive interference between both paths. This interference is stronger for sound rays close to the horizontal, i.e. at sufficiently long ranges. Indeed, at short ranges, the propagation is dominated by relatively steep rays bouncing off the seabed so the destructive interference is not substantial. On the other hand, at long distances, the steeper rays are getting wiped out by boundary reflection losses and the horizontal rays are dominant which increases the Lloyd mirror effect. The strongest sharp off occur in deep water up to 40logR.

The short-range region - for which spherical spreading (i.e. a transmission loss of 20logR) can be often applied up to an unknown transition range - is not of importance in this paper as most of the noise loggers recorded air-gun sounds at ranges beyond 100 m. Moreover, received levels for short ranges are easily predicted using numerical models and are not subject to strong variations.

The long-range received levels and the distribution of the air-gun acoustic energy within the ocean waveguide are then the central topics. A cylindrical spreading can be calculated - using the SEL value at 1 m from the air-gun signature (see Fig. 36) - and plotted with the empirical air-gun received levels. This can be useful to compare the empirical decreases with a 10logR slope. The air-gun depth was around 5.4 m in the trials which naturally generates a clear drop off at sufficiently long distance. On the other hand, the presence of soft rock outcrops is suspected in the area, especially along the coast. The external knowledge on the geology of the region is developed in the next section dealing with refraction seismic.

Before presenting the results, a covered area by the 1-month trials can be defined from the two recurring survey tracks - i.e. north and east runs - and the sets of noise logger positions. Fig. 50 illustrates this covered area which ignores sets 2898 and 2913 deployed up north the area for which data had not easily discernible air-gun signals. Recall that the bathymetry blue lines indicating the water depth in the area come from an international generic atlas and are likely to be inaccurate. The area is approximately 8 km long and 10 km large.

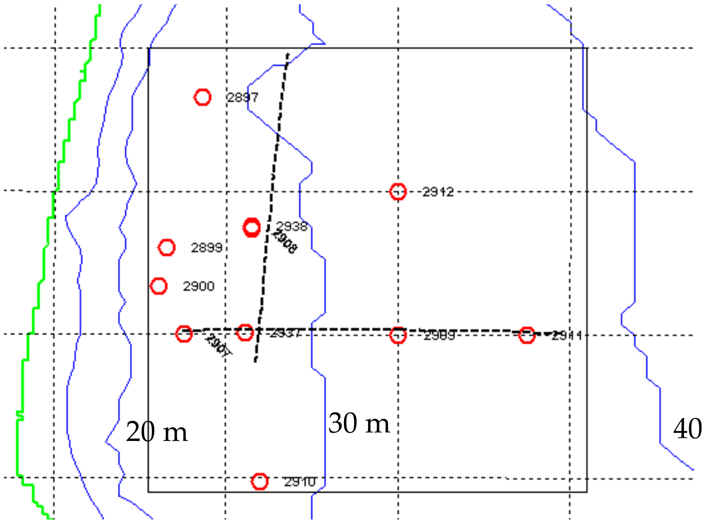

**Figure 50:** *Covered area by the 1-month JIP 2010 survey represented with the black square. Noise logger positions are indicated with the red circles. The two recurring tracks of air-gun runs are indicated with the dotted black lines.*

For most of the receivers in Fig. 50, each survey is split into air-gun approach and departure. Fig. 51 illustrates it for a north survey (AG08) and set 2908.

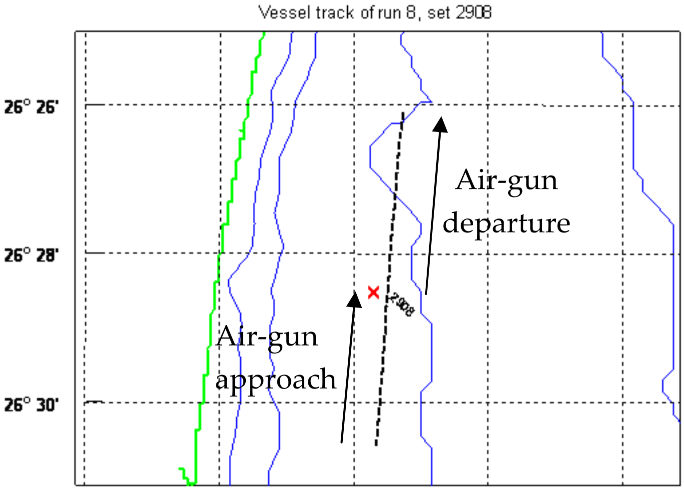

**Figure 51:** *Air-gun shot positions of survey AG08 in black dotted line and position of set of noise logger 2908 in red cross. The air-gun was approaching and moving away from the receiver which generates two sets of received levels with range.*

The analysis can therefore respectively deal with received levels from the east runs and the north runs. The levels are plotted versus range in log scale. Thus, the decrease of received levels is often described with straight lines, which is convenient.

#### 3.3.2.3 East runs results

The east runs relevant to analyse were AG05, AG07, AG09, AG13 and AG14. They follow a slight downward bottom slope, from 25 to 35 m water depth.

The results of noise loggers deployed along the run track are first presented, i.e. set 2907, 2937, 2909 and 2911. Their results of received SEL were quite consistent and show typical results of air-gun transmission in shallow water over a reasonably reflective seabed. Only some data sets are presented, i.e. the ones which are the more representative.

Fig. 52 gives the SEL results for survey AG07 recorded by set 2909. The chosen transition range between spherical and cylindrical spreading was 100 m for all results but it not of actual importance as only slope comparisons with the experimental results are relevant.

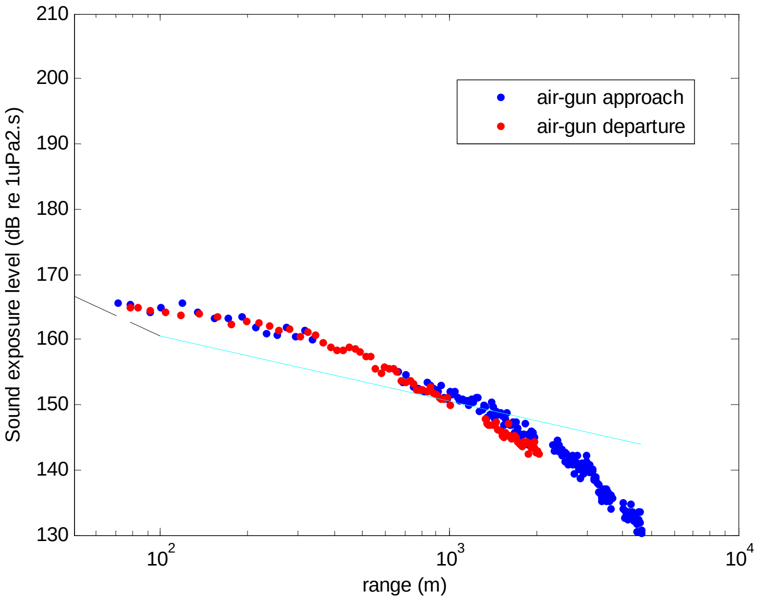

**Figure 52:** *SEL (dB re 1µPa².s) vs. range (log scale) of survey AG07 recorded with set 2909. The black dotted line up to 100 m is spherical spreading and the cyan line is cylindrical spreading.*

Recall that each data point in Fig. 52 represents the calculated SEL of a received shot. The data is split into air-gun approach and departure with a maximum received SEL of 165.8 dB re 1µPa².s at the closest range (71 m). For clarity, Fig. 53 plots the geometry of set 2909 and run AG07 which denotes air-gun approach and departure.

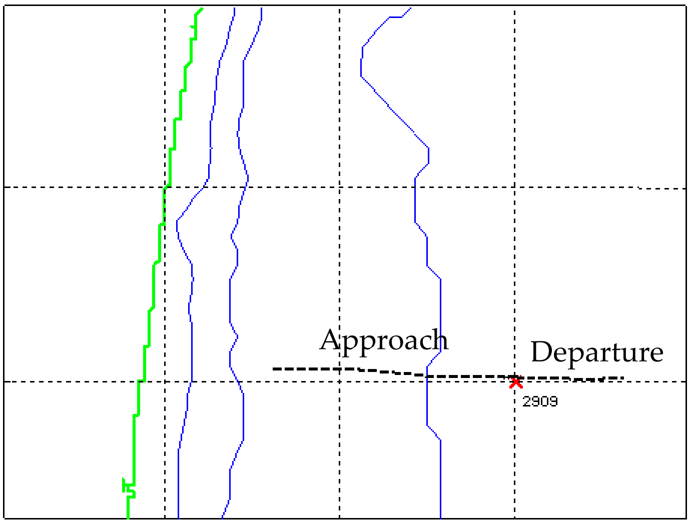

**Figure 53:** *Location of set 2909 and vessel track of survey AG07.*

The short-range levels up to 700-800 m in Fig. 52 decrease in a similar manner as cylindrical spreading, i.e. with a rough 10logR slope. For this region, the destructive interference related to the shallow air-gun and the Lloyd mirror effect is not dominant as the sound rays are still relatively steep.

From 800 m, a smooth drop off in SEL levels occurs which is clearly related to the Lloyd mirror effect. The sound rays are getting close to the horizontal with range as the steeper rays are wiped out due to bottom penetration. Recall that bottom loss occurs for any type of sea bottom and is substantial for steep grazing angles, i.e. for low-frequency acoustic energy.

At the longest ranges - at the beginning of the survey - from 4.5 km to 3 km a slight drop is discernible which may due to a change in sea bottom type.

Note that the downward bottom slope along the east runs seem to have no or very little effect on air-gun sound transmission.

SEL results do not provide information on the geoacoustic properties of the sea bottom but still can give an idea of the seabed reflection properties (i.e. reflective or absorptive) in case of sudden drop off along the curve.

The values of SEL were consistent between the surveys, with typical values around 160 dB re 1μPa².s at 200-300 m down to 130 dB re 1μPa².s at 4-5 km.

The run AG13 detected with sets 2937 and 2911 gives interesting results as it started slightly closer to the shore than the other east runs. Fig. 54 provides the SEL vs. range for this survey and set 2937 which was deployed at the beginning of the east runs.

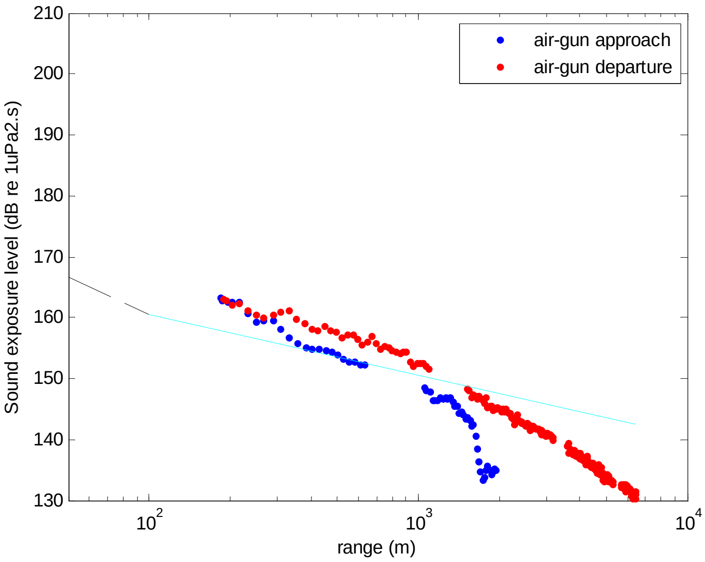

**Figure 54:** *SEL (dB re 1μPa².s) vs. range in m (log scale) of survey AG13 recorded with set 2937.*

Fig. 55 shows the corresponding geometry source-receiver.

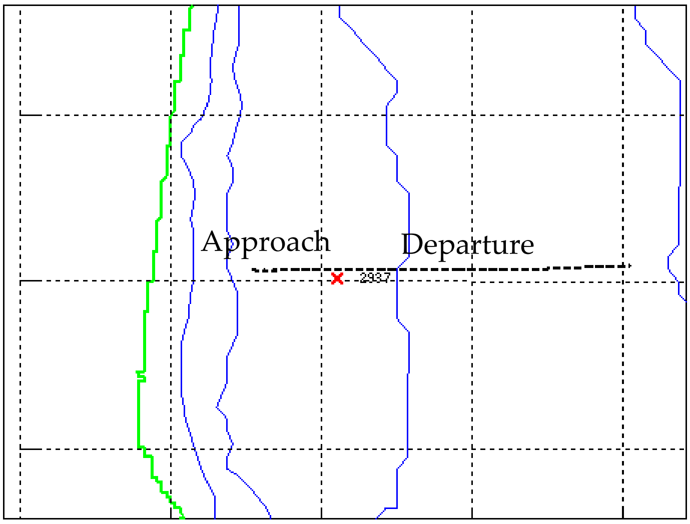

**Figure 55:** *Location of set 2937 and vessel track of survey AG13.*

The SEL of the air-gun departure in Fig. 54 show the typical pattern related to the Lloyd mirror effect, i.e. a significant slope from around 800 m. From the shortest range (183 m) to 800 m, the decrease in SEL is close to cylindrical spreading as in Fig. 52. Of a particular note in Fig. 54 are the low levels for the air-gun approach which is clearly related to a change in sea bottom type. The other environmental factors as bottom slope or variations in water temperature are not likely to generate such variations in received levels. The drop off was not well discerned in Fig. 52 in the same area (start of run AG07, i.e. ranges from 4 to 5 km) and this is probably due to the position of set 2909 - far away from the shore - and the log scale for the x-axis.

More precisely, the results suggested an anomalous seabed type was present in patches throughout the area which was degrading sound transmission. This was later found to be the case where the presence of exposed or partially exposed rocks having a shear wave speed slightly slower than the water sound speed ($c_s < 1500$ m/s) and having a rough interface causing scattering loss.

The results of sound spectrum levels are then very interesting to look at in parallel of SEL curves to analyse what frequency band of the air-gun energy is transmitted with range, which is closely related to the sea bottom properties.

The sound spectrum levels (dB re 1. $\mu Pa^2/Hz$) are plotted vs. range and frequency. They can also be plotted versus the time of the survey. These 2-D plots take therefore into account the sound spectrum levels of each received shot vs. frequency, as the one showed in Fig. 56.

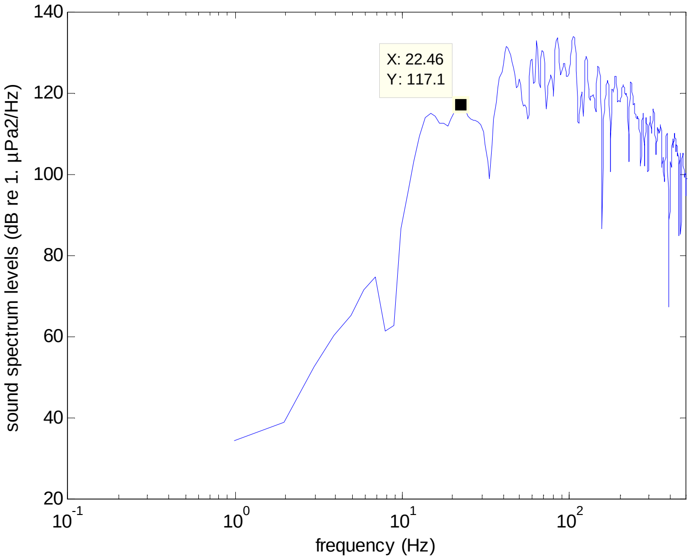

**Figure 56:** *Sound spectrum levels (dB re 1. µPa²/Hz) for 95th recorded shot from AG13 (set 2937) vs. frequency. The plot shows frequency up to 500 Hz and the range for this shot was 900 m.*

Fig. 57 gives the 2-D plot of sound spectrum levels for survey AG13 recorded with set 2937.

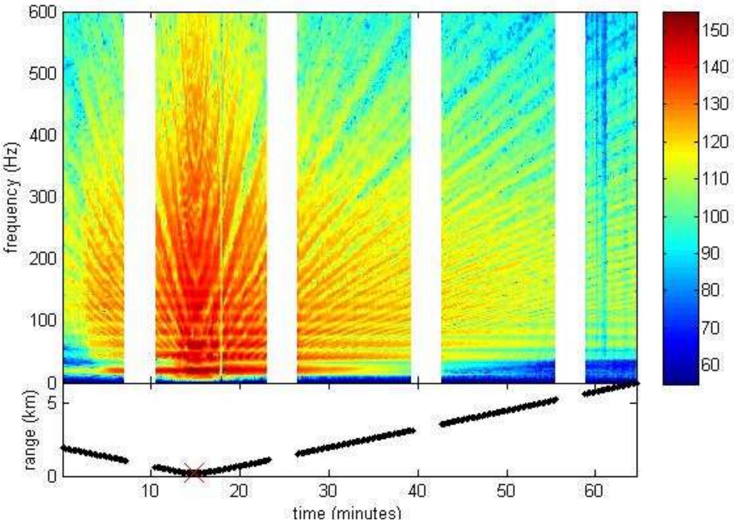

**Figure 57:** *Sound spectrum levels (dB re 1. µPa²/Hz) for survey AG13 recorded with set 2937 vs. time (minutes) and frequency (Hz) in the upper plot. The lower plot gives the range receiver-source vs. time.*

In the same manner as the results in SEL, the gaps in the plot of Fig. 57 correspond to the 3-minute breaks during the noise logger recording.

This result is quite typical of the distribution of the transmitted air-gun energy in an ocean waveguide, therefore the result from survey AG13 and set 2937 can be analysed as a typical ones - especially for the air-gun departure and frequencies above 100 Hz. The lower frequencies are subject to substantial variations between the data sets, due to bottom loss. However, scattering loss can occur as well in some cases as well which imply variations in frequencies above 100 Hz.

A first observation is that transmitted air-gun energy for ranges above 600-700 m is below 500 Hz with main energy from 100 to 300 Hz at great distances. At closer range, transmitted energy exceeds 500 Hz but it low compared to low-frequency components.

A second observation is the presence of regular horizontal bands of high transmitted energy. These bands are clearly related to the source spectrum levels plotted previously in Fig. 37. Thus, the lowest band at 20.5 Hz in Fig. 57 corresponds to the primary pulse of the air-gun signature and the consecutive bands are the bubble pulses energy. In the same manner, low-energy regions correspond to the drops in the spectrum levels at the source.

Therefore, the results of sound spectrum levels do not represent the actual effect of the acoustic environment on the transmitted signals and it is relevant in this way to calculate and analyse the transmission loss instead.

Thus, a measured transmission loss spectrum level can be approximately calculated from the data in dB re 1. μPa$^2$/Hz at the source. The transmission loss is a positive quantity and can be defined as:

$$TL(f) = SL(f) - RL(f) \tag{26}$$

With values in dB re 1. μPa$^2$/Hz (spectrum levels); and TL the transmission loss, SL the source levels and RL the received levels.

Equation (26) does not take into account the noise level within the signal and that introduces a small error in the transmission loss results. In fact, the received signals may not be reduced as much as the depth of the null in the source spectrum would predict. It adds therefore additional horizontal bands of high transmission loss in the plots. These bands do not have a physical meaning and have to be ignored in the analysis.

As mentioned earlier, the negative values of transmission loss are usually plotted to see the evolution of the sound field with range but the positive values are considered in the analysis, with high transmission loss levels meaning strong attenuation of the sound field.

For the calculations, the mean source spectrum of each considered survey (see Fig. 37) was taken into account.

Fig. 58 gives the transmission loss spectrum levels calculated from the received spectrum levels for survey AG13 and set 2937 and can be compared with Fig. 57.

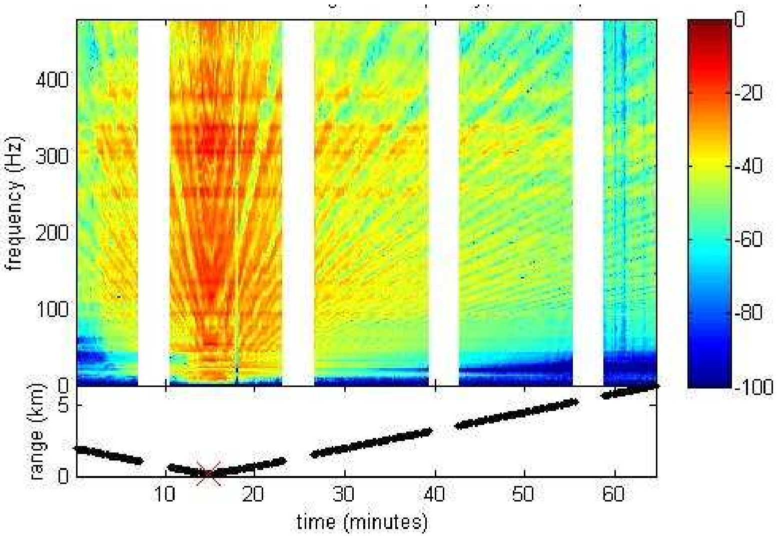

**Figure 58:** *Transmission loss spectrum level (dB re 1. µPa²/Hz) vs. time and frequency in the upper plot for run AG13 and set 2937. The lower plot gives the range vs. time.*

As said previously, this result is typical of air-gun sound transmission in shallow water. At first, the air-gun departure data can be analysed, i.e. survey times from 15 to 65 minutes. As said previously, the horizontal bands of high transmission loss (e.g. at 250 Hz) can be ignored. The interpretation below uses concepts already dealt with in the theoretical aspects of this paper.

A complicated interference pattern exists at high frequencies above 120 Hz which is related to normal mode theory and results in low transmission loss. This high-energy region has strong levels up to the longest range considered and show the efficient propagation of air-gun sound in shallow water. As the frequency is increased, the interference pattern becomes more and more complicated as the number of in-water acoustic modes increase. The source spectrum is focused in the low-frequencies (15 - 600 Hz) and limits then the propagation of high-frequency energy. For frequencies below 100 Hz, transmission loss is high as most of the modes are cut-off and strong bottom loss occurs for high-angle energy. Indeed, any type of seabed (fluid or rocks) implies a strong conversion of acoustic energy into compressional waves for angles above the critical angle for P-waves. As the range is increased, the low-frequency energy attenuates quickly, leaving then only the higher-frequency energy.

Of a particular note is the presence of a high-intensity line around 15-16 Hz which is most likely due to the lower attenuation of the in-water mode 1 at this frequency corresponding to the P-wave critical angle. This reflected energy comes from a given sea bottom layer which is likely to be a deeper elastic layer. In fact, the sharp peak in the reflection coefficient curves at the P-wave critical angle occurs only for elastic materials (see Fig. 23). This propagation is not substantial regarding the distribution of acoustic energy in the waveguide but allow the reinforcement of the headwave propagation - bottom-travelling wave at the interface of the considered layer. This aspect is discussed in detail in the section dealing with refraction seismic.

It is convenient to plot the data vs. range and showing both the air-gun approach and departure in order to compare air-gun sound transmission with range for two distinct regions with possible different sea bottom geoacoustic properties.

In fact, strong variations in the transmitted signal levels occur between the air-gun approach departure for survey AG13 according to the previous results in SEL and Fig. 58. Thus, the transmission loss levels for the air-gun approach (from 0 to 15 minutes) present two distinct regions of abnormal low-levels, at high frequencies (from 150 to 400 Hz) and at low frequencies (below 100 Hz). The diminution in high frequencies is less strong and diffuse and can be associated with scattering loss from a high interface roughness seabed. The wedge shaped high transmission loss region below 100 Hz is manifestly a result of bottom loss and more precisely acoustic conversion into shear waves in the bottom.

It can be best viewed in plotting the transmission loss spectrum levels in the low-frequencies up to 150 Hz - see Fig. 59 below.

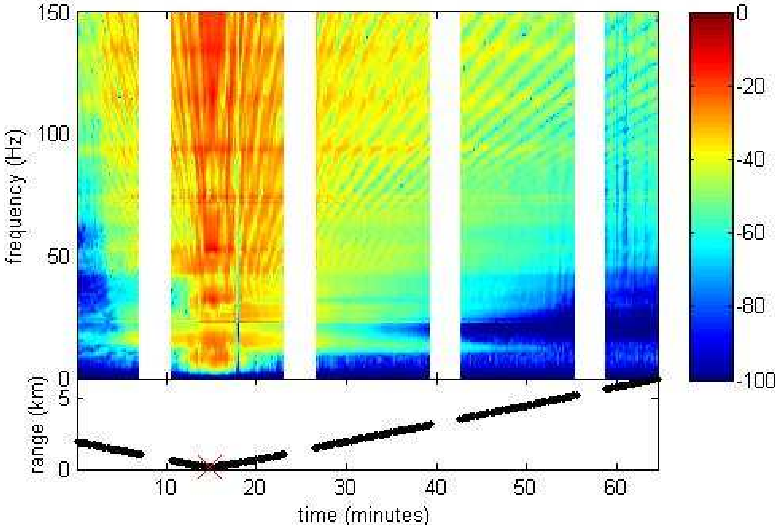

**Figure 59:** *Zoom of Fig. 58 up to 150 Hz (set 2937, run AG13).*

Fig. 59 shows clearly the strong bottom loss at the air-gun approach, represented by the high transmission loss region from 20 to 100 Hz. Note that the high-intensity line around 16 Hz is still present which shows that it may be related to a deep and consistent layer. The low-frequency region of the air-gun departure shows typical results of sound propagation over a reflective seabed (Pekeris waveguide with a sand seabed) with low-frequency attenuation up to 50 Hz.

Appendix 22 gives results of SEL vs. range and transmission loss levels for the east runs from other sets of noise loggers with further interpretations.

The global analysis of east runs results denotes a reflective seabed for most of the run part (to the east) and the presence of one or a few localized soft rock outcrops close to the shore. The knowledge about the area makes believe that it could be a type of soft rock termed coffee rock which is known to occur in the area – see later text.

### 3.3.2.4 North runs results

The relevant north surveys are AG04, AG06, AG08, AG11, AG12, AG15 and AG16. As for the east runs, the receivers deployed along the runs are considered first, i.e. sets 2937, 2908 and 2938.

The receivers 2908 and 2938 were deployed almost at the exact positions; consecutively their respective data do not differ much. Fig. 60 displays the SEL vs. range for run AG08 recorded with set 2908.

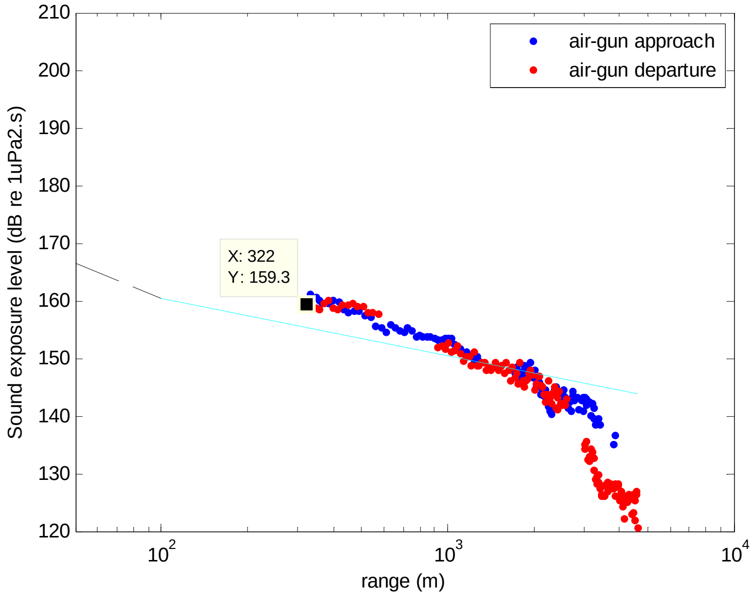

**Figure 60:** *SEL vs. range (log scale) of survey AG08 recorded with set 2908.*

Recall that set 2908 was deployed in the middle of the north runs, as shown in Fig. 61.

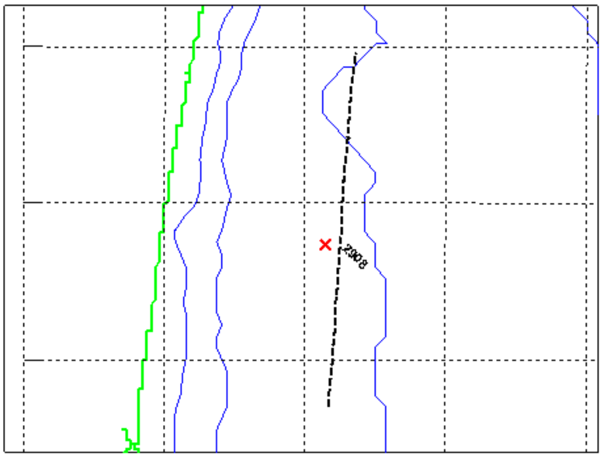

**Figure 61:** *Geometry source-receiver of set 2908 and survey AG08.*

The SEL results for the air-gun approach in Fig. 60 (300 m up to 4 km) are pretty typical and similar to the east runs, i.e. the substantial slope of the Lloyd mirror effect. The SEL values for the approach go from 159 dB re 1. μPa²/Hz down to 138 dB re 1. μPa²/Hz.

The air-gun departure data also follow the same slope but then undergoes a sudden significant drop off with levels down to 120 dB re 1. µPa²/Hz from a range of 3 km. This steep slope reveals the presence of exposed or partially exposed soft rocks at the end of the north runs, at least 3 km north of set 2908 deployment location.

This particular result is consistent in all data sets recording north runs which denote the great size of the rock outcrop. Fig. 62 below giving the calculated transmission loss spectrum levels for set 2908 and survey AG08 confirms clearly this interpretation.

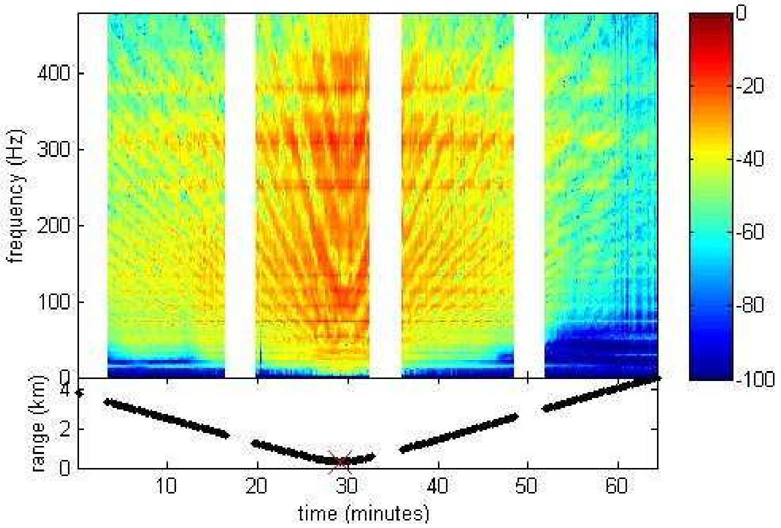

**Figure 62:** *Transmission loss spectrum level (dB re 1. µPa²/Hz) vs. time and frequency in the upper plot for north run AG08 and set 2908. The lower plot gives the range vs. time.*

In the last block of data, i.e. from 52 minutes / 3 km, the transmission loss levels increase markedly in a manner which is typical from a soft and rough rock outcrop effect on sound transmission. A broad frequency band of the acoustic energy in the low frequencies up to 80-90 Hz is transmitted into the bottom and converted into shear waves. This result can be compared with the modelled result of transmission loss over a calcarenite seabed in Fig. 24 of the paper.

Furthermore, a lighter increase of transmission loss occurs also for higher frequencies within the modal interference pattern which may imply a reasonably rough seabed generating scattering loss.

The results in Fig. 62 are very representative of the dominant effect of the sea bottom type in sound propagation, when comparing the frequency distribution of the transmitted signals between the air-gun approach (roughly sand seabed) and the air-gun departure (soft rock seabed).

Fig. 63 zooms in the low frequencies and shows clearly the impact of acoustic conversion into shear waves. It also points up the presence of the mode 1 component at 16 Hz - previously mentioned - resulting from total internal reflection at the P-wave critical angle for a given sea bottom layer.

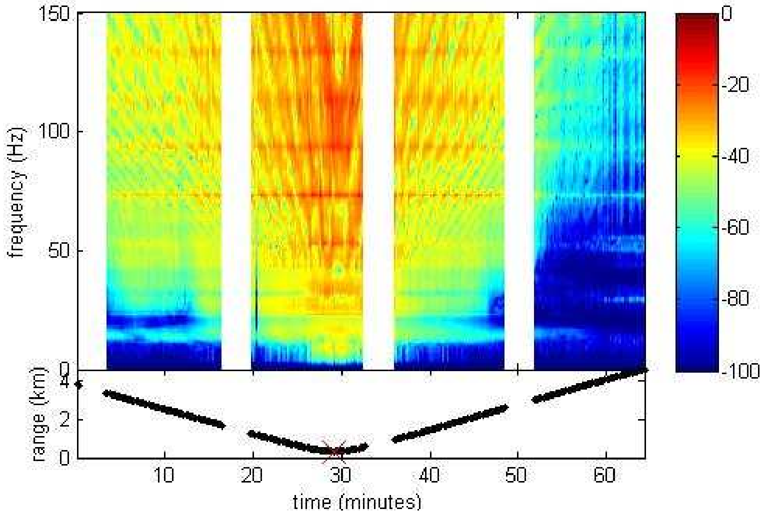

**Figure 63:** *Zoom of Fig. 62 from 0 Hz up to 150 Hz (set 2908, run AG08).*

The results recorded with set 2937 are similar to set 2908 and show the same behaviour in range. They are catalogued in Appendix 23.

Other relevant data sets of received levels for the north runs are from set 2909 - noise logger deployed to the east. Fig. 64 gives the geometry source-receiver of set 2909 and run AG06.

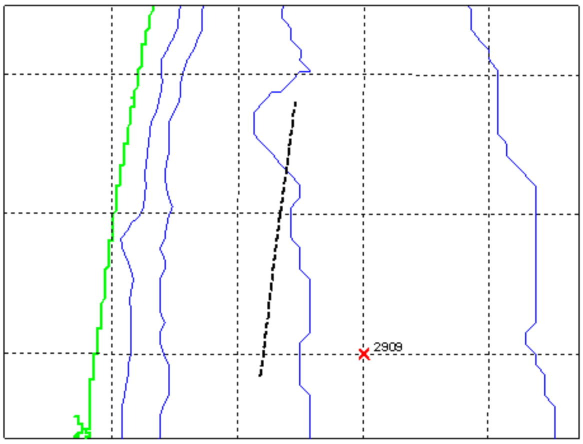

**Figure 64:** *Geometry source-receiver of set 2909 and survey AG06.*

The receiver 2909 was therefore deployed far away from the north run, with closest range around 2.6 km. Fig. 65 gives the corresponding SEL vs. range curve.

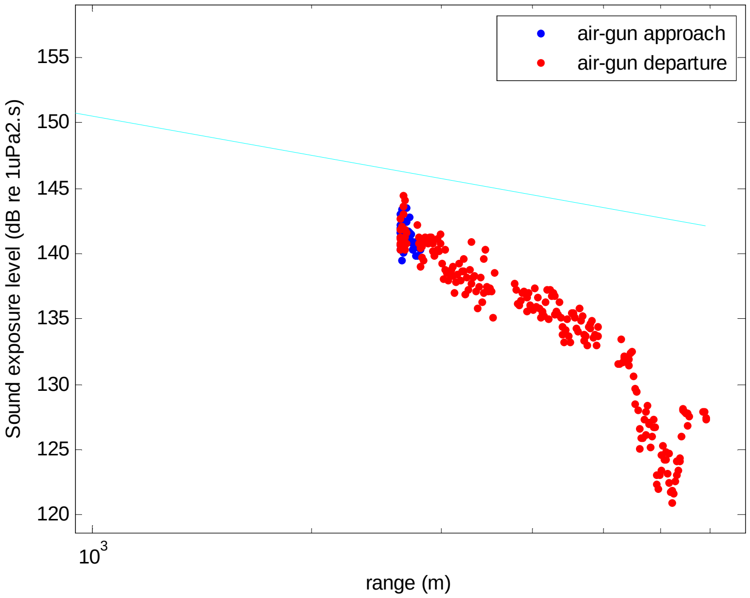

**Figure 65:** *SEL vs. range (log scale) of run AG06 recorded with set 2909. Range goes from 2.6 to 7 km with a substantial drop off around 6 km.*

The results for the air-gun approach are not relevant with only a few received shots. The curve of the air-gun departure up to 5.5 km shows the typical drop of the Lloyd mirror effect combined with a reasonably reflective seabed. The SEL values decrease from 143 to 130 dB re 1. µPa²/Hz for this region. Above 5.5 km, the same sudden decrease as in Fig. 60 is noticed, revealing as well the presence of the northern rock outcrop. After the minimum SEL (around 121 dB re 1. µPa²/Hz), the levels increase markedly at and reach the previous slope - corresponding to a reflective seabed-, showing the limited size of the rock outcrop. This can be clearly viewed in the transmission loss level plot in Fig 66.

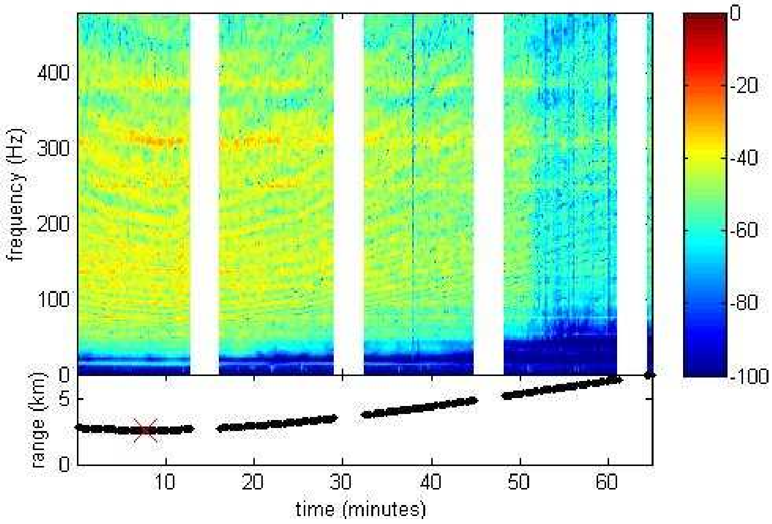

**Figure 66:** *Transmission loss spectrum level (dB re 1. µPa²/Hz) vs. time and frequency in the upper plot for north run AG06 and set 2909. The lower plot gives the range vs. time of the survey.*

The shape of the transmission loss levels with range (or time) is different from the other ones presented previously as the shortest range is 2.6 km instead of a few hundred meters. Anyway, the sound transmission pattern is similar, with the main presence of high-frequency energy in the interval 100-400 Hz corresponding to the modal interference pattern - and significant attenuation in low-frequencies.

The effect of the soft rock sea bottom is clear in Fig. 66 from 50 minutes with a strong increase in transmission loss in a broad frequency band as discussed previously. The attenuation from bottom loss (i.e. below around 80 Hz) is stronger than the attenuation from scattering loss in higher frequencies as predicted.

Set 2912 - also deployed to the east of the north run - gives similar interpretation of set 2909 and its results are catalogued in Appendix 23.

The global results of the north run data sets show clearly a reflective seabed for the south part of the run and the presence of a substantial rock outcrop in the north part. The seabed at the end of the run seems to be made of a reflective seabed, showing a seabed possibly alternating between sand and rock outcrops along the shore.

However, the actual geoacoustic properties of the sea bottom are not known from this analysis of the noise logger data sets and it requires using refraction seismic technique to obtain them. For instance, the depth of the different geological layers is an important parameter and might affect the sound field in the water column, depending on the frequency of the acoustic energy taken into account.

### 3.3.3 Refraction seismic technique and geoacoustic parameters

#### 3.3.3.1 External information regarding the geology of the area

Some rock outcrops - or exposed rocks - are known to be present along the 30-meter bathymetry line of the area, i.e. along the north runs. The geological knowledge on the region seems to suggest that the rock outcrops are likely to be made of friable, limonite-cemented sand, called "coffee rock" - shown in Fig. 67.

**Figure 67:** *Underwater picture of a coffee rock outcrop.*

The geoacoustic parameters of coffee rocks are not well-known but this formation is roughly similar to a soft rock as calcarenite with a shear speed slightly smaller than the water sound speed ($c_s$ < 1500 m/s). As discussed earlier, this feature has considerable effects on sound transmission within the ocean waveguide because of strong acoustic conversion into shear waves.

Besides, Fig. 67 gives an idea how rough such a rock outcrop is. Coffee rock presents small and large scale roughness and can be therefore considered as a high interface roughness seabed. Thus, in addition of bottom loss, such a seabed implies strong loss from scattering effect. A part of the acoustic energy in high frequencies is then distributed in the entire space generating according high transmission loss regions.

An interesting document is a screenshot from the radar of the seismic vessel - see Appendix 24. It zooms on a small part of the covered area - at the starts of both run - between the 25 and 30-m bathymetry lines. The shallowest regions in orange are likely to be exposed rocks, showing regular outcrops forming finger-like shapes from the shore with possible sand areas in between.

Geological surveys of the coast nearby the area points up the presence of arenite-mudrock (formation made of silt and clay) which is likely to have similar geoacoustic properties to coffee rock. Appendix 25 provides a map produced from Queensland's IRTM system.

Everywhere else within the area, the seabed characteristics are not quite known but sand seabed is believed to be dominant. In fact, external geological grabs have been made up north of the experimental area of the JIP 2010 trials (see Appendix 26), corroborating the important presence of sand. The data are from the MARine Sediment (MARS) database (Geoscience Australia). They only give information on the first meters of the seabed composition. As discussed earlier, the depth of the superficial sand layer is a crucial parameter regarding sound propagation and can be seen as isolating acoustically the deeper layers. Thus, the air-gun acoustic energy below 80 Hz penetrates deeply the earth and interacts with deep sub-bottom structures. On the other hand, higher frequencies are likely to only interact with superficial layers and the seabed interface - through scattering effect for example.

There was no external information regarding the deeper layers as the basement.

#### 3.3.3.2 Theory regarding refraction seismic

Refraction seismic is a technique to obtain geoacoustic properties of geological layers. Before using the method and detailing the steps followed to process the noise logger data to this end, some theory is required to explain the physical aspects and the limitations of the technique.

As for reflection seismic, a seismic source (e.g. an air-gun array) is used to produce a powerful bottom-directed pulse in the low-frequencies. As said earlier, the lower the frequency in the power spectrum of the pulse, the better the bottom penetration.

Refraction seismic aims at measuring the time arrivals of the headwaves propagating at the interface between two geological layers. The theory about headwave has been already briefly discussed. Recall that the headwave is a refracted wave that occurs when the grazing angle equals the compressional wave critical angle of the lower layer. Strong headwaves arrivals occur only in presence of high-speed elastic media - due to the sharp spike in their reflection coefficient at the critical angle for P-waves.

Indeed, at this particular low grazing angle - which corresponds to low frequency energy - there is reinforcement between the in-water modes and the headwaves. Headwaves propagate at the compressional speed of the lower layer, which is usually much greater than the sound speed in the water column.

To summarize, the headwave arrivals can only be resolved in geological layer having a compressional sound speed much greater than the water sound speed (i.e. $c_P >> 1500$ m/s). Such a structure is called a high-speed-marker layer by Dobrin (1960). Headwaves do propagate in slow-speed materials but with high attenuation and give late arrivals compared with waterborne energy.

After propagating along the interface, the energy from a headwave is re-radiated back into the water along the propagation path, at a given distance from the source. The received signal is then recorded using either a receiver deployed on the seabed or a far hydrophone array. The noise loggers deployed on the seabed during the JIP project are suitable receivers for refraction seismic. Their fixed positions provide headwave arrivals - likely to be unusable - at small ranges (R < 1 km), i.e. when the seismic vessel is too close.

Fig. 68 below illustrates a typical deployment showing the propagation of headwaves. The direct propagation on the scheme represents the waterborne arrivals (i.e. the propagating modes) which undergo in the reality successive sea surface and bottom reflections. Recall that the propagating in-water modes are slightly slower than the water sound speed of a horizontal plane wave. Only the propagation of headwaves is represented into the bottom in Fig. 68 (i.e. compressional and shear wave propagations are missing).

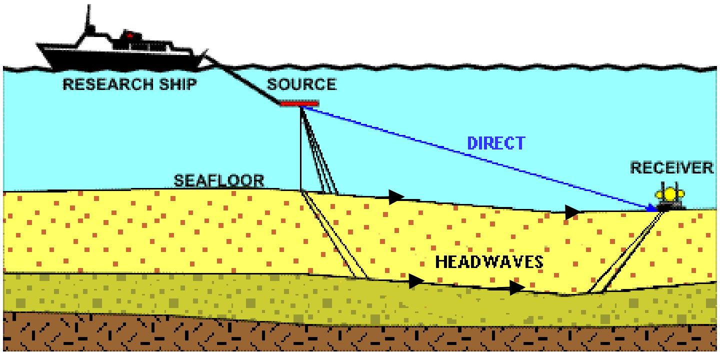

**Figure 68:** *Simplified refraction seismic deployment.*

For an appropriate elastic layer, the early-arriving headwaves can be processed and separated efficiently from the waterborne arrivals. In addition of their different time arrivals, headwave peak energy is in very low frequencies (VLF), usually below 20 Hz since this is the energy passed in the seabed. A band-pass filter is usually applied to the hydrophone data to extract the headwaves. Fig. 69 gives an example of spectral energy partitioning between ground and waterborne paths. It shows an overlap of energy between the two paths but the low-frequency waterborne energy is much slower and that avoids any confusion.

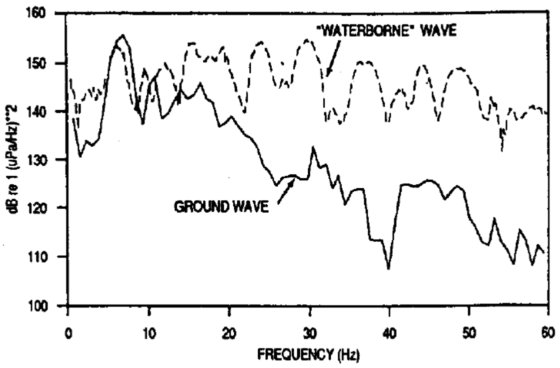

**Figure 69:** *Example of spectral energy partitioning between ground and waterborne paths (Hassan, 1993).*

To understand the propagation of the headwave, Fig. 70 gives a computed time evolution of the sound field as a sequence of snapshots from 20 ms to 120 ms. Two fluid halfspaces with compressional speeds $V_1$ and $V_2$ are considered with $V_1 = 1500$ m/s $< V_2 = 2500$ m/s - assuming no shear wave propagation. A pulse source is modelled at (0,0) in the upper layer. The condition of having a lower layer with a greater P-wave sound speed is a necessary condition for using refraction seismic. An example of the error incurred by velocity inversion is given when dealing with the limitations.

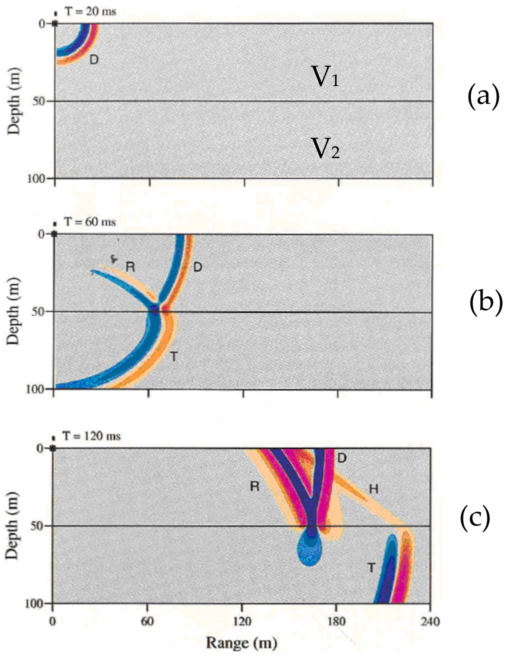

**Figure 70:** *Snapshots of the pulse at 20, 60 and 120 ms showing the spatial positions of the direct wave (D), the reflected wave (R), the transmitted wave (T) and the headwave (H) (Jensen, 1993).*

In the initial frame, Fig. 70(a), only a spherical wave is seen since the pulse has not yet contacted the interface. In Fig. 70(b), the pulse has interacted with the lower medium, and both a reflected (R) and a transmitted wave (T) are clearly visible. Since the P-wave sound speed is higher in the second layer, the pulse is longer in the bottom than in the top. In Fig. 70(c), the P-wave in the lower medium has pulled ahead of the direct wave due to its greater P-wave speed. Note that the scale was changed in order to highlight the weak headwave arrival. The wave front of the headwave (H) is clearly visible forming a line segment starting from the transmitted wave (T) and touching tangentially the reflected wave front in the upper medium.

The snapshot in Fig 70(c) shows therefore that the headwave is a first arrival at the interface and is not noticeable at the top of the upper layer. In the reality, this is a good reason to place the receiver on the seabed. Nevertheless, its amplitude is weaker at the interface.

Dobrin (1960) provides a method to analyse receiver data using refraction seismic (land and marine applications) in his book *Introduction to geophysical prospecting*. A general case of marine application is considered here, using a single air-gun as seismic source and noise loggers deployed on the seabed as receivers. Although it is a rough analysis of the subsea geological layers, the results are likely to define the characteristics of surface layers which are significant in shallow water sound propagation [9]. The outcomes of the method are seismograms or seismic time-distance curves.

At first, for a given air-gun survey, received signals at regular ranges R - e.g. every 100 or 200 m - were extracted. As explained earlier, the air-gun shots were located and extracted from the noise loggers during post-processing in Matlab. A series of received shot waveforms at each range R was then stored, using the same time base. The signals with a low signal-to-noise ratio - i.e. with confounding whale noise in the JIP data - were not usable.

The second step consisted in high-pass filtering each signal with a typical passband frequency of 100Hz, in order to define the waterborne arrival. The time corresponding to the leading edge of the spike on each waterborne arrival was taken as a reference time. At a given range R, this time can be approximated as the travel time of a direct wave propagating in the water medium, using the measured mean sound speed $c_w$ within the water column:

$$T_{travel} = \frac{R}{c_w} \approx T_{waterborne} \tag{27}$$

The relation (27) is not true as discussed earlier given that the speeds of the propagating modes are lower than the water sound speed and frequency-dependent. However, it is a way of defining a reference point between each signal in order to compare them on the same time base. The mean sound speed was required to be accurately measured and calculated.

The third step is to band-pass filter (or low-pass filter) each initial received signal in the low frequencies, e.g. up to 20Hz. This is to highlight the frequency band for which the headwave arrivals are the strongest. The time base of these band-pass filtered signals are adjusted using the zero time point of the waterborne arrival $T_{waterborne}$ and the calculated travel time $T_{travel}$. Fig. 71 below summarizes the three steps through an example, i.e. the initial air-gun waveform (a), the waterborne arrival (b) and the band-pass filtered signal in the VLF (c).

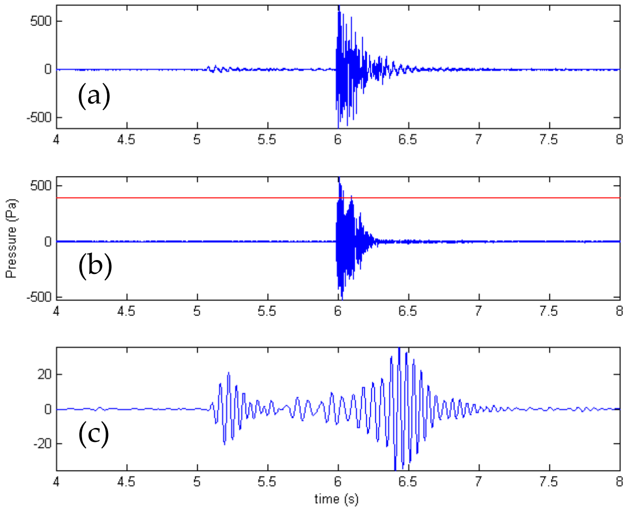

**Figure 71:** *Example of a received shot at 2.56 km. Initial waveform (a), high-pass filtered signal (> 100 Hz) (b) and band-pass filtered signal (7-18 Hz) (c). The zero time point defined in (b) is 6.0123 s, using a threshold and the leading edge of the spike.*

Fig. 71(a) and Fig. 71(b) are very similar which illustrate well the fact that acoustic energy in the ocean waveguide is dominated by the trapped "low loss" in-water modes. Fig. 71(c) points up a headwave arrival just after 5 s. The slower wave arrivals are not of interest in the method for determining seabed parameters and are likely to be late low-frequency waterborne arrivals. Other slow arrivals such as Scholte waves or shear headwaves may be discerned. The theory on these waves is detailed in section 2.3.4.1. Note that shear headwaves are discerned only in very fast elastic formations and, for the most part, the headwaves are produced by faster travelling P-waves [9].

The seismograms are then obtained by presenting the band-pass filtered signals as vertically stacked signals aligned by travel time with range. To visualize the waterborne arrivals on the seismogram, the calculated travel times versus range is plotted. Fig. 72 gives an example of seismogram. The blue line represents the waterborne arrivals. Then, by selecting the leading edge of consistent groups of headwave arrivals, information of the P-wave sound speed and boundary depth can be interpreted.

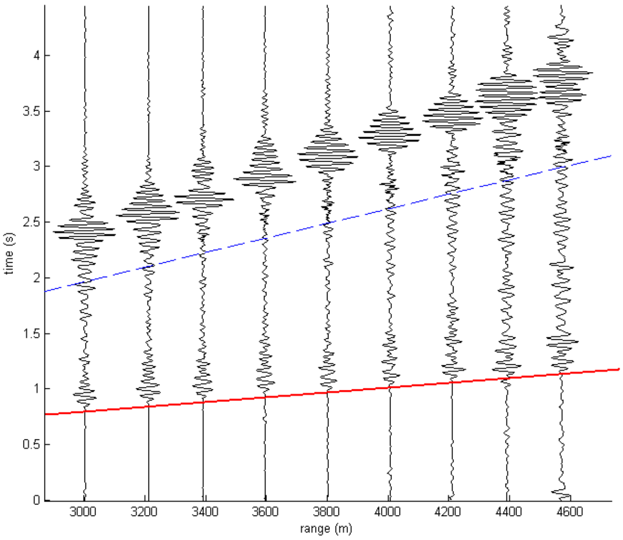

**Figure 72:** *Example of a seismogram for 9 received signals from 3 km to 4.6 km (JIP data). The blue line gives the waterborne arrivals and the red line is fitted to a set of discerned headwaves.*

In Fig. 72, there is only one clear group of consistent headwaves, fitted with the red line. There is thus only one detected boundary between two formations along which the discerned headwaves propagate. That does not mean that this is the actual first geological boundary as upper boundaries might not support headwaves or might provide late-arriving headwaves. This is discussed when dealing with the limitations of the technique.

Dobrin (1960) provide the mathematical material to define the geoacoustic parameters. The P-wave sound speed of the lower layer is defined as the inverse of the fitted curve slope.

$$V_{\text{lower layer}} = \frac{1}{\text{curve slope}} \tag{28}$$

An idealized three-layer case is considered with respective P-wave velocities $V_0$, $V_1$ and $V_2$ (with $V_2 > V_1 > V_0$) as shown in Fig. 73. It is assumed that all boundaries are detected and that each layer is homogenous and has a constant depth. $V_0$ is always taken as the mean water sound speed (noted $c_w$ earlier and known from the measurements).

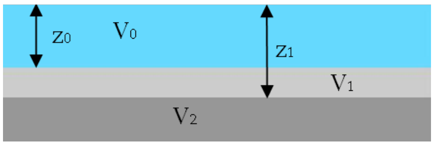

**Figure 73:** *Idealized 3-layer case.*

The depth below sea surface $z_0$ for the first layer of the sea bottom is a function of $V_0$, $V_1$ and the range $x_c$ at the intersection of the waterborne arrivals line and the fitted line of the first set of headwaves.

$$z_0 = \frac{1}{2} \cdot \sqrt{\frac{V_1 - V_0}{V_1 + V_0}} x_c \tag{29}$$

The depth below sea surface $z_1$ for the second formation is a function of $V_0$, $V_1$, V2 and the intercept time $T_{i2}$ of the second fitted curve, i.e. the y-intercept of the headwave curve.

$$z_1 = \frac{1}{2} \cdot \left( T_{i2} - 2 \cdot z_0 \cdot \frac{\sqrt{V_2{}^2 - V_0{}^2}}{V_2 V_0} \right) \cdot \frac{V_2 V_1}{\sqrt{V_2{}^2 - V_1{}^2}} \tag{30}$$

From this information of compressional sound speed and boundary depth, a probable layer composition can be determined by comparing the layer P-wave speeds with those from known materials. Any external knowledge on the geographical area as listed in the previous section can help to cross-check the information.

As mentioned earlier, refraction has some limitations. The main one being that slow-speed materials - as sediments or sand - found in the upper layers provide headwave arrivals which cannot be resolved.

A second major limitation if that the method is valid only where successively deeper layers have successively higher P-wave speeds [10]. Thus, according to Huygens ' Principle, if there is velocity inversion, the refraction in the lower layer takes place away from the interface instead of being re-radiated back into the water as noticeable in Fig. 70(c). Fig. 74(a) below shows a three-layer case with $V_1 > V_2 < V_3$. As explained, the headwave arrivals of the slow intermediate medium disappear at the point P, at the interface $V_1V_2$.

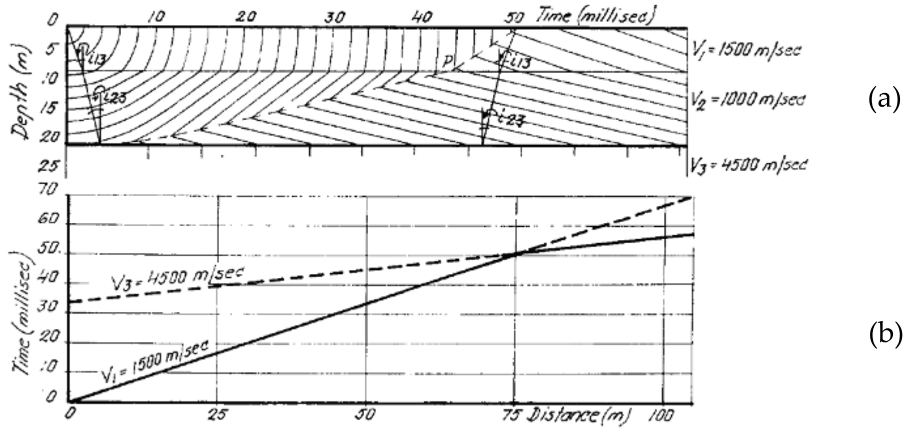

**Figure 74:** *Low speed layer after Huygens' Principle [11].*

Consequently, the headwaves do not reach the seabed and are not detected by the receiver. There is no segment of inverse slope $V_2$ on the analytical seismogram in Fig. 74(b) and this leads to an error in the computation of depths to all deeper interfaces

Another limitation is that the technique is not sensitive enough to detect thin geological layers - with the limitation being the length of the headwave pulse [9]. In the presence of a thin layer, the headwave arrivals may arrive later than the deeper layer having a greater P-wave speed.

To summarize, Dobrin (1960) explains that the refraction method is particularly valuable for reconnaissance in area where structure have a large relief and where there is at least one high-speed-marker bed overlain by lower speed formations.

As for any marine geological survey, the fact that real sea bottom formations do not consist of discrete homogeneous layers makes the analysis difficult. Thus, the fitted curves of headwave sets often do not consist in lines but in slightly curved segments, indicating dipping of subsea layers [10]. A special care has to be taken to plot meticulously the fitted curves. Significant variations in the results are noticed in function of the provided care to fit a straight line for each headwave set. The best is to cross-check the results from different measurements made in similar conditions.

### 3.3.3.3 Refraction seismic technique applied on the JIP 2010 trials data

As mentioned in the previous section, hydrophone data from the noise loggers deploying during the JIP experiments is well-suited for refraction seismic. The waveforms of each air-gun shot were extracted as explained in section 3.3.1.

The following steps were taken for a given air-gun and noise logger:

1. All received shot waveforms at regular ranges R - with no consistent whale vocalisation (see Fig. 75 for an example of unusable data) - were selected and stored. The range step was either 200 or 100 m, in function on the covered distance. The samples were centred on the maximum peak value (waterborne arrival) and 12-second length;
2. If the considered noise logger was deployed at a position which splits the air-gun run into approach and departure, the data was split accordingly;
3. Each signal was converted from V to Pa using calibration data;
4. Each signal was high-pass filtered (> 100 Hz) to define the waterborne path;
5. Using a threshold equals to two-third of the peak maximum pressure, the time of the leading edge of the spike on the waterborne signals was taken as a zero time point. This time was stored for each signal/range.
6. Each initial shot signal was band-pass filtered in the very low frequencies with a typical passband interval of [7-18 Hz] to highlight the headwave arrivals;
7. The time base of each band-pass filtered signal was adjusted to the previously defined zero time point;
8. The travel time $T_{travel}$ of a hypothetical direct wave propagating in the water medium was calculated for each range R - see relation (27). It required the mean measured sound speed within the water column defined previously as 1527.43 m/s;

9. The time base of the band-pass filtered signals were finally adjusted - in order to align them - by setting the travel time $T_{travel}$ to the waterborne arrival time defined earlier. Each new band-pass filtered sample was taken as 6-second length and stored.
10. Each band-pass filtered signal was normalised to itself and its amplitude adjusted to twice the range step used;
11. The band-pass filtered signals were presented as vertically stacked signals, giving rise to a seismogram;
12. If required, the signals at short ranges were amplified before the waterborne arrival to highlight possible weak headwave arrivals - see Appendix 27 for an illustration;

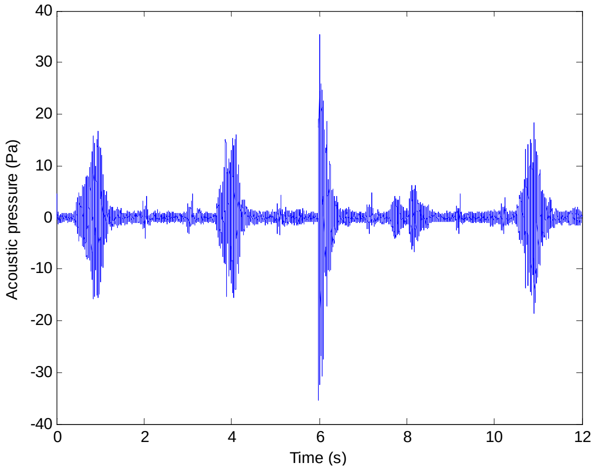

**Figure 75:** *Example of shot waveform with a low signal-to-noise ratio from run 2 and set 2900 (range is 4.9 km). The maximum peak value is centred at 6 s. The noise was whale vocalisations with pressure amplitudes up to 15 Pa.*

It should be emphasized that low-energy signals do not provide relevant data for refraction seismic. In this case, the different wave arrivals cannot be resolved and the analysis is biased. As mentioned earlier, some noise logger data had a low signal-to-noise ratio for three main possible reasons, i.e. a too-long range, an abnormal ambient noise or a low gain set within the considered noise logger.

In this way, data from distant noise loggers are likely to give unusable data and the best signals are given by loggers deployed along each run type (either east or north).

The data for the east runs can be first analysed. The seismogram given in the next page in Fig. 76 is from set 2938 and run AG13. The signals were band pass filtered in the interval [7-18 Hz]. The sound spectrum and transmission loss levels for this data set indicates a high-intensity line around 13-14 Hz. As explained earlier, this low transmission band is closely related to the headwave propagation as it corresponds to energy reflected as well as re-radiated at the P-wave critical angle of a bottom layer. There is then reinforcement between the in-water modes and the headwave propagation at this particular angle. The headwaves visible in the seismogram are then likely to travel at the interface of this specific layer.

Only one set of headwave arrivals is discernible in the seismogram in Fig. 76, denoted by the dashed red line. The dotted blue line indicates the main waterborne arrivals in each received signal. The waterborne arrival is not shown in the seismogram as it was band pass filtered in low frequencies. However, low-frequency waterborne energy is visible in the seismogram which is much slower than the main waterborne energy and corresponds to the airy phase of the propagating modes (see Fig. 19). The confusion of this late-arriving wave with the Scholte wave is possible as the Scholte waves have low-frequency energy and propagate at a speed slightly slower than the shear speed of the layer considered. Recall that Scholte wave is a boundary wave which exists only in the presence of a shear speed contrast and a lower elastic layer with a substantial shear speed. Investigations were made in applying band-pass filter in higher frequency bands and these late arriving waves were identified as waterborne energy.

An important value in the seismogram is the distance $x_c$ at the intersection of the waterborne arrivals line and the fitted line of the set of headwaves. In this case, $x_c$ is around 528 m and it assesses directly the depth of the layer. The compressional sound speed given by the slope inverse of the fitted line is around 4545 m/s. The calculation according to equation (28) of the depth of the interface $z_0$ below sea surface gives 186 m.

Fig. 77 gives another seismogram for the same run (AG13) but with a different receiver (set 2937). It is interesting then to compare the influence of the receiver position. In this second seismogram, only one set of headwave arrivals is discernible, given rise to similar results of geo-acoustic parameters.

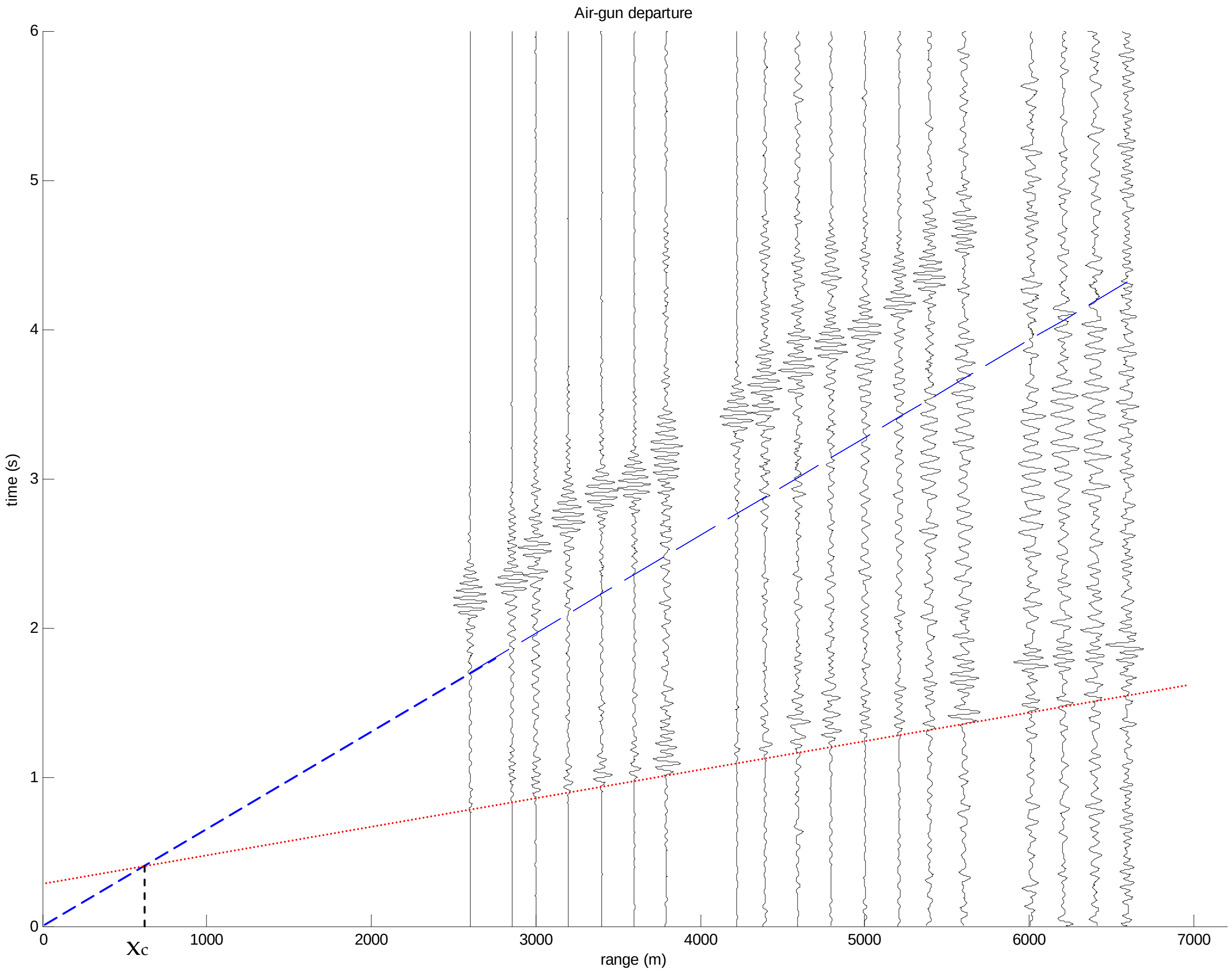

**Figure 76:** *Seismogram for set 2938 and run AG13. Band-pass filtered in [7-18 Hz]. The blue line is the waterborne arrival and the red line fits the first set of headwaves.*

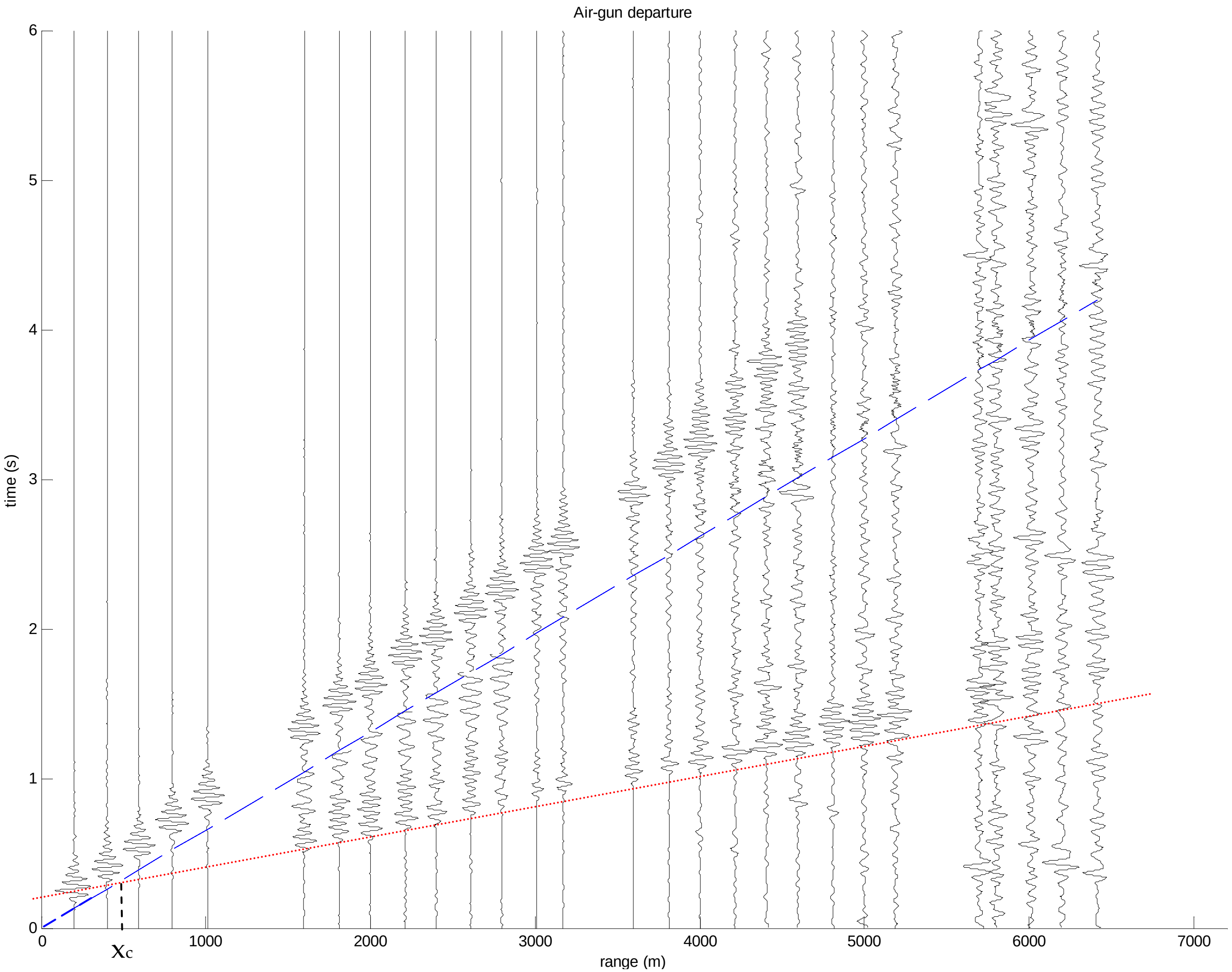

**Figure 77:** *Seismogram from refraction seismic for set 2937 and run AG13 (departure). Signals band-pass filtered in [7-18 Hz]. Weak headwaves highlighted from 1.6 to 2.8 km.*

Note that the same x-axis limits were used for every seismogram generated in order to compare the data between the data sets.

The headwaves signals were highlighted in Fig. 77 from range 1.6 to 2.8 km. This second seismogram gives a compressional sound speed of around 4490 m/s and a depth below sea surface of 175.4 m. Recall that the precision of the graphical solution is not accurate and it was required to compare many seismograms from similar data sets. In this case, the calculated parameters are very similar in the two data sets.

In both seismograms and other east run seismograms which were analysed, only one consistent set of headwave arrival was discernible. Some other features are interesting to point up as the disappearing of the late-arriving waterborne waves at sufficiently long distance. This is natural due to the substantial attenuation of low-frequencies in the waveguide. Of a particular note is also the sudden disappearing of the headwave signals at long distance showing manifestly their great attenuation when re-radiating towards the water column. This shows clearly the important presence of fluid materials in the area as sediments or sand with strong acoustic attenuation.

The table in Fig. 78 gives the results for some relevant data sets of the east runs.

| | Compressional sound speed (m/s) | depth below sea surface (m) |
|---|---:|---:|
| set 2938 run 13 (departure) | 4545 | 186.1 |
| set 2937 run 13 (departure) | 4490 | 175.4 |
| set 2909 run 7 (approach) | 4894 | 185.4 |
| set 2911 run 13 (approach) | 4964 | 189.2 |
| set 2909 run 5 (departure) | 5054 | 212.3 |

**Figure 78:** *Table gathering geo-acoustic parameters from the consistent discernible set of headwaves for some seismograms of the east run data sets.*

From the table, an average measured sound speed of the detected layer can be assessed around 4800 m/s and a depth below sea surface about 180-190 m.

Given that the water depth for the east runs was approximately from 25 to 35 m, the layer seems to be around 150-160 m below seabed. This is a therefore a deep layer which can be considered as the basement (or bedrock) of the area, i.e. a hard rock with a great compressional sound speed as basalt. The geo-acoustic properties of basalt give a compressional sound speed of 5250 m/s (Jensen, 1993) which is close to the empirical results in Fig. 78. Such material has a density around 2700 kg/m$_3$, a shear speed of 2500 m/s, a compressional wave attenuation of 0.1 and a shear wave attenuation of 0.2. For extended analysis, Appendix 28 presents the seismograms from other data sets of the east runs.

In the same manner, the next pages give seismograms from the north run data. Respectively, run AG11 and receiver 2937 (air-gun departure) in Fig.79 and run AG08 and receiver 2908 in Fig. 80 and 81 (air-gun approach and departure).

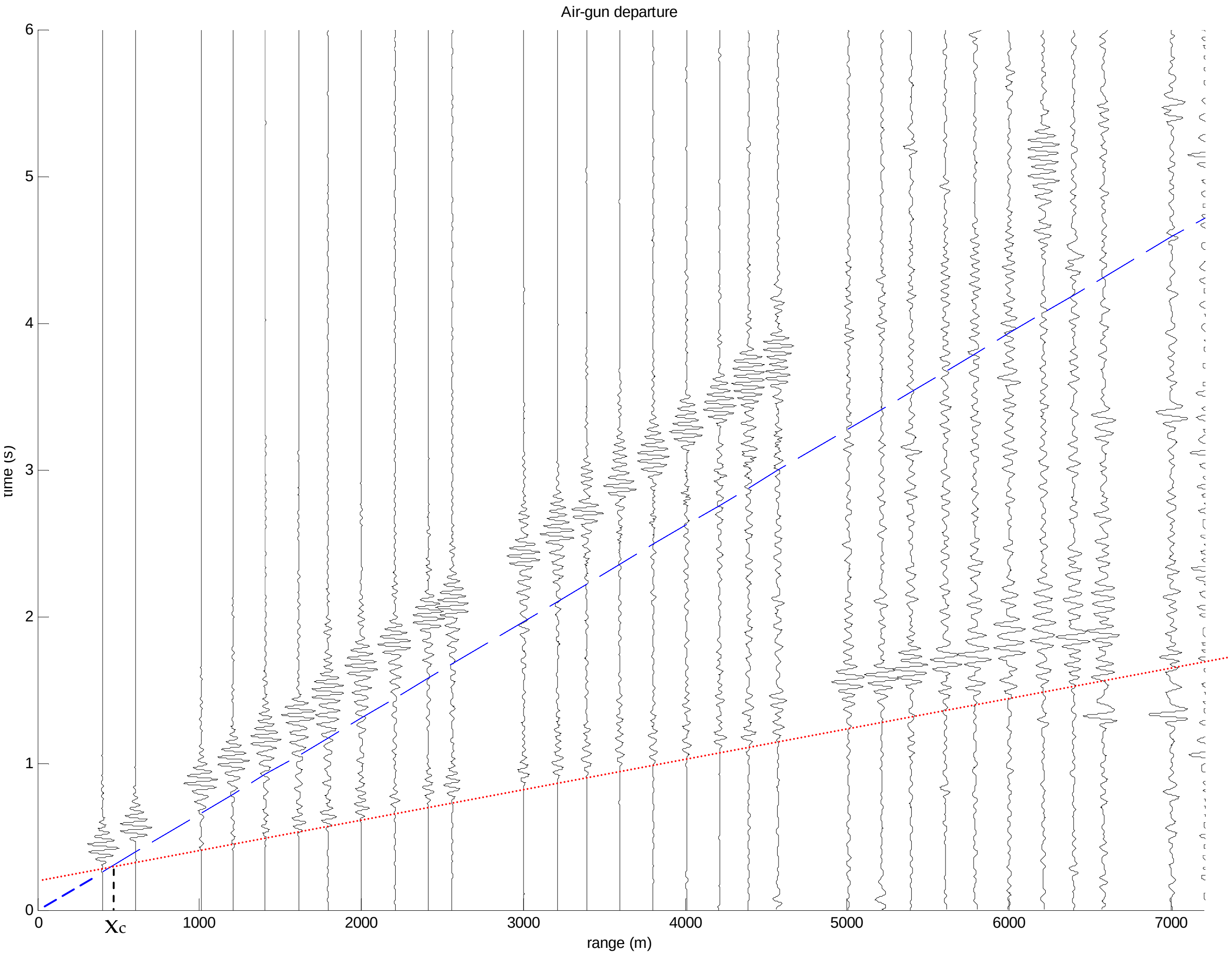

**Figure 79:** *Seismogram from refraction seismic for set 2937 and north run AG11 (air-gun departure). Signals band-pass filtered in [7-18 Hz].*

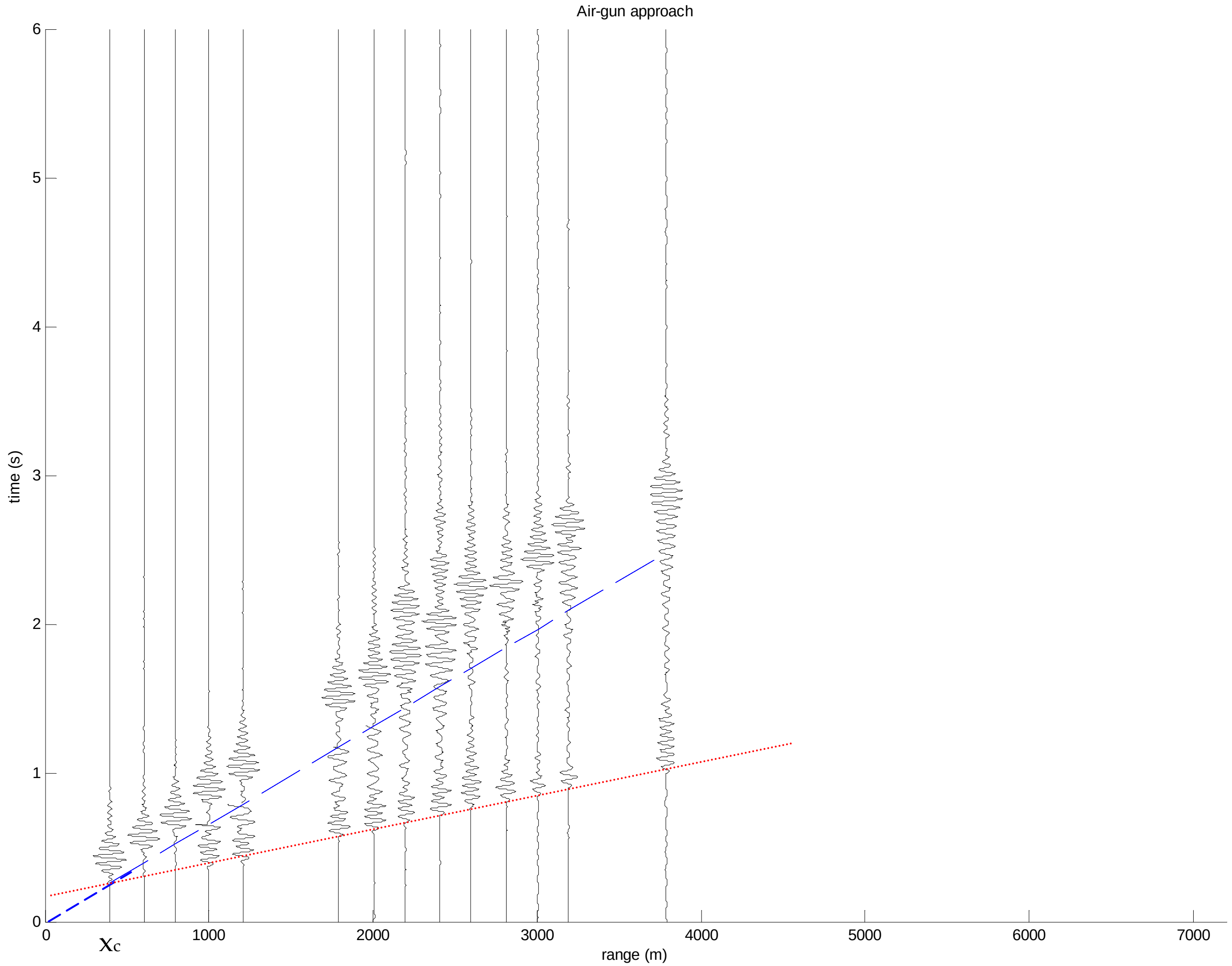

**Figure 80:** *Seismogram from refraction seismic for set 2908 and north run AG08 (air-gun approach.) Weak headwaves highlighted from 1 to 2 km.*

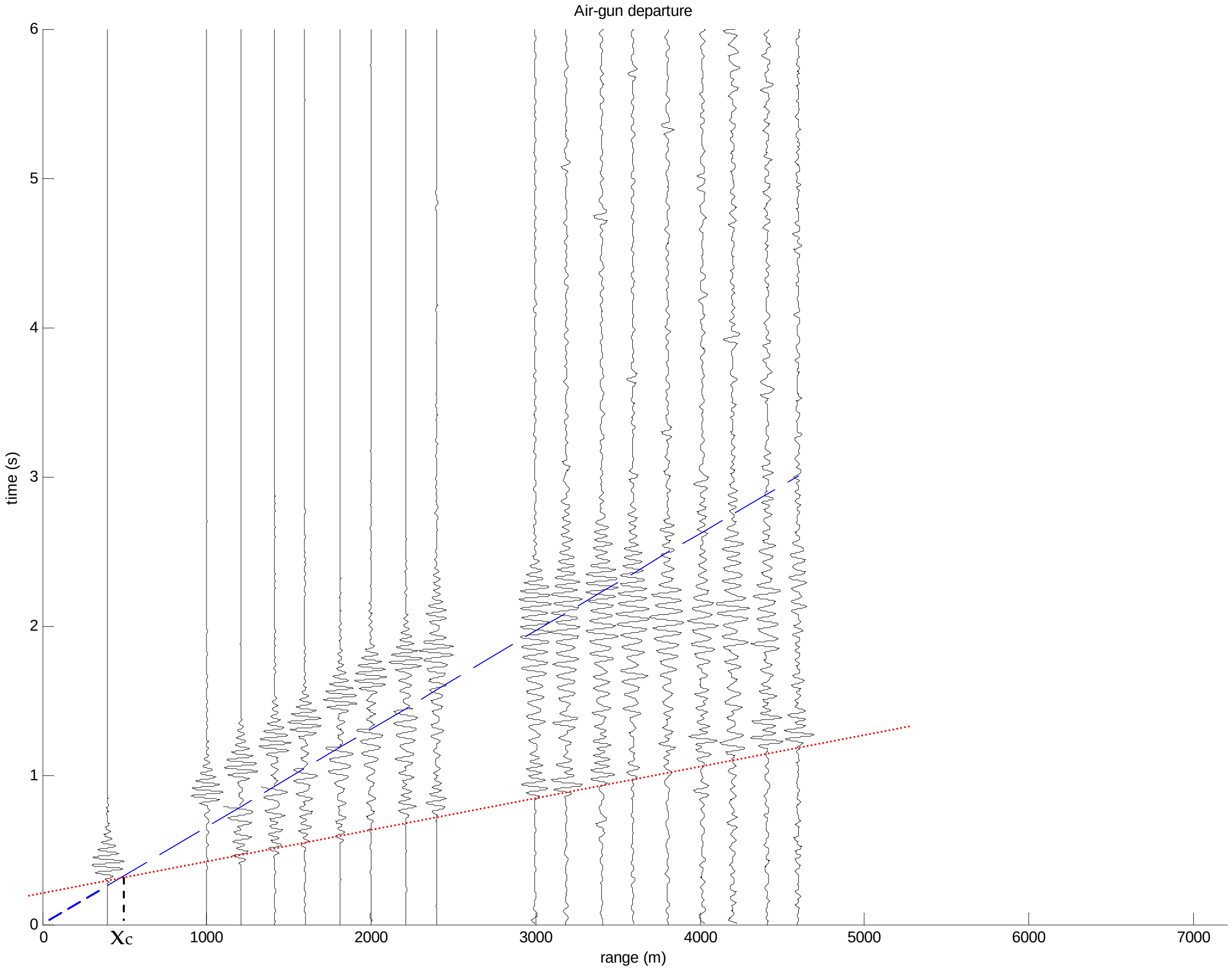

**Figure 81:** *Seismogram from refraction seismic for set 2908 and north run AG08 (air-gun departure.). Weak headwaves highlighted from 1.2 to 2.2 km.*

The first main observation is that there is also only one consistent and discernible set of headwave arrivals for the north runs. The slope of the fitted lines and the values of $x_c$ may imply that it is the same result from the east run data, i.e. the detection of the deep basement. However, the values of the depth below sea surface of the layer are slightly lower for the north run seismograms. The basement could be then 10-20 m shallower in the region along the north runs but the precision of the technique does not allow such conclusions.

In fact, in most cases, the fitted line is slightly curved and it is a tough task to obtain consistent results. More particularly, the technique of highlighting the short-range headwave arrivals (< 2 km) lead to some confusion as it lowers clearly the $x_c$ value and it results in a shallower calculated depth of the detected layer. The curves were then more fitted according to the consistent long-range headwaves. Some smooth transitions occurred at a given distance but the headwaves arrivals are too fuzzy to conclude that there a second headwaves arrivals from deeper layers.

The seismogram in Fig.81 (air-gun departure of run AG08 and receiver 2908) is relevant as it shows a clear transition in the received signals from 3 km. This transition corresponds to the substantial rock outcrop visible in the previous section through the sound exposure levels and sound spectrum levels results. Thus, waterborne waves almost disappear when the source is over rock which is related to strong attenuation of the sound field in the water column. The re-radiated headwaves are still visible in the rock outcrop region as they come from the deep basement. From this transition, it is clear that the basement in the southern and central parts of the north track consisted of a more consolidated sediment (e.g. high density limestone) with the shear wave speed larger than that in water. On the other hand, the rock outcrop in the northern part was softer, so that the shear wave speed was smaller than that in water and therefore the sound attenuation was much higher - as explained before.

In addition, Fig. 81 points out a sudden wave arrival at this transition which propagates faster than the waterborne ones (i.e. > 1527 m/s) but slower than the headwaves in the basement. Its physical meaning is not obvious and only accurate modelling would allow a proper investigation.

The table in Fig. 82 below gives detail on the geo-acoustic parameters of some north run seismograms.

| | Compressional sound speed (m/s) | depth below sea surface (m) |
|---|---:|---:|
| set 2937 run 11 (departure) | 4380 | 151.8 |
| set 2937 run 12 (departure) | 4639 | 187.2 |
| set 2908 run 4 (approach) | 4494 | 147.2 |
| set 2908 run 4 (departure) | 4602 | 154.4 |
| set 2908 run 8 (approach) | 4166 | 141.5 |
| set 2908 run 8 (departure) | 4763 | 179.3 |
| set 2912run 11 (approach) | 5227 | 205.9 |

| | | |
|---|---|---|
| set 2912run 11 (departure) | 4947 | 107.3 |
| set 2938 run 11 (approach) | 4273 | 129.8 |
| set 2938 run 11 (departure) | 4343 | 141.3 |

**Figure 82:** *Table gathering geo-acoustic parameters from the consistent discernible set of headwaves for some seismograms of the north run data sets.*

The average compressional wave speed is then around 4600 m/s and the average depth below sea surface around 150-160 m. The basement would be then at 120-130 m below seabed in the north run area. These results are globally similar to the east run seismograms and denote only the presence of the deep high-speed basement. For extended analysis, Appendix 29 gives more results of north run seismograms.

The refraction seismic method applied to the JIP data did not allow then to provide geo-acoustic information on the shallower geological layers above 100 m below seabed. This is clearly an issue to understand the sound transmission in the water column as the superficial layers are of more importance here. Indeed, the basement only affects low-frequency acoustic below 20 Hz and the main frequency band of the propagated waterborne energy from air-gun noise is around 100-400 Hz at range above 1 km.

The non-detection of the layer above 100 m below seabed may result from different causes. First, the first layers usually made of sand and sediments do not provide headwave arrivals which are discernible in the seismograms. Secondly, the next layers which may be made of rocks can be too thin to be detected by refraction seismic. It is then possible that the first 100 meters of the sea bottom is made of many different materials having small contrasts in densities of geo-acoustic properties.

From this poor information, the numerical models will be hardly close to the real geo-acoustic environment of the JIP area. On the other hand, different tests of geo-acoustic models can be carried out to obtain similar results of received levels and transmission loss levels with the empirical results.

### 3.3.4 Results of received air-gun levels at followed whales

This method of defining received air-gun levels at distant whales was simply carry out using the sound exposure levels results previously presented. There are many ways of carrying out this empirical approach and only one is presented here. The main idea is to use the measured data sets of the noise loggers to reconstruct the received signal levels at the whale during the considered survey.

Recall that the empirical receivers were deployed at fixed locations and that studying the received levels at the whales implies a moving air-gun and a moving receiver.

During each day on task, whale observations were made and a shore based system allowed to record tracks of single whales or pods. The whale tracks of interest are therefore the ones which overlap the times of the 1-hour air-gun runs.

Only one relevant and discernible whale track is analysed in this paper but the technique can be applied to other situations of source-receiver geometries. A whale track recorded on the 17th October was chosen showing a whale movement heading south meanwhile the air-gun was operated north following the north run pattern (run AG12). On this day, the four noise loggers deployed were set 2911, 2912, 2938 and 2937. Eleven whale positions were recording using the Easting and Northing coordinates (E and N). The whale passed nearby the run track and only set 2937 and 2938 deployed along the north track are interesting to reconstruct the received air-gun levels at the whale. Sets 2911 and 2912 deployed further to the east may imply a too big difference in sound propagation path with possible change in sea bottom properties and slight bottom slope. Set 2937 is considered first.

Fig.83 shows the relevant portion of the whale track in cyan as well as the locations of each shot recorded by set 2937 and the position of the set.

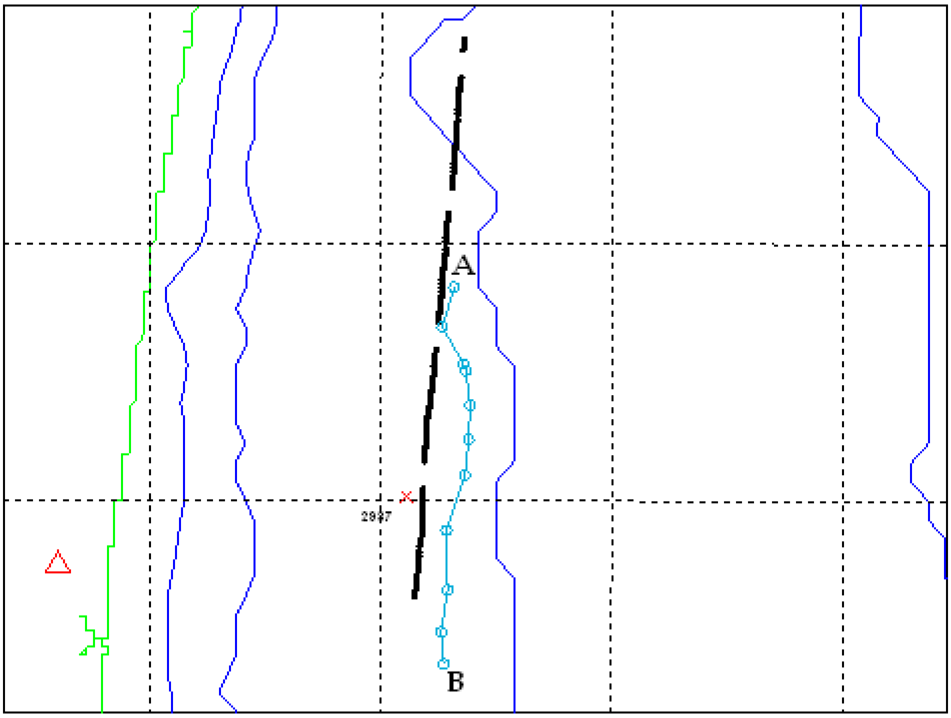

**Figure 83:** *The black points forming an interrupted line denote the locations of each received shot at receiver 2937. The red cross indicates the fixed position of set 2937. The cyan line is the considered whale track built from 11 whale coordinates. The red triangle denotes the uphill location on the coast from where whale observations were made.*

As explained earlier, the gaps in the run track come from the 3-minutes breaks meant to store data within the noise logger. Thus, a total of 315 shots were emitted during run AG12 according to the near-field hydrophone data but only 268 shots were recorded by set 2937. Notice that the ambient noise was sufficiently low in the noise logger data considered (set 2937 and 2938) to obtain high signal-to-noise ratio shot waveforms. Each gap in the data missed between 11 and 15 shots given that the repetition rate was around 11.5 s.

For more precisions, the whale track started at position A at 13:30:29 and finished at point B at 14:28:18. The first recorded air-gun by set 2937 was at 13:30:13 and the last one at 14:30:37. Thus, 259 shots over the 268 recorded shots at set 2937 data overlap precisely the logged whale track.

Moreover - as the idea is to extrapolate the whale position at each fired shot -, it is then required defining 259 whale positions corresponding to the 259 received shots at set 2937. For that, an extrapolation of the position data was carried out using a Matlab code and based on the time of each recorded whale position. The extrapolation was made using the actual number of shots received at the whale during this portion of track (i.e. 295 shots in this case) and some positions were deleted afterwards - to obtain the same gaps than in the noise logger data. Fig. 84 shows the extrapolated whale track (259 positions). The positions of the received shots at set 2937 are shown again in the figure. Only the shot positions in blue overlap precisely the time of the considered whale track.

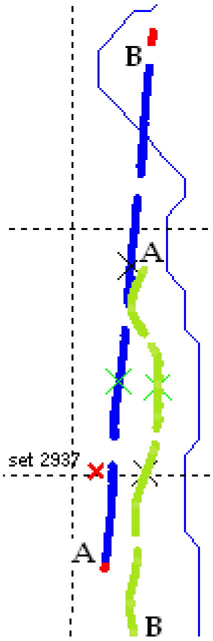

**Figure 84:** *Precise source-receiver geometry of the considered data and time. The points A and B on the track of run AG12 denote the first and last positions of the received shots at the followed whale. As previously, the points A and B on the whale track denote its first and last positions. The shot positions in red are not of interest.*

Thus, it is easily visible in Fig. 84 that there are 4 considered blocks of received shots, either for set 2937 or the whale. The distance between both cyan crosses on each track represent the smallest distance airgun-whale. The black crosses represent an almost exact match of source-receiver distance between set 2937 and the whale (distance around 3 km). The airgun-whale distances were calculated using the northing and easting coordinates as in relation (31).

$$Range = \sqrt{(E(airgun) - E(whale))^2 + (N(airgun) - N(whale))^2} \quad (31)$$

Where E(airgun) and E(whale) indicate the easting coordinates of respectively the air-gun and the whale; and N(airgun) and N(whale) the corresponding northing coordinates.

The two ranges of source-receiver can then be plotted vs. time as Fig. 85 shows it.

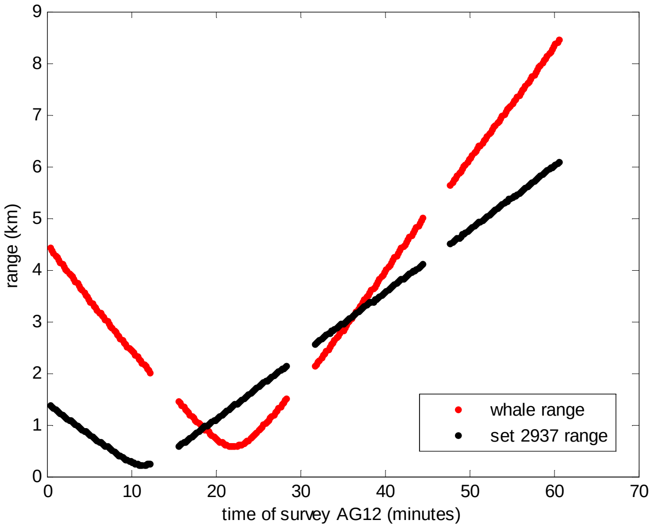

**Figure 85:** *Curves of the ranges (km) vs. time (minutes) for run AG12 and the two considered receivers: whale and set 2937.*

The air-gun approach of the whale occurred then up to 22 minutes with a minimum range of 586 m, with an initial range of 4.43 km. The air-gun departure of the whale corresponds therefore to increasing range up to 8.46 km when the whale was located the furthest in the south. The air-gun approach of set 2937 occurred up to 11 minutes with a minimum range of 231 m. Most of run AG12 was an air-gun departure for set 2937 with a maximum range at 6.1 km.

The result analysis of the sound exposure and sound spectrum levels of the north run data in section 3.3.2.4 showed the presence of a soft rock outcrop in the northern part of the runs. The central part results showed typical decrease of SEL with range related to the Lloyd mirror effect (shallow air-gun) with a quite reflective seabed (e.g. sediments). The extreme south part showed a possible presence of localized rock outcrops with abnormal slightly lower levels at the start of the runs.

The assumption is made that the whale was swimming along a track which does not have sudden change in sea bottom geoacoustic properties. This assumption is fair as the portion of whale track is located in central and southern parts of the north runs where the seabed is likely to be sand everywhere. However, the assumption is not valid anymore for the last whale positions (range source-whale above 6 km) because of the possible presence of localized coffee rock seabeds.

In this manner, the results of SEL from set 2937 can be used to reconstruct the received levels at the followed whales but special care has to be taken to match properly both sound propagation paths. The ranges considered are notably of importance. Thus, the air-gun approach data of set 2937 going from 1.38 km to 231 m are unlikely to reflect the received levels for the whale air-gun approach going for much greater ranges.

A first step is to fit the empirical SEL results with range with appropriate functions. Fig. 86 gives the corresponding curve for AG12 and set 2937 considering the 259 studied shots.

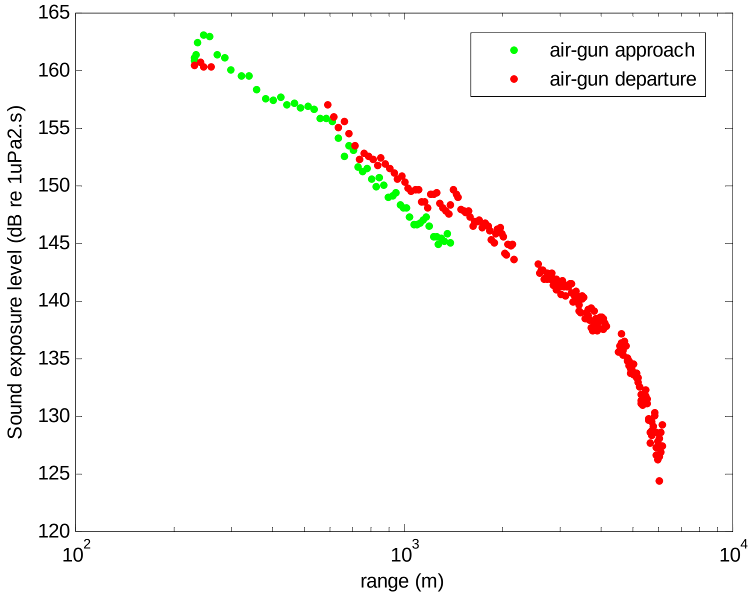

**Figure 86:** *Measured sound exposure levels (dB re 1µPa²$.s$) vs. range in m (log scale) for set 2937 and run AG12.*

The SEL curve for the air-gun departure in red in Fig. 86 can be considered having two distinct slopes, i.e. the typical slope from 580 m related to the Lloyd mirror effect and the drop off from 3.7 km due to the presence of the coffee rock outcrop. Recall that the great acoustic attenuation is due to scattering loss and acoustic conversion into shear waves. Fig. 87 gives the best fitted lines for the considering slopes, using for both a power-law distribution of the form a*x^b+c.

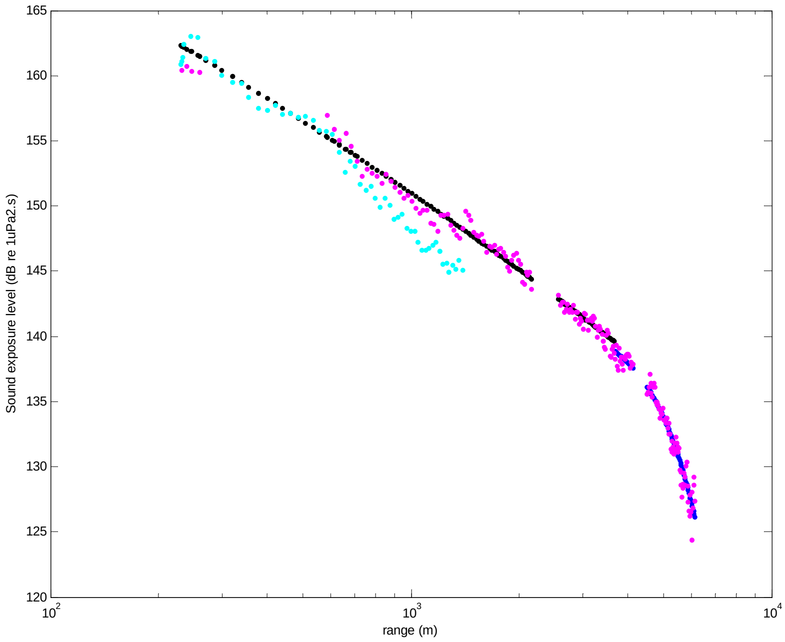

**Figure 87:** *Same plot than Fig. 86, i.e. sound exposure levels (dB re $1\mu Pa^2.s$) vs. range in m (log scale). The black line fits the first slope of the air-gun departure. The blue line fits the slope corresponding to sound attenuation from the northern rock outcrop.*

The whale air-gun approach data was reconstructed from another set of receiver, i.e. set 2938 (see appendix 5 for its position along the north runs). The same analysis as shown previously was therefore done for set 2938 and the same whale track (considering 255 received shots). The fitted line for the air-gun approach of this receiver was taken to reconstruct the levels at the whale of this localized region. Fig. 88 compares the variation of range between the whale and set 2938.

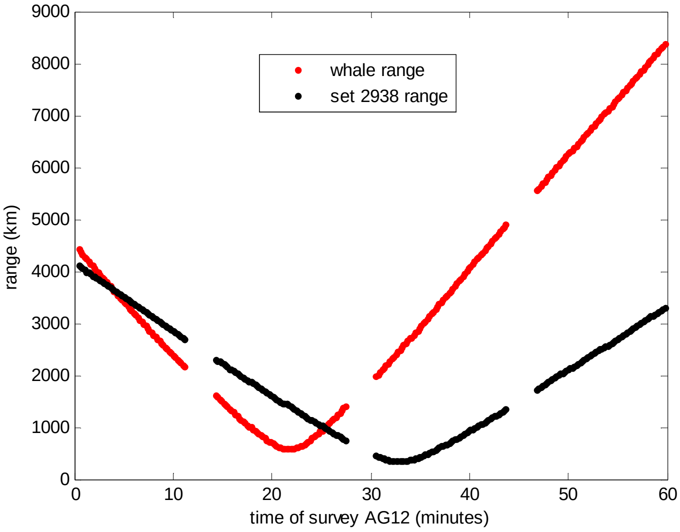

**Figure 88:** *Curves of the ranges (km) vs. time (minutes) for run AG12; and for the whale and set 2938.*

There is a good match in range in Fig. 88 between the two receivers for the air-gun approach (range from 4.5 km to 1 km) and the data of received levels of set 2938 are likely to well reflect the actual levels at the whale. Fig. 89 shows the corresponding SEL results vs. range with the best fitted curve for the air-gun approach (of the form p1*x + p2).

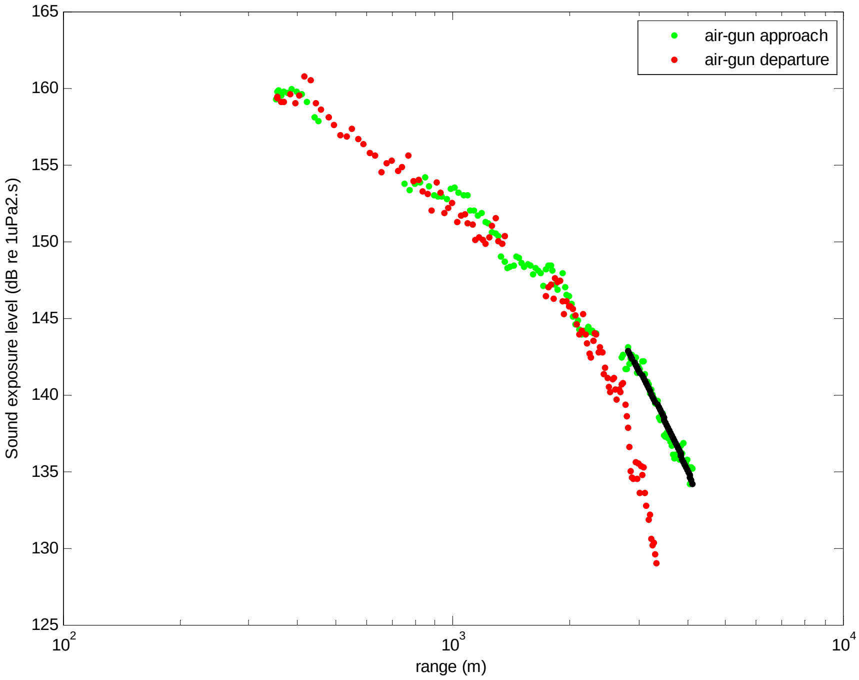

**Figure 89:** *Sound exposure levels (dB re 1μPa²).s) vs. range in m (log scale) for AG12 and set 2938. The black line fits the first slope of the air-gun approach.*

The results of the fitted line in Fig. 89 correspond to the localized area in the southern part of the north run with possible rock outcrops. The other SEL data in this figure are not of a use in the empirical approach for this specific whale track.

Finally, the SEL along the whale track can be reconstructed from these 4 functions of range corresponding to three regions along the north track.

$$SEL(4.43km \leq R \leq 3.23km) = -0.006582 \cdot \mathrm{R} + 162 \qquad (32)$$

$$SEL(3.23km < R \leq 0.586km) = -46.78 \cdot \mathrm{R}^{0.09295} + 239.9 \qquad (33)$$

$$SEL(0.586km > R \geq 4.15km) = -46.78 \cdot \mathrm{R}^{0.09295} + 239.9 \qquad (34)$$

$$SEL(4.15km > R \geq 6.1km) = -1.056^{-12} \cdot \mathrm{R}^{3.477} + 142.5 \qquad (35)$$

Equations (32) and (33) represent the whale air-gun approach and equations (34) and (35) the whale air-gun departure. Note that equation (33) and (34) are the same functions corresponding to the slope related to the Lloyd mirror effect with a sand seabed.

Fig. 90 exposes the result in SEL of the extrapolation of the received levels at the considered followed whales for both the air-gun approach and departure.

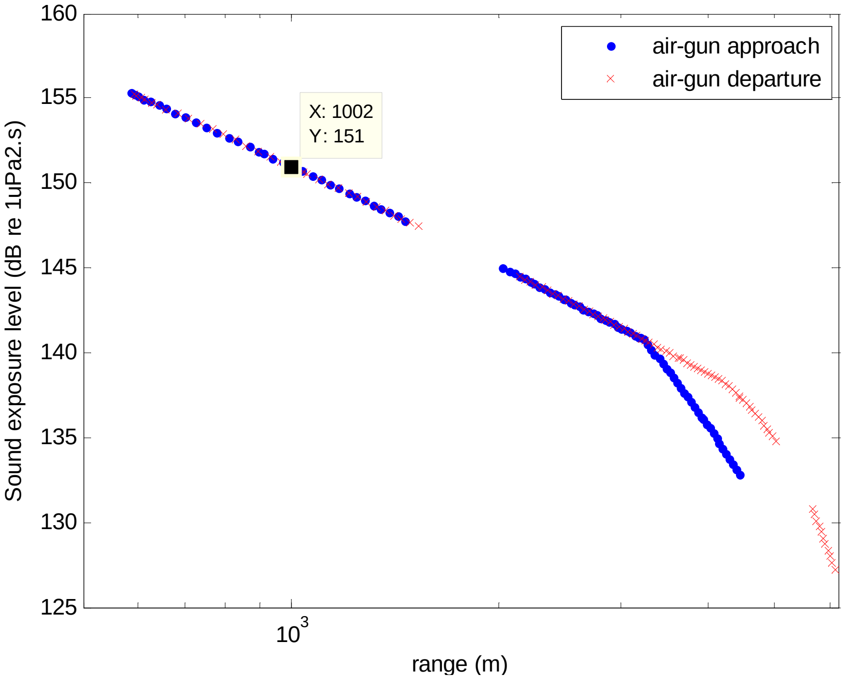

**Figure 90:** *Sound exposure levels (dB re 1µPa².s) vs. range in m (log scale) for AG12 and the considered whale. The results are reconstructed from the SEL at receiver 2937 and 2938.*

Note that the SEL at the whales were not reconstructed for ranges above 6.1 km due to the lack of knowledge from the measurements regarding sound propagation in the south, below the north run starting point.

The received SEL at the whale were assessed around 155.3 dB re 1µPa².s for the closest range (586 m), 151 dB re 1µPa².s at 1 km and down to 127 dB re 1µPa².s at 6.1 km.

The aim of assessing received levels at a followed whale was then carried out and the same task can be followed for other whale tracks passing nearby air-gun survey tracks and empirical receiver locations. This technique implies substantial simplification as assuming the followed whales at the seafloor (where the experimental receivers were) and consistent geoacoustic properties of the sea bottom along the whale track.

The next and final chapter of the paper introduces a numerical model of the simplified acoustic environment of the JIP 2010 trials - mainly in order to benchmark against the measured results.

# 4 Numerical approach

Modelling accurately air-gun transmission in the shallow waters of the JIP 2010 trials is not straightforward. It requires defining the inputs of the model which result from the measured data sets. There are mainly the air-gun signature (section 3.2.1), the mean sound speed profile in the water column (section 3.2.3) and the gained knowledge about the geo-acoustic properties of the sea bottom (section 3.3.2 and 3.3.3). The latter information is substantial and lead to define a so-called geoacoustic model. The first step was to choose properly a known numerical implementation. The idea is to cover the considered propagated air-gun acoustic energy - i.e. 10 - 800 Hz - in a 30-m ocean waveguide.

## 4.1 Choice of the model

Many numerical models of horizontal underwater acoustic propagation exist such as ray tracing models, normal mode models, parabolic equation models or wavenumber integration models. Each model has its own advantages and drawbacks and is often appropriate for a specific acoustic environment.

The analysis of each model limitations is important and allows making an appropriate choice. The wavenumber integration technique was chosen for the JIP project even if it requires substantial simplifications of the real environment. Porter (2007) provides a code called SCOOTER using wavenumber integration programs which was used to carry out calculations in this study. It can be briefly explained why the other models are likely to be less accurate than SCOOTER.

First, the normal mode theory based on Pekeris work (1948) breaks the acoustic wave vector into horizontal and vertical components as previously discussed in 2.2. These models treat the ocean as an acoustic waveguide as they require the vertical components to satisfy appropriate boundary conditions at the water surface and seabed [8]. They only work efficiently for low-frequency acoustics for which the water depth is a relatively small number of wavelengths deep. Moreover, they can only handle slow variations of depth and other acoustic properties with range.

Ray tracing models predict acoustic propagation by calculating the refraction and reflection along individual ray paths. These models are appropriate for frequencies sufficiently high that the ocean can be considered to be many wavelengths deep. For instance, in a 30-m waveguide at 100 Hz, the acoustic wavelength is about half the water depth and the approximation inherent in ray codes is definitely not valid.

Parabolic equations (PE) have now become the most popular wave-theory technique for solving range-dependent propagation problems in ocean acoustics [5]. These models make certain assumptions that allow the acoustic wave equation to be reduced to a parabolic equation form which can be efficiently solved numerically. Thus, the PE method is based on an approximation to the Helmholtz equation that is valid for sound propagating close to the horizontal (paraxial approximation). This results in a range marching algorithm in which the acoustic field at one range can be calculated from the field at a preceding range, resulting in an efficient algorithm that is easy to generalise to range dependent scenarios. Modern PE codes (e.g. RAM) use techniques that allow the paraxial approximation to be relaxed up to 80° - at the cost of very slow computations. The main problem related to PE codes is their instability for geoacoustic models with elastic materials. More particularly, there is no PE code to deal with seabed with thin, fluid-like layers over layers with reasonably high shear speed.

Finally, the wavenumber integration method is based on applying separation of variables to the Helmholtz Equation, resulting in a depth equation and a range equation - as seen in the next section. It is exact for range independent waveguides and can deal exactly with layered seabeds of arbitrary complexity, including both fluid and elastic layers. However, the main drawback is that it cannot be applied to range dependent situations.

The use of SCOOTER code (Porter 2007) combined with the FIELDS program - in order to obtain a sequence of snapshots of the acoustic field as a function of range and depth - lead then to the most accurate results in a 30-m ocean waveguide in the frequency interval 10-800 Hz. However, to the cost of not being able to model change in sea bottom acoustic properties with range as it occurred in the JIP 2010 area.

## 4.2 Wavenumber integration technique

This approach is applicable to range independent or horizontally stratified environments as shown in Fig. 91. All media are isotropic.

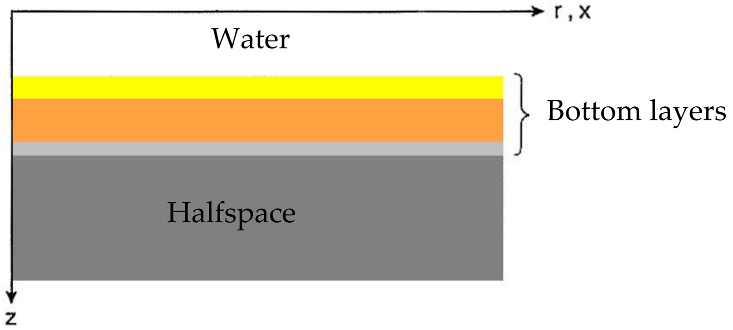

**Figure 91:** *Horizontally stratified environment.*

For a source distribution along a vertical axis in a horizontally stratified environment, a cylindrical coordinate system (r,φ,z) is introduced. The sound field is naturally independent of azimuthal angle φ.

Some mathematic materials are given in this section but they only aim at defining the basis of the wavenumber integration method. Therefore, some mathematical derivations as the Hankel transform or Green's theorem are used but not explained. For complete information, see Jensen et al, "Computational Ocean Acoustics" (1993).

For the isotropic media considered here, the acoustic field with time dependence $e^{-i\omega t}$ in layer m containing the source (i.e. the water column) can then be expresses in term of scalar displacement potential $\psi_m(r,z)$ which satisfy the Helmholtz equation [5].

$$[\nabla^2 + k_m^2(z)] \cdot \psi_m(r,z) = f_s(z,\omega) \cdot \frac{\delta(r)}{2\pi r} \tag{36}$$

Where $k_m(z)$ is the medium wavenumber for layer m, $f_s$ is the forcing term and δ is the so-called Kronecker delta.

The medium wavenumber for layer m is defined in the water column as:

$$k_m(z) = \frac{\omega}{c(z)} \tag{37}$$

If the layer m contains the source, then the forcing term $f_s$ is non-zero. In a case of an omni-directional point source, it has the form:

$$f_s(z,\omega) = S_\omega \delta(z - z_s) \tag{38}$$

Where $S_\omega$ is the source strength and $z_s$ the source depth.

Applying the forward Hankel transform to (36) leads to the depth-separated wave equation:

$$\left[\frac{d^2}{dz^2} - \left[k_r^2 - k_m^2(z)\right]\right] \cdot \psi_m(k_r,z) = \frac{f_s(z)}{2\pi} \tag{39}$$

Where kr is the horizontal wavenumber in layer m, defined as:

$$k_r = \sqrt{k_m^2 - k_z^2} \tag{40}$$

Equation (39) is an ordinary differential equation in depth. Thus, the solution is a sum of a particular solution $\hat{\psi}_m(k_r,z)$ and any linear combination of the two independent solutions $\psi_m^+(k_r,z)$ and $\psi_m^-(k_r,z)$ to the homogeneous equation. The total solution for the depth-dependence of the field, the so-called depth dependent Green's function if therefore:

$$\psi_m(k_r,z) = \hat{\psi}_m(k_r,z) + A_m^+(k_r)\cdot\psi_m^+(k_r,z) + A_m^-(k_r)\cdot\psi_m^-(k_r,z) \qquad (41)$$

Where $A_m^+(k_r)$ and $A_m^-(k_r)$ are arbitrary coefficients to be determined from the boundary conditions at the interfaces between the layers.

In order to obtain the numerical solution, the first step is to find the depth-dependent Green's function at a discrete number of horizontal wavenumbers for the selected receiver depths. Secondly, the so-called wavenumber integral is evaluated yielding the transfer function of the channel at the selected depths and ranges. This integral is given by:

$$f(r,z) = \int_0^\infty f(k_r,z)\cdot J_0(k_r r)\cdot k_r \cdot dk_r \qquad (42)$$

Finally, upon repetition of these two steps at selected frequencies, the frequency integration given in (43) can be performed to yield the total response in time.

$$f(t) = \int_{-\infty}^{\infty} f(\omega)\cdot e^{-i\omega t} d\omega \qquad (43)$$

The wavenumber integration technique has one main condition of validity given in relation (44).

$$\Delta r < \lambda_{high} \qquad (44)$$

Where $\Delta r$ is the step in range and $\lambda_{high}$ is the wavelength at the highest frequency of interest.

Modelling requires in any case some simplifications. The first one is the use of a standard measured waveform air-gun signature, calculated at 1 m. As seen previously in the near-field hydrophone data analysis, variations did occur between the conducted air-gun runs and within each run. However, the chosen waveform (see the 1-s sample in Fig. 34) is likely to reflect the actual air-gun contribution to the sound field during the JIP 2010 trials.

In the same manner, inputting a mean measured sound speed profile within the water column is not exact. However, the sound speed data is not likely to change dramatically the air-gun transmission with range as it is investigated in the next section.

The defined geoacoustic model is likely to be a dominant factor of differences between empirical and numerical received air-gun levels. First, the wavenumber integration approach is only valid for range independent environment which is never the case in the real ocean and especially in the JIP project area. In this way, the modelled received levels can be defined only for one type of seabed type at a time, e.g. a sand seabed or a soft rock outcrop seabed. It is a pity as the interesting transition between both types of seabeds in the north runs as analysed in the measured data sets cannot be modelled in this case. The model will aim then at defining the received levels along the east runs which has a consistent type of seabed (reflective) along the track.

Moreover, the method assumes all interfaces plane and parallel which is far from reality.

Last but not least, there is a substantial lack of knowledge on the geoacoustic properties of the superficial sea bottom layers of the JIP area - as refraction seismic only provided data on the deep basement. However, as mentioned previously, the geoacoustic properties and depth of the basement are still relevant inputs especially for low-frequency acoustics.

## 4.3 Results of transmission loss levels with range

A first Matlab code was used to define an acoustic environment file. This file is then used in SCOOTER in order to calculate the depth-dependent Green's functions for a discrete number of horizontal wavenumbers for the selected receiver depths.

The first input is the measured sound speed profile. Fig. 92 gives the average values from Fig. 45. Thus, the water depth of the waveguide is 32.2 m in the numerical model and is a constant as explained earlier.

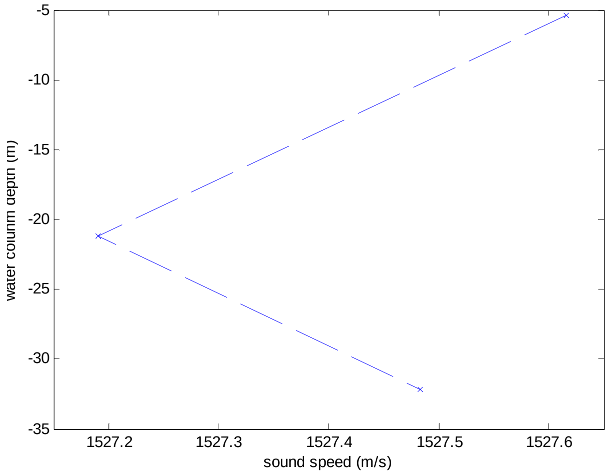

**Figure 92:** *Mean measured sound speed profile from JIP temperature data. The 3 considered depths are averaged over the 3 different sound speed calculations in Fig. 45.*

The chosen air-gun depth for all models was 5.35 m which is a typical value in the measurements given that the mean air-gun depth between the runs was 5.43 m.

The next set of input is all geoacoustic properties of the sea bottom. A few simple geoacoustic models were analysed, all considering a 500-m thick basement at 158 m below seabed. The acoustic properties and the depth of this layer were taken from the refraction seismic technique. Three different materials were used in the models, i.e. sand, a calcarenite-like material and the basement. The soft rock layer aimed at modelling the presence of the coffee rock outcrop. The table in Fig. 93 gives the chosen geoacoustic parameters of these materials. Note that these parameters were taken from Jensen et al, "Computational Ocean Acoustics" but other papers dealing with acoustic properties of seafloor material give different values for the same materials. Thus, some parameters as the compressional wave attenuation $\alpha_P$ may be modified in the model to obtain results close to the measured data.

| Material | Sand | Soft rock (coffee rock) | Basement (basalt) |
|---|---|---|---|
| Density (kg.m$^{-3}$) | 1900 | 2400 | 2700 |
| Compressional wave speed (m/s) | 1650 | 2800 | 4800 |
| Compressional wave attenuation (dB/$\lambda_P$) | 0.15 - 0.8 | 0.1 | 0.1 |
| Compressional speed gradient (s$^{-1}$) | 1 | 1 | 0 |
| Shear wave speed (m/s) | - | 1400 | 2400 |
| Shear wave attenuation | - | 0.2 | 0.2 |
| Shear wave gradient (s$^{-1}$) | - | 1 | 0 |

**Figure 93:** *Chosen geoacoustic parameters of the three considered materials used in the SCOOTER models.*

Note that the compressional wave attenuation for sand was particularly investigated. The first model considered a sand seabed up to 158 m which should provide results close to a waveguide of type Pekeris. Recall that a Pekeris waveguide assumes an infinite fluid seabed. This model is naturally not faithful to the first 158 m of the real sea bottom which may consist in many different materials with various acoustic properties. However, it is hard to input such unknown layers and it is still relevant to compare numerical and experimental results. More particularly, it may reflect the air-gun transmission along the east runs. The seabed along these tracks is believed to be made of a reasonably thick reflective seabed. Fig. 94 gives the scheme of the model (note that the scales are wrong).

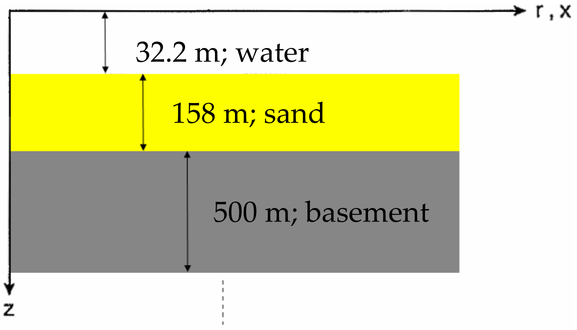

**Figure 94:** *First model investigated with SCOOTER (model 1).*

The choice of the basement thickness (500 m) equals at considering an infinite basement.

The frequency range of the numerical approach was chosen properly, i.e. finding a compromise between the actual frequency distribution of air-gun energy with range and reasonably fast calculations. Note that all models were configured to avoid calculations times above 5-6 hours. The chosen frequency band was 10-500 Hz. Then, the highest frequency here cut emitted air-gun energy above 500 Hz which is still significant according to Fig. 38 (sound spectrum levels at 1 m). However, if the sound spectrum level data with range from the noise logger are observed carefully, it can be noticed that no energy above 500 Hz is transmitted for range from around 1 km. Fig. 95 shows the sound spectrum levels for run AG14 (east run) and set 2937 vs. time/range and frequency.

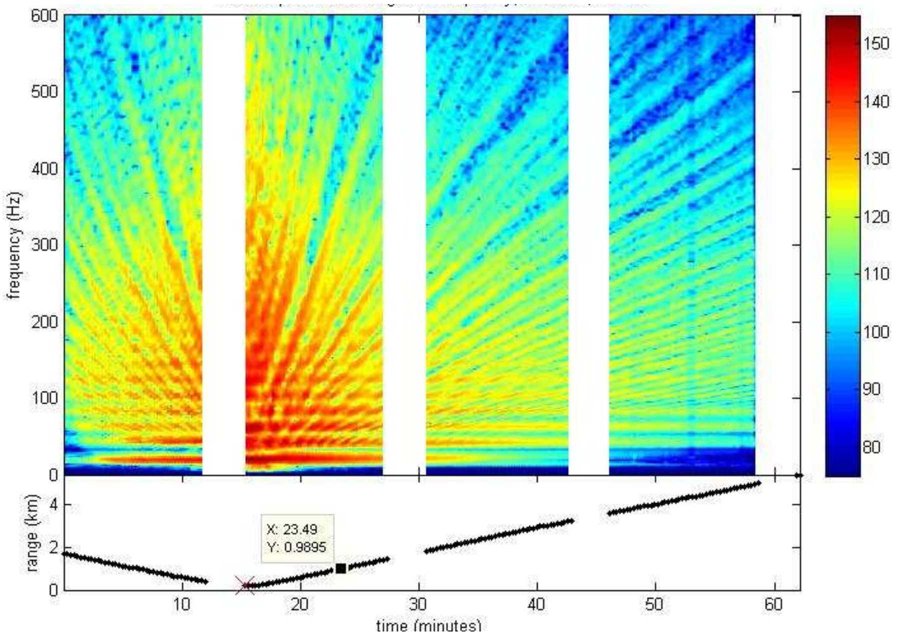

**Figure 95:** *Sound spectrum levels (dB re 1. µPa²/Hz) for east run AG14 recorded with set 2937 vs. time (minutes) and frequency (Hz) in the upper plot. The lower plot gives the range receiver-source vs. time. It shows that no air-gun energy above 500 Hz is transmitted beyond 1 km.*

Thus, the energy above 500 Hz at the source is not taken into account in the models. Thus, the sound spectrum levels vs. frequency curve calculated from the chosen air-gun signature is similar to the results in Fig. 37.

An important parameter is the maximum time delay in s for modelling the received waveforms at a specified range. This is a substantial criterion which - based on the measured data - have to take into account the arrival times of the signal through the water and the bottom as well as the time from geometrical dispersion. Recall that the first arrivals are the compressional headwaves which travel along sea bottom interfaces. In the case of the first model in Fig. 94, the headwave arrivals will show the presence of the basement only - as discussed earlier in the paper. The main arrival is a result of the waterborne propagation which is frequency dependent. The low-frequency components arrive then slightly later than high-frequency energy (see Fig. 20). The choice of this parameter was investigated and the chosen value was 7 s which allows the consideration of the two criteria. Besides, it is a relevant choice according to the seismogram results presented in the refraction seismic section.

The frequency resolution of the model is directly taken as the inverse of the chosen time delay, i.e. $f_s$ was equalled at 0.1429 Hz in all models. This fine resolution allows a fair precision of the results according to the measured sound spectrum levels at the source (see Fig. 37). A lower value of the time delay introduces a significant error in the modelled received waveforms (similar to an anti-aliasing problem).

The range of the covered distances was from 100 m to 7 km with a range step lower than 3 m. In fact, the SCOOTER necessary condition (relation (44)) has to be respected, i.e. in this case a range step roughly lowers than 1527/500 which is 3.05. An even lower range step (e.g. 1 or 2 m) made the calculations too slow.

The first result given by the calculations is a complex sound field which depends on the range and the frequency for the selected received depths. Only two receiver depths were investigated in all models for a calculation time reason, i.e. at a depth equals to the air-gun depth and at the seabed - respectively 5.35 and 32.2 m. The received waveforms and levels are interesting to compare with the empirical results as the noise loggers were all deployed on the seafloor. Note that the position in range of either the source or the receiver is a meaningless data in a range independent model.

This calculated sound field is then complex and corresponds to the response to a continuous, sinusoidal source signal at the specified frequency. It considers a received amplitude pressure of 1 Pa at 1 m. Its amplitude calculation provides directly the results of transmission loss in dB.

$$\left|Soundfield\right|^2 = TL(dB) \tag{45}$$

As mentioned earlier, several tests were made to find appropriate geoacoustic parameters. The first test used the exact values from "Computational Ocean Acoustics" giving a compressional wave attenuation $\alpha_P$ of 0.8 dB/$\lambda_P$ for sand. The importance of the seabed attenuation in the case of the model in Fig. 94 is great and affects directly sound propagation. Sand is a highly variable material, depending on the grain size and other factors which modify its acoustic properties. The reflectivity of sand may change therefore from place to place and the measured data of sound exposure levels vs. range in section 3.3.2.2 (east run data) imply a quite reflective seabed. It is therefore crucial to find out the right parameters to obtain a similar decrease of levels with ranges than the measured received levels at the noise logger positions. Fig. 96 recall a typical SEL curve with range for an east run data set (run AG14, set 2937), only for the air-gun departure.

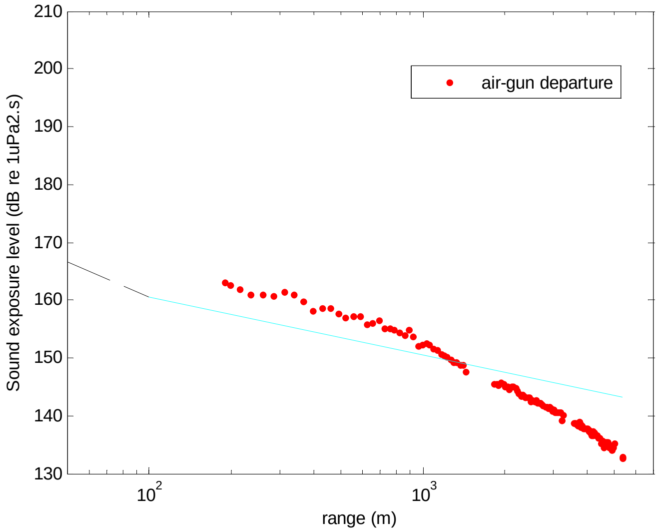

**Figure 96:** *Measured SEL (dB re 1μPa².s) vs. range in m (log scale) for east run AG14 and set 2937. Only the air-gun departure is plotted. The black line denote a spherical spreading up to 100 m and the cyan line a cylindrical spreading from 100 m.*

As discussed in the result analysis, the SEL for this region decrease typically with a rough cylindrical spreading up to 800 m before undergoing a much steeper slope, related to the Lloyd mirror effect a great distances.

Fig. 97 below gives the modelled transmission loss averaged in the frequency interval from 70 to 100 Hz - for model 1 with two cases of compressional wave attenuation values for sand (0.15 and 0.8 dB/$\lambda_P$). The curves of spherical and cylindrical spreading are also plotted to give an idea of the slope of each modelled curve.

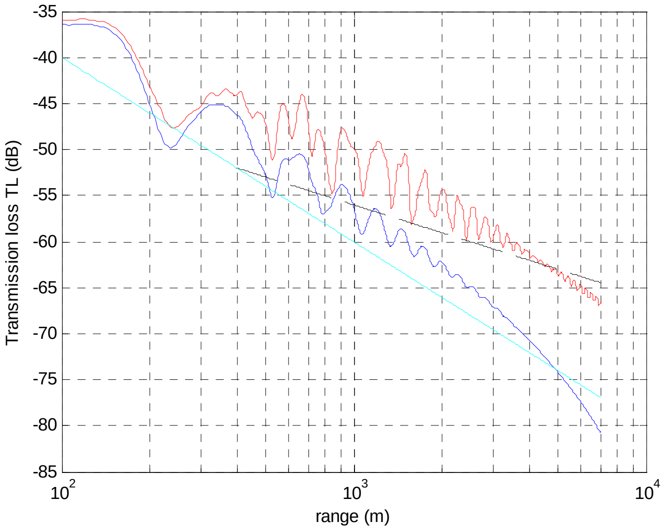

**Figure 97:** *Modelled transmission loss (dB) vs. range (m) averaged in the frequency interval from 70 to 100 Hz. The model is model 1 (Fig. 94). The blue curve was calculated with a compressional wave attenuation for sand of 0.8 dB/$\lambda_p$ and the red curve with an attenuation of 0.15 dB/$\lambda_p$. The cyan curve shows a spherical spreading and the black dotted curve a cylindrical spreading from 100 m.*

Fig. 98 gives the same results but averaged in the interval from 200 to 300 Hz.

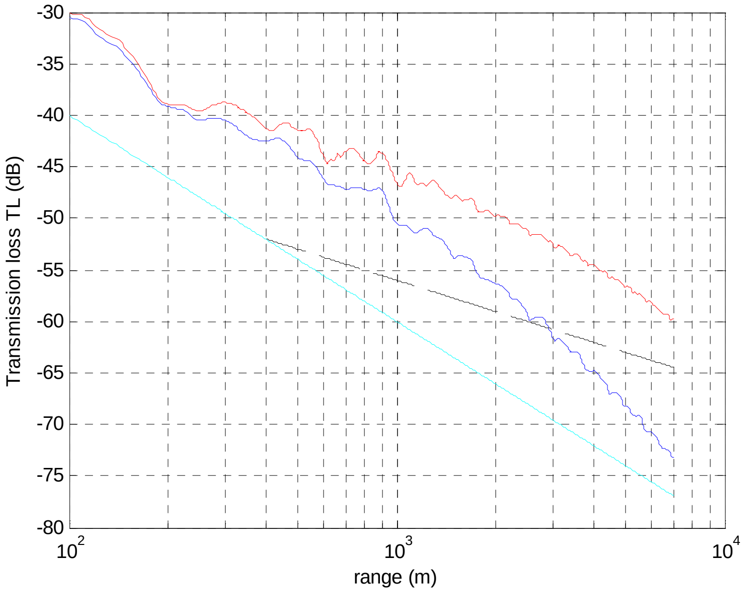

**Figure 98:** *Same plot as Fig. 97 but averaged between 200 and 300 Hz.*

Fig. 96 and Fig. 97 show how substantial is the seabed compressional wave attenuation considering transmission loss results with range. A value of 0.8 dB/$\lambda_P$ implies a substantial increase in transmission loss (recall that transmission loss is usually plotted downwards as in Fig. 96 and Fig. 97). On the other hand the red curves with an attenuation of 0.15 dB/$\lambda_P$ looks more realistic with a slope close to cylindrical spreading up to 2 km. From 2 km, there is a clear drop off in both figures, which also appears in the experimental results - related to the Lloyd mirror effect. Recall that the wavenumber integration method and particularly SCOOTER code is exact in such a model as in Fig. 94 and take into account physical phenomenon as the Lloyd mirror effect. However, it does not take into account special acoustic attenuation like scattering loss from a rough seabed. In the latter case, an additional loss can be added given that scattering losses vary linearly with distance [1].

Thus, from the comparison between the two values of compressional wave attenuation, the value of 0.15 dB/$\lambda_P$ was chosen to calculate the received waveforms with range.

Firstly, the model in Fig. 94 can be used to investigate the influence of the small vertical structure of the sound speed profile in Fig. 92 on the transmission loss level results in dB. For that, the same model was run with a constant sound speed within the water column ($c_w$ = 1527.43 m/s for all depths). Fig. 99 overplots the considered sound speed profiles in both models used in this investigation. They are noted models 1A and 1B.

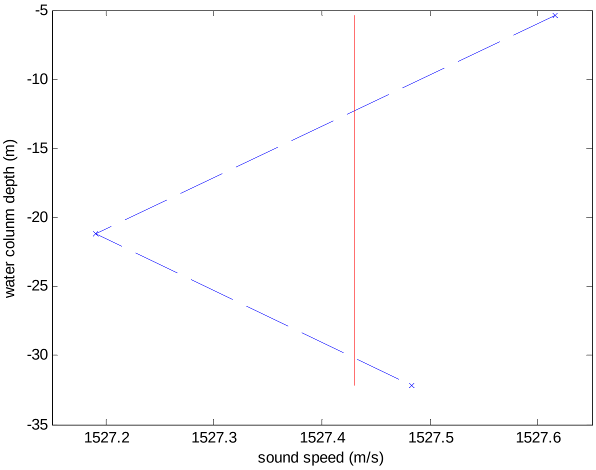

**Figure 99:** *Mean measured sound speed profile from JIP temperature data in blue (model 1A) and constant sound speed profile with depth in red (model 1B) averaged from the blue curve.*

The transmission loss level results at a receiver depth of 5.35 m gives a quasi-identical plot for both models and is not relevant to show. On the other hand, the results at the seabed (32.2 m) present slight differences. Fig. 100 gives the transmission loss levels vs. range and frequency respectively for model 1A (measured sound speed profile) and model 1B (constant sound speed profile).

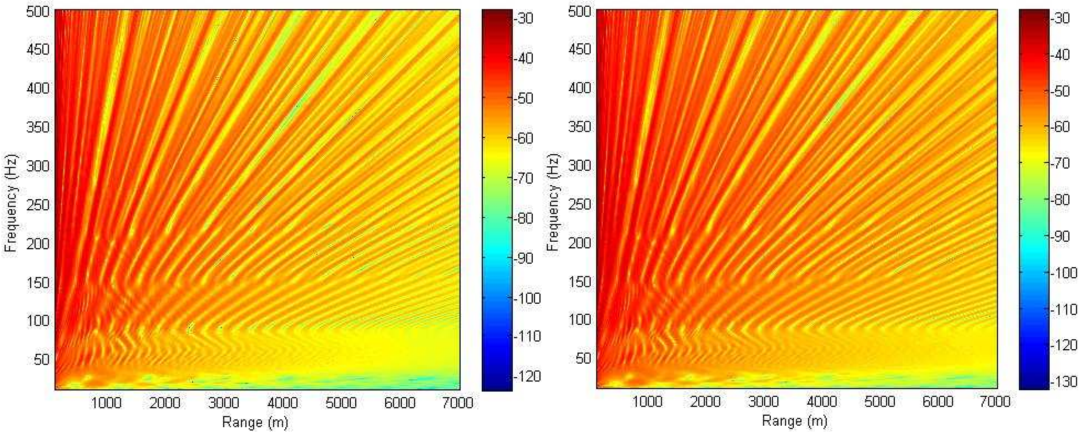

**Figure 100:** *Comparison of the transmission loss levels (dB) vs. range and frequency for the model in Fig. 93 with the measured sound speed profile (left) and a constant sound speed profile (right). Source depth is 5.35 m and receiver depth is 32.2 m (seafloor).*

It is interesting to compare both plots in Fig. 100 and notice that the constant sound speed profile model provides lower values of transmission loss levels, i.e. a more effective distribution of the acoustic energy in the waveguide. It shows a noticeable difference but a small vertical structure in the sound speed profile cannot be considered as a dominant factor for sound transmission. However, this observation justifies clearly the use of the measured sound speed profile in the model to obtain accurate results. A slight upward refraction of the acoustic waves caused by the variations of sound speed in the water column may explain the variations which are only noticeable at the seabed.

The physical meaning of the pattern with range of the transmission loss level plots in Fig. 100 was already discussed in section 2.2. Notice that they are naturally similar to Fig. 18, modelled transmission loss levels in a Pekeris waveguide.

The next simple model which was investigated (model 2) assumed a 158-m thick limestone seabed. Fig. 101 shows the scheme of the corresponding geoacoustic model. Mention that all geoacoustic parameters were taken from the table in Fig. 93.

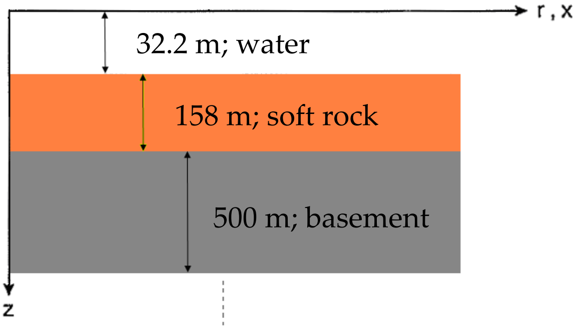

**Figure 101:** *Scheme of model 2.*

Introducing a soft rock seabed imply significant acoustic conversion into shear waves which increase sound attenuation with range. The scattering losses were not added in the model so that the experimental received levels over the identified coffee rock outcrops should be more attenuated for frequencies above 100 Hz. However, the effect from bottom loss can be compared between modelling and measurements. Fig. 102 gives the transmission loss level plot at a receiver depth of 5.35 m.

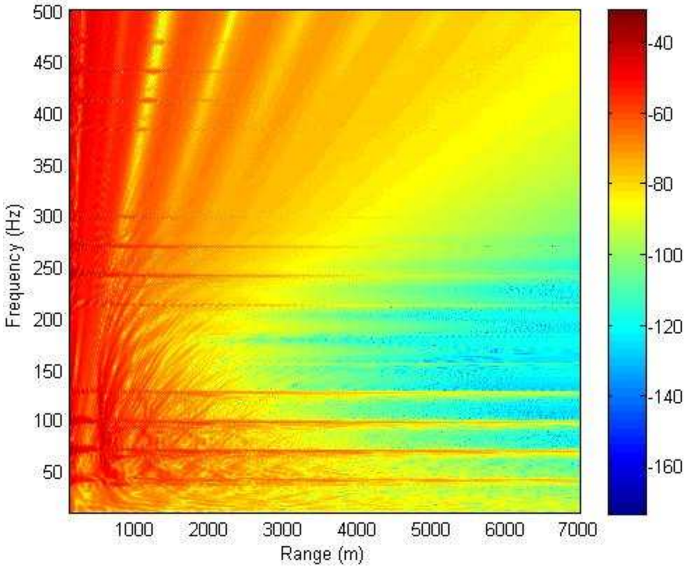

**Figure 102:** *Transmission loss levels (dB) vs. range and frequency for model 2. Source depth is 5.35 m and receiver depth is 5.35 m.*

As discussed earlier, there is a substantial acoustic attenuation in Fig. 102 compared to the plots in Fig. 100. This is directly related to the reflection coefficient curve vs. grazing angle in Fig. 23(b) which implies strong bottom penetration for frequencies around 200-250 Hz. Note that once again the choice of geoacoustic parameters is not a straightforward task and the values of compressional and shear wave attenuations ($\alpha_p$ and $\alpha_s$ chosen as 0.1 dB/$\lambda_p$ and 0.2 dB/$\lambda_s$) have direct impacts on sound transmission with range. Fig. 103 shows the averaged transmission loss levels from 200 to 300 Hz with the latter values of attenuations.

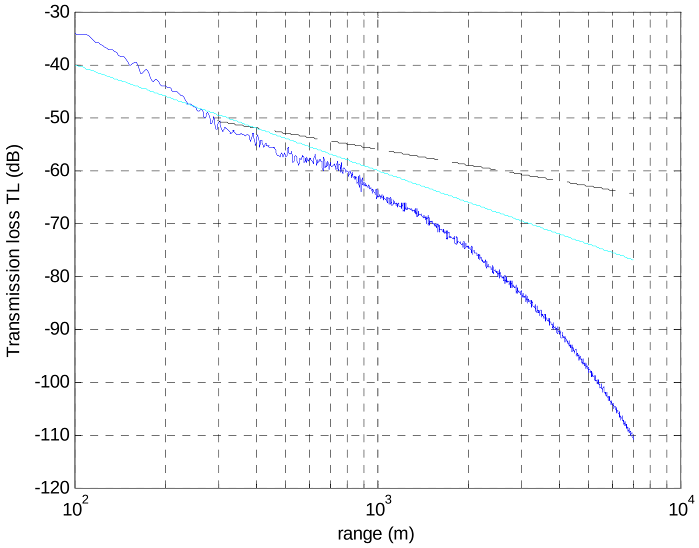

**Figure 103:** *Modelled transmission loss (dB) vs. range (m) averaged for frequencies from 200 to 300 Hz for model 2 (Fig. 101). The cyan curve shows a spherical spreading and the black dotted curve a cylindrical spreading from 100 m.*

The blue curve in Fig. 103 undergoes a decrease close to spherical spreading from 300 m to 1 km. For long ranges, the levels decrease in a manner greater than spherical spreading which was also observed in the measured SEL with range (e.g. see Fig. 60). The last model which was investigated assumes a 149-m thick soft rock layer overlain by a 9-m thick sand layer. Fig. 104 gives the scheme of this last model.

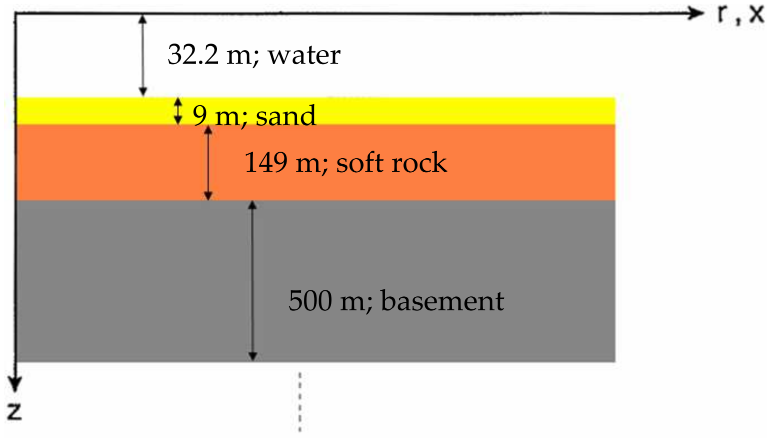

**Figure 104:** *Scheme of model 3.*

This last model does not aim at modelling the measured received levels as the sea bottom structure in Fig. 104 is hypothetical. Its results of transmission loss levels are still interesting to analyse, especially to point up that a superficial fluid layer on the top of a rock layer works as an acoustic isolation. Fig. 105 gives the corresponding transmission loss level plot vs. range and frequency for a receiver depth at the seafloor.

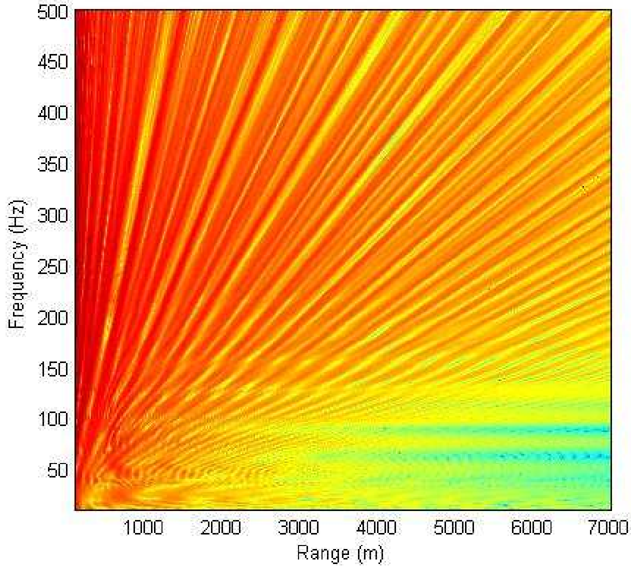

**Figure 105:** *Transmission loss levels (dB) vs. range and frequency for model 3. Source depth is 5.35 m and receiver depth is 32.2 m (seafloor).*

For such a thick layer of sand (9 m), its effect is already quite apparent. Indeed, the modal interference pattern is extended to low frequencies down to 100 Hz. So that, the high transmission loss wedge visible in Fig. 102 is reduced quite significantly. However, the soft rock layer has an influence on the sound field in the water column for low frequencies with a strong attenuation in the frequency region from 20 to 80 Hz. Fig. 106 illustrates how a sand layer isolates acoustically the deeper layer by plotting the reflection curve coefficient vs. grazing angles for different sea bottoms.

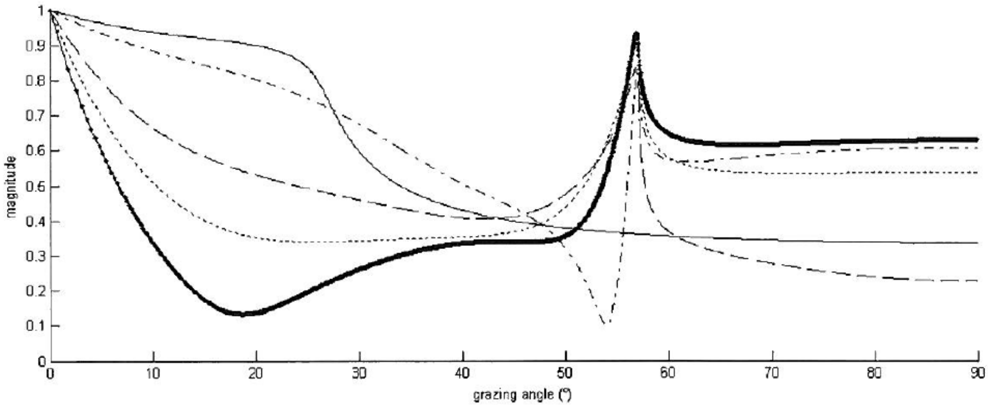

**Figure 106:** *Magnitude of reflection coefficient vs. grazing angle for seabeds comprising a calcarenite halfspace covered by sand of thickness 0λ (thick line), 0.1λ (dotted line), 0.2λ (broken line), 0.5λ (dash-dot line) and ∞ (thin solid line). λ denote the compressional wavelength in the sand layer (Duncan, 2009).*

The curves in Fig. 106 result from a numerical model. The interesting region is for grazing angles from 10° to 30° where there is substantial acoustic conversion into shear waves into the sea bottom. The reflection coefficient is the lowest for a calcarenite seabed (thick line) and increase as the sand layer thickness is increased further. Note that the sharp peak at 58° is present for all configurations except for the infinite sand seabed. Then, the corresponding propagation of headwave along the calcarenite interface is theoretically visible in the water column.

The received waveforms and sound exposure levels presented in the next section are only calculated for model 1 and 2 (Fig. 94 and Fig. 101).

## 4.4 Results of modelled received waveforms and SEL

A second Matlab code aimed at calculating the received waveforms from the complex sound field obtained from SCOOTER. For that, the impulse response was calculated using the inverse discrete Fourier transform.

A vector of the measured source signal was created, of the same length as the impulse response. The maximum considered frequency in all models was 500 Hz so that the sampling frequency in the received waveforms was 1000 Hz (i.e. two times the Nyquist frequency). The first step was then to decimate the near-field waveform at 1 m (Fig. 35) to obtain a 1 kHz sampling frequency signal instead of 32 kHz used in the measurements. An arbitrary time offset of 1 s was added at the beginning of the source signal in order to avoid problems. This has no consequence on the results of received waveforms, except that the actual arrival time is 1 s before the calculated one. Fig. 107 gives the plot of the used source signal for all calculations.

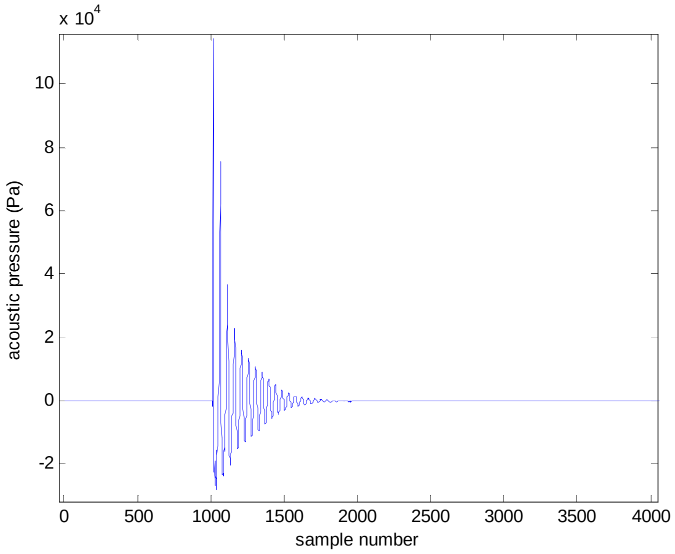

**Figure 107:** *Source signal used in the analysis, acoustic pressure (Pa) versus sample number. A time delay of 1 s was added. The actual sample length was 13722.*

Then, by doing a convolution between the source signal in Fig. 107 and the impulse response at each desired range, the modelled received waveforms were calculated.

$$\mathrm{Re}\,ceived\_waveform = conv(Source\_signal, impulse\_response) \quad (46)$$

The received signals from model 1 and for a receiver at the seafloor are first presented. Recall that this model aims at reflecting the air-gun transmission along the east tracks. The chosen compressional wave attenuation for sand was 0.15 dB/$\lambda_P$.

Fig. 108, 109 and 110 provide respectively the modelled received waveforms at a horizontal range from the air-gun of 1.3 km, 3.7 km and 6.85 km.

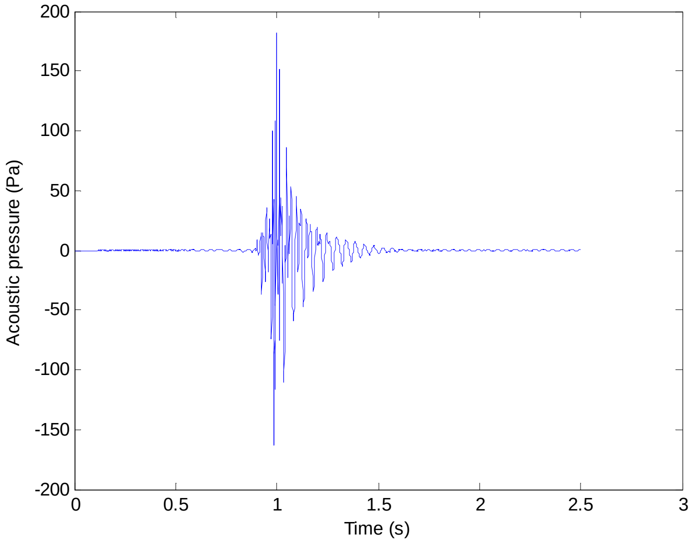

**Figure 108:** *Modelled received signal at 1.3 km (Pa vs. s). 2.5-s sample. Receiver at the seafloor.*

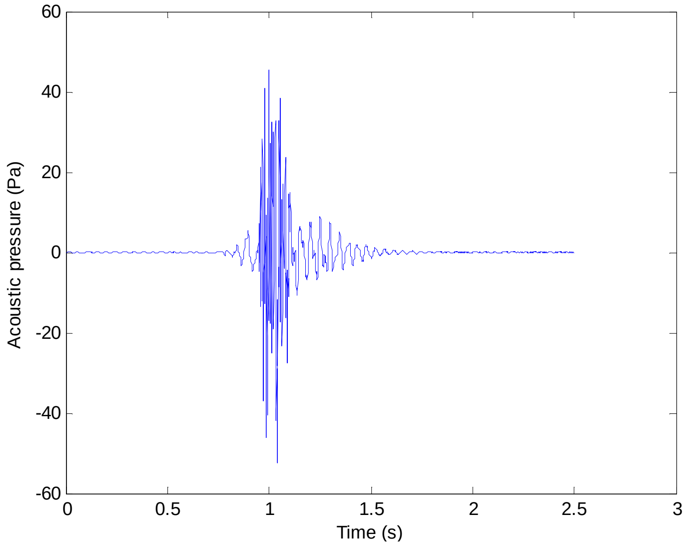

**Figure 109:** *Modelled received signal at 3.7 km (Pa vs. s). 2.5-s sample. Receiver at the seafloor.*

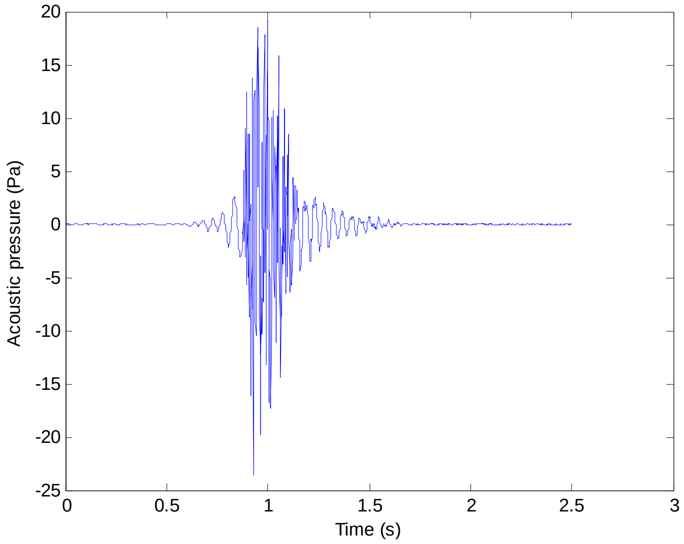

**Figure 110:** *Modelled received signal at 6.85 km (Pa vs. s). 2.5-s sample. Receiver at the seafloor.*

The modelled received signals at different ranges in the upper figures look reasonable according to model 1. It can be noticed that the numerical results well illustrate the geometrical dispersion of the air-gun energy. Thus the total time dispersion of received signal in Fig. 108 is 0.7 s and extends up to 1 s in Fig. 110 at 6.85 km. The slow trailing edges are low-frequency waterborne energy as explained earlier.

Fig. 111 compares the modelled and measured received waveforms at the same range (4 km). The measured waveform is from the east run AG13 and set 2937.

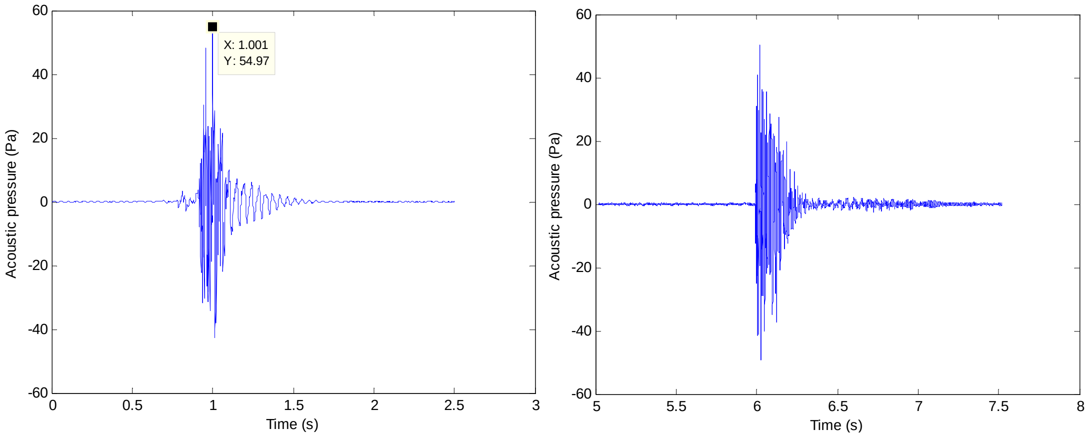

**Figure 111:** *Modelled received signal (left) and measured received signal (right) at 4 km. Both receivers are at the seafloor.*

Fig. 111 points up a good agreement between the model and the measured data, especially in term of pressure amplitudes. Indeed, the modelled signal has a maximum peak pressure of 55 Pa and the measured one of 50 Pa. This shows a reasonably relevant choice of geoacoustic parameters in model 1, especially for the compressional wave attenuation for sand (0.15 dB/$\lambda_P$). On the other hand, both signals present a difference in total time dispersion (0.6 s in the model and 0.3 s in the measurements). This disparity may likely result from the geoacoustic model which does not attenuate the low-frequency components of the waterborne energy as much as in the reality.

As an example, Fig. 112 gives the modelled received shot with model with the same model with a $\alpha_P$ of 0.8 dB/$\lambda_P$.

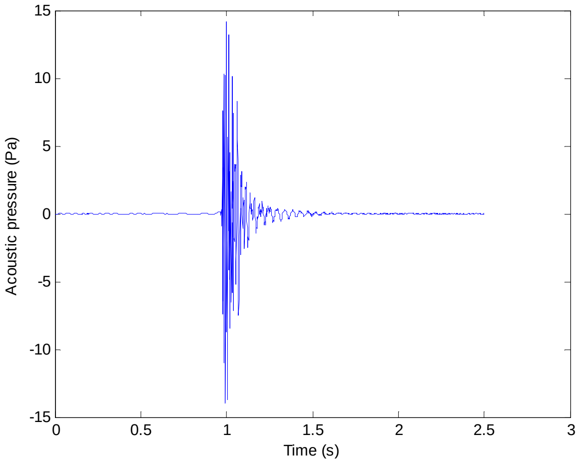

**Figure 112:** *Modelled received signal at 4 km with model 1 ($\alpha_p$=0.8 dB/$\lambda_p$). Receiver at the seafloor.*

As noticed earlier in Fig. 97 and 98, a high compressional wave attenuation for sand leads to a much stronger sound attenuation with range. In fact, the modelled signal in Fig. 112 has a maximum peak pressure around 14 Pa. It confirms that 0.15 dB/$\lambda_P$ is a much more realistic choice.

The main advantage of modelling the air-gun transmission is to obtain the waveforms and sound levels at a different water depth. Fig. 113 exposes the received waveform at 4 km at a received depth of 5.35 m (with $\alpha_P$=0.15 dB/$\lambda_P$).

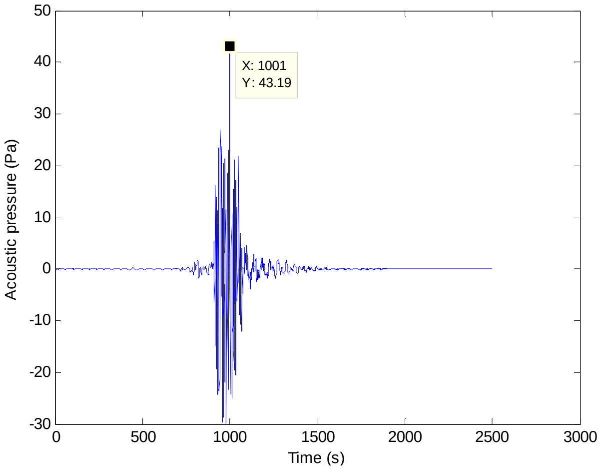

**Figure 113:** *Modelled received signal at 4 km with model 1 ($\alpha_p$=0.15 dB/$\lambda_p$). Receiver is at 5.35 m.*

The maximum peak pressure in the waveform in Fig. 113 is 43 Pa showing that the received air-gun energy is lower at the sea surface than at the seafloor. This was discussed earlier and is caused by the Lloyd mirror effect.

The modelled waveforms at different ranges (range step of 150 m, i.e. 46 shots) are used to calculate the sound exposure levels (dB re 1μPa².s) in the same manner as it was undertaken with the measured data (see section 3.1.2.). The cumulative energy for each shot was obtained and the last 1/20th portion of the curve was taken to calculate the sound exposure level of the shot. The noise levels were taken before the main waterborne arrival in each signal.

Firstly, the results of SEL are showed for model 1 (Fig. 94). Note that from now on, the compressional wave attenuation for sand was 0.15 dB/$\lambda_P$ in all calculations. Fig. 114 gives an example of modelled cumulative energy (in Pa².s) vs. time (range is 4 km).

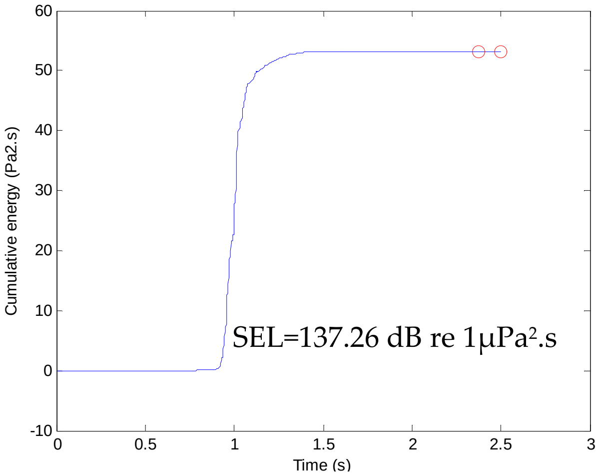

**Figure 114:** *Cumulative energy (Pa².s) vs. time (s) for the modelled shot at 4 km. Receiver at the seafloor. The two red dots denote the portion used to calculate the SEL.*

Fig. 115 shows then the result of SEL with range for model 1 (either air-gun approach or departure).

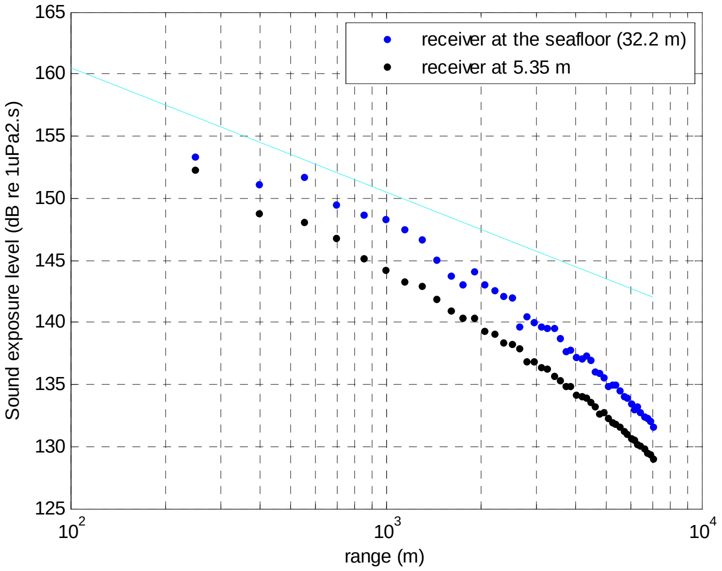

**Figure 115:** *Modelled SEL (dB re 1μPa².s) vs. range (m) for model 1. The two receiver depths are considered. The cyan line denotes the calculated cylindrical spreading (from 100 m).*

In order to compare modelled and measured sound exposure levels with range, Fig. 116 gives the SEL for the air-gun departure of the east run AG14 and set 2937. Note that Fig. 115 and 116 use the same x-axis and y-axis scales.

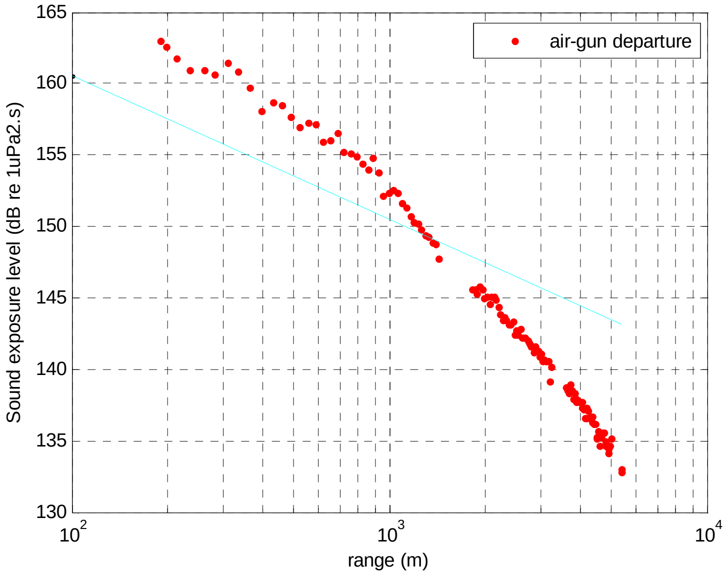

**Figure 116:** *Measured SEL (dB re 1µPa².s) vs. range (m) for the air-gun departure of AG14 and set 2937. Results were measured at the seafloor. The cyan line denotes the calculated cylindrical spreading (from 100 m).*

The two results show a good agreement from 2 km, i.e. when the decrease of received levels is related to the Lloyd mirror effect. For shorter ranges, the measured data provide much higher levels which mean that model 1 does not take into account one or a few significant acoustic properties of the real environment. The geoacoustic parameters for sand could be investigated further to try to match both results. More interestingly, the difference is highly likely due to the fact that the model assumes a 158-m thick sand layer as a first layer. In the JIP area, the first 100m of the sea bottom is probably made of many different types of materials. Thus, the contribution of the sea bottom in model 1 and the reality is manifestly not similar, especially for small ranges below 1 km where cylindrical spreading occurs in Fig. 116.

Of an interesting note is the difference in levels in Fig. 115 between a receiver at the seafloor and at 5.35 m. The SEL values for the receiver below sea surface are much weaker which confirm the effect of a shallow source (the air-gun is at 5.35 m) generating the Lloyd mirror effect.

Finally, the results of modelled received waveforms for model 2 (Fig. 101) are used to reconstruct the measured data over the northern coffee rock outcrop. Fig. 117, 118 and 119 give examples of modelled signals at horizontal ranges of 1.01 km, 3.6 km and 6 km.

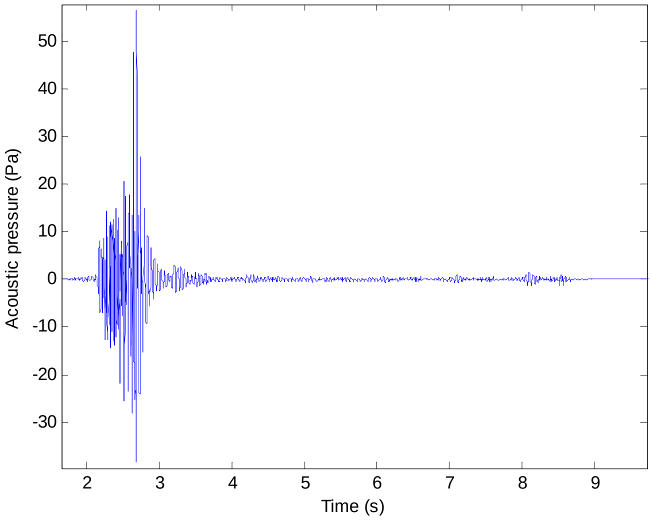

**Figure 117:** *Modelled received signal at 1.01 km with model 2. Receiver at the seafloor.*

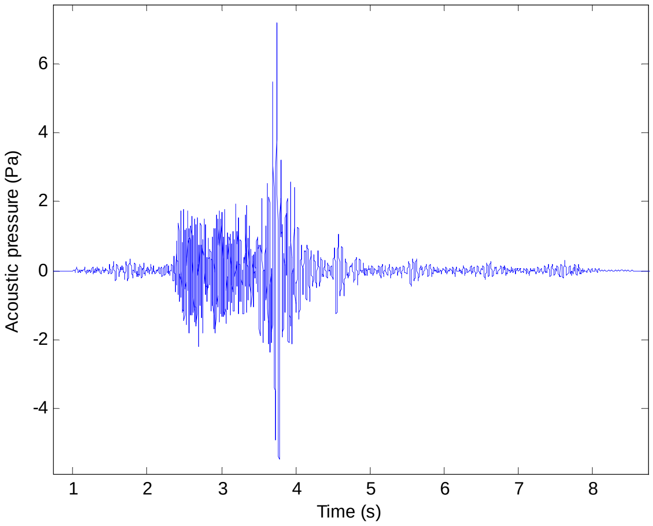

**Figure 118:** *Modelled received signal at 3.6 km with model 2. Receiver at the seafloor.*

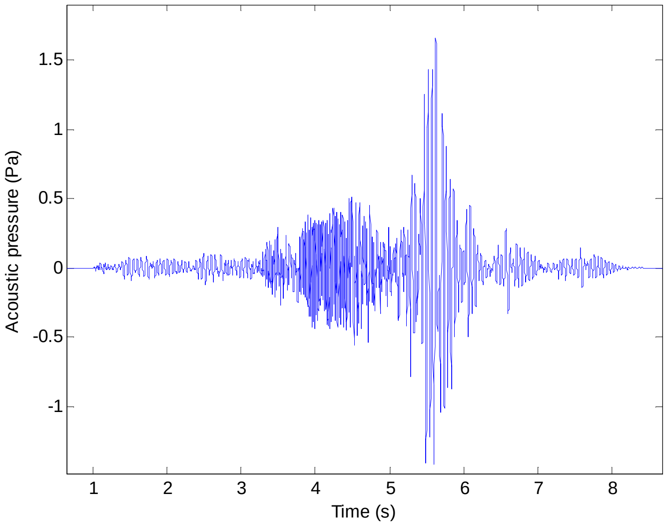

**Figure 119:** *Modelled received signal at 6 km with model 2. Receiver at the seafloor.*

The numerical results in the three upper results show strange effects from the calculation of the received waveforms, especially at ranges 3.6 and 6 km. Indeed, there is an abnormal increase of the acoustic pressure in these waveforms after the main waterborne energy (e.g. around 4. 5 s in Fig 118). This shows a problem from the model which requires being investigated. Except from this issue, the results are reasonable showing a strong acoustic attenuation from acoustic conversion into shear waves within the soft rock seabed. This attenuation is substantial as model 2 assumes a 158-m thick soft rock layer which has effect on both high and low frequencies (recall that the thickness of the layer in acoustic wavelength determines its effect on the propagation). Thus, the received waveforms have maximum peak pressure as low as 7 Pa at 3.6 Pa, which means that the propagated energy would be much lower than ambient noise in the real sea. Note also that the total time dispersion are much longer that the results from model 1. The latter effect may be explained by the fact that the seabed in model 2 is much less reflective, generating a much higher delay between high and low frequency components of the waterborne energy bouncing off the seabed and the sea surface. Besides, the presence of the headwave arrivals propagating at the seabed interface explains early arrivals in Fig. 118 and 119.

The sound exposure levels for model 2 were not straightforward to obtain and the error of abnormal energy arriving after the main waterborne arrival bias the results. Moreover, according to the measured data, the received levels below 2 km are not of interest. Fig. 120 shows the measured SEL for north run AG08 and set 2908 (air-gun departure), pointing up the presence of the northern coffee rock outcrop from 2.2-2.3 km from the source.

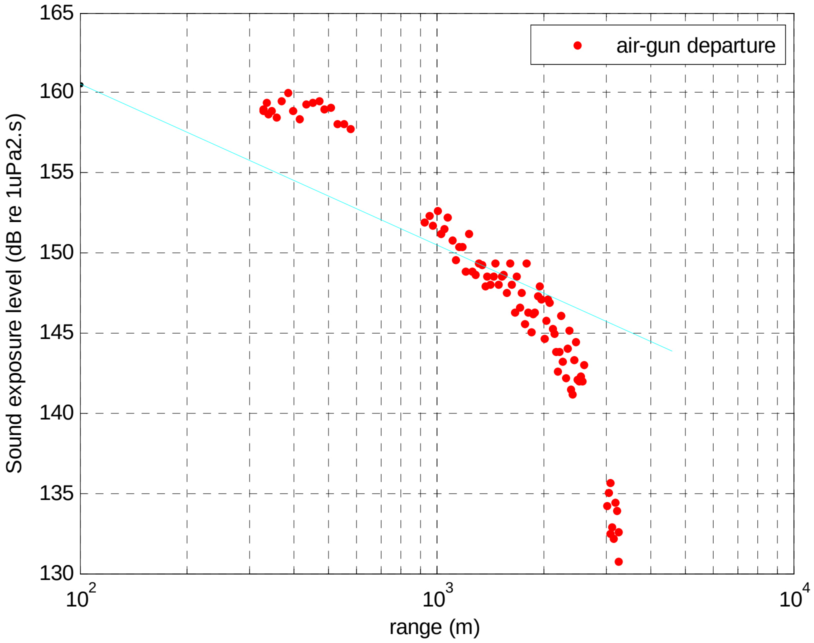

**Figure 120:** *Measured SEL (dB re 1μPa².s) vs. range (m) for the air-gun departure of AG08 and set 2908. Results were measured at the seafloor. The cyan line denotes the calculated cylindrical spreading (from 100 m).*

Fig. 121 gives an example of cumulative energy from a received shot of model 2 (range at 2.2 km) as well as its corresponding SEL value.

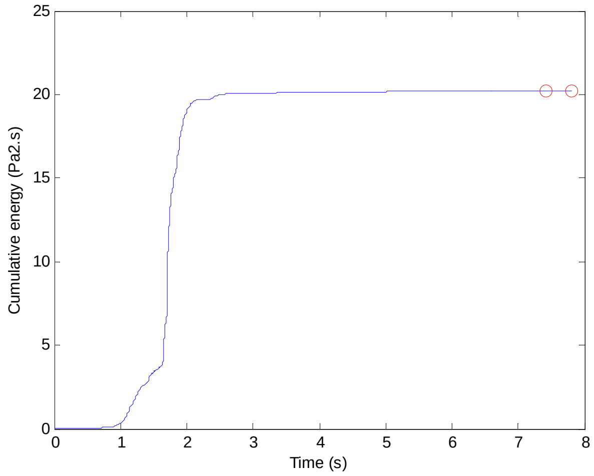

**Figure 121:** *Cumulative energy (Pa$^2$.s) vs. time (s) for modelled received signal at 2.2 km (model 2). Receiver at the seafloor. The two red dots denote the portion used to calculate the SEL.*

Finally, Fig. 122 presents the SEL results with range which aim at reproducing the measured SEL from 2.2 km up to 4.5 km in Fig. 120 corresponding to the northern rock outcrop.

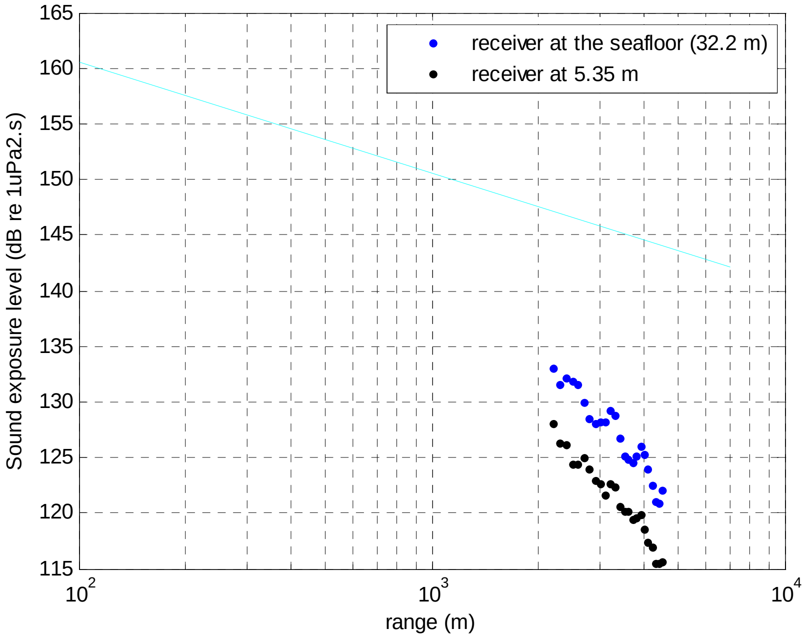

**Figure 122:** *Modelled SEL (dB re 1µPa$^2$.s) vs. range (m) for model 2. The two receiver depths are considered. Only ranges from 2.2 km up to 4.5 km are plotted. The cyan line denotes the calculated cylindrical spreading (from 100 m).*

As noticed earlier, the modelled SEL at the sea surface (5.35 m) are much lower than the results at the seafloor. Besides, the agreement between measurements and the model is not successful. Indeed, the substantial slope in Fig. 120 from 2.2 km is not as high in Fig. 122. The SEL from the model are around 5 dB lower than the measured ones. There are many potential explanations for this difference and this is clearly related to the geoacoustic model. In fact, the latter does not take into account a sudden change with range of the sea bottom type which may result in specific effects on sound propagation. Last but not least, assuming a 158-m thick soft rock layer is not realistic at all and results in the very low values of SEL in Fig. 122.

Finally, modelled seismograms similar to the experimental ones could be obtained from the modelled waveforms, applying appropriate filters. Nevertheless, this task requires using accurate geoacoustic models. The results of waveforms and SEL for model 3 are not presented.

# 5 Conclusion

This paper presents results of measurements of sound exposure levels with range generated from a single air-gun in shallow water. They point out the importance of the air-gun deployment depth and changes in sea bottom structures in term or air-gun transmission. The method using the measured data to reconstruct received levels at experimentally followed whales could be applied for other cases of whale tracks and air-gun runs. However, there is several simplifications implied in this approach and setting an accurate numerical model is more relevant.

The main output of this work is the numerical model of sound propagation in shallow water. The accuracy of the model inputs – especially the geoacoustic properties - is a substantial parameter. In this way, refraction seismic did not provide extensive knowledge on the area and the chosen geoacoustic models were then hypothetical. Nevertheless, the correlation between measured and modelled data is reasonable and points up the accuracy of the wavenumber integration technique codes in shallow water.

The numerical approach for defining received levels at experimentally followed whales was not carried out, due to the lack of knowledge regarding the sea bottom in the area. Additional measurements or geological grabs in the same area are required – which was planned for the JIP 2011 trials. More specifically, surveys were conducted in September 2011 using an echo sounder - allowing the definition of the superficial layers. Besides, the 2011 trials use a 6-airgun array which will provide extensive information on the environment as the emitted energy is much stronger.

On a personal aspect, my 10-month thesis within the Centre for Marine Science and Technology was a thorough initiation into marine acoustics and seismic survey signal analysis. The literature review mainly consisted in describing sound propagation in shallow water and the factors involved – which is a useful knowledge for many applications.

The use of the data sets from the JIP 2010 trials was a major part of my work and allowed to improve markedly my skills in Matlab. I also learnt the basics of shallow water sound propagation modelling through the wavenumber integration method.

I worked independently most of the time which gave me skills in sorting information out and choosing relevant literature in specific fields.

# Appendix 1

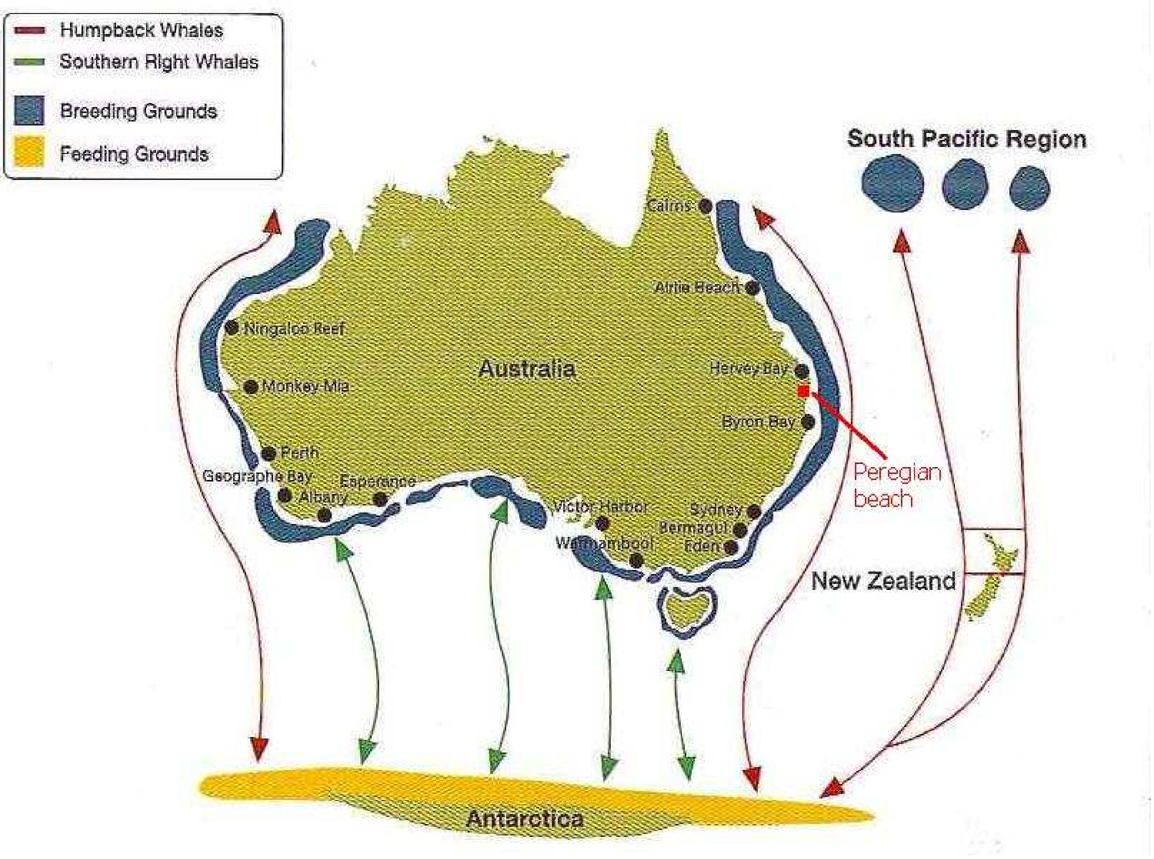

*Migration paths of humpback whales and southern right whales around Australia. Humpback whales migrate north in June and south in September, following two main paths along western and eastern Australian coasts. The JIP 2010 experiments were made off Peregian beach, South Queensland.*

# Appendix 2

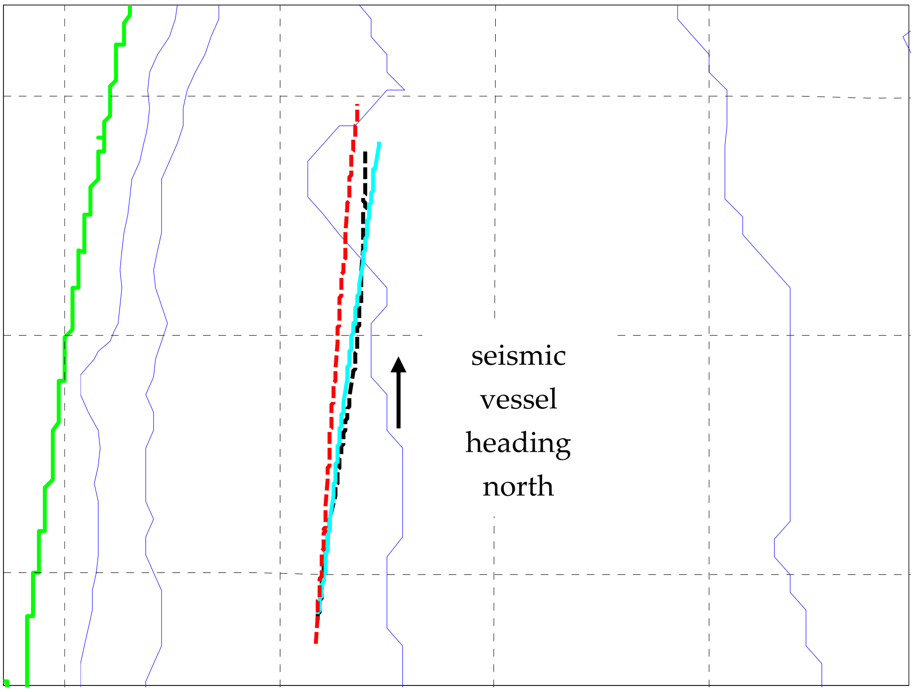

*Comparison of vessel tracks from surveys AG04 (black dotted line), AG06 (cyan line) and AG08 (red dotted line) which followed the north pattern. As in Fig. 27, the green line denotes the coast and the blues lines are the bathymetry contours. Slight variations (around a few hundred meters) can be noticed, especially at the end of the runs. Each run is approximately 7 km long.*

# Appendix 3

| **Date** | **Run** | **Head** | **start** | **end** |
|---|---|---|---|---|
| 26-Sep-2010 | AG-01 | | | |
| 27-Sep-2010 | AG-02 | E | 12:39:04, 26 30.123, 153 7.360 | 13:48:37, 26 30.150, 153 11.908 |
| 28-Sep-2010 | CT-01 | N | 11:47:46, 26 31.949, 153 07.807 | 13:12:30, 26 26.800, 153 08.599 |
| 29-Sep-2010 | CT-02 | E | 10:35:00, 26 30.184, 153 06.870 | 11:37:52, 26 30.085, 153 11.905 |
| | AG-03 | N | 14:21:56, 26 30.489, 153 8.337 | 15:06:24, 26 29.715, 153 8.226 |
| 02-Oct-2010 | AG-04 | N | 14:13:23, 26 30.448, 153 8.346 | 15:51:56, 26 26.215, 153 8.639 |
| 03-Oct-2010 | AG-05 | E | 10:33:06, 26 29.862, 153 7.252 | 11:48:03, 26 29.977, 153 12.036 |
| 04-Oct-2010 | CT-03 | N | 11:21:10, 26 30.618, 153 08.319 | 12:26:30, 26 26.396, 153 08.795 |
| | AG-06 | N | 14:43:50, 26 30.379, 153 8.352 | 15:53:44, 26 26.274, 153 8.914 |
| 05-Oct-2010 | CT-04 | E | 10:44:10, 26 29.834, 153 07.516 | 11:44:00, 26 29.813, 153 11.646 |
| | AG-07 | E | 14:35:31, 26 29.880, 153 7.229 | 15:37:02, 26 29.972, 153 11.307 |
| 06-Oct-2010 | AG-08 | N | 10:25:54, 26 30.620, 153 8.323 | 11:27:08, 26 25.985, 153 8.733 |
| | CT-05 | N | 14:05:46, 26 30.682, 153 08.294 | 15:05:47, 26 26.369, 153 08.703 |
| 07-Oct-2010 | AG-09 | E | 09:52:36, 26 29.841, 153 7.242 | 11:13:33, 26 29.819, 153 12.533 |
| 14-Oct-2010 | CT-06 | E | 09:57:00, 26 29.891, 153 07.347 | 10:57:00, 26 29.816, 153 11.764 |
| | AG-10 | | 15:16:53, 26 32.846, 153 9.053 | 15:22:34, 26 33.299, 153 9.080 |
| 15-Oct-2010 | CT-07 | N | 10:15:09, 26 30.827, 153 08.320 | 11:15:00 26 27.285, 153 08.562 |
| 16-Oct-2010 | CT-08 | E | 10:04:21, 26 29.927, 153 07.405 | 11:04:26, 26 29.818, 153 12.726 |
| | AG-11 | N | 14:16:34, 26 30.418, 153 8.400 | 15:16:49, 26 26.030, 153 8.872 |
| 17-Oct-2010 | CT-09 | N | 09:34:39, 26 30.748, 153 08.390 | 10:34:39, 26 26.351, 153 08.422 |
| | AG-12 | N | 13:28:56, 26 30.811, 153 8.259 | 14:32:04, 26 26.284, 153 8.726 |
| 18-Oct-2010 | AG-13 | E | 09:47:21, 26 29.888, 153 7.127 | 10:54:24, 26 29.795, 153 12.171 |
| | CT-10 | E | 14:30:00, 26 29.878, 153 07.216 | 15:30:00, 26 29.787, 153 11.523 |
| 19-Oct-2010 | CT-11 | N | 10:31:00, 26 30.729, 153 08.303 | 11:31:00, 26 26.220, 153 08.759 |
| | AG-14 | E | 14:30:07, 26 29.871, 153 7.213 | 15:30:18, 26 29.840, 153 11.499 |
| 22-Oct-2010 | CT-12 | E | 09:20:00, 26 29.891, 153 07.163 | 10:20:00, 26 29.857, 153 11.718 |
| | AG-15 | N | 14:28:44, 26 30.651, 153 8.302 | 15:24:27, 26 26.369, 153 8.573 |

| | | | | |
|---|---|---|---|---|
| 23-Oct-2010 | CT-13 | N | 09:30:00, 26 25.835, 153 08.590 | 10:30:00, 26 30.794, 153 08.754 |
| | AG-16 | N | 14:55:00, 26 30.794, 153 08.221 | 15:53:00, 26 26.371, 153 08.703 |
| 24-Oct-2010 | AG-17 | N | 13:52:45, 26 30.614, 153 8.303 | 14:20:14, 26 28.747, 153 8.469 |

*Vessel activities each day on task. The run type is either air-gun run (AG) or control run (CT). The run heading is north (N) or east (E). The last columns give the time an location of run start and end points. Time is EST. Locations give degrees and decimal units (latitude and longitude). The time and locations of air-gun runs were given by the GPS air-gun logging data. The greyed out lines are not of importance in this paper, i.e. either control runs or air-gun runs providing no relevant data.*

# Appendix 4

| Sea noise logger set | Sampling rate. Gain. Sample-length (s) / sample increment (min) | Location (S & E) | Depth (m) | Date time first and last logger samples | Hydrophone and serial number | Temp. logger seabed | Temp. logger 11 m above seabed | AG runs |
|---|---|---|---|---|---|---|---|---|
| 2897 E17 | 8 kHz G17 737 / 15 | 26 26.683,  153  7.724 | 28.0 | 25-Sep-2010 23:42:00 28-Sep-2010 01:49:00 | Reson 3105045 | 928 | 864 | 1-2 |
| 2898 E21 | 8 kHz G17 737 / 15 | 26 21.363,  153  8.763 | 32.4 | 26-Sep-2010 00:28:00  28-Sep-2010 01:01:00 | Massa 501 | 867 | 862 | 1-2 |
| 2899 E22 | 8 kHz G17 737 / 15 | 26 28.796,  153  7.305 | 24.8 | 26-Sep-2010 00:17:00  28-Sep-2010 02:10:00 | Massa 502 | 874 | 889 | 1-2 |
| 2900 E24 | 8 kHz G-3 676 / 15<br>8 kHz G17 676 / 15 | 26 29.325,  153  7.214 | 24.1 | 25-Sep-2010 23:56:00  28-Sep-2010 00:59:00 | Massa 500 | 873 | 927 | 1-2 |
| 2907 E17 | 8 kHz G17 737 / 15 | 26 30.000,  153  7.513 | 23.9 | 28-Sep-2010 14:43  07-Oct-2010 13:00 | Reson 3105045 | 873 | 927 | 3-9 |
| 2908 E24 | 8 kHz G17 737 / 15 | 26 28.529,  153  8.299 | 28.4 | 28-Sep-2010 14:15  07-Oct-2010 12:47 | Massa 500 | 862 | 864 | 3-9 |
| 2909 E22 | 8 kHz G17 737 / 15 | 26 30.000, 153 10.010 | 33 | 28-Sep-2010 15:00  07-Oct-2010 12:30 | Massa 502 | 867 | 928 | 3-9 |
| 2910 E21 | 8 kHz G17 737 / 15 | 26 32.046, 153 8.396 | 27.1 | 28-Sep-2010 15:24:00 7-Oct-2010 14:02:00 | Massa 501 | 874 | 889 | 3-9 |
| 2937 E22 | 8 kHz G17 737 / 15 | 26 29.968,  153  8.220 | 27.8 | 08-Oct-2010 08:35:00 24-Oct-2010 15:52 | Massa 502 | 867 | 889 | 10-17 |
| 2938 E21 | 8 kHz G17 737 / 15 | 26 28.487,  153  8.294 | 28.5 | 08-Oct-2010 08:59:00 19-Oct-2010 08:12:00 | Massa 501 | 874 | 928 | 10-13 |

| | | | | | | | | |
|---|---|---|---|---|---|---|---|---|
| 2911 E19 | 4 kHz G20 1598 / 30<br>4 kHz G40 1598 / 30 | 26 30.000, 153 11.498 | 35.7 | 14-Oct-2010 12:00:00 24-Oct-2010 12:46:00 | HTI 454046 | 862 | 927 | 10-17 |
| 2912 E18 | 4 kHz G20 1598 / 30<br>4 kHz G40 1598 / 30 | 26 28.000, 153 10.000 | 33.1 | 14-Oct-2010 14:30:00 24-Oct-2010 15:00:00 | HTI 454048 | 864 | 873 | 10-17 |
| 2913 E21 | 8 kHz G17 737 / 15 | 26 24.000, 153 9.000 | 25.4 | 19-Oct-2010 13:00:01 24-Oct-2010 14:30:00 | Massa 501 | 874 | 928 | 14-17 |

*Details of CMST noise logger deployments during the 1-month JIP 2010 trials. Given are: the CMST set number and electronics used, the sampling parameters (note that 2900, 2911 and 2912 used two gains); latitude and longitude, water depth interpolated from the Geoscience Australia 0.0025*$^0$ *bathymetry grid; date and time of first and last sample on noise logger for this period (noting that the loggers may have gone into the water after the start time and was pulled out before the end time); the hydrophone serial number; the temperature logger serial number for the logger at the seabed; the temperature logger serial number for the logger 11 m above the seabed and the overlapping air-gun runs (see Appendix B for cross reference). Sets 2898 and 2913 provided only low signal-to-noise ratio data.*

# Appendix 5

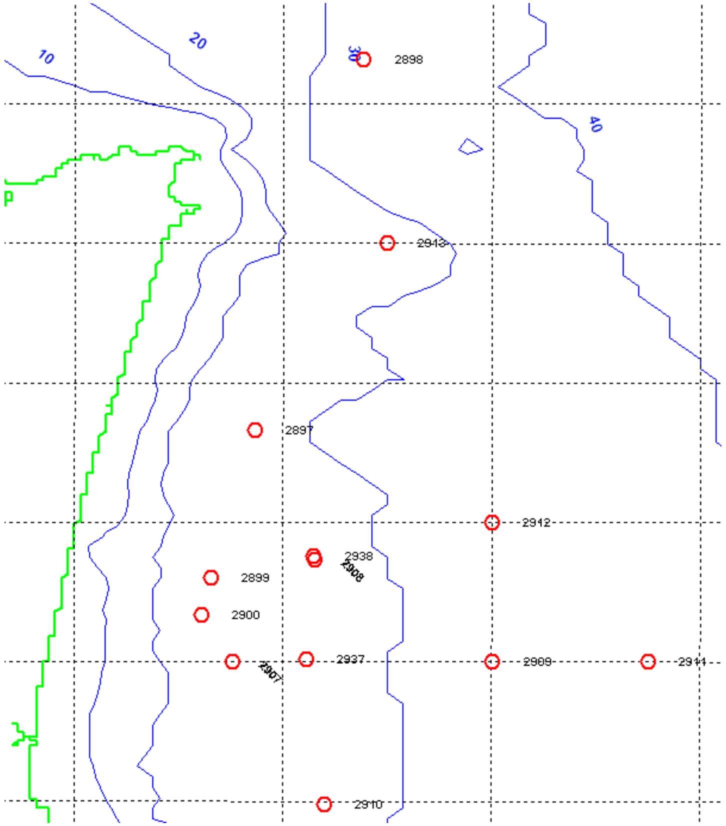

*13 noise logger positions over the 1-month JIP trials.*

# Appendix 6

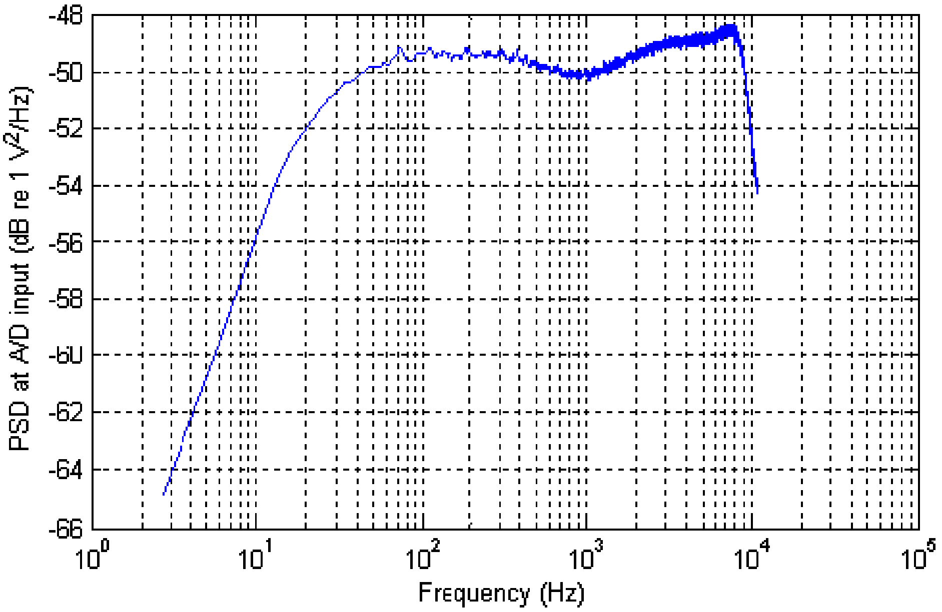

*Frequency response of a CMST-design noise logger, equipped with a Massa TR1026 C hydrophone. The response below 800 Hz is of interest for the JIP 2010 trials.*

# Appendix 7

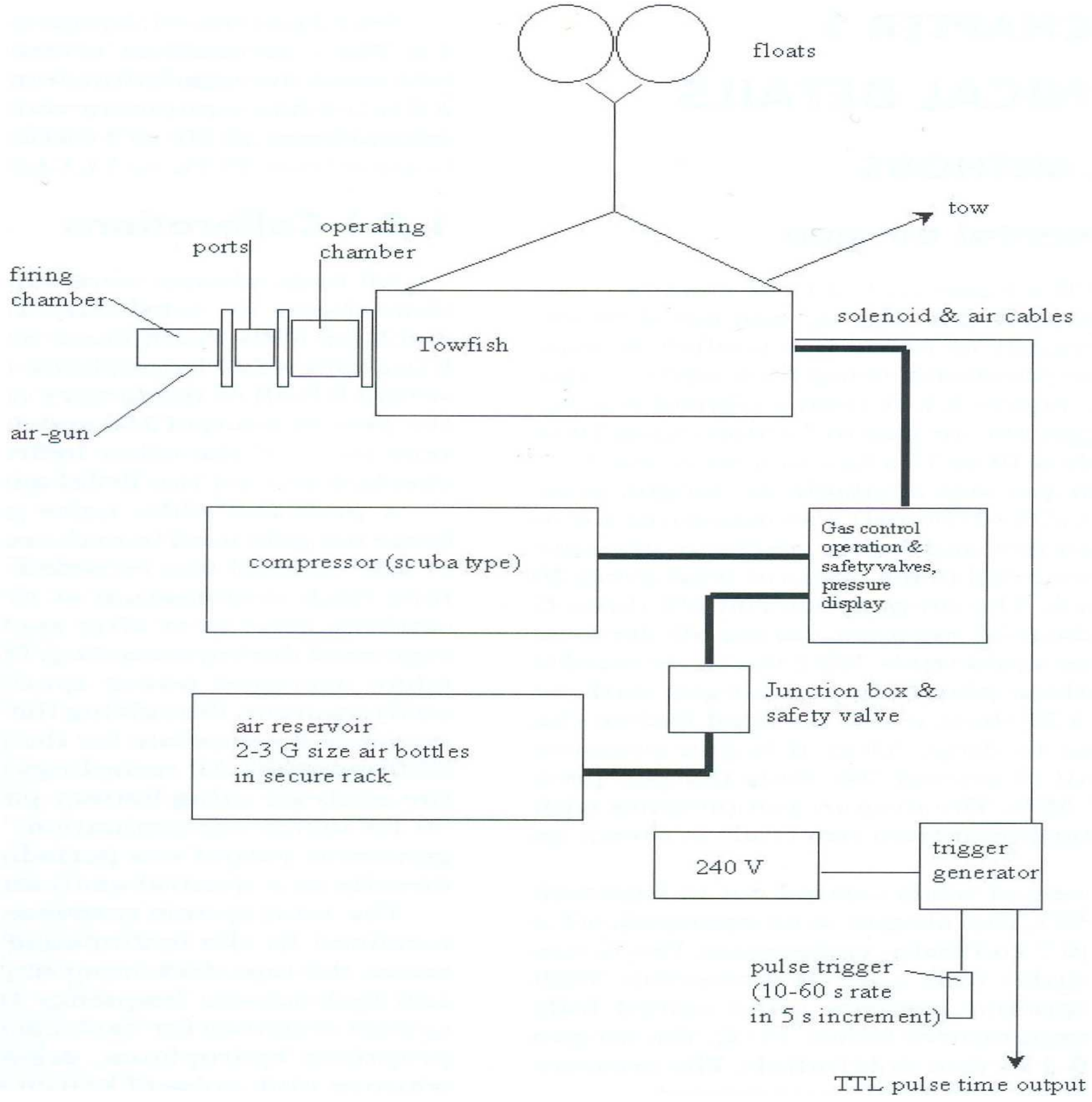

*Typical air-gun operational setup.*

# Appendix 8

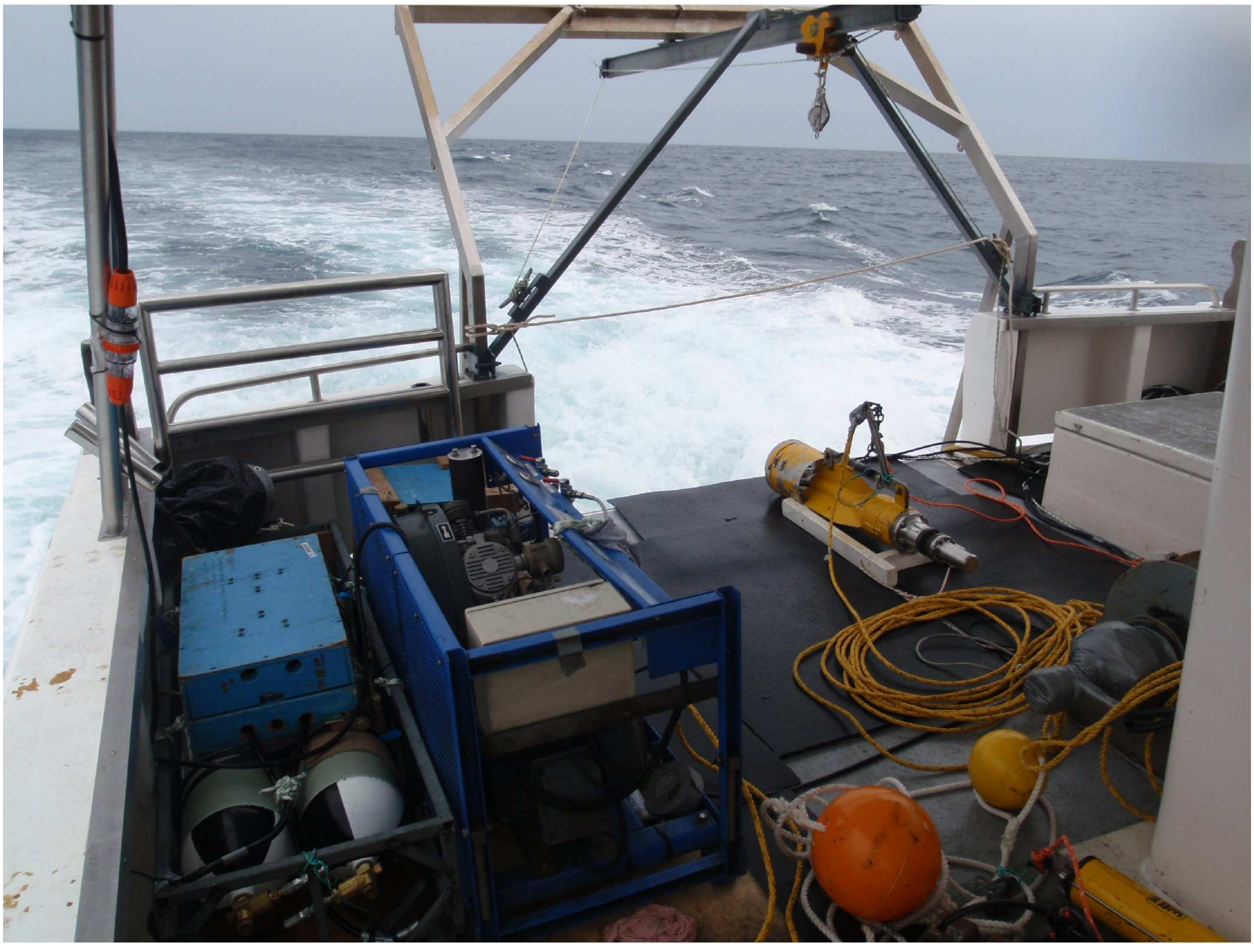

*Picture during the JIP 2010 trials, on the seismic vessel. In foreground, the gas bottles and compressor and in the background, the air-gun and deployment gantry.*

# Appendix 9

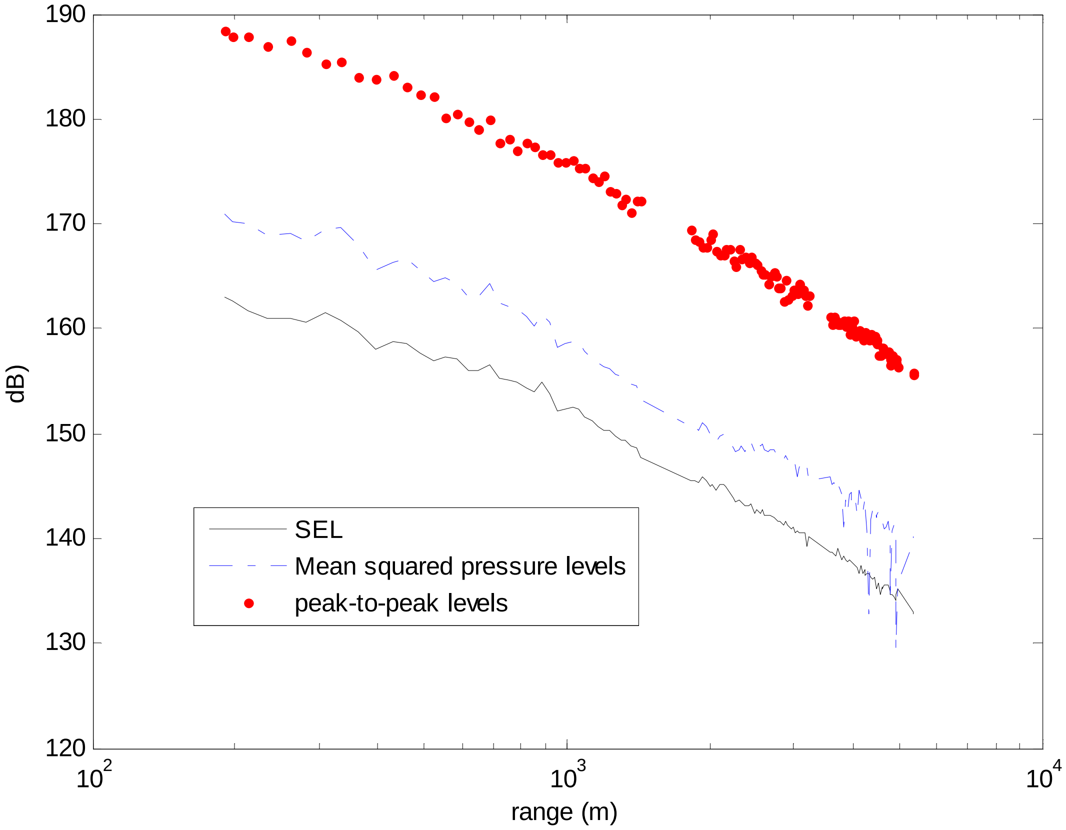

*Comparison between received sound exposure, mean squared pressure and peak-to-peak levels with range for a given air-gun survey (recorded with set 2937 and air-gun survey AG14 from JIP data). Log scale for x-axis.*

# Appendix 10

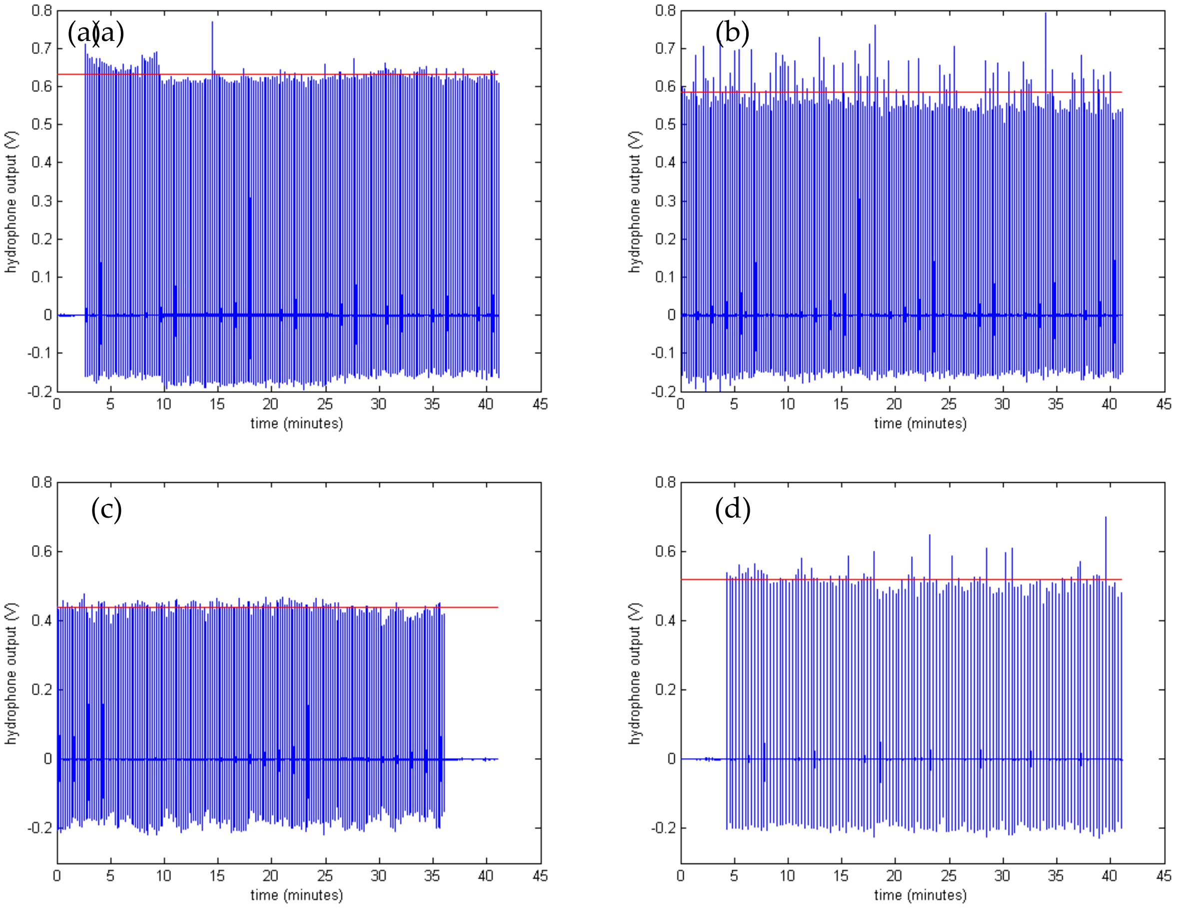

*JIP project results: examples of near-field hydrophone output (V) placed 0.85 m away from the air-gun vs. time (minutes) for surveys AG02 (a), AG06 (b), AG11 (c) and AG14 (d). The data blocks are around 41-minute long and do not contain all the shots of the 1-hour surveys. The red lines denote the mean primary pulse amplitude of the shots within the considered data block. AG02 has the highest amplitudes and shows even higher amplitudes during the first 7 minutes. AG06 presents two types of shot strength which lead to the highest standard variation of primary pulse amplitudes (around 0.052 V). AG11 gives the lowest values (with AG12). The plot for AG14 points up its different shot repetition rate (17.5 s instead of 11.5 s in other surveys). All these information are gathered in the table of Appendix 11.*

# Appendix 11

| Date | Run | Head | Number N of shots in the 41-min block | mean primary pulse amplitude for the N shots in the block (V) | Standard variations of primary pulse amplitudes (V) |
|---|---|---|---|---|---|
| 27-Sep-10 | AG-02 | E | 200 | 0.6316 | 0.0217 |
| 2-Oct-10 | AG-04 | N | 177 | 0.5979 | 0.0355 |
| 3-Oct-10 | AG-05 | E | 214 | 0.5659 | 0.0403 |
| 4-Oct-10 | AG-06 | N | 212 | 0.5836 | 0.0521 |
| 5-Oct-10 | AG-07 | E | 197 | 0.5436 | 0.0276 |
| 6-Oct-10 | AG-08 | N | 207 | 0.5457 | 0.0312 |
| 7-Oct-10 | AG-09 | E | 208 | 0.5475 | 0.0264 |
| 16-Oct-10 | AG-11 | N | 188 | 0.437 | 0.017 |
| 17-Oct-10 | AG-12 | N | 175 | 0.483 | 0.0387 |
| 18-Oct-10 | AG-13 | E | 176 | 0.4842 | 0.0322 |
| 19-Oct-10 | AG-14 | E | 127 | 0.518 | 0.0358 |
| 22-Oct-10 | AG-15 | N | 208 | 0.5793 | 0.0214 |
| 23-Oct-10 | AG-16 | N | 173 | 0.5463 | 0.0315 |
| | | | | 0.543353846 | |

*Comparison of near-field hydrophone waveforms for the 13 relevant surveys - considering 41-minute data blocks. The table presents respectively the mean maximum amplitude of the shot waveforms within each block and the corresponding standard variations. Values are in V. The green cell gives the mean maximum amplitude of all considered blocks from each survey. This value is used to pick a typical shot waveform from the JIP project which is used afterwards in the numerical model.*

# Appendix 12

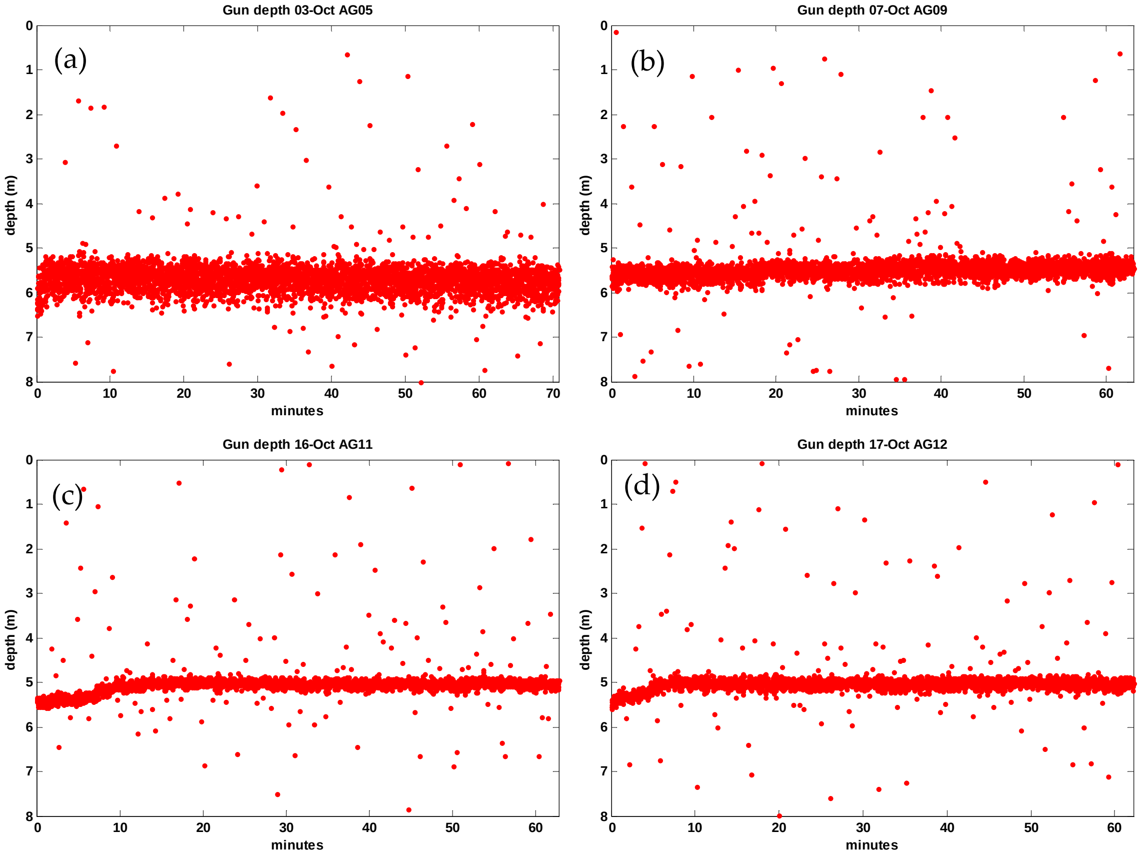

*JIP project results: examples of air-gun depths measured data (m below sea surface) vs. time (minutes), for surveys AG05 (a), AG09 (b), AG11 (c) and AG12 (d). AG05 presents the greatest air-gun depth, with a mean around 5.72 m. AG09 points out a slight increase with time. AG11 and AG12 have the lowest values or air-gun depths and present a sudden change at the beginning of the survey, probably due to a change in the seismic vessel speed.*

# Appendix 13

| **Date** | **Run** | **Head** | **Air-gun depth start (m)** | **Air-gun depth end (m)** | **mean air-gun depth in the survey (m)** |
|---|---|---|---|---|---|
| 27-Sep-10 | AG-02 | E | 5.815 | 5.5885 | 5.6485 |
| 2-Oct-10 | AG-04 | N | 5.6734 | 5.5413 | 5.6585 |
| 3-Oct-10 | AG-05 | E | 6.523 | 5.4941 | 5.7222 |
| 4-Oct-10 | AG-06 | N | 5.5224 | 5.5507 | 5.5938 |
| 5-Oct-10 | AG-07 | E | 5.4846 | 5.4658 | 5.6566 |
| 6-Oct-10 | AG-08 | N | 5.1637 | 5.1826 | 5.246 |
| 7-Oct-10 | AG-09 | E | 5.8433 | 5.4563 | 5.4869 |
| 16-Oct-10 | AG-11 | N | 5.4469 | 4.9561 | 5.0667 |
| 17-Oct-10 | AG-12 | N | 5.6074 | 5.0127 | 5.0385 |
| 18-Oct-10 | AG-13 | E | 5.579 | 5.3336 | 5.3685 |
| 19-Oct-10 | AG-14 | E | 5.4752 | 5.4752 | 5.5128 |
| 22-Oct-10 | AG-15 | N | 5.4941 | 5.1826 | 5.2365 |
| 23-Oct-10 | AG-16 | N | 5.192 | 5.3714 | 5.3126 |

5.4268

*Comparison of air-gun depth data between the 13 relevant surveys. The depth at the start and end points of each survey is given. The last column provides the mean air-gun depth within each 1-hour survey. The mean depth for the 13 surveys is around 5.4268 m.*

# Appendix 14

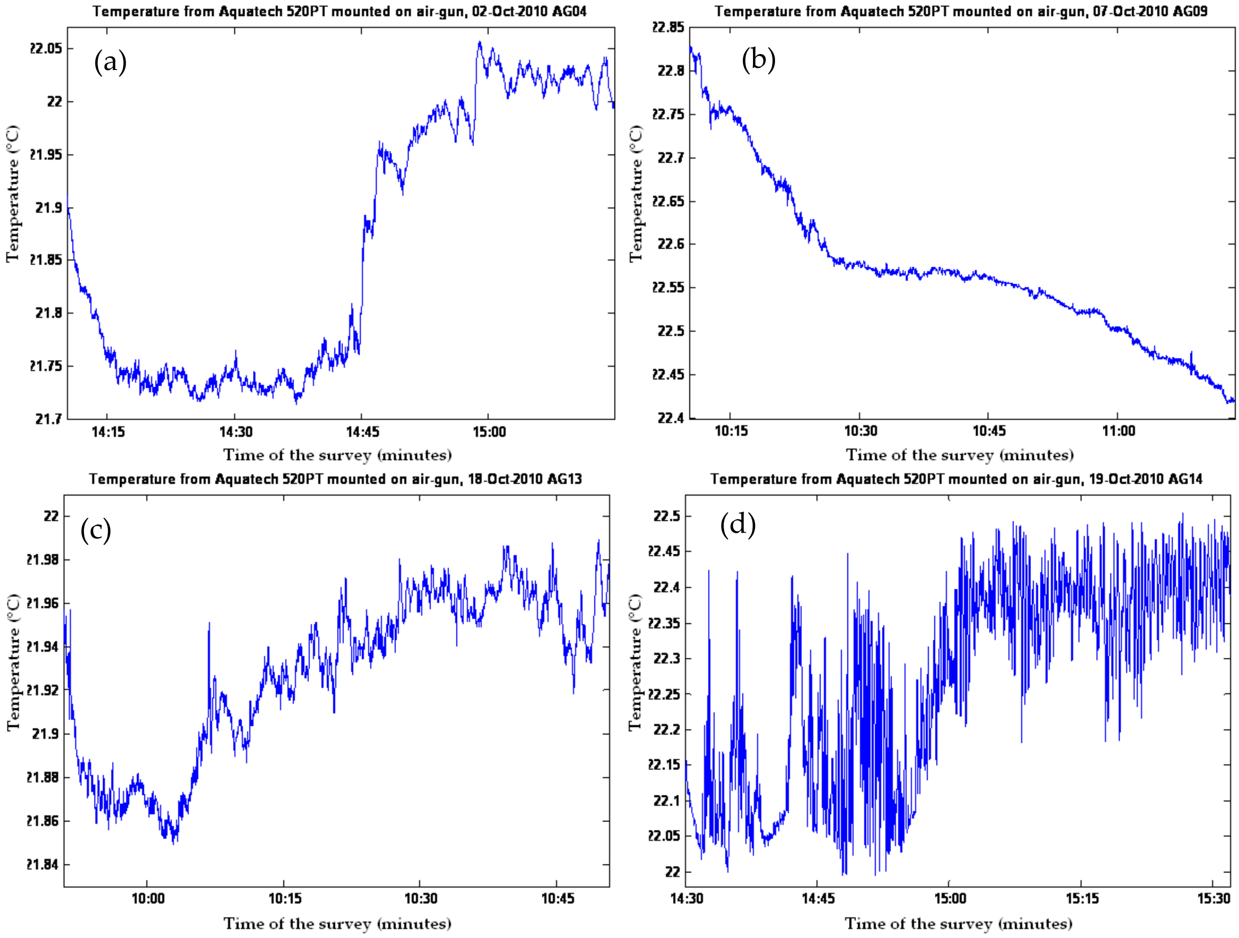

*JIP project results: examples of water temperature at the air-gun (in °C ) vs. time for surveys AG04 (a), AG09 (b), AG13 (c) and AG14 (d). AG04 and AG14 point out a sudden change of temperature during the surveys. AG09 presents a continuous decrease in temperature, from around 22.83 °C to 22.42 °C. AG13 is the survey with the smallest variations in water temperature at the air-gun, with a standard variation of 0.037 °C. All these information are gathered in the table of Appendix 15.*

# Appendix 15

| Date | Run | Head | Water temperature at the air-gun - start and end points (°C) | Mean water temperature at the air-gun for the survey (°C) | Standard variations within the survey (°C) |
|---|---|---|---|---|---|
| 27-Sep-10 | AG-02 | E | 22.2835 - 22.1297 | 22.2879 | 0.061 |
| 2-Oct-10 | AG-04 | N | 21.9111 - 21.9935 | 21.864 | 0.1261 |
| 3-Oct-10 | AG-05 | E | 21.901 - 22.0196 | 21.8792 | 0.078 |
| 4-Oct-10 | AG-06 | N | 22.2559 - 21.8736 | 21.9398 | 0.0827 |
| 5-Oct-10 | AG-07 | E | 22.2777 - 22.2371 | 22.3647 | 0.0991 |
| 6-Oct-10 | AG-08 | N | 22.4465 - 22.4932 | 22.3843 | 0.0434 |
| 7-Oct-10 | AG-09 | E | 22.8237 - 22.4203 | 22.5725 | 0.0914 |
| 16-Oct-10 | AG-11 | N | 22.0616 - 22.1036 | 22.1008 | 0.0182 |
| 17-Oct-10 | AG-12 | N | 21.9386 - 22.1094 | 22.0824 | 0.0699 |
| 18-Oct-10 | AG-13 | E | 21.9574 - 21.9791 | 21.9276 | 0.037 |
| 19-Oct-10 | AG-14 | E | 22.1456 - 22.3868 | 22.2704 | 0.144 |
| 22-Oct-10 | AG-15 | N | 22.3926 - 22.4014 | 22.3472 | 0.0535 |
| 23-Oct-10 | AG-16 | N | 22.1979 - 22.3854 | 22.3787 | 0.103 |
| | | | | 22.18457692 | |

*Comparison of water temperature data at the air-gun for the 13 relevant surveys. Temperature is in °C. The fourth column gives the first and last temperature value for the survey which gives an idea of the evolution of temperature. The two last columns present the mean temperature for each survey and the corresponding standard variation. The mean water temperature at the air-gun for the 13 surveys is around 22.18 °C.*

# Appendix 16

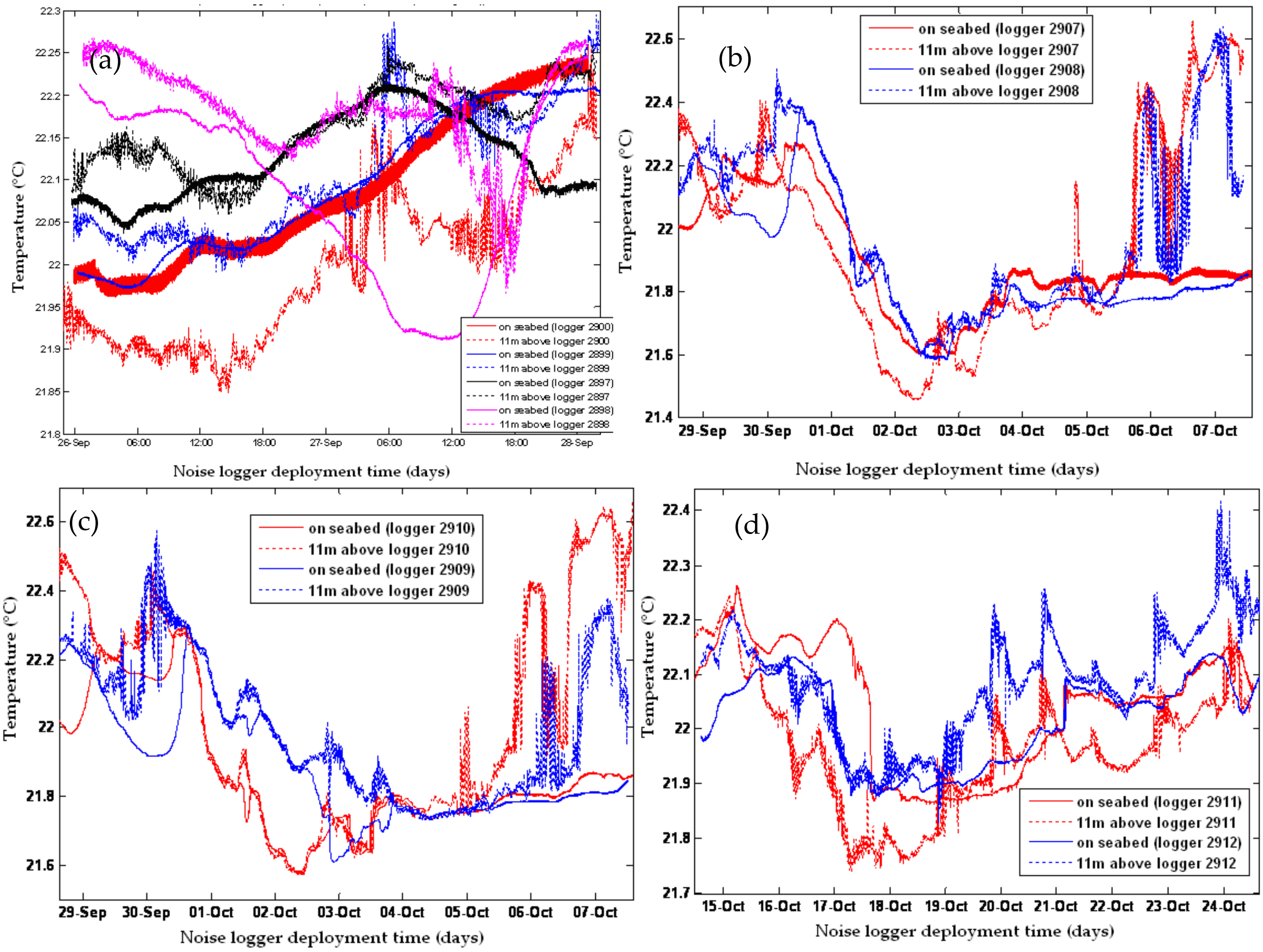

*JIP project results: examples of water temperature at the noise logger positions (in °C), at the seabed and 11 m above seabed for sets 2897, 2898, 2899 and 2900 (a); sets 2907 and 2908 (b); sets 2909 and 2910 (c); and sets 2911 and 2912. A significant variation in temperature can be observed for the data 11 m above seabed around the 6th and 7th October as seen in (b) and (c).*

# Appendix 17

| Set of noise logger | Overlapping surveys | Noise logger depth (m) | Date and time of first and last sample from temperature sensor at the seabed. | Mean water temperature at the seabed for the set of noise logger (°C) | Standard variation within the deployment time of the set of noise logger (°C) |
|---|---|---|---|---|---|
| 2897 | AG01-02 | 28 | 25/09/10 23:42 - 28/09/10 01:49 | 22.1276 | 0.0488 |
| 2898 | AG01-02 | 32.4 | 26/09/10 00:28 - 28/09/10 01:01 | 22.0888 | 0.1041 |
| 2899 | AG01-02 | 24.8 | 26/09/10 00:17 - 28/09/10 02:10 | 22.0956 | 0.0848 |
| 2900 | AG01-02 | 24.1 | 25/09/10 23:56 - 28/09/10 00:59 | 22.0839 | 0.0899 |
| 2907 | AG03-09 | 23.9 | 28/09/10 14:54 - 07/10/10 13:39 | 21.8958 | 0.1811 |
| 2908 | AG03-09 | 28.4 | 28/09/10 14:38 - 07/10/10 12:47 | 21.8763 | 0.1912 |
| 2909 | AG03-09 | 33 | 28/09/10 15:09 - 07/10/10 12:30 | 21.8887 | 0.1667 |
| 2910 | AG03-09 | 27.1 | 28/09/10 15:24 - 07/10/10 14:02 | 21.8655 | 0.1866 |
| 2937 | AG10-17 | 27.8 | 08/10/10 08:35 - 24/10/10 15:52 | 21.9276 | 0.1547 |
| 2938 | AG10-13 | 28.5 | 08/10/10 08:59 - 19/10/10 08:12 | 21.9499 | 0.1616 |
| 2911 | AG10-17 | 35.7 | 14/10/10 12:00 - 24/10/10 12:46 | 22.043 | 0.1147 |
| 2912 | AG10-17 | 33.1 | 14/10/10 14:38 - 24/10/10 15:31 | 22.0151 | 0.0824 |
| 2913 | AG14-17 | 25.4 | 19/10/10 12:52 - 24/10/10 14:58 | 22.0688 | 0.0648 |
| | | | | 21.994 | |

*Water temperature data from temperature sensor placed at the noise logger position on the seabed for the 13 sets. The mean temperature on the seabed is around 22 °C over the 1-month experiments. The strongest variations occured for set 2908.*

# Appendix 18

| Set of noise logger | Overlapping surveys | Noise logger depth (m) | Date and time of first and last sample from temperature sensor at 11 m above seabed | Mean water temperature 11 m above seabed for the set of noise logger (°C) | Standard variation within the deployment time of the set of noise logger (°C) |
|---|---|---|---|---|---|
| 2897 | AG01-02 | 28 | 25/09/10 23:42 - 28/09/10 01:45 | 22.1621 | 0.05 |
| 2898 | AG01-02 | 32.4 | 26/09/10 00:47 - 28/09/10 00:56 | 22.1823 | 0.0556 |
| 2899 | AG01-02 | 24.8 | 26/09/10 23:54 - 28/09/10 02:06 | 22.1072 | 0.0766 |
| 2900 | AG01-02 | 24.1 | 25/09/10 22:52 - 28/09/10 01:51 | 21.9932 | 0.0886 |
| 2907 | AG03-09 | 23.9 | 28/09/10 14:43 - 07/10/10 10:30 | 21.9606 | 0.3227 |
| 2908 | AG03-09 | 28.4 | 28/09/10 14:34 - 07/10/10 10:41 | 22.0033 | 0.269 |
| 2909 | AG03-09 | 33 | 28/09/10 15:09 - 07/10/10 12:25 | 22.0005 | 0.2008 |
| 2910 | AG03-09 | 27.1 | 28/09/10 15:24 - 07/10/10 14:00 | 22.026 | 0.315 |
| 2937 | AG10-17 | 27.8 | 08/10/10 12:46 - 24/10/10 15:28 | 22.0289 | 0.2681 |
| 2938 | AG10-13 | 28.5 | 09/10/10 02:25 - 19/10/10 08:04 | 21.9495 | 0.1607 |
| 2911 | AG10-17 | 35.7 | 14/10/10 12:00 - 24/10/10 12:42 | 21.9679 | 0.1167 |
| 2912 | AG10-17 | 33.1 | 14/10/10 14:45 - 24/10/10 15:29 | 22.0861 | 0.1029 |
| 2913 | AG14-17 | 25.4 | 19/10/10 13:09 - 24/10/10 14:54 | 22.2043 | 0.1333 |
|  |  |  |  | 22.051 |  |

*Water temperature data from temperature sensor placed 11 meters above each noise logger deployed. The mean temperature 11 m above seabed is around 22.05 °C over the 1-month experiments. The strongest standard variation is for set 2908 (0.32 °C).*

# Appendix 19

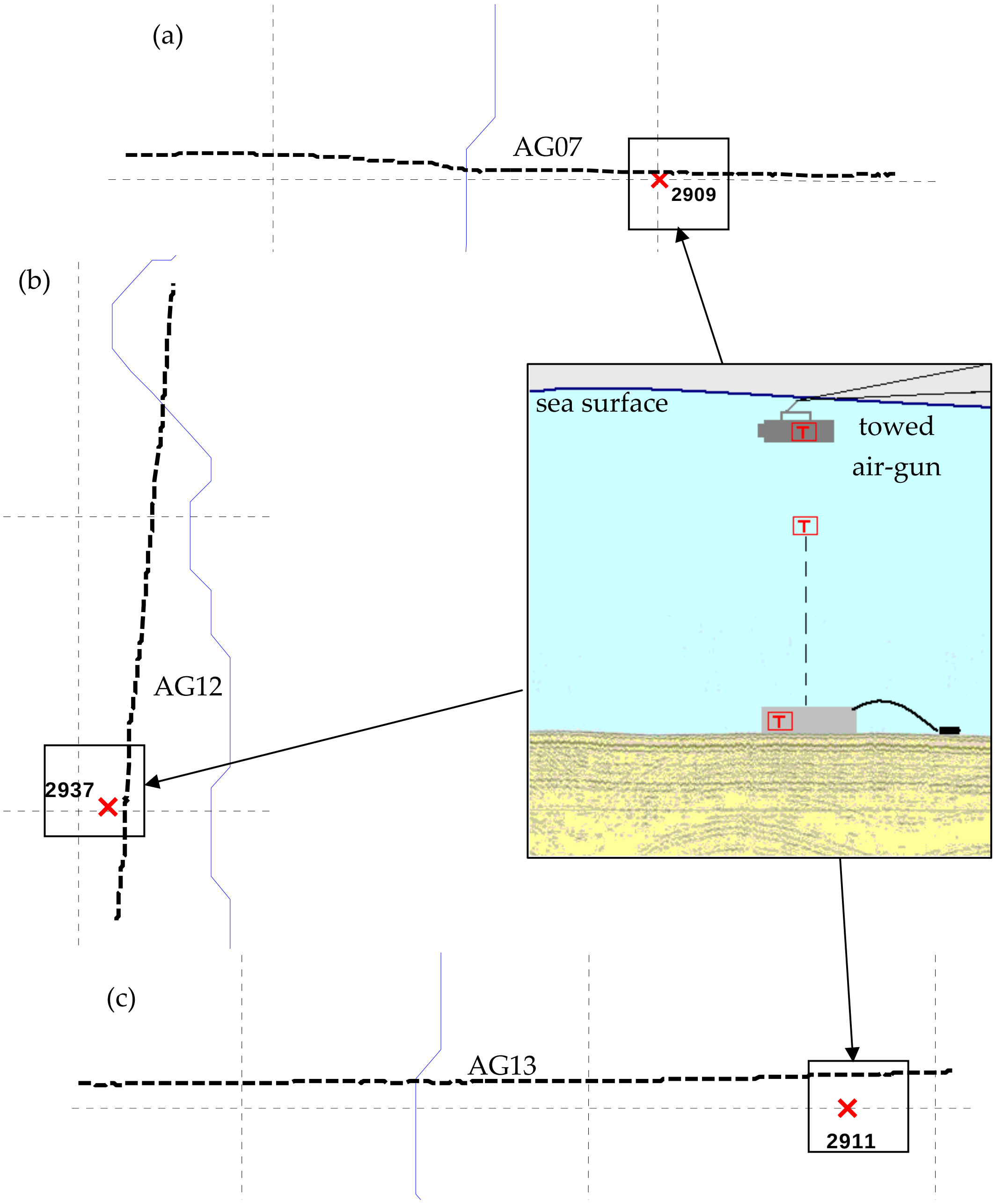

*Three cases of air-gun passing nearby a set of noise logger location, used to calculate mean temperature values within the water column and then sound speed profiles. The dotted black lines are air-gun survey tracks and red crosses denote the set of noise logger positions. The drawing illustrates the quasi-alignment of the temperature sensors for these particular times, 5th October (a), 17th October (b) and 18th October (c). The closest distance air-gun - noise logger occurred for set 2909 and survey AG07, i.e. a distance around 71 m. As an example, the same distance for set 2937 and survey AG12 was around 230 m. Depths of the loggers (2909, 2937 and 2911) are respectively 33, 27.8 and 35.7 m.*

# Appendix 20

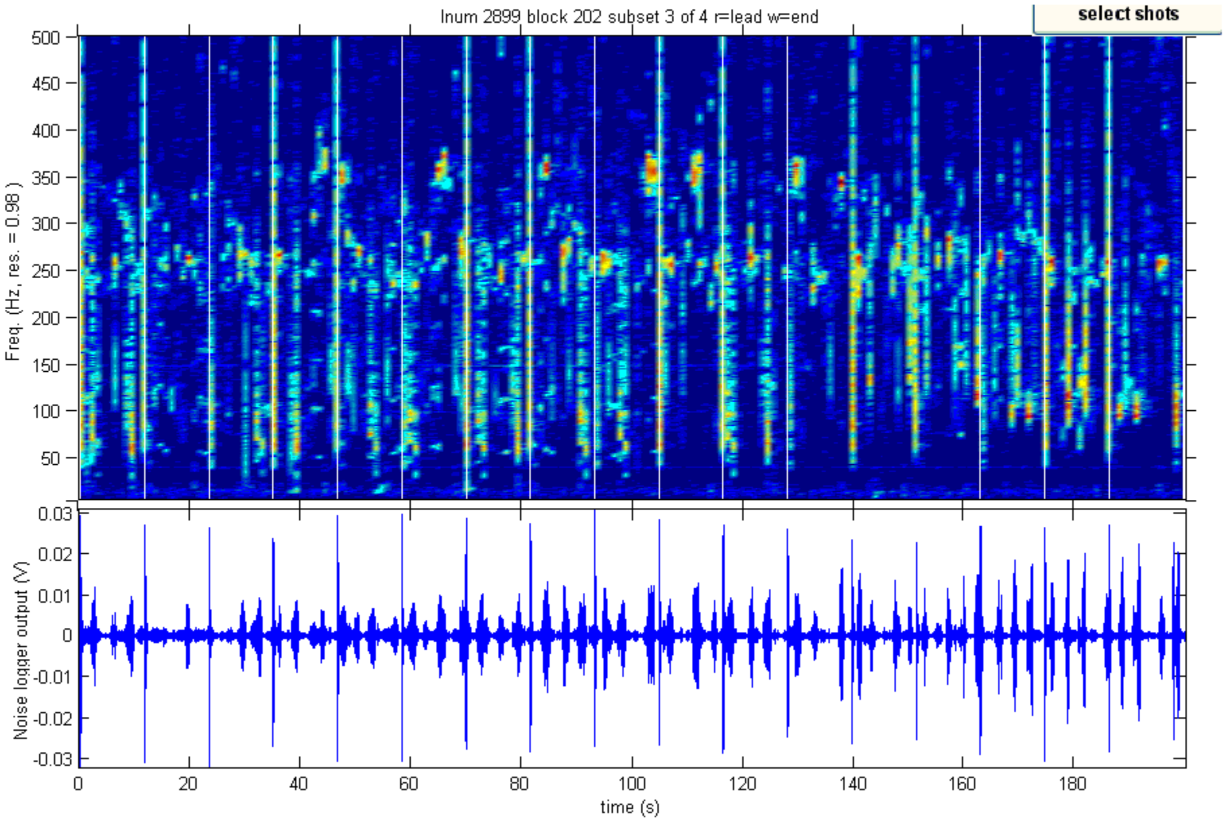

*JIP project result: screenshot from the process which aimed at selecting visually the low signal-to-noise ratio air-gun shots. The plotting data correspond to a part (200 s) from a 12-minute block recorded with the set of noise logger 2899 which was detecting the considered survey AG02 (27th September). The upper plot is the sound pressure density spectrum levels (in dB re 1. μPa²/Hz, freq. res. = 0.98 Hz) and the lower plot is the waveform in V vs. time in seconds. The shots already stored by peak detection were denoted with the white vertical bands on the upper plot. On this example, two shots were not stored, at 140 and 151 s. At the discretion of the user, they can be visually selected and stored. The air-gun pulses are well distinct on both plots, showing a repetitive pattern and a broadband characteristic, forming vertical bands on the upper plot. Note the these shots were received approximately 6 km away from the air-gun. In the background, consistent whale vocalizations are visible on both plots with two clear consistent frequency components at around 250 and 350 Hz. It is a good illustration of the frequency overlapping between distant air-gun energy and humpback whale songs range.*

# Appendix 21

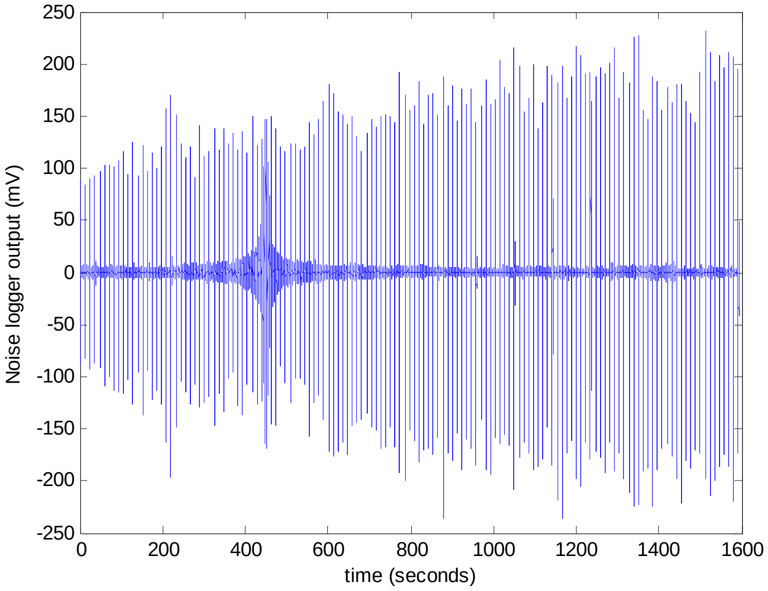

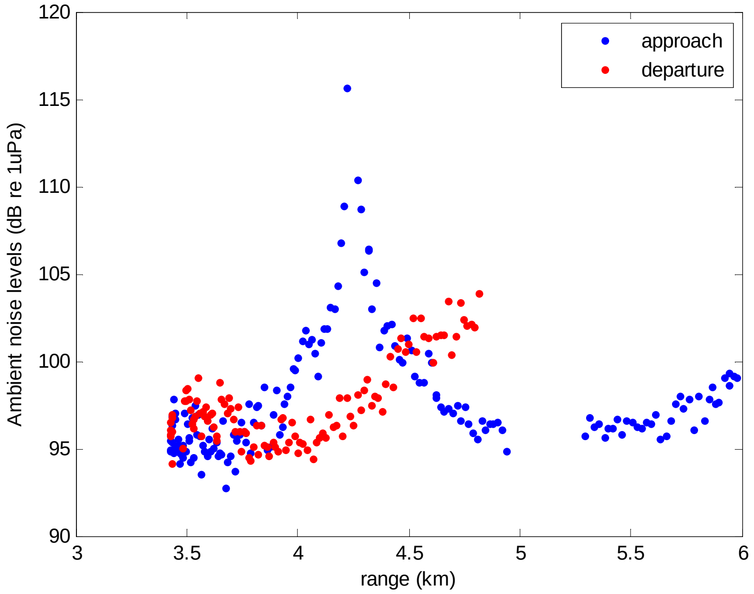

*Data from set of noise logger 2912 recording survey AG13. An abnormal strong background noise occurred for this data, as seen in the upper figure showing a data block of the noise logger output (mV vs. s). The noise was a second source of man-made noise (engine noise-like). The lower plot gives the ambient noise level (dB re 1µPa) for each shot of survey AG13 vs. range in km (air-gun approaching and moving away from the receiver). The ambient noise level - taken between the air-gun shots - is then naturally much higher than normal for this specific time. The highest ambient noise level (115.6 dB re 1µPa) is at range around 4.22 km, during the approach of the air-gun.*

# Appendix 22 - East run results

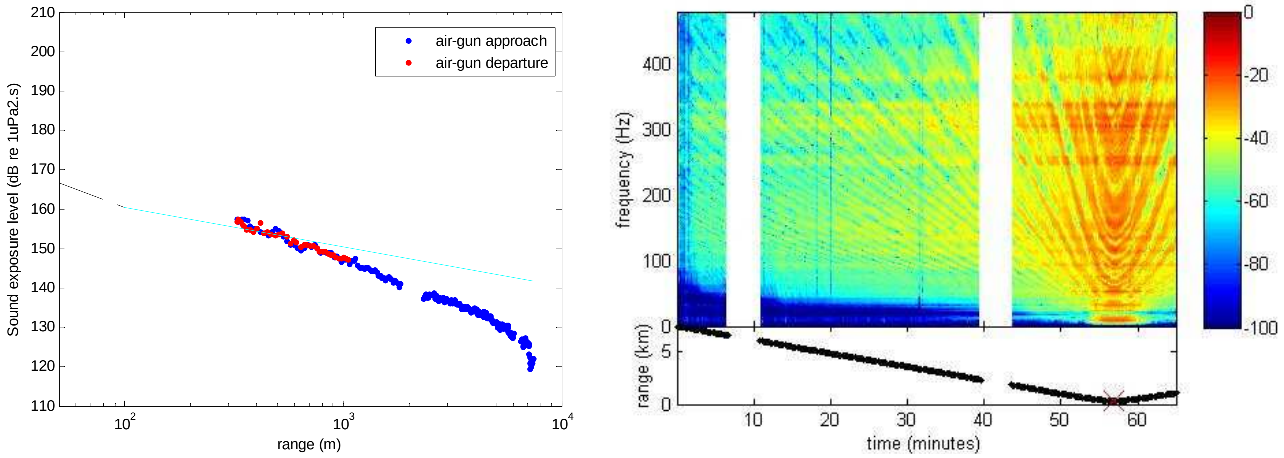

*SEL in dB re $1\mu Pa^2$.s vs. range (left) and transmission loss spectrum levels in dB re 1. $\mu Pa^2/Hz$ vs. time and frequency (right) for survey AG13 and set of noise logger 2911. This data is interesting as the results for the same survey were analyzed in section 3.3.2.3. Both graphs show the same characteristics, i.e. a reflective seabed to the east for most part of the run. The presence of a rock outcrop is shown with a clear drop off in SEL at the start of the run and high transmission loss values - both in low and high frequencies (acoustic conversion into shear waves in the bottom and scattering loss). Anyway, the transmitted signals seem less affected when considering this receiver position and demonstrates the importance of this parameter in sound propagation.*

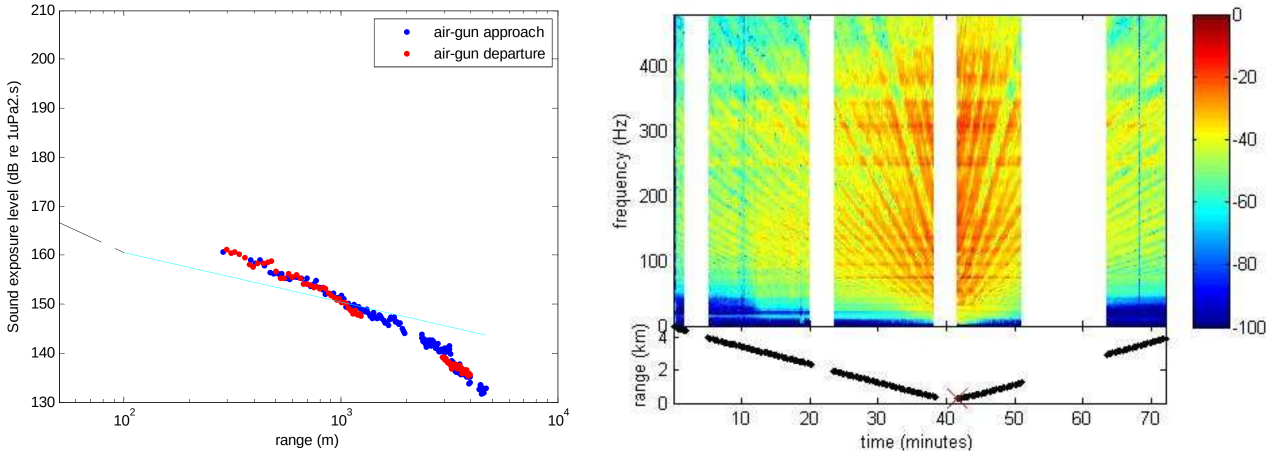

*Same results for AG09 recorded with set 2909. As this noise logger was deployed in the middle of the run track, the results permit to point out the fait symmetry in levels of transmitted air-gun signals, i.e. for the air-gun approach and departure The presence of a rock outcrop to the west is not shown for this set of data. Such results can be easily modelled using a waveguide of Pekeris type with a fluid seabed..*

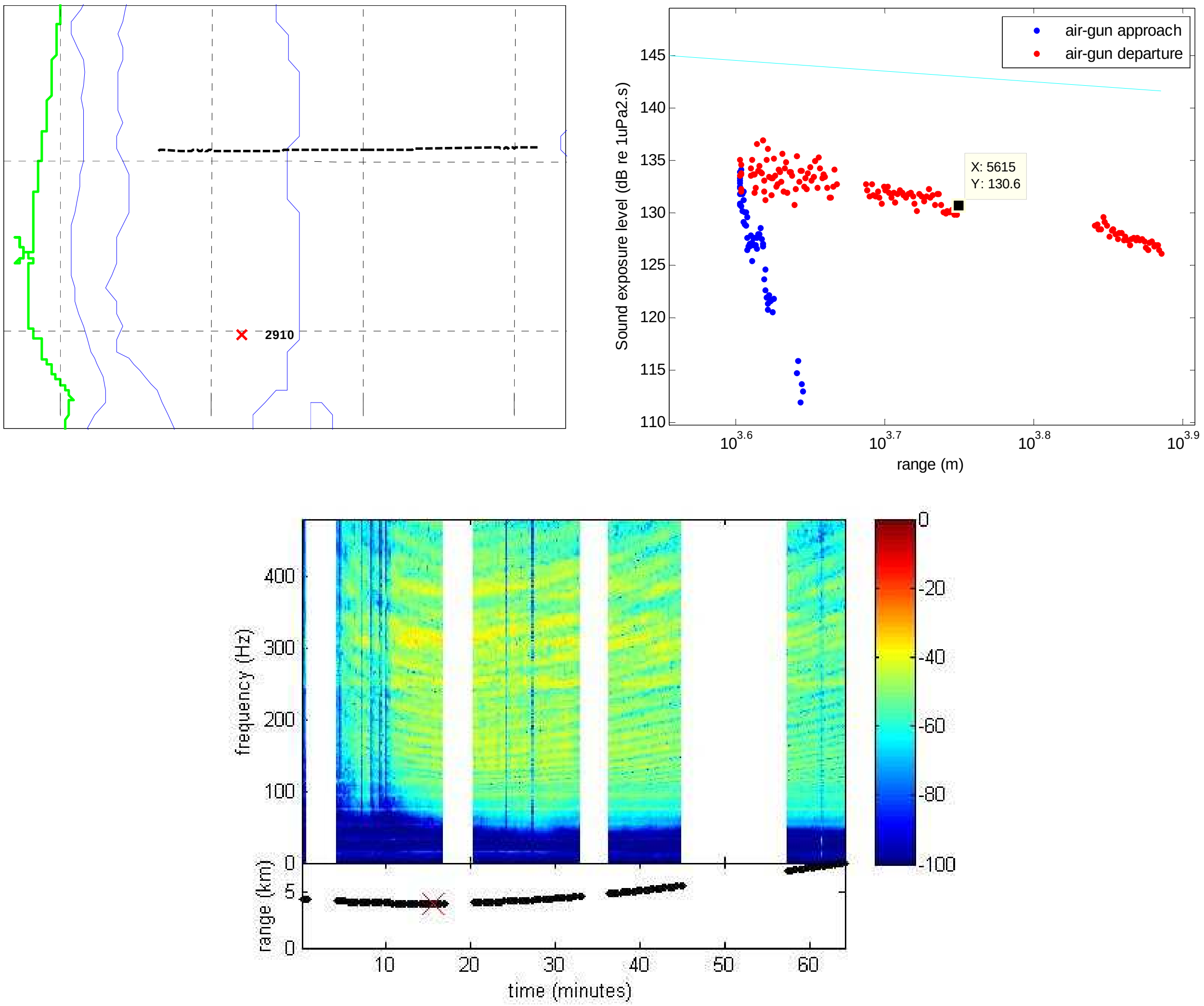

*Sane results for survey AG09 and set 2910. Upper left figure: receiver-source geometry. Upper right figure: SEL vs. range and cylindrical spreading slope. Only great ranges are considered for this data, from 4 km. Bottom figure gives the transmission loss spectrum levels vs. time and frequency. Of a particular note if the substantial drop off in SEL results and the high transmission loss values for the beginning of the survey. This shows clearly the presence of a the localized rock outcrop along the shore and south of the run, i.e. along the propagation path of the air-gun approach for set 2910. The strong and constant attenuation at all range below 50 Hz is interesting and show that a particular sub-bottom layer - quite absorptive - is sufficiently shallow to have effect on these frequencies. In fact, a sand layer can be seen as acoustically isolating the deeper layers. The higher frequencies penetrate the superficial layers of the bottom (first ten meters).*

# Appendix 23 - North run results

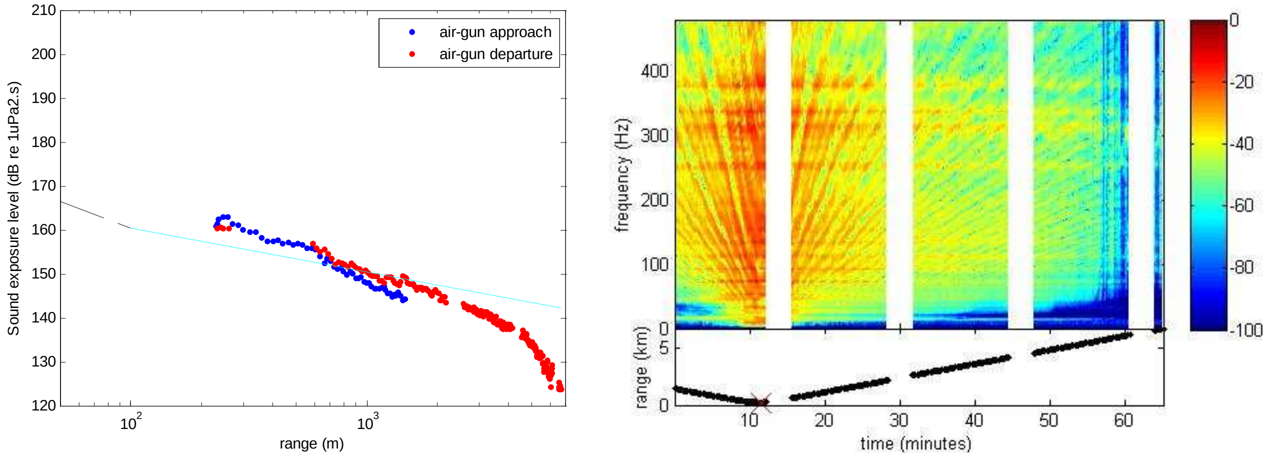

*SEL in dB re 1$\mu$Pa$^2$.s vs. range (left) and transmission loss spectrum levels in dB re 1. $\mu$Pa$^2$/Hz vs. time and frequency (right) for north run AG12 and set 2937. This logger was deployed along the run. It clearly shows the presence of the rock outcrop in the north, with drop off in the SEL levels from 4.5 km. Typical strong attenuation also occur in the transmission loss levels from 57 minutes both in low and high frequencies. Note that this data set may also show the presence of a soft rock seabed at the very beginning of the run. In fact, the SEL are slightly lower at the start of the air-gun approach and attenuation in the interval 20 - 50 Hz is noticed in the transmission loss for the same ranges.*

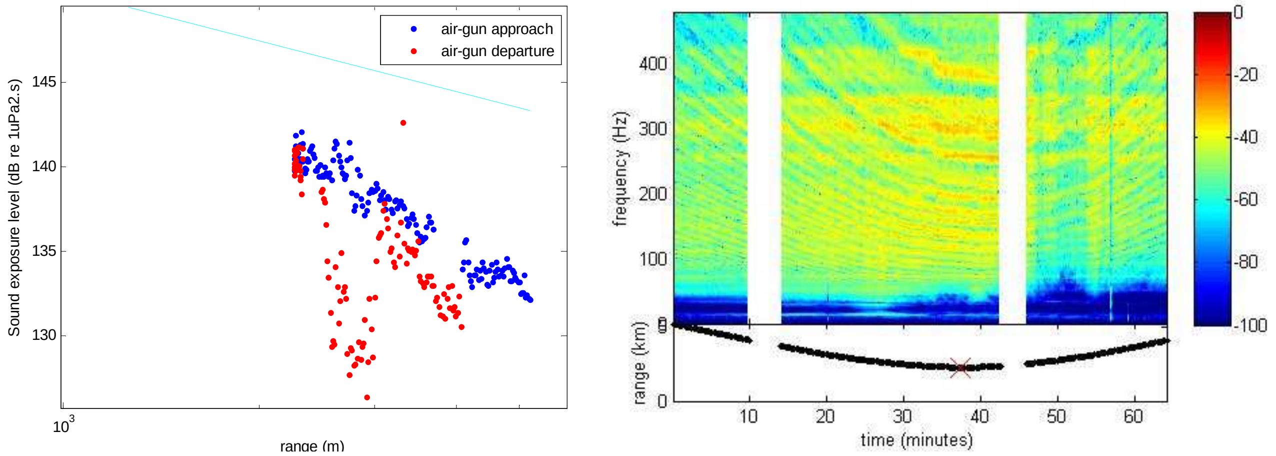

*Same results for set 2912 and run 11. The logger 2912 was deployed to the east of the north runs, with closest range around 2.3 km. Once again, the presence of the rock outcrop is clearly visible on both graphs. The levels increase when moving away from the outcrop and the interference pattern in the interval 100-400 Hz is visible in the transmission loss level plot at the end of the air-gun departure. The transmission loss levels also show a consistent attenuation at all range below 40-50 Hz which may imply the presence of an absorptive layer (e.g. made of limestone) affecting low-frequency acoustic energy. The consistent reflected energy of the mode 1 around 15Hz is visible for short ranges.*

# Appendix 24

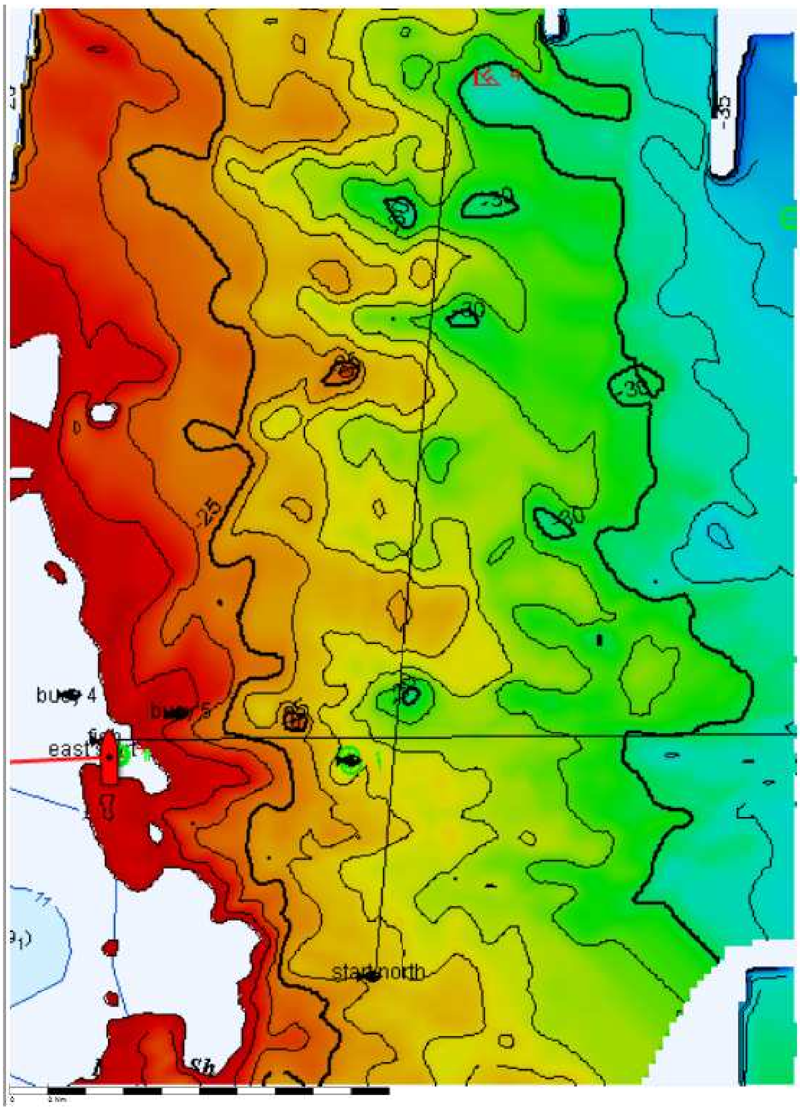

*Screenshot from the radar of the seismic vessel, zooming on the South part of the North runs. The 2 black bathymetry lines are 25 and 30 m.*

# Appendix 25

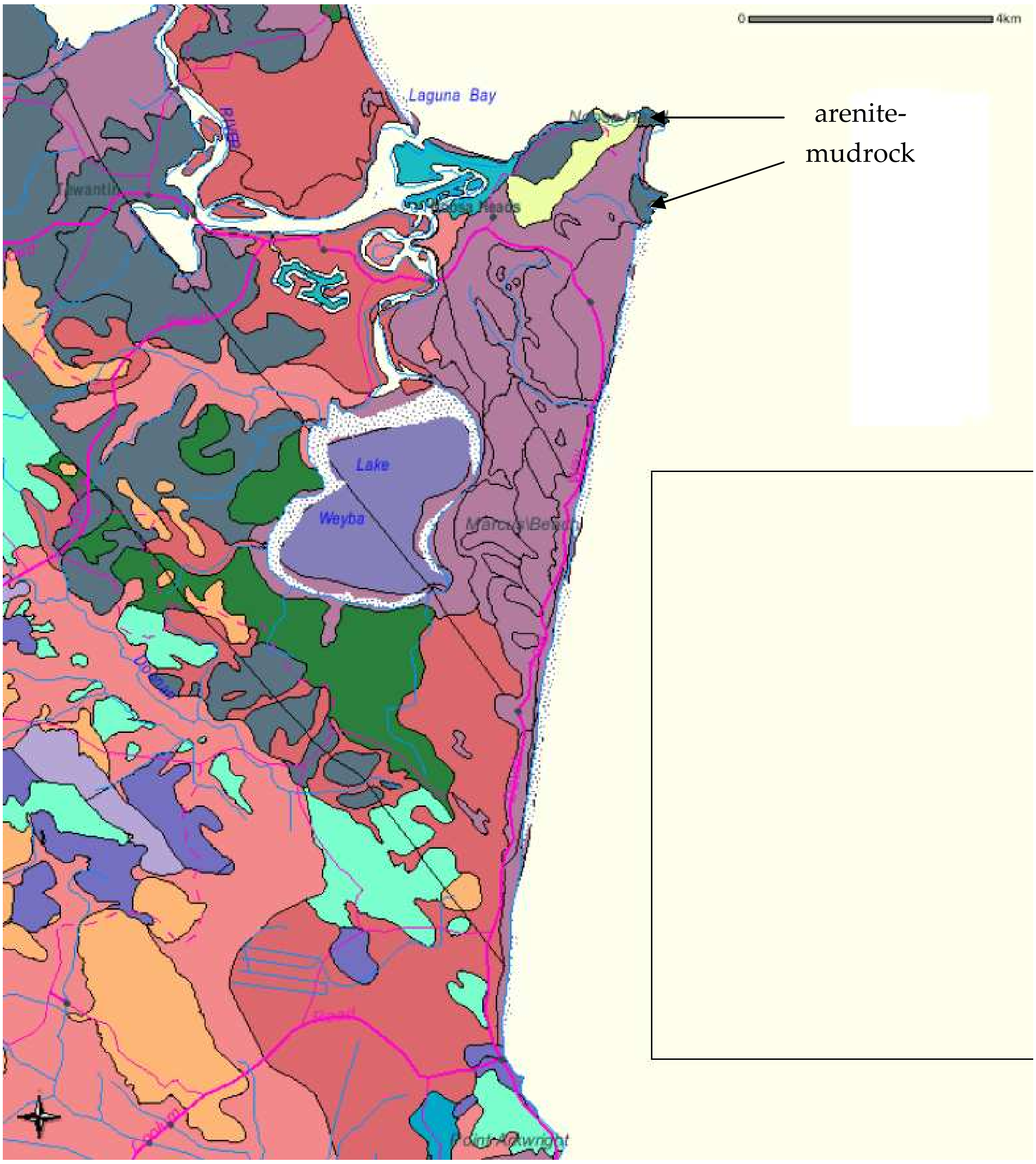

*Geological map of the coast nearby the covered area from the 1-month JIP survey. The black square indicates the western side of the covered area. Other coastal formations than arenite-mudrock are not of main interest, i.e. showing mainly sand or unconsolidated sediments.*

# Appendix 26

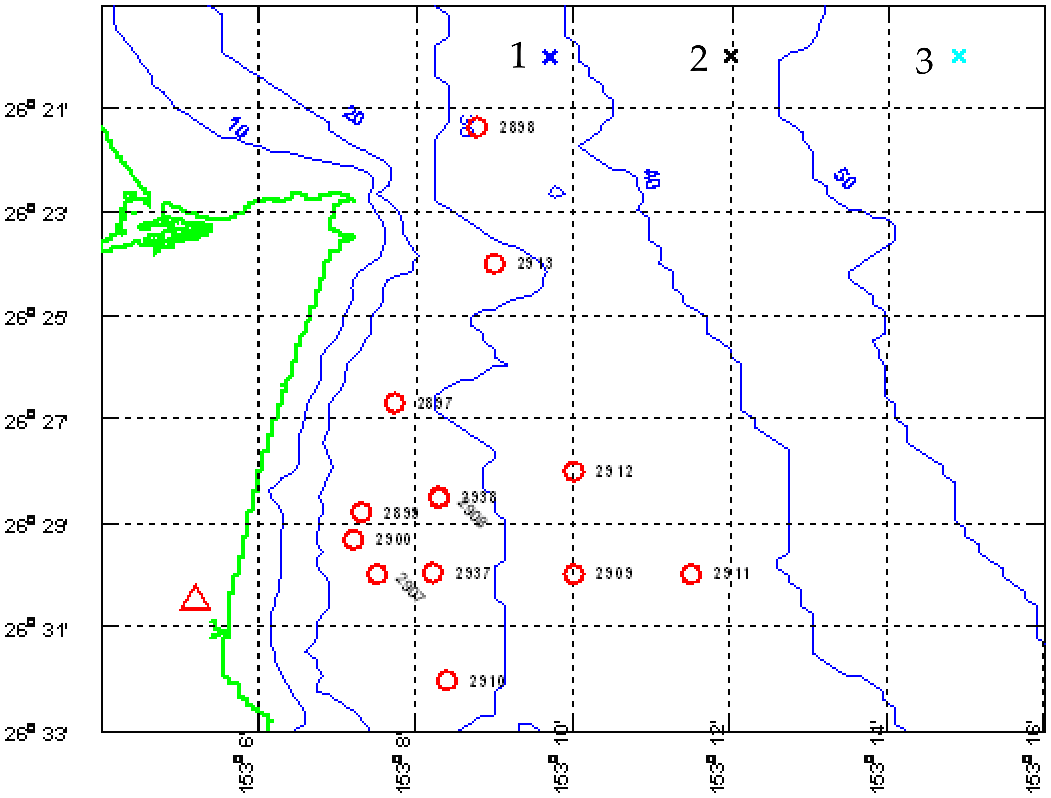

| | |
|---|---|
| 1 | 35-m water depth. Grab indicating 99.7% of sand, 0.2% of mud and 0.1% of gravel. |

| | |
|---|---|
| 2 | 42-m water depth. Grab providing a 1.32-m deep sand layer. 76 cm of brownish poorly sorted sand and 56 cm of olive sand. |

| | |
|---|---|
| 3 | 54-m water depth. Grab indicating 80% of fine quartose sand and 20% of medium sand. |

*Geological grabs data in the North of the covered area by the 1-month JIP survey. Source: MARine Sediment (MARS) database.*

# Appendix 27

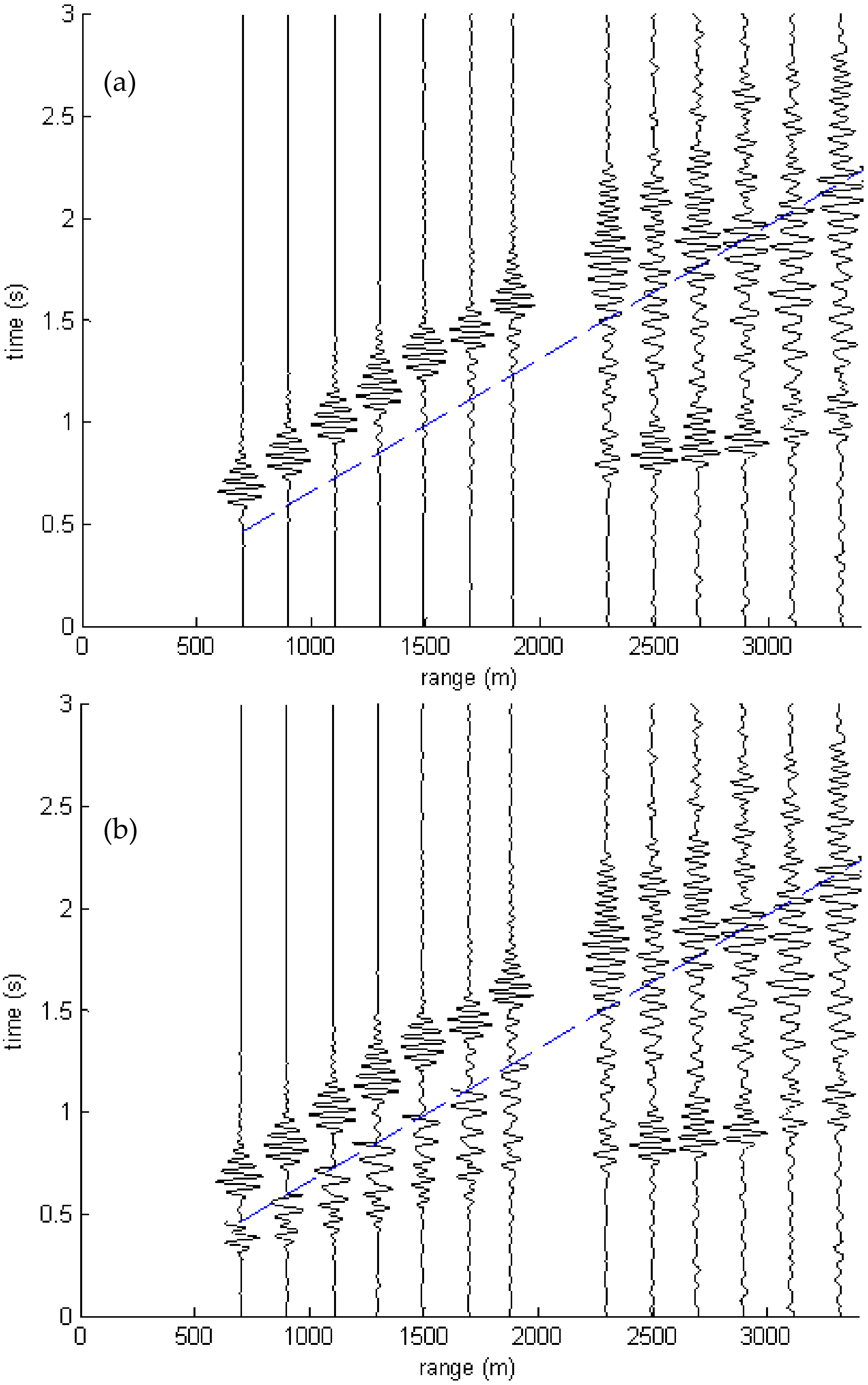

*Time-distance curve of run 6, set 2908 (a) and the same curve with wave arrivals highlighted before the waterborne arrivals - denoted by the blue line - for short ranges up to 1.9 km (b). This technique is not relevant for very short ranges shots (approximately below 1 km) as headwaves are usually re-radiated at long distances.*

# Appendix 28 - East run seismograms

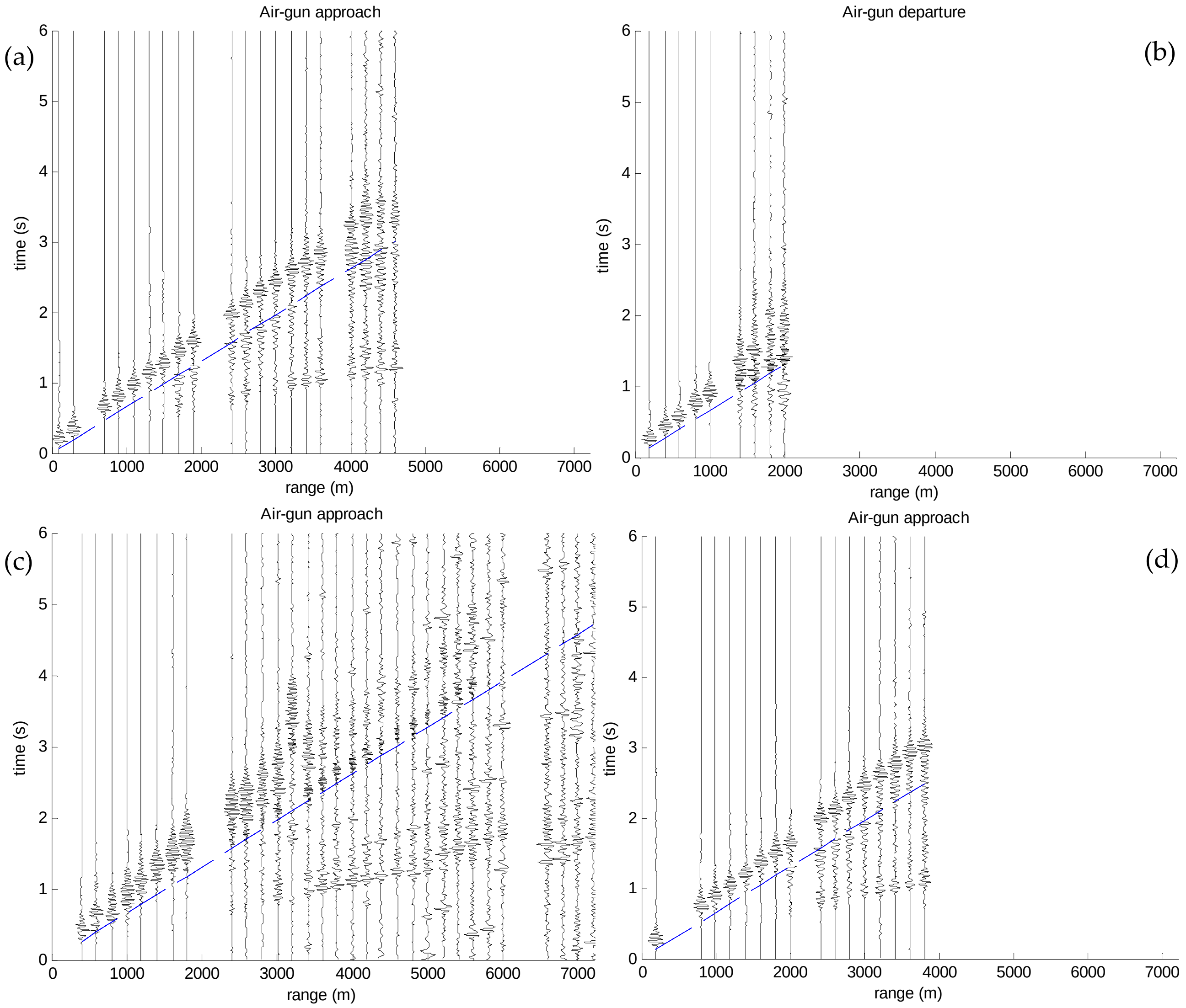

*Seismograms for various east run data sets: set 2909, run 7, air-gun approach (a); set 2909, run 7, air-gun departure (b); set 2911, run 13, air-gun approach (c); set 2909, run 5, air-gun approach (d). The blue lines denote the calculated waterborne arrivals. These seismograms show all one set of headwave arrivals, corresponding to the deep basement at a depth below seabed around 150 m and with a compressional sound speed around 4800 m/s. Note that the seismogram in (b) is not actually usable as it does not cover enough received signals at long distances.*

# Appendix 29 - North run seismograms

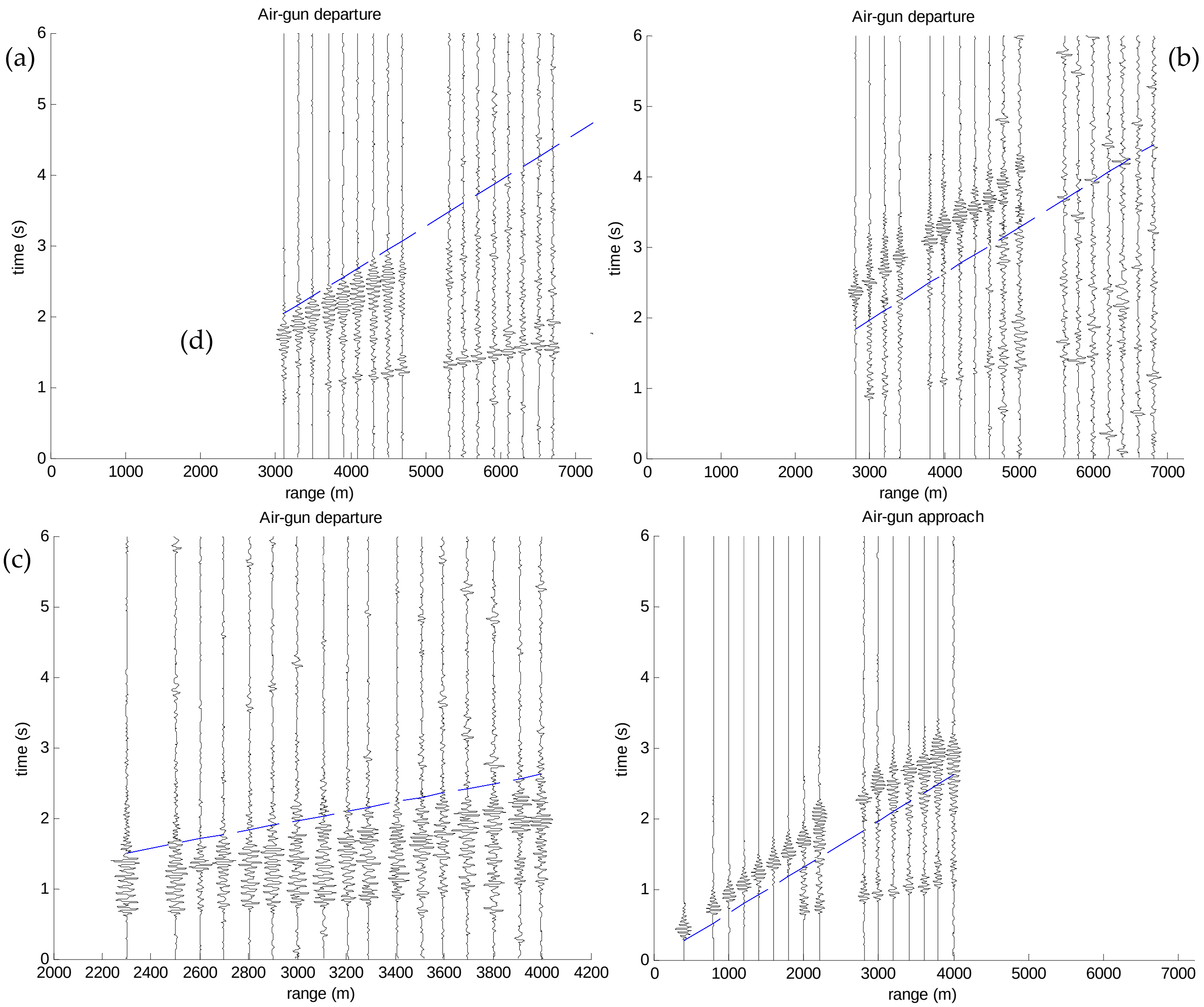

*Seismograms for various north run data sets: set 2910, run 8, air-gun departure (a); set 2909, run 4, air-gun departure (b); set 2912, run 11, air-gun departure (c); set 2938, run 12, air-gun approach (d). Note that the x-axis boundaries are different for (c). All seismograms show one set of headwave arrivals corresponding to the deep basement. The data from set 2910 in (a) are particularly interesting as no low-frequency waterborne arrivals appear in the seismogram. It is related to the position of receiver 2910, in the south of the area and close to the shore where there are coffee rock outcrops. The strong acoustic attenuation in low-frequencies explain this result. Note also the arrival of an unknown wave mentioned in the analysis, which appear over the rock outcrops and which is slower than the headwave but faster than the waterborne energy. The same result is observed for set 2912 in Fig (c).*

# Bibliography

[1] Richardson, W.J., Greene, Jr. C. R., Malme, C. I., Thomson, D.H. *Marine mammals and noise.* 1995, San Diego, USA.

[2] Tashmukhambetov, A. M. *Three-dimensional seismic array characterization study: experiment and modelling.* 2008, New Orleans, USA.

[3] Urick, R.J. *Principles of underwater sound (third edition).* 1967, Los Altos, USA.

[4] Duncan, A. J., Gavrilov, A., Fan, L. *Acoustic propagation over limestone seabeds.* 2009, Perth, Australia.

[5] Jensen, F. B.. *Computational ocean acoustics.* 1993, New-York, USA.

[6] Duncan, A. J., Gavrilov, A., Fan, L. *Propagation and inversion of airgun signals in shallow water over a limestone seabed.* 2009, Perth, Australia.

[7] Lurton, X. *An introduction to underwater acoustics*. 2002. Plouzané, France.

[8] McCauley, R. *Marine seismic surveys: analysis and propagation of air-gun signals; And effect of air-gun exposure on humpback whales, sea turtles, fishes and squid.* 2000, Perth, Australia.

[9] McCauley, R. *Measurements of air-gun signals from the Jean, Rita and Cheryl seismic surveys, Dongara to Abrolhos islands.* 2003, Perth, Australia.

[10] Dobrin, M. B. *Introduction to geophysical prospecting (second edition).* 1960, Calgary, Canada.

[11] Kangas, T. *On the geological sources of errors in refraction surveys.* 1963, Leppiniemi, Finland.